THE DEFORMATION OF COPPER-TUNGSTEN COMPOSITES

By

WARREN JAMES POOLE

A Thesis
Submitted to the School of Graduate Studies
in Partial Fulfilment of the Requirements
for the Degree
Doctor of Philosophy

McMaster University

THE DEFORMATION OF
COPPER-TUNGSTEN
COMPOSITES

DOCTOR OF PHILOSOPHY (1993)
(Materials Science and Engineering)

McMASTER UNIVERSITY
Hamilton, Ontario

TITLE: The Deformation of Copper-Tungsten Composites

AUTHOR: Warren J. Poole, B.E.Sc. (University of Western Ontario)

SUPERVISOR: Professor J.D. Embury

NUMBER OF PAGES: xiv, 222

ABSTRACT

A series of plane strain compression experiments and finite element method (FEM) calculations were performed on continuous fibre composites to examine the role of volume fraction and fibre arrangement on the mechanical behaviour when the fibre axis was perpendicular to the loading direction. The flow pattern in the matrix was quantified by measuring the shape change of a fine gold grid which had been fabricated on the surface of the sample prior to deformation. It was determined that the pattern of deformation in the matrix was controlled by the spacing and geometric arrangement of the fibres. The damage process (i.e. by fibre cracking or interfacial decohesion) can be understood by the local distribution of stresses (as calculated by FEM) in the fibres and at the fibre matrix interface. The development of the deformation texture in the matrix and the observations of the pattern of subsequent recrystallization events can be related to the flow pattern in the matrix. The combination of careful experiments with finite element method calculations represents a powerful approach to studying problems involving composite materials.

ACKNOWLEDGEMENTS

The author would like to express his sincere thanks to his advisor Dr J. David Embury for his constant encouragement and guidance throughout this work. The discussions in Los Alamos were especially useful and enjoyable. I would also like to thank David for his many especially creative suggestions.

Special thanks are dedicated to Dr. U.F. Kocks of Los Alamos National Laboratory for allowing me to spend time in Los Alamos. His hospitality and friendship during this time will be long remembered. The time I spent in Los Alamos was very productive from an academic and personal point of view.

Many thanks to Dr. S. MacEwen and Dr. I. Hansson for allowing me to spend time at Alcan's Kingston Research and Development Centre in order to perform the various finite element method calculations. The help of Al Langille in constructing and executing the finite element models is greatly appreciated.

Gratitude to Dr. T. Özturk for his friendship and help in developing the technique for preparation of fiducial grids. Mr. J. Garrett supplied endless help and advice in preparation of the samples. Dr. S.R. Chen and Mr. D. Nye (Los Alamos) were always pleasant and helpful colleagues to work with in the laboratories at Los Alamos.

The author wishes to express his thanks to Dr. S. Corbin for the many stimulating discussions at McMaster. These were always useful and pleasurable.

Finally, this work could not have been completed without the encouragement and support of my family and close friends.

TABLE OF CONTENTS

LIST OF FIGURES

LIST OF TABLES

CHAPTER 1

INTRODUCTION

The technological significance of metal matrix composites (MMCs) has increased recently due to lower production costs for the reinforcing materials and advances in fabrication and processing technologies for these composites. Composites such as the Alcan Ltd. aluminum-silicon carbide particulate (Al-SiC_p) system are presently being produced in commercial quantities. These materials have advantages such as improved stiffness to density ratios, increased wear resistance, lower coefficient of thermal expansion and improved high temperature mechanical properties. However, these materials also suffer from lower ductility and fracture toughness compared to conventional aluminum alloys. The mechanical properties of these composites are obtained by a combination of traditional aluminum alloy strengthening mechanisms (i.e. precipitation and solid solution hardening) as well as strengthening by load transfer due to the presence of the reinforcing phase (usually SiC or Al_2O_3).

The majority of the theoretical and experimental work on these composite materials has focused on the initial load bearing capacity in the elastic region and the elastic-plastic transition. The mechanical response of these materials has been described by both dislocation and continuum models depending on the scale of the structure. The outstanding problem in this regime is to describe the partitioning of load and displacement between the matrix and the reinforcement. This is further complicated by the intervention of alternative processes such as particle cracking or interface decohesion. The partitioning of load and displacement will be related to the mechanical properties of the constituent phases, the properties of the interface between the matrix and the reinforcement and the spatial distribution, size and shape of the reinforcing phase. This presents a more complicated problem than precipitation hardening, for example, where only a) the interaction between a dislocation and a particle and b) the distribution, size and volume fraction of particles need be considered.

Very little experimental or theoretical work exists for the large strain behaviour of composite materials. The majority of this work is concerned with the parameters which control the fracture process. Some experimental observations also have been made on texture development in the matrix and the kinetics of recrystallization in composites, however, little theoretical consideration has been given to these problems.

The purpose of the present work is to examine in detail the local distribution of stress and strain in a model composite system as a function of the geometric arrangement and volume fraction of the reinforcing phase. This information may then be used to understand a) macroscopic properties such as mechanical response and matrix texture development and b) to understand local behaviour such as the spatial distribution of recrystallization events and the formation of damage in the sample.

The approach taken to examine this problem was to carry out a series of careful experiments while concurrently conducting a series of finite element method simulations of deformation processes geometrically similar to the experimental work. The experimental work consisted of a series of plane strain compression tests on copper-tungsten fibre composites with the fibres perpendicular to the loading direction. A fine gold grid was prepared on the surface of the sample using an electron beam lithography technique in order that the local deformation pattern could be measured by examining changes in the local shape of the gold grid.

The copper-tungsten system was chosen for the experimental work in this study for the following reasons:

i) a wide range of mechanical properties data was available for this composite system.

ii) fabrication techniques have been established and the spatial distribution of the tungsten fibres can be controlled.

iii) the interface between copper and tungsten is relatively simple. There are no intermetallics formed and the elements have very low mutual solubilities.

iv) the mechanical properties of the constituent materials have been well studied in the literature.

This allowed for the study of a relatively simple system where the variables could be well controlled.

The thesis is organized in the following manner. Chapter 2 is a literature review of some of the relevant work which has been conducted by other researchers. It is not meant to be exhaustive, but rather to consider the different approaches taken to examining behaviour of these complicated materials. Chapter 3 describes the experimental and the computational techniques used in this work including details of the fabrication and processing of the samples for the mechanical tests. Chapter 4 presents the experimental results. Where appropriate the experimental and modelling results are presented together so that an easy comparison of them may be conducted. Chapter 5 is a discussion of the results with an emphasis on developing simple physically based models to understand the experimental and modelling results. Finally, Chapter 6 is a summary of the important conclusions that can be drawn from the present work and suggestions for future work in this field.

CHAPTER 2

LITERATURE REVIEW

2.1 Introduction

The literature review will start by presenting a brief overview of the previous work which has been done on copper-tungsten composites. This provides a historical context for the present work. After reviewing previous work, an overview of the theoretical approach which has been applied to understand the behaviour of two-phase materials will be presented.

2.2 Summary of Previous Work on Copper-Tungsten Composites

When considering the experimental observations on deformation of two-phase materials, it is important to consider questions of scale (i.e. size and volume fraction of the reinforcement), anisotropies (both elastic and plastic), thermal history and the nature of the loading path. The work on copper-tungsten systems is especially useful since a variety of scales of structures have been examined and as a result the behaviour has been described by both continuum and dislocation models. Not only is the question of scale as it relates particle size to dislocation spacing important but also the relative scale of the matrix to the fibre size (i.e. matrix grain size to mean fibre spacing).

The tensile behaviour of copper-tungsten composites with the fibres aligned with the loading direction was first studied by Kelly and Tyson (1965) and McDanels et al.

(1963 and 1965). They described four stages in the tensile behaviour of the composites (volume fractions ranging from 5-70 %, fibre diameters of 75-250 μm). In the first stage, both the matrix and fibre behave elastically and the modulus values agree well with a rule of mixtures analysis which assumes equal strain in both components. This predicts that the elastic modulus of the fibre composite ($E_{I\text{-composite}}$) is a function of the elastic moduli (E) and the volume fractions (V_f) of the matrix and the fibres, i.e.:

$$E_{I\text{-composite}} = E_{matrix} * V_{f\text{-matrix}} + E_{fibre} * V_{f\text{-fibre}} \tag{2.1}$$

The second stage of the tensile behaviour is characterized by a sharp drop in the slope of the stress-strain curve. This is associated with yielding of the matrix material. To a first approximation, the slope of the stress-strain curve in this regime is given by:

$$E_{II\text{-composite}} = E_{fibre} * V_{f\text{-fibre}} \tag{2.2}$$

The behaviour of the matrix in this region has been the subject of controversy in the literature. In stage III of tensile deformation, the fibres reach their yield stress and the composite has a region where both the matrix and the fibre are deforming plastically. Stage IV begins once the uniform elongation of the fibres has been reached and involves necking of the fibres followed by fibre failure. Several investigators have observed embrittlement of the tungsten fibres during fabrication (e.g. Kelly and Tyson, 1965 and Pederson, 1990). In this case, stage III and IV are not observed. Stage II is directly followed by a region of brittle fibre failure. The first three stages of deformation are illustrated from the data of Kelly and Lilholt (1969) in Figure 2.1.

These preliminary studies were followed by a series of in-depth examinations of the low strain behaviour. Cheskis and Heckel (1968) performed a series of *in situ* x-ray

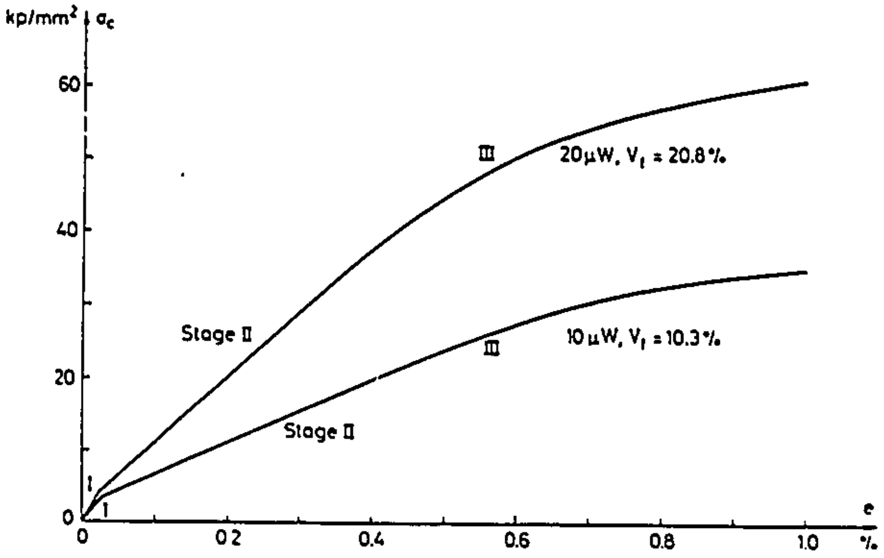

Figure 2.1 - Plot of lattice strain (measured by x-ray diffraction) vs. macroscopic strain in the composite (measured by a strain gauge attached to sample), (Cheskis and Heckel, 1968).

diffraction experiments on copper-tungsten composites prepared by electrodepositing copper on to 20 μm tungsten fibres. The lattice parameter of the tungsten and the copper were measured as a function of the applied strain. The applied strain was measured by a strain gauge on the back of the sample. The results of their measurements are shown in Figure 2.2. Their results indicate that there is a 1:1 relationship between the strain in the tungsten fibre measured by the change in lattice parameter and the applied strain. However, the ratio of strain measured by change in lattice parameter in the copper to the imposed strain was 0.75. It is difficult to understand how the strains in the matrix could be less than in the fibres. This is important because an elaborate analysis of the Cheskis and Heckel data was performed by Pederson (1990). Pederson has attributed a strong deviation in the behaviour of the matrix to the presence of the fibres based on this data. Later work by Cheskis and Heckel (1970) indicated that this effect was not observed in aluminum-tungsten composites. The analysis of this data was simpler since both tungsten and aluminium are close to being elastically isotropic.

Kelly and Lilholt (1969) presented a set of experiments on copper-tungsten composites with 10 and 20 μm fibres in a single crystal of copper with volume fractions ranging from 5 to 40 %. These samples were prepared by liquid metal infiltration. The derived matrix curves in stage II showed a large deviation from that expected in single crystals of copper (see Figure 2.3). This deviation was attributed to a strong interaction between the matrix and the fibres. As a result of the inability of continuum models to describe this interaction, dislocation models were proposed to describe the behaviour (Neumann and Haasen, 1971 and Brown and Clarke, 1977).

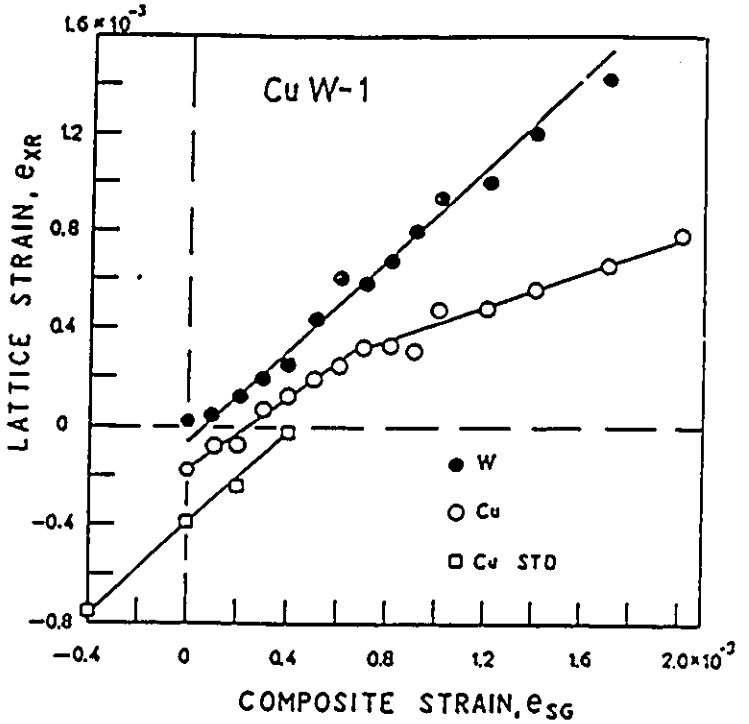

Figure 2.2 - Experimental stress-strain curves for copper-tungsten composites illustrating the different stages in deformation behaviour of the composite (Kelly and Lilholt, 1969).

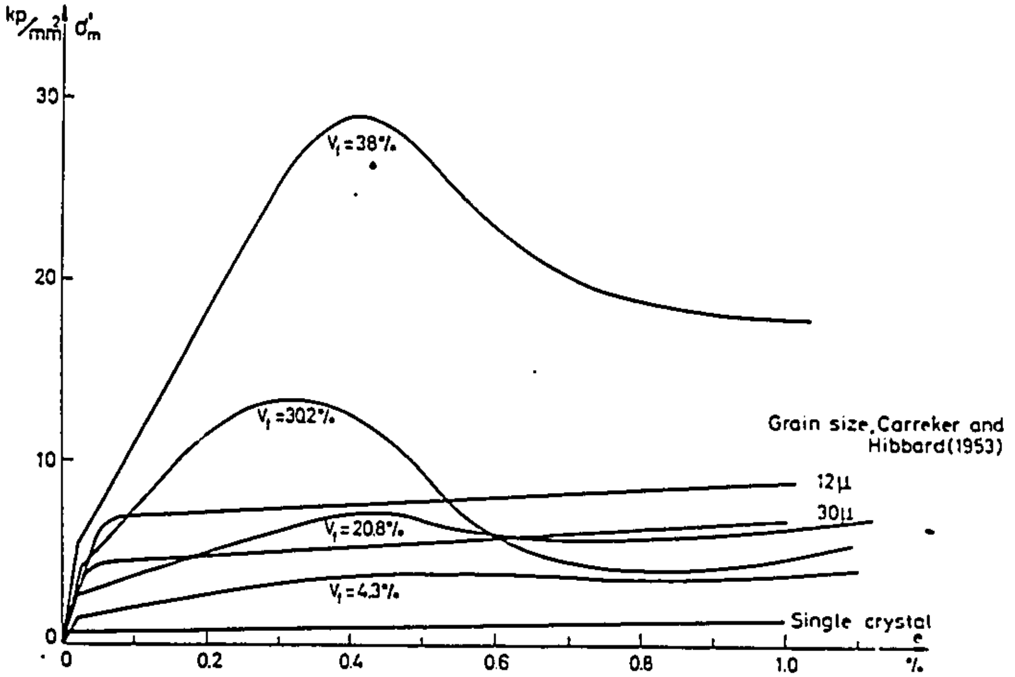

Figure 2.3 - Derived stress-strain curves for copper matrix from Cu-W composites reinforced with 20 μm fibres, (Kelly and Lilholt, 1969).

Chawla and Metzger (1972 and 1977) published results on copper tungsten composites with 230 μm fibres which were prepared by liquid metal infiltration. The matrix was a single crystal of copper and the volume fractions of tungsten ranged from 1-30%. The initial dislocation distribution after fabrication was examined by etch-pit studies. Chawla and Metzger (1972 and 1977) found that there was an increased dislocation density near the fibres as shown Figure 2.4 in which they interpreted as arising due to difference in thermal expansion coefficients during cooling of the samples. Analysis of the stress-strain behaviour of the matix in Stage II demonstrated that the flow curve was modified due to the presence of the fibres.

Lee and Harris (1974) performed tensile tests on samples fabricated by electrodepositing copper on to tungsten fibres of 11-48 μm and then hot pressing a set of layers to produce a flat sample. The matrix grain size in these samples was reported to vary between 1.5 and 7 μm while the volume fraction of tungsten was held constant at 37 %. The results of the derived matrix curves in stage II as a function of fibre diameter are shown in Figure 2.5. No attempt was made to relate the derived matrix flow curves to the grain size in the matrix.

In a pair of articles, Lilholt (1977a and 1977b) performed a series of strain reversal tests (i.e. Bauschinger effect) on copper-tungsten composites at 77 K and 273 K. The Bauschinger effect was defined as the difference between the forward and reverse flow stress. The volume fraction of tungsten fibres (20 μm) was between 0.5 and 4 % and the samples had single crystal matrices prepared by liquid metal infiltration. Some of the results at room temperature and 77 K are shown in Figure 2.6. Further

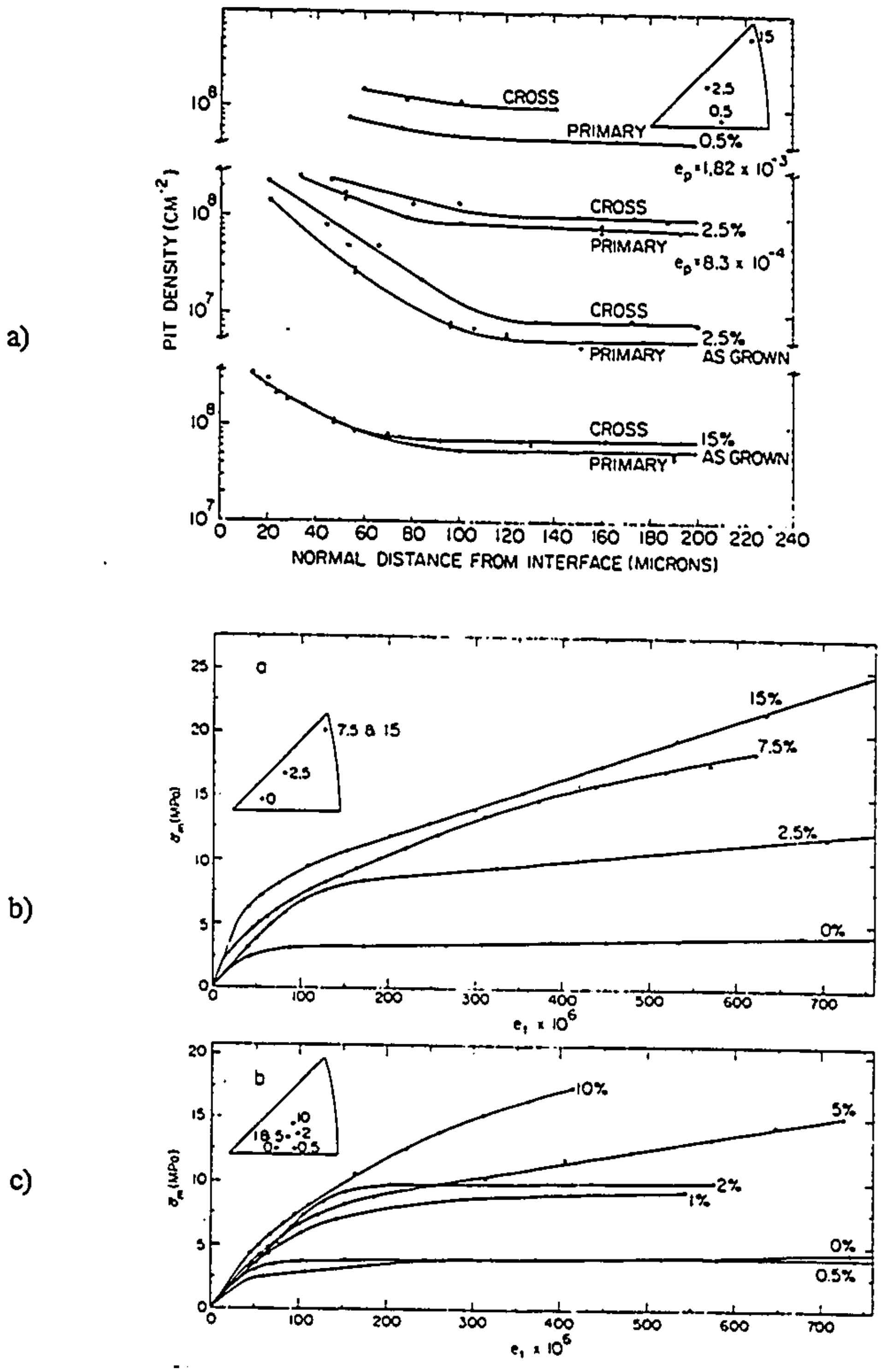

Figure 2.4 - a) Etch pit density for primary and cross-glide planes as a function of distance from the interface (numbers in % refer to volume fraction), b) and c) derived matrix stress-strain behaviour for composites (Chawla and Metzger, 1977).

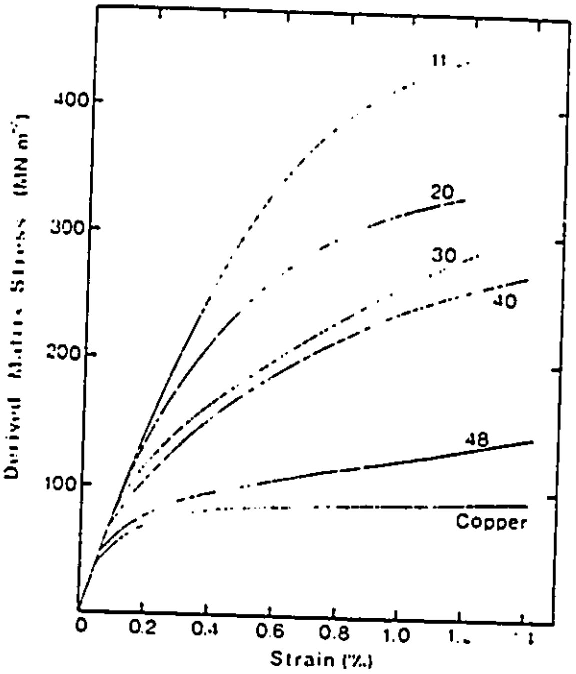

Figure 2.5 - Derived matrix stress-strain behaviour as function of fibre diameter (Lee and Harris, 1974).

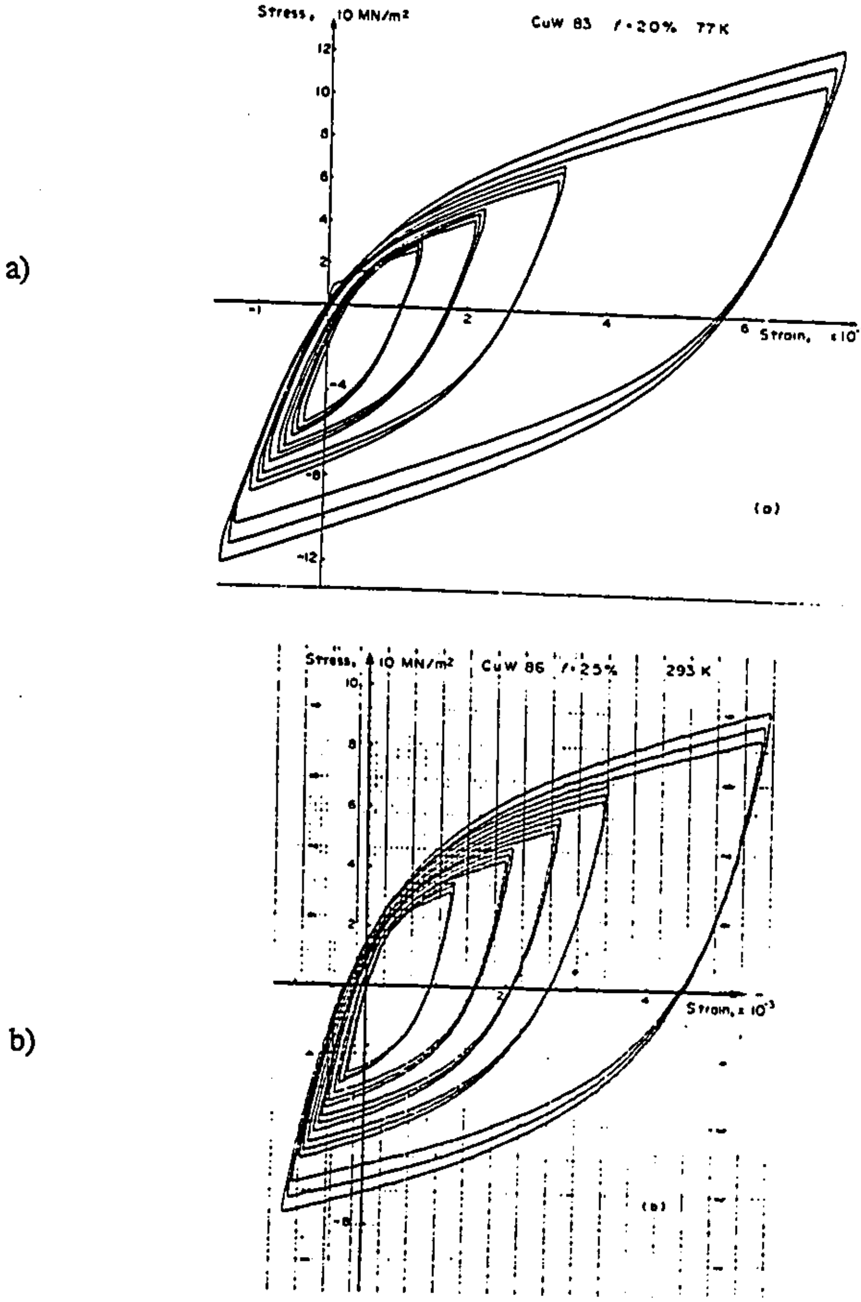

Figure 2.6 - Experimental stress-strain curves of Bauschinger tests, a) Cu-W volume fraction 2.0 % at 77 K and b) Cu-W volume fraction 2.5 % at room temperature. (Lilholt, 1977a).

results at higher volume fractions of tungsten fibres (100 μm) were obtained by Pederson (1990) at 77 K. In these cases a large Bauschinger effect was observed and a linear relationship was obtained between the magnitude of the Bauschinger effect and the forward plastic strain up to 1 % plastic strain (see Figure 2.7).

The experimental work on copper matrices reinforced with discontinuous tungsten fibres is limited. Kelly and Tyson (1965) studied properties at 250 °C (i.e. above the ductile-brittle transition for tungsten) for aspect ratios of 5-40 and volume fractions of tungsten between 27 and 53 % (see Figure 2.8). These composites were prepared by laying fibres which had been cut to the appropriate length in the graphite mould prior to infiltrating the mould with liquid copper. Harris and Ramani (1975) prepared discontinuous fibre samples by hot pressing. The samples contained 380 μm tungsten fibres at a volume fraction 25 % and were hot pressed at 550 °C. The microstructure of the copper matrix was not reported but is was noted that the interfacial strength was lower in these samples then for samples prepared by liquid metal infiltration.

Some very interesting experiments on dimensional stability of copper-tungsten composites were performed by Yoda and co-workers (1978). These experiments involved a series of thermal cycles between 800 °C and 200 °C (note: the coefficients of thermal expansion for copper and tungsten are 16.6×10^{-6} C^{-1} and 4.5×10^{-6} C^{-1}, respectively). Figure 2.9 is a plot of the axial extension of the sample vs. number of thermal cycles. It is clear that very large plastic strains (i.e. > 10 %) were observed. This is an extreme example of dimensional instability but it is always a concern in two-phase materials which experience thermal cycles.

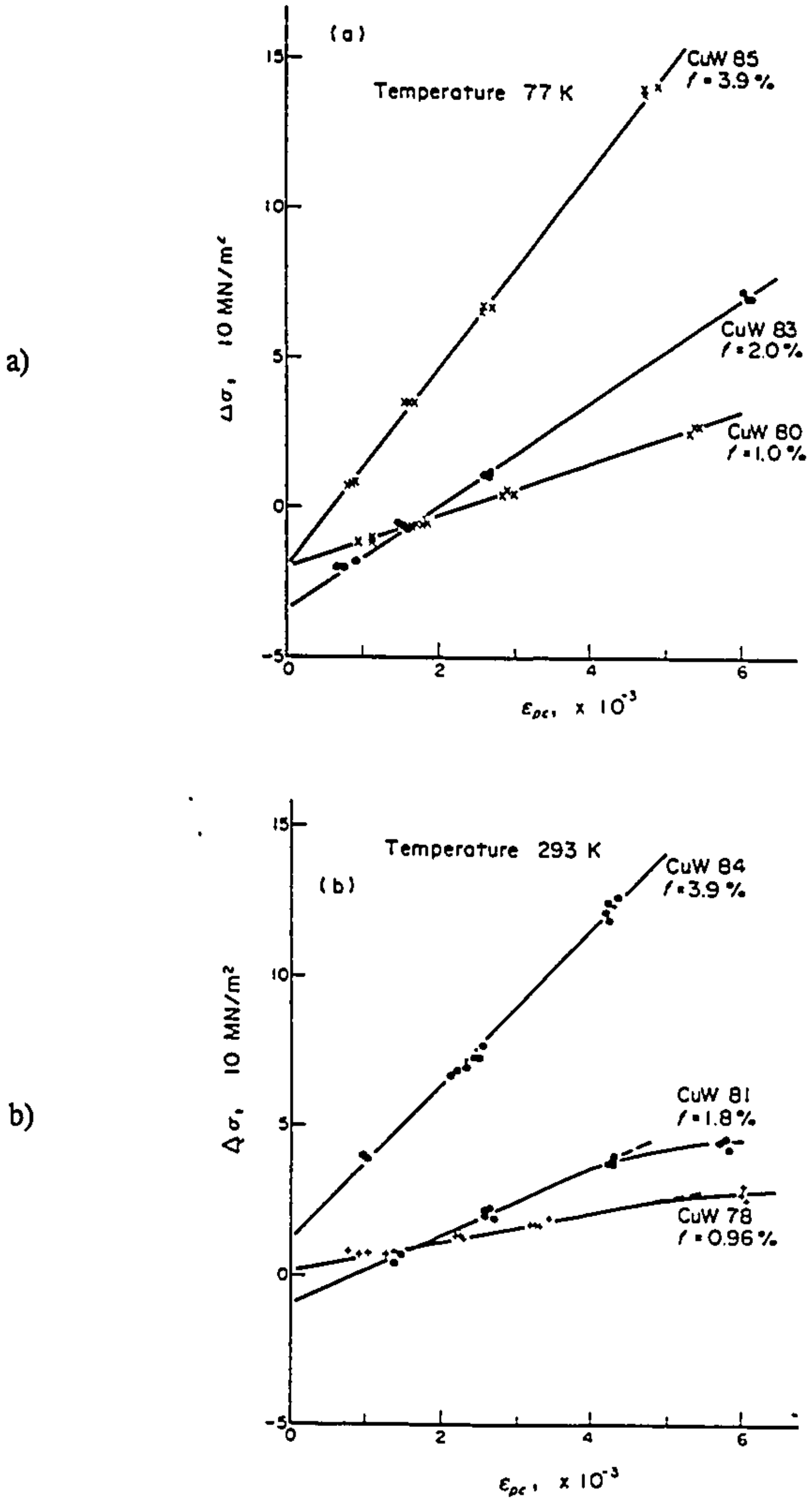

Figure 2.7 - The stress difference, $\Delta\sigma$ vs. forward plastic strain at a) 77K and b) room temperature. (Lilholt, 1977a).

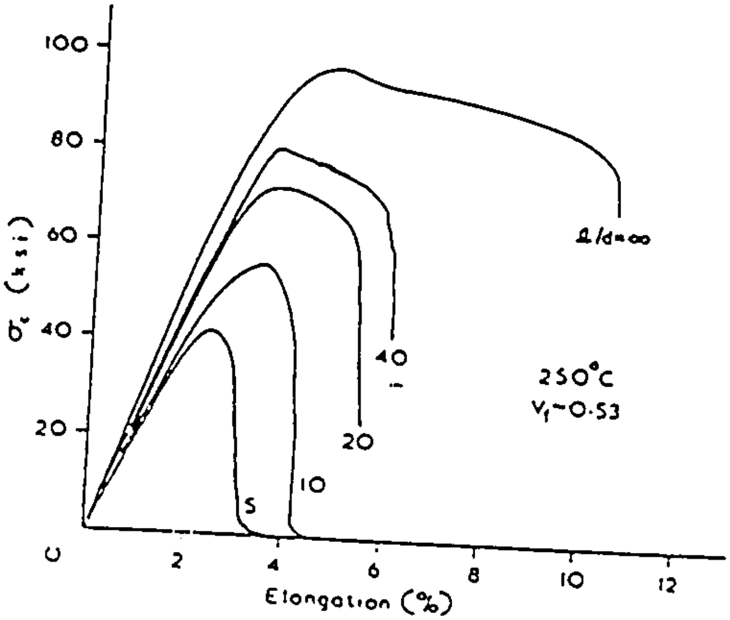

Figure 2.8 - Stress-strain curves for discontinuous copper-tungsten composites, (Kelly and Tyson, 1965).

a)

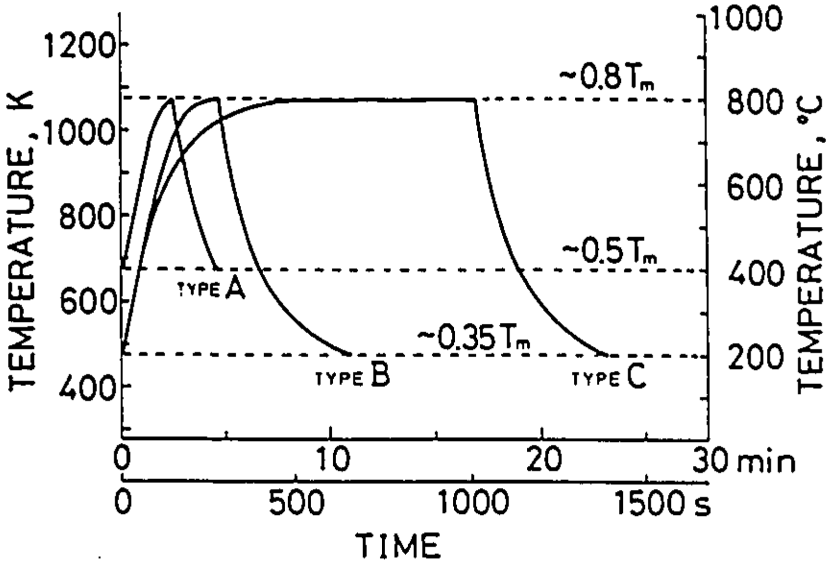

b)

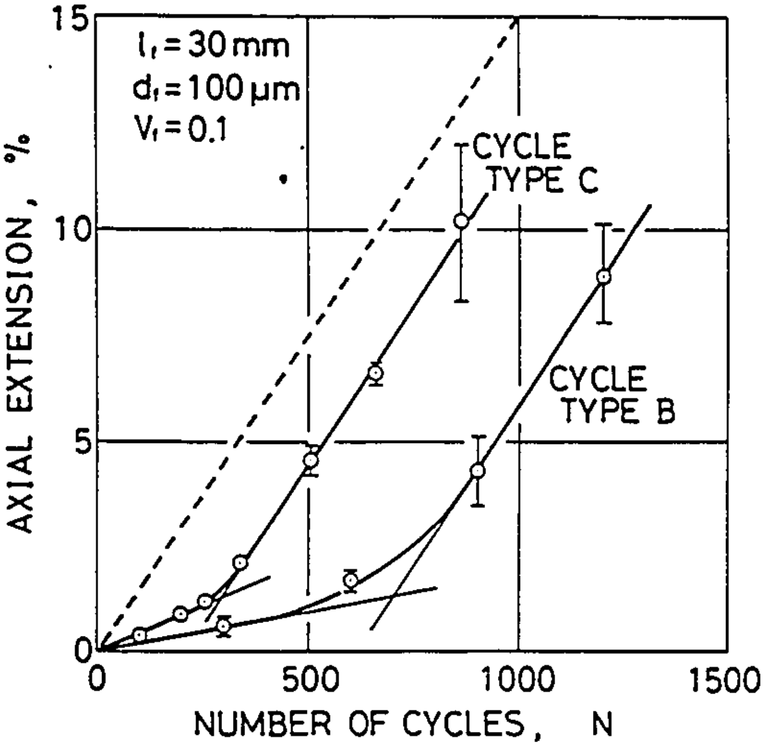

Figure 2.9 - a) schematic of thermal cycles and b) percentage axial extension vs number of thermal cycles for different thermal cycles (Yoda et al., 1978).

There is a wide variety of previous work on copper-tungsten system although most of the work has involved tension tests parallel to the fibre direction. The work has also been primarily concerned with low strain behaviour. The modifications in matrix behaviour in these materials indicate that scale effects and thermal history must be considered. This has led to application of both continuum and dislocation models to understand the behaviour of this system. This background provides a good framework for the experimental and modelling work which is considered in the present work.

2.3 - Strengthening Mechanisms in Two-phase Materials

Theories for the mechanical response of composite materials can be divided into two main groups. Continuum models depend on macroscopic properties of the materials and do not deal with the details of the process at the microscopic level (i.e. the dislocation level). These models are scale independent but depend on the volume fraction, shape and intrinsic properties of the reinforcing phase and the matrix. The other main type of model, dislocation models, depend on a detailed analysis of the dislocation behaviour at the local level and produce results dependent on the scale of the second phase.

2.3.1 - Continuum Models

This group of models can be further divided into models for elastic behaviour and models which include plastic deformation. A wide range of models is encompassed under this description from elasticity models such as Eshelby's equivalent inclusion to models of plasticity such as slip line field analysis.

Elastic Models

Analytical solutions of elastic problems are appealing due to the closed form of the solution. Unfortunately, exact solution can only be obtained for a few special cases. However, these special cases are of practical importance and have widely been applied to the analysis of composite materials. There are two main approaches to solving elasticity problems. The traditional approach involves solving the Airy stress function under the appropriate boundary conditions. A novel approach to solving elasticity problems was offered by Eshelby (1957) who considered a series of cutting and welding exercises to determine the elastic stress and strain fields around an inclusion. Using this technique Eshelby (1957) was able to develop solutions for spherical and ellipsoidal inclusions embedded in infinite media.

It is of value to present the elastic solution for a cylinder embedded in an infinite medium since this is of relevance to the present work. This can also be used as an illustration of some of the strengths and weaknesses of this approach. With the assumptions of elastically isotropic materials and plane strain deformation, Muskhelishvili (1953) has derived the following results:

Stresses outside the particle:

$$\sigma_{xx} = (PR^2/2r^2)\cos 2\Theta\,(\beta - \gamma) + (PR^2/2)\cos 4\Theta\,[\beta/r^2 + 3\delta R^2/r^4] \qquad (2.3)$$

$$\sigma_{yy} = P + (PR^2/2r^2)\cos 2\Theta\,(\beta + \gamma) - (PR^2/2)\cos 4\Theta\,[\beta/r^2 + 3\delta R^2/r^4] \qquad (2.4)$$

$$\tau_{xy} = -(P\gamma R^2/2r^2)\sin 2\Theta - (PR^2/2)\sin 4\Theta\,[\beta/2r^2 + 3\delta R^2/2r^4] \qquad (2.5)$$

Inside the particle

$$\sigma_{xx} = P/2(\alpha + \lambda) \tag{2.6}$$

$$\sigma_{xx} = P/2(\alpha - \lambda) \tag{2.7}$$

where :

P = applied stress
r = radius of particle
R = radial distance from centre of particle
Θ = angle
G = shear modulus of matrix
G_o = shear modulus of inclusion
ν = Poisson's ratio of matrix
ν_o = Poisson's ratio of inclusion
$\beta = -2(G_o - G/(G+G_o\chi_o)$
$\gamma = [G(\chi_o-1)-G_o(\chi-1)]/[2G_o + G(\chi_o-1)]$
$\delta = G_o - G/(G+G_o(\chi-1))$
$\alpha = k(\chi+1)/(2k+\chi_o-1)$
$\lambda = k(\chi+1)/(k\chi+1)$
$k = G/G_o$
$\chi = 3-4\nu$
$\chi_o = 3-4\nu_o$

Several important observations can be made from this solution: i) the stresses inside the particle are uniform and are at a higher value than the far-field stress for the case where the particle is stiffer than the matrix ii) the stresses outside the particle fall off as inversely proportional to the square of distance and iii) the stresses, outside the particle have a strong orientation dependence. The results of Eshelby for spherical and ellipsoidal inclusions indicate a uniform stress field in the inclusion with a decay in stresses outside the particle inversely proportional to the cube of the distance from the inclusion . The detailed information of the stress distribution outside the particle is important for an understanding of subsequent processes such as matrix yielding or interfacial debonding. The disadvantage of these solutions is the fact that the treatment is rigourous only in the case of an infinite matrix.

The exact treatment of many-particle problems represents a large increase in the difficulty of the problem and to best knowledge of this author has not be solved at present. For this reason, simplifying assumptions are made to investigate these more complicated problems. For example, various approaches such as mean field models (Pederson, 1983 and 1990) and self-consistent models (Hill, 1965) have been to predict elastic properties of two-phase materials. An excellent review of Eshelby models and the application of mean field models has been given by Withers et al. (1989). Recently, Corbin (1992) has extended the self-consistent model to predict elastic-plastic behaviour for both uniform and non-uniform distribution of particles. The main drawback of these models is their inability to treat the detailed nature of the stress distribution in the matrix.

Plasticity Models

Drucker (1965) presented an argument based on application of the upper bound theory from plasticity to examine the effect of second phase particles on the stress-strain behaviour of the matrix. He proposed that a regular arrangement of spherical particles in a perfectly plastic matrix would only affect the yield behaviour due to the resulting non-homogeneous stress distribution (see Figure 2.10a). In the case of a strain hardening matrix, the prediction was that the stress-strain curve would be modified due to a compression of the plastic strain scale due to the presence of the non-deforming phase (see Figure 2.10b). Drucker concluded that only in the cases of large constraint between the two phases (i.e. high volume fractions or closely spaced platelets) would

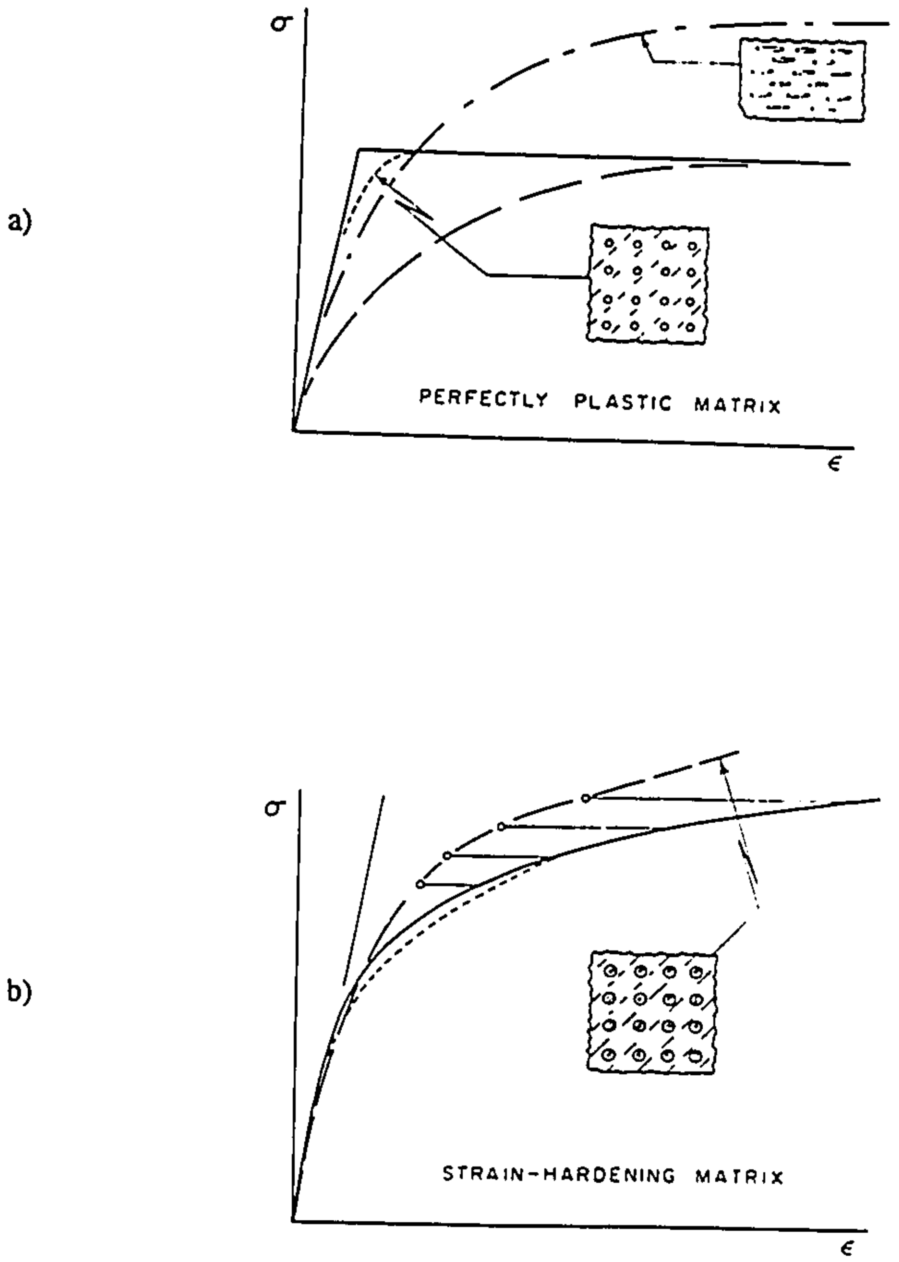

Figure 2.10 - The effect of inclusion which are large on the microstructural scale on stress-strain behaviour, a) perfectly plastic material and b) strain hardening matrix. (Drucker, 1965).

there be substantial strengthening of the material.

Brown and Stobbs (1976) proposed the use of upper and lower bound method from the theory of plasticity to investigate the development of stresses in second phases. In this treatment, the second phase particle is treated in a similar manner to the classic upper and lower bound calculations for a hardness indentor. The flow pattern for the upper bound and the stress distribution for the lower bound are shown in Figure 2.11. Based on this approach, Brown and Stobbs predicted that the stress in the particle must be between 3.8 and 4.7 times the local stress.

Finite Element Method Calculations

Recently, a series of finite element method (FEM) calculations have appeared in the literature (e.g. Christman et al., 1989, Brockenbrough et al., 1991, Bohm and Rammerstorfer, 1991). These types of models have become more common due to the increased availability of the required computing capabilities. These models divide the material into a series of small elements connected at nodal points. Each element is assigned a set of materials properties (elastic and plastic) which are usually representative of the bulk materials. The model is then tested by applying a set of boundary conditions and calculating the displacements and forces at each nodal point. From the forces and displacements of the nodal points the stress and strain in each element may be calculated.

Christman et al. (1989) have used FEM calculations to examine the effects of reinforcement shape and distribution on the elastic and plastic properties of Al-SiC$_p$ composites. Figure 2.12a and b shows a comparison of the effect of spherical and whiskers (aspect ratio of 5) respectively. It is apparent that the FEM calculations predict

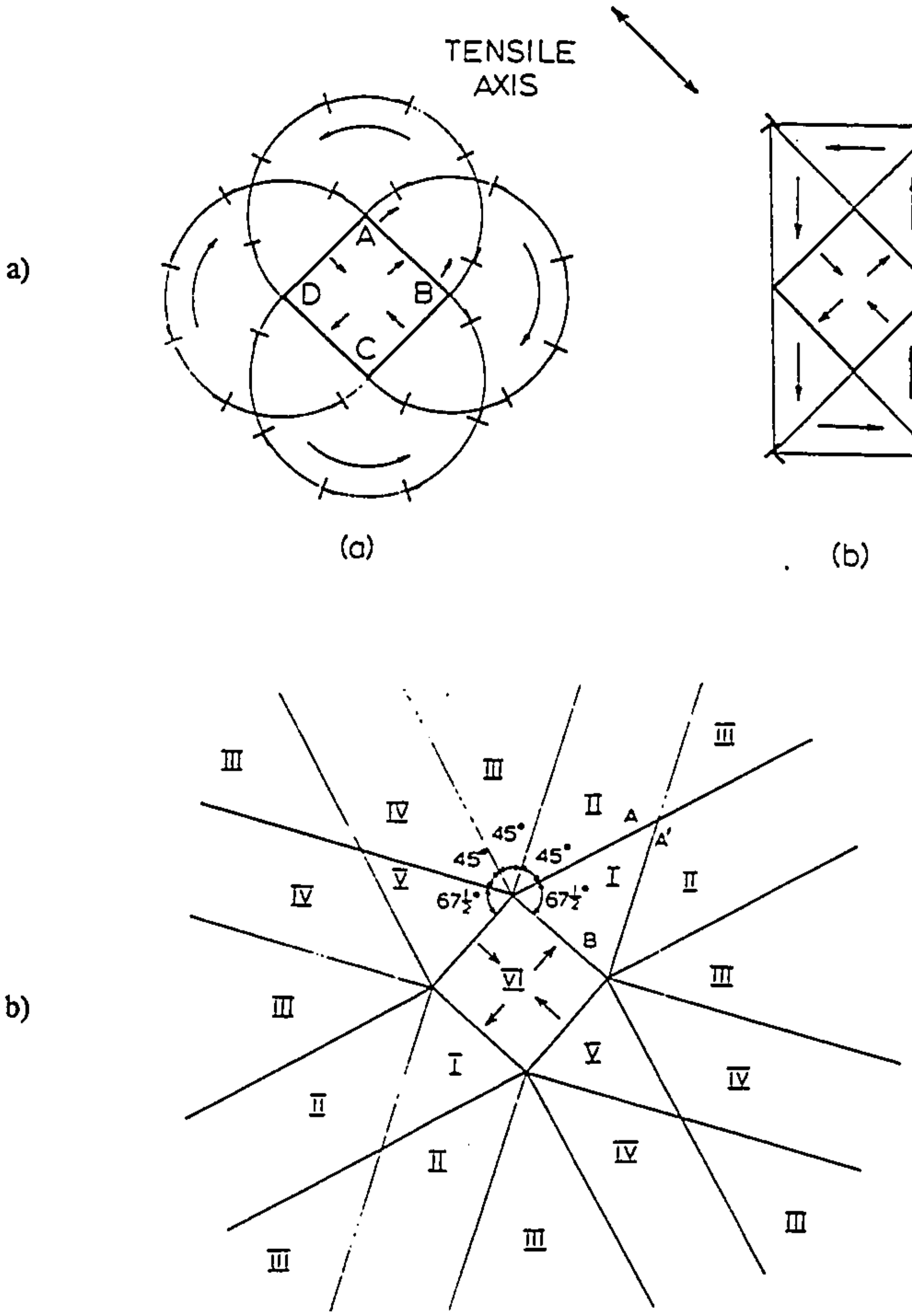

Figure 2.11 - Possible plasticity solutions to particle embedded in matrix a) lower bound and b) upper bound. (Brown and Stobbs, 1976).

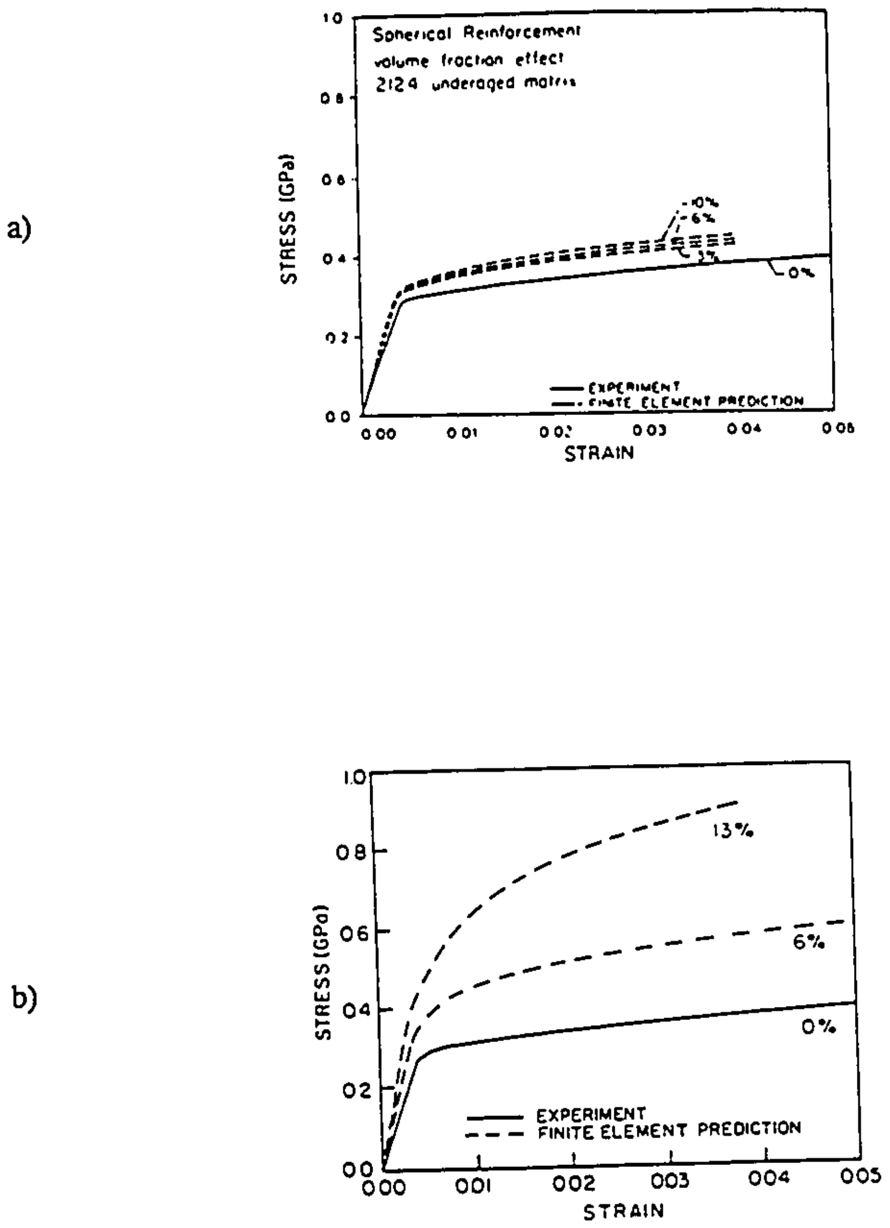

Figure 2.12 - FEM predictions for the effect of volume fraction on stress-strain behaviour, a) spheres and b) cylinders (aspect ratio 5). (Christman et al. 1989)

a very strong effect of particle shape as has been observed experimentally. This work showed that the arrangement of the reinforcing phase had a large effect on the stress-strain behaviour especially in the case of whisker reinforcements. Similar work investigating the role of particle shape and volume fraction on the mechanical response of metal-matrix composites has been conducted by Bao et al. (1991).

The effects of reinforcement distribution have been further examined by Brockenbrough et al. (1991). In this case, however, the emphasis was on continuous fibre composites loaded parallel and perpendicular to the fibre axis. It is was observed that the FEM calculations predicted a strong effect of fibre arrangement on properties in transverse tension especially at high volume fraction but no effect on the properties of composites where the loading axis and the fibre axis were parallel (see Figure 2.13a and b). It is important to note that these calculations were limited to small far-field strains (i.e. a true strain of less than .01) because of the low ductility in the composites.

McHugh et al. (1991) have incorporated a single-crystal plasticity model as a constitutive equation to examine plane strain compression of a coarse grained composite (i.e. matrix grains are the same size as the reinforcing phase) using finite element method calculations. The initial orientations of the matrix grains were determined by random. Figure 2.14 shows a map of accumulated slip for a rectangular arrangement of the reinforcing phase after 25 % compression. It is clear that the flow is very heterogeneous with regions adjacent to the fibres which are relatively undeformed and regions between the fibres with much higher than average deformation. A low strain hardening rate was used in the single crystal constitutive relationship leading to flow localizations from the

a)

b)

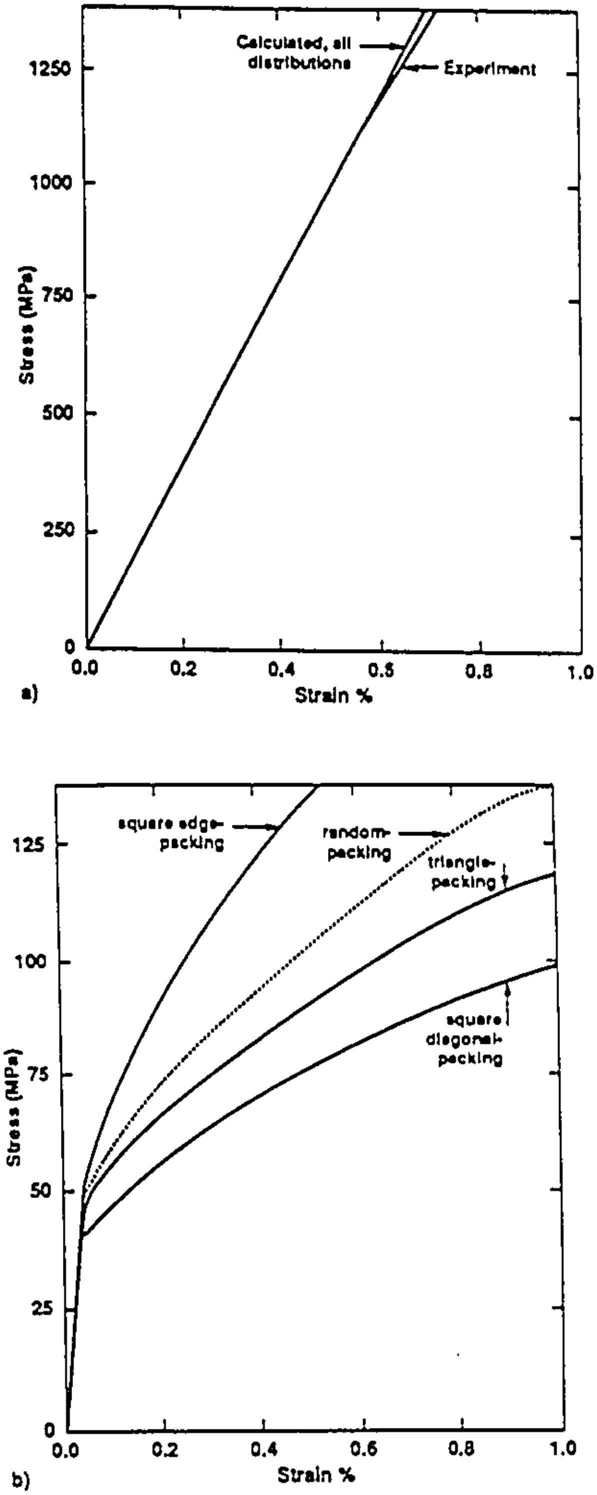

Figure 2.13 - Finite element method predictions for the effect of fibre arrangement on mechanical response a) fibre parallel to loading axis and b) fibres perpendicular to loading axis at 20 and 46 % volume fraction. (Brockenbrough et al., 1991).

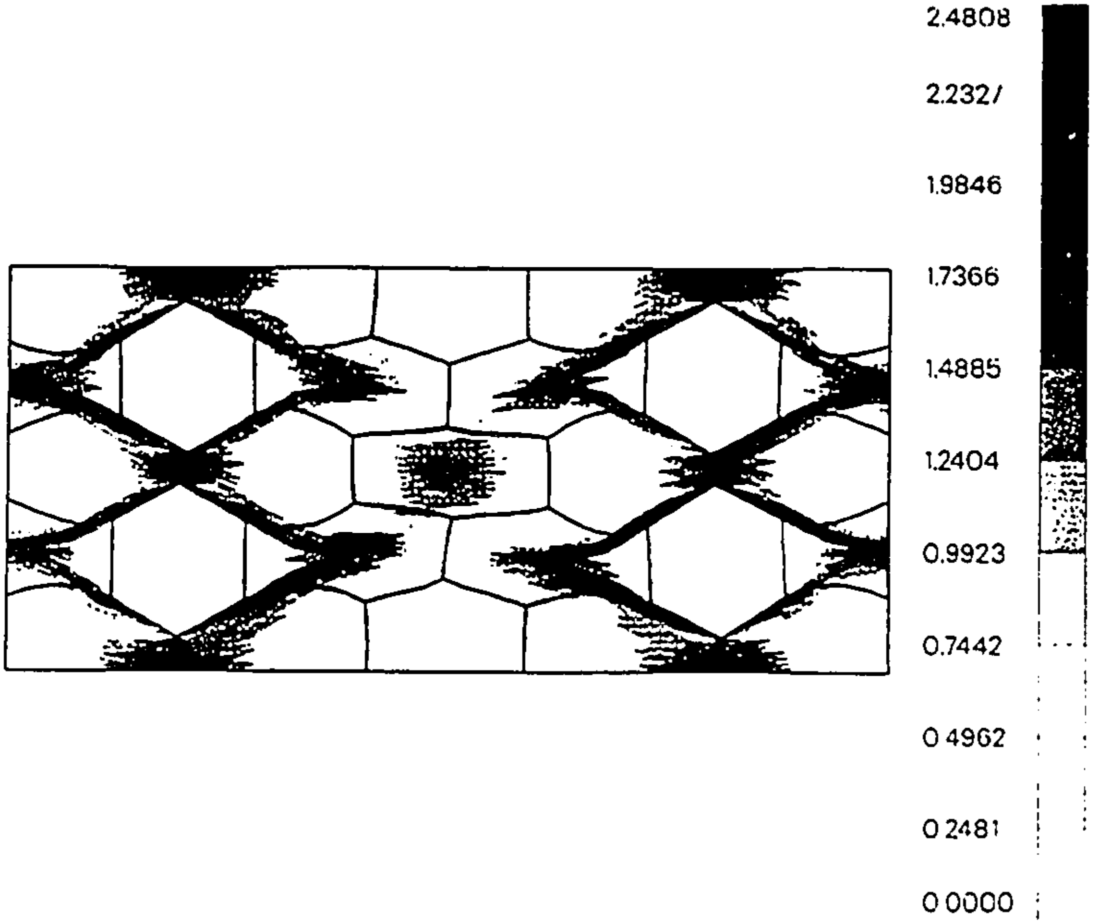

Figure 2.14 - Map of accumulated slip from FEM calculations incorporating single crystal plasticity for a deformation level of 0.25. (McHugh et al., 1991). Note, the high degree of strain localization arises due to the low work-hardening rate used in FEM model.

onset of plastic deformation.

FEM calculations represent a powerful approach to studying elastic and plastic behaviour in composite materials. A wide range of reinforcement parameters and loading conditions can be examined. However, these are continuum calculations and therefore scale independent since every element is considered to be representative of the bulk material. The results are also dependent on the flow theory used in the FEM code which is usually a von Mises yield surface with isotropic hardening.

2.3.2 - Dislocation Models

It is possible to obtain a detailed understanding of the mechanical behaviour of some two-phase systems such as Cu-SiO_2 using dislocation modeis. The seminal work of Ashby (1971) described the general behaviour of these materials. Ashby has proposed that the strain misfit upon deformation between the matrix and second phase (assumed to be elastic and non-deformable) could be relaxed by the generation of geometrically necessary dislocations (as illustrated in Figure 2.15). It is important to emphasis the scale dependence of this behaviour. This can be seen in equation 2.8 relating the density of geometrically necessary dislocations to the applied shear strain.

$$\rho^G = \frac{4\gamma}{\lambda^G b} \tag{2.8}$$

where:

ρ^G = density of geometrically necessary dislocations
γ = shear strain
λ^G = geometric slip distance, (function of shape, for spheres = r/f)

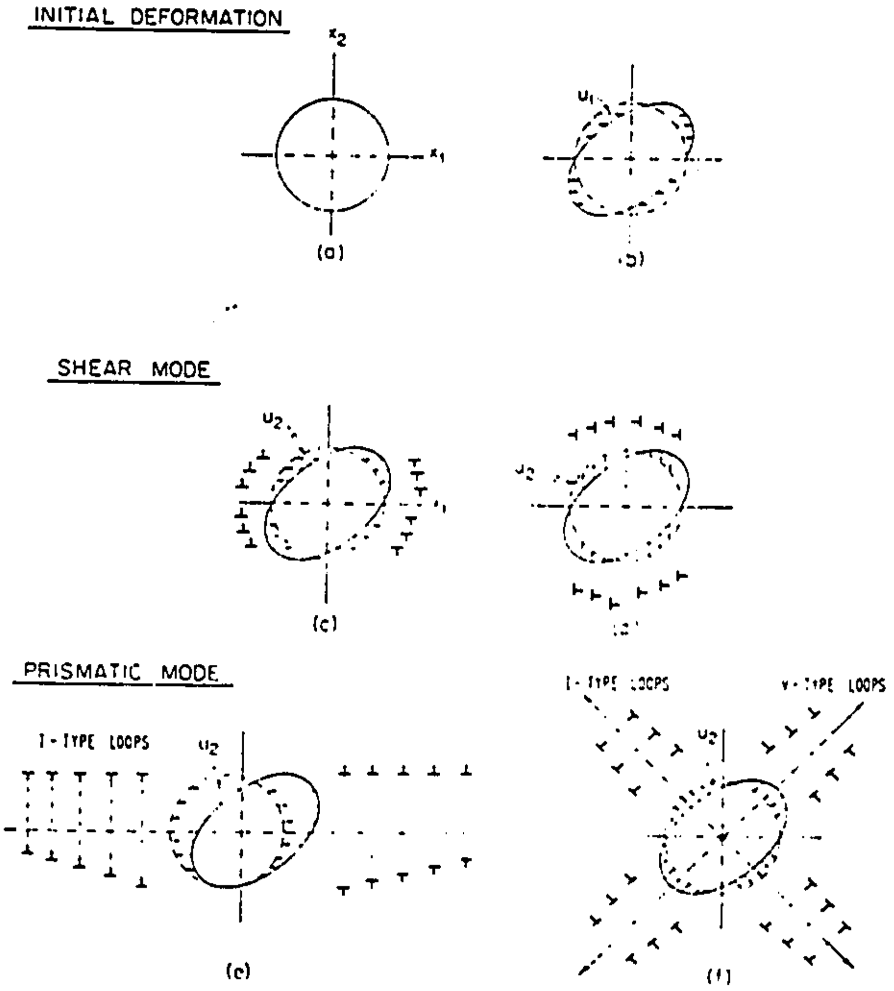

Figure 2.15 - Possible relaxation mechanisms involving the nucleation of dislocation at the particle matrix interface. (Ashby, 1971).

b = Burgers vector of the dislocation
r = particle radius
f = volume fraction of second phase particles

As can clearly be seen in Figure 2.16, the concept of geometrically necessary dislocations is important only when the scale of the structure is fine (i.e. only when λ_g is less than 10^{-4} cm is θ/G affected). This model was very successful in explaining the parabolic hardening in dispersion hardened system without a detailed consideration of the nature of the relaxation processes.

The details of the relaxation process have been studied extensively by Brown and Stobbs (1971a,b) and by Hirsch and Humphreys (1970). One of the drawbacks of Ashby's simple model was its inability to predict the large Bauschinger effect which was experimentally observed in these materials. In a series of papers Brown and Stobbs (1971a, 1971b and 1976) developed a detailed model of the distribution of internal stresses in this material. This model incorporated a continuum model based on Eshelby's equivalent inclusion and a more detailed consideration of the nature of the plastic relaxation processes at the dislocation level.

The scale dependence of relaxation processes is important and was emphasized in the initial work of Ashby (1971). The processes of nucleation of dislocation at second phase particles is a relatively difficult process (i.e. the nucleation stress is of the order of G/100, (Weatherly, 1968) and should only be expected in cases where relaxation by plastic flow of existing dislocation cannot occur. A complete picture can be obtained by considering the buildup of stresses around a particle based on the theory Eshelby's

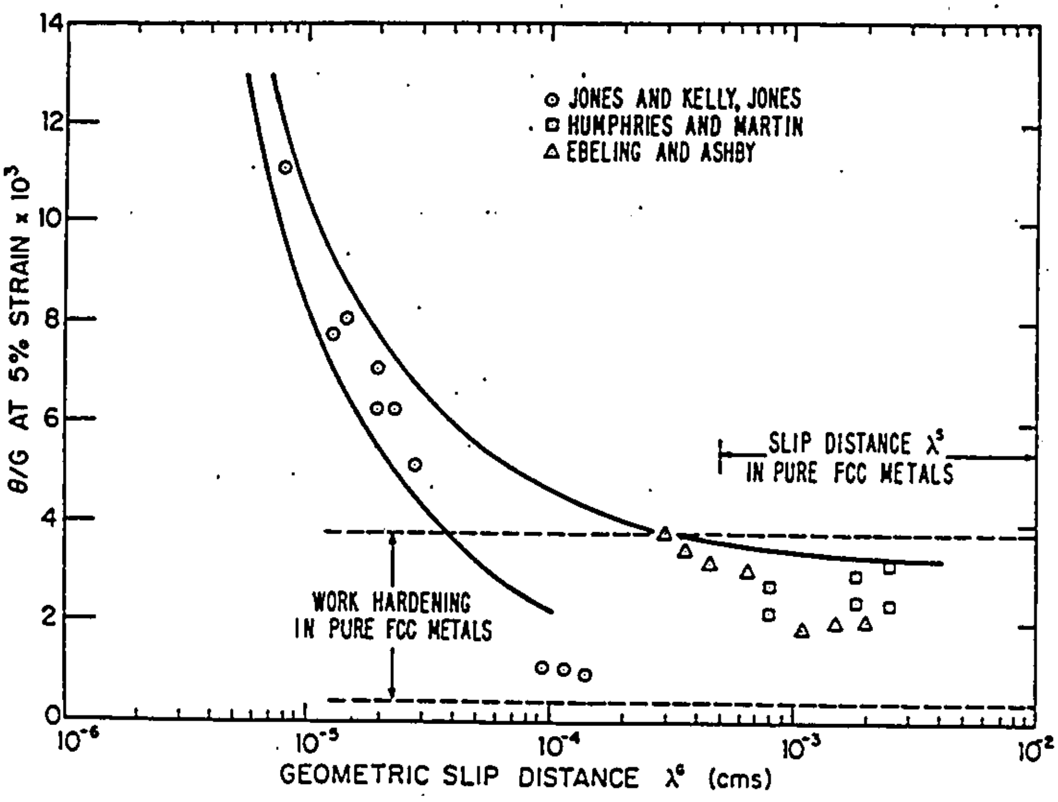

Figure 2.16 - Diagram of work-hardening rate at 5 % strain, θ/G, vs. geometric slip distance (i.e. r/f). (Ashby, 1971).

equivalent inclusion. As described by Brown and Stobbs (1971a) a complicated stress state will develop around the particle with the presence of shear stresses. The most energetically favourable process to occur would be the glide of existing dislocations present in the vicinity of the particle. The additive flow stress around the particle would be inversely proportional to the square root of the *local* dislocation density. In the case of small particles (i.e. smaller than the average dislocation spacings), the probability of finding a dislocation of the appropriate sign to relax the stress is very low. Here, the stresses in and around the particle would continue to rise until an alternative process can intervene such as prismatic punching of dislocations or particle fracture.

In the spirit of Ashby's original model, Taya and Arsenault (1989) have proposed that the observed strengthening seen in metal-matrix composites is a result of the generation of thermal dislocations due to the difference in coefficients of thermal expansion upon cooling. They have shown that the following relationship may be obtained :

$$\rho_{thermalmisfit} = \frac{bf\epsilon}{rb[1-f]} \qquad (2.9)$$

where:

B = is a geometric factor

This is essentially the same as (eqn. 2.8) but has been corrected to apply at high volume fractions. Once again, a strong particle size dependence is observed in the development of local dislocation substructure. However, these authors have ignored the possibility of other relaxation mechanisms such as glide of existing dislocations or diffusional relaxation.

The outstanding question for modelling of composite materials is whether continuum models (i.e. scale independent) or dislocation models (i.e. scale dependent) is the most appropriate approach to the problem. Unfortunately, most engineering composites of interest fall the borderline region where scale effects are starting to become important (i.e. reinforcing phases of 0.5-3 μm and volume fraction of 0-20 %). However, as can be seen from the work of Brown and Stobbs, it is possible to combine the two approaches for a comprehensive theory.

2.4 - Damage in Metal Matrix Composites

Damage in metal matrix composites can be defined as processes which degrade the mechanical properties of the material as measured by decreases in the load carrying capacity of the material or in the most extreme case, failure. Typical examples of damage are particle fracturing and interfacial debonding. There are two components which control these processes. The first parameter is the intrinsic properties of the volume element which participates in a damage event. In the case of particle fracture, this includes the intrinsic fracture stress of the particle and the distribution of flaws in the particle. For interfacial decohesion, this process is controlled by the properties of the interface. The second component of importance is the detailed nature of the stress distribution in the volume element where a damage event may occur. This is a function of i) the difference in properties of the two phases , the shape of the reinforcing phase, the spatial distribution of the reinforcing phase and the nature of the externally applied stress state. Many observations of damage in MMC's have been conducted recently (e.g.

Lewandowski and Liu (1989), Mummery and Derby (1991), Lloyd (1990), Embury, Newell and Tao (1991)). Some of the important results will be summarized in this section.

The majority of the work on damage in MMC's has focused on particle fracture. However, it is important to realize that there is a competition of processes in MMC's as the stress in the composite increases. There are two alternatives: i) the process of load transfer may continue leading to higher stresses in the particle or ii) the stresses in the particles may be relaxed by either fracture of the particle or decohesion of the interface. These processes will be controlled by the intrinsic properties of each element in the system (i.e. the interface, the particle and the matrix). A good example of this is given by the work of Ribes, Da Silva, Surey and Bretheau (1990). They showed the behaviour, as observed by *in situ* SEM tensile tests, was controlled by the preparation of the material. In some cases interfacial decohesion was observed while in other cases particle cracking was dominant. This indicates the importance of processing of the materials on the subsequent behaviour.

A variety of experimental approaches to studying particle fracture and damage accumulation in MMC's have been taken. The most common approach is based on microstructural observations of damage events, however other techniques have been applied such as acoustic emission studies (Mummery and Derby, 1991, 1993) and measurements of changes in elastic modulus (Mummery and Derby, 1991, Corbin, 1992). The effects of particle size, particle shape, volume fraction and the distribution of particles have been found to be important parameters.

Mummery and Derby (1989, 1991) have conducted an systematic study of the effect of particle size on particle fracture in Al-SiC$_p$ composites. This work has included *in situ* SEM fracture studies, measurements of modulus changes as a function of damage, acoustic emission observations and traditional metallographic observations. It is clear from this work and others (e.g. Brechet et al., 1991, Lloyd , 1991, Yang et al., 1990) that particle cracking becomes a more difficult process as the particle size decreases (see Figure 2.17 from Brechet et al.). Mummery et al. attribute this size effect to two probable factors: i) the elastic energy stored in the particle is proportional to its volume and ii) the increased probability of finding a critically sized flaw in a larger particle.

The effect of particle shape is well illustrated by the work of Tao (1991) who showed that the probability of particle failure was strongly dependant on the particle aspect ratio in Al-SiC$_p$ composites (e.g. Figure 2.18). This effect can be understood in terms of the increasing efficiency of the load transfer process as the aspect ratio increases. Metallographic observations have also indicated that damage events occur in regions of particle clustering (e.g. Lloyd, 1991, Yang et al., 1990, Tao, 1991). Yang et al. attribute this effect to development of local constraints in clusters which lead to larger stresses in the particles.

Another important factor influencing the progression of damage in composites is the externally applied stress state. Embury et al. (1991) have used detailed metallographic observations to examine the effect of stress state on damage accumulation in Al-SiC$_p$ composites. This work includes observations of particle cracking for tension

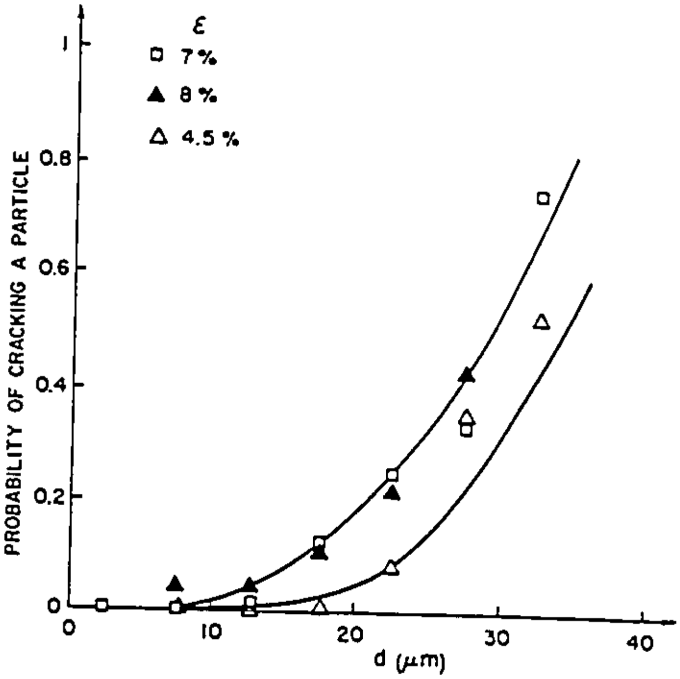

Figure 2.17 - Probability of particle fracture as a function of particle size in a 20 % Al-SiC$_p$ tested in 4-point bending, (Brechet et al., 1991).

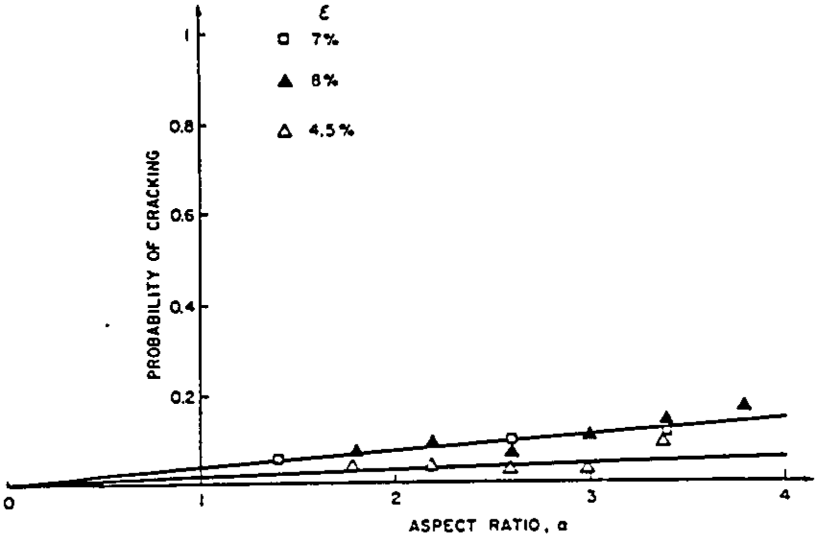

Figure 2.18 - Probability of particle fracture as a function of particle aspect ratio for a 20 % Al-SiC$_p$ tested in compression, (Tao, 1991).

tests with superimposed hydrostatic pressure, torsion tests and compression tests. It was observed that the fracture strain of the composite was strongly influenced by the stress-state. For example, Newell (1990) found that the failure strain for an Al-10%SiC_p composite was 6 % in tension and greater than 40 % in compression. It is also important as Hu (1992) has pointed out that the nature of the damage in different in tension and compression (see Figure 2.19). In compression particle cracking occurs parallel to the loading axis while in tension cracking is perpendicular to the loading axis. In the case of compression tests, Tao (1991) observed that damage accumulation was a linear function to the imposed strain with the rate of damage accumulation increasing as the volume fraction of the reinforcing phase increased. Lloyd (1991) has examined damage accumulation in tensile tests. This work indicated the level of damage occurred at higher rate than in compression. Deviations from the linear dependence of damage accumulation with increasing strain have been observed for tensile tests under hydrostatic pressure (Newell, 1990). This has been attributed to a process of damage healing where the matrix material is can be extruded into the gap between the fractured particle resulting in the formation of two particles where there was originally one. Brechet et al. (1991) have modelled this process based on the extrusion of matrix material in to the gap that results when the a particle is fractured.

Having described some of the important experimental observations of damage processes in MMC's, it useful to review some of the consequences of the damage on macroscopic behaviour such as mechanical response. Hu (1991) has emphasized that the importance of the difference in cracking modes between compression and tension (see

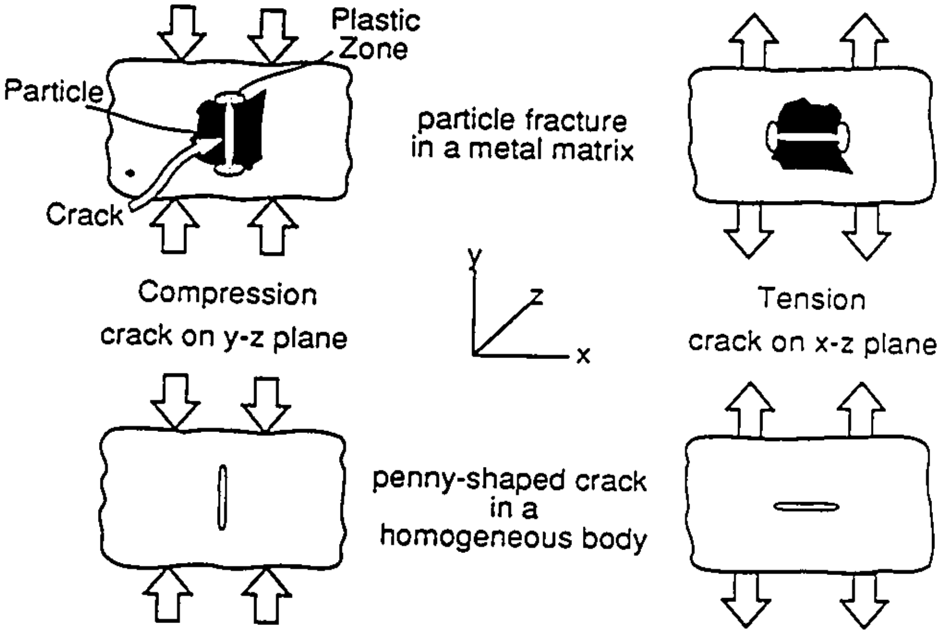

Figure 2.19 - Comparison between particle cracking behaviour for tensile and compressive loading, (Hu, 1991).

Figure 2.19). It is clear that particle cracks perpendicular to the loading direction such as observed in tension tests, have a much larger detrimental effect on the load bearing capacity of the composite than cracks which are parallel to the loading direction (i.e. as observed in compression tests). This has been modelled by considering the effects of penny shaped cracks on the mechanical response of the material (He and Hutchinson, 1981). In a different approach, Bao (1992) has used a FEM calculations to predict tensile stress-strain behaviour of a MMC. In this work arbitrary, damage evolution paths (see Figure 2.20a) were used to study the sensitivity of mechanical response to the progression of damage. The details of the damage process (i.e. the local stress state) were not examined here. The results are that there are large reductions in the load bearing capacity of the material as result of damage as shown in Figure 2.20b.

The work of Zok et al. (1988) examined the effect of superimposed hydrostatic pressure on tensile tests of Al-SiC_p and Al-Ni composites. It was observed that the ductility measured by fracture strain was a strong function of hydrostatic pressure. A model for describing the fracture stress of the composite based on local stresses in the particles calculated using the Eshelby equivalent inclusion method was found to overestimate the failure stress but demonstrated the correct trend.

In summary, many factors are important when considering damage events in MMC's. These include local properties such as the interfacial properties, the fracture stress of the particle and the size, shape, volume fraction and distribution of the reinforcing phase. The externally applied stress state will also be important in controlling the local response of the system.

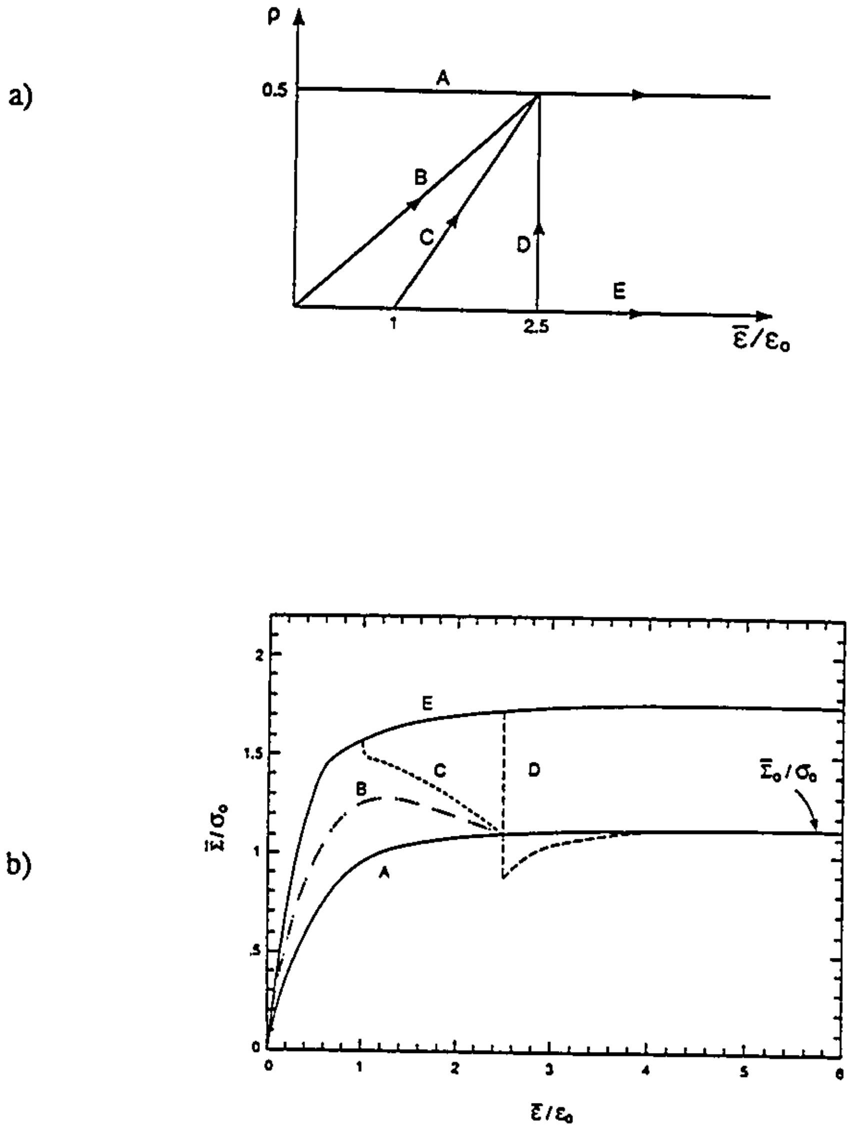

Figure 2.20 - a) damage paths used in numerical simulation and b) resulting stress-strain curves for different damage paths, (Bao, 1992).

2.5 - Deformation Texture Development in Metal Matrix Composites

Relatively few observations have been made on texture development in metal matrix composites. As Bunge (1985) has pointed out, this may due to the fact that state properties such as yield surfaces are less sensitive to matrix texture in two-phase materials compared to single phase materials (i.e. anisotropy in the shape of the reinforcing phase dominates). Most observations have indicated that the presence of a hard non-deformable second phase will inhibit the formation of a strong deformation texture in the matrix.

Bergmann, Frommeyer and Wassermann (1978) have emphasized the importance of the relative yield stresses of the constituents. They observed that the texture development in the matrix was inhibited for the case of non-deformable particles. At the other extreme, they found that texture development in the matrix was intensified if the second phase had a lower yield stress than the matrix. Examples of wire drawing textures include: i) textures in aluminum containing 10 % Al_2O_3 particulates (5 μm) which were weaker than in monolithic aluminum and ii) textures in aluminum-tin two-phase materials which were much stronger than observed in monolithic aluminum (see Figure 2.21). In a related paper, Wassermann et al. (1978), offered a qualitative explanation of their results. In cases where the flow stress of the matrix was greater than that of the second phase, it was proposed that the deformation of the matrix grains would be less constrained than in a polycrystal and therefore, have greater rotations of the

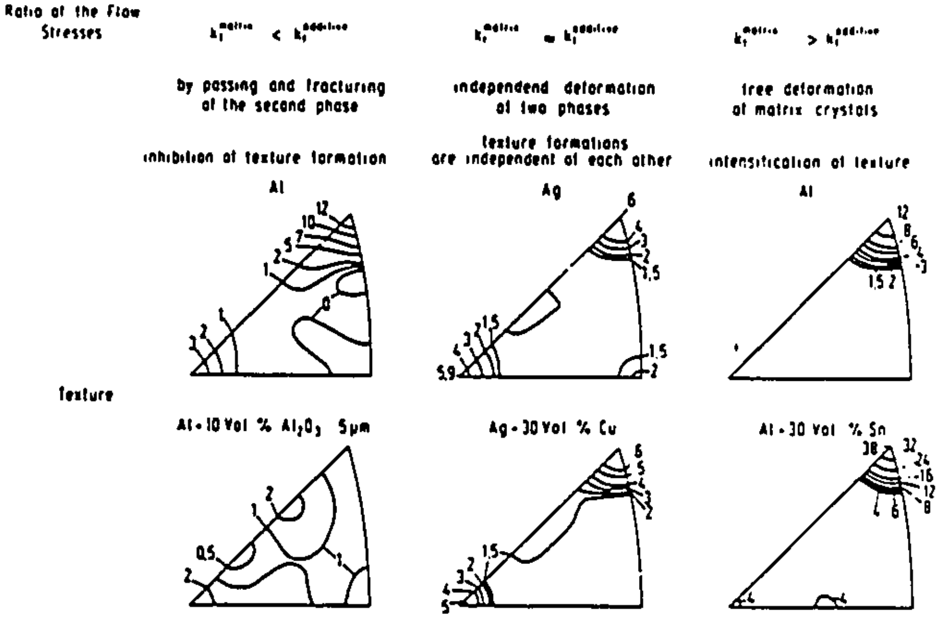

Figure 2.21 - Inverse pole figures for different ratios of matrix to second phase flow stress, (Bergmann et al., 1978).

crystal axes (i.e. stronger texture development). When the second phase is undeformable or slightly deformable, they proposed the flow pattern in the matrix would be altered resulting in a lower level of texture development for the matrix. They point out that the processes controlling this have not been adequately examined.

In a series of papers by Humphreys and co-workers (i.e. Porter and Humphreys (1979), Humphreys, Miller and Djazeb (1990), Humphreys and Kalu (1990)) the role second phase particles, such as silicon, SiO_2 and SiC_p, on development of deformation structures in aluminum has been examined. The work initially considered the effects of the particles on the deformation zones around particles in single crystals assuming single slip models. However, in the most recent work (Humphreys and Kalu (1990)), the model has been extended to polycrystalline materials where multiple slip is present. The systems studied have had particles in the range .1 to 10 μm with volume fractions of approximately 1 -20 %. This work has emphasized the development of deformation zones around the hard particles and the development of large misorientations near the particles. Figure 2.22 is a schematic diagram illustrating the subgrain structure around a SiO_2 particle embedded in an copper after cold rolling. The important point here is the emphasis on local rotations adjacent to the particle. From the most recent work on aluminum-silicon alloys, Figure 2.23 demonstrates the variation of local rotations at silicon particles (2 different size ranges) versus deformation strain. The local rotations were measured using electron diffraction patterns obtained from thin foils. It is proposed that the presence of the local rotations creates essentially random matrix orientations near the second phase particles and a resulting weakening of global texture measurements.

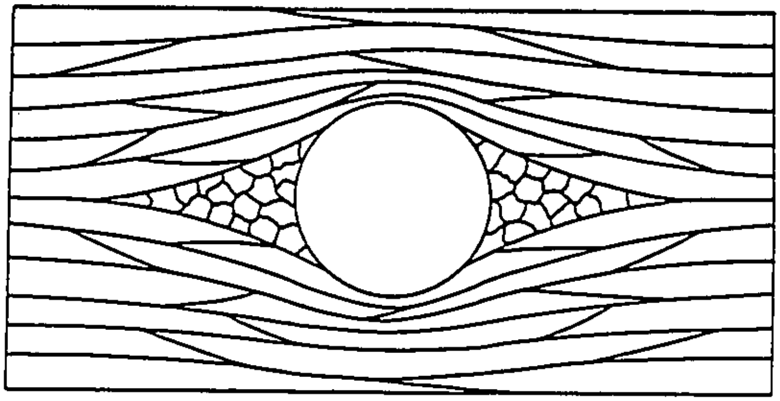

Figure 2.22 - Schematic diagram of subgrain structure around non-deforming particle after 90% rolling reduction, (Porter and Humphreys, 1979).

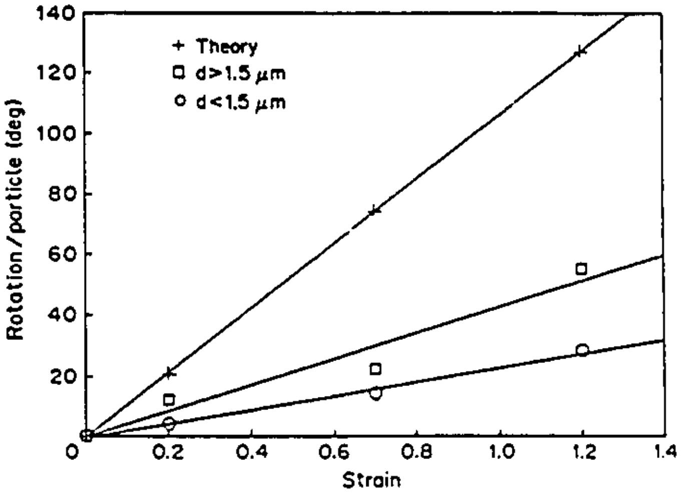

Figure 2.23 - The amount of lattice rotation per particle for different particle diameters, (Humphreys and Kalu, 1990).

In summary, this work has been a detailed examination of local effects near second phase particles. The range of particle sizes examined was much smaller than the grain size of the matrix. The volume fraction of particles was low so that possible particle-particle interactions were not considered.

Recently, quantitative experimental measurements of textures in metal-matrix composites have been reported. In this case the scale of the second phase is larger (particle size 10 -20 μm) and the volume fraction are typically 10-20 %. For example, Jin, Burger and Lloyd (1992) have reported measurements of textures for 6061 aluminum alloys reinforced with SiC and Al_2O_3 after cold rolling. They reported much weaker deformation textures in the composite compared to the unreinforced matrix material (Figure 2.24). Other examples include results on hot extrusion of aluminum alloys reinforced with SiC . Poudens, Bretheau and Bacroix (1991) observed that textures were weaker in the composite and noted that the weakening of the texture increased with increases in volume fraction of the second phase. Juul Jensen, Liu and Hansen (1991) also observed weaker texture in the composites. They also found that the weakening of the texture depended on the particle shape (i.e. the textures were weaker for whisker reinforced compared to particulate reinforced materials).

A different theoretical approach to understanding the weaker deformation textures in composites has been proposed by Bolmaro et al. (1992). In this work it has been emphasized that the flow pattern in the matrix will be important for controlling the development of texture when a significant part of the deformation is perpendicular to the fibre direction. Finite element method (FEM) calculations were used to understand the

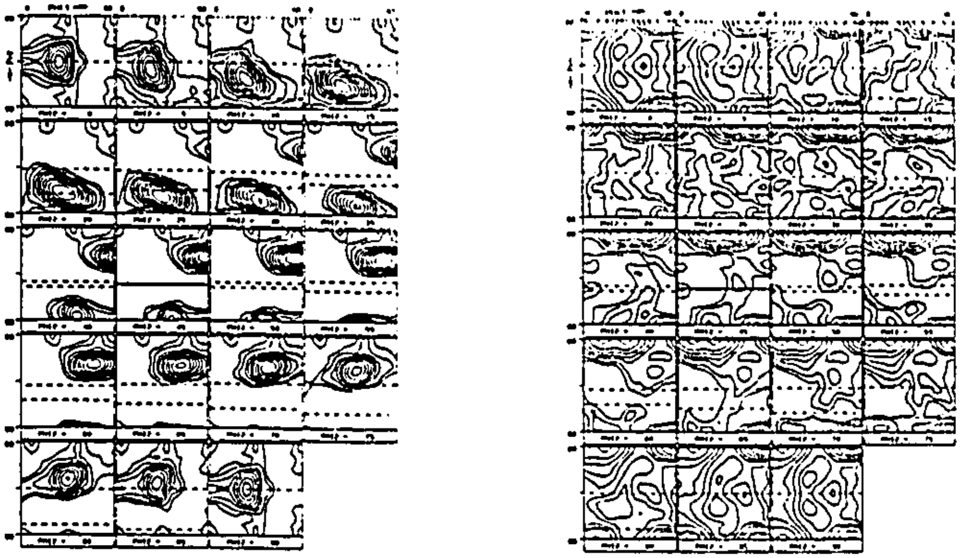

The ODFs of unreinforced A356 (a) cold rolled (b) recrystallised (Sections in the Φ - O, plane, contours at 0.8, 1.0, 1.3, 1.6, 2.0, 2.5, 3.2, 4.0, 5.0, 6.4.

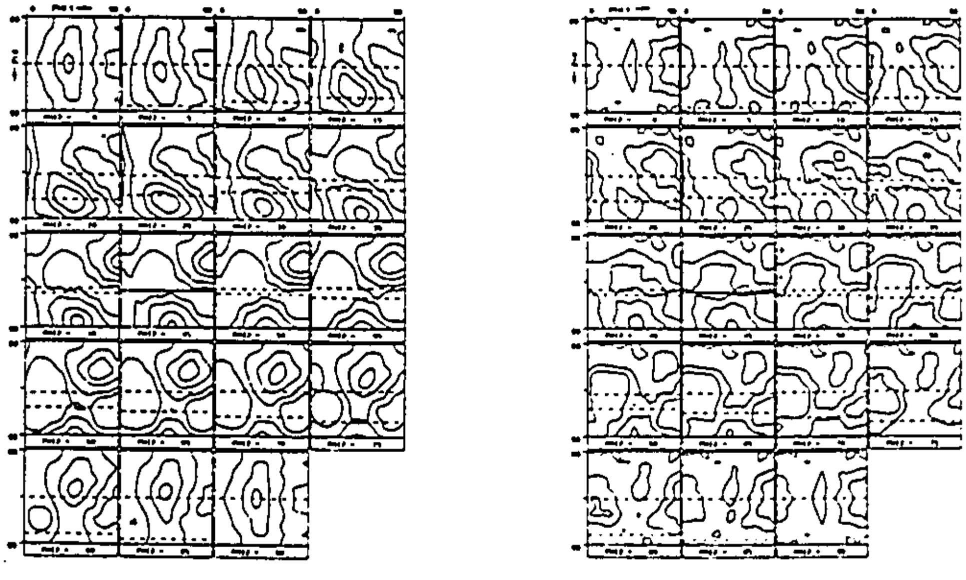

The ODFs of Al-7Si-2.0Mg-1.0Cu-15v% SiC (a) cold rolled (b) recrystallised (sections in the Φ - O, plane, contours at 0.8, 1.0, 1.3, 1.6, 2.0, 2.5, 3.2, 4.0, 5.0, 6.4).

Figure 2.24 - Orientation distribution functions for a) an A356 aluminum alloy cold rolled, b) A356 recrystallized, c) A356-15v% SiC_p cold rolled and d) A356 15v% SiC_p, recrystallized, (I. Jin et al., 1992)

flow pattern in the matrix for a model composite system. Plane strain compression of a copper-tungsten fibre composite where the fibres were perpendicular to the loading axis (i.e. in the direction of zero strain) was examined. The flow pattern in the matrix was observed to be controlled by the spatial arrangement of the second phase (i.e geometric arrangement and particle-particle spacings). It is important to note that in this work the grain size of the matrix was assumed to be small compared the reinforcing phase. They have concluded that the regions adjacent to the second phase particles are of a small volume and do not have a large effect on the global texture development. The characteristics of the flow pattern in the matrix which controlled the global texture development could be summarized by two regions. In the region marked B in Figure 2.25, the deformation was similar in nature to applied deformation but of a larger magnitude. In the region marked C and C′, a more complicated form of deformation was observed. In this region, the matrix experiences rigid body rotations and a variable straining path during the deformation. By extracting the velocity gradient tensor from the FEM calculations, they were able to use this information for input into the texture simulation program (U.F. Kocks, 1988). These results indicated that the texture produced in region B was essentially a standard rolling texture (although it was intensified due to the strain amplification in this region). In region C, the texture was observed to have a high random background with a relatively weak texture superimposed. The random background was interpreted as arising due to the rigid body rotations which vary with position and, more importantly, strain path changes as a function of strain at each position. Their conclusion was that the global texture could be understood as an

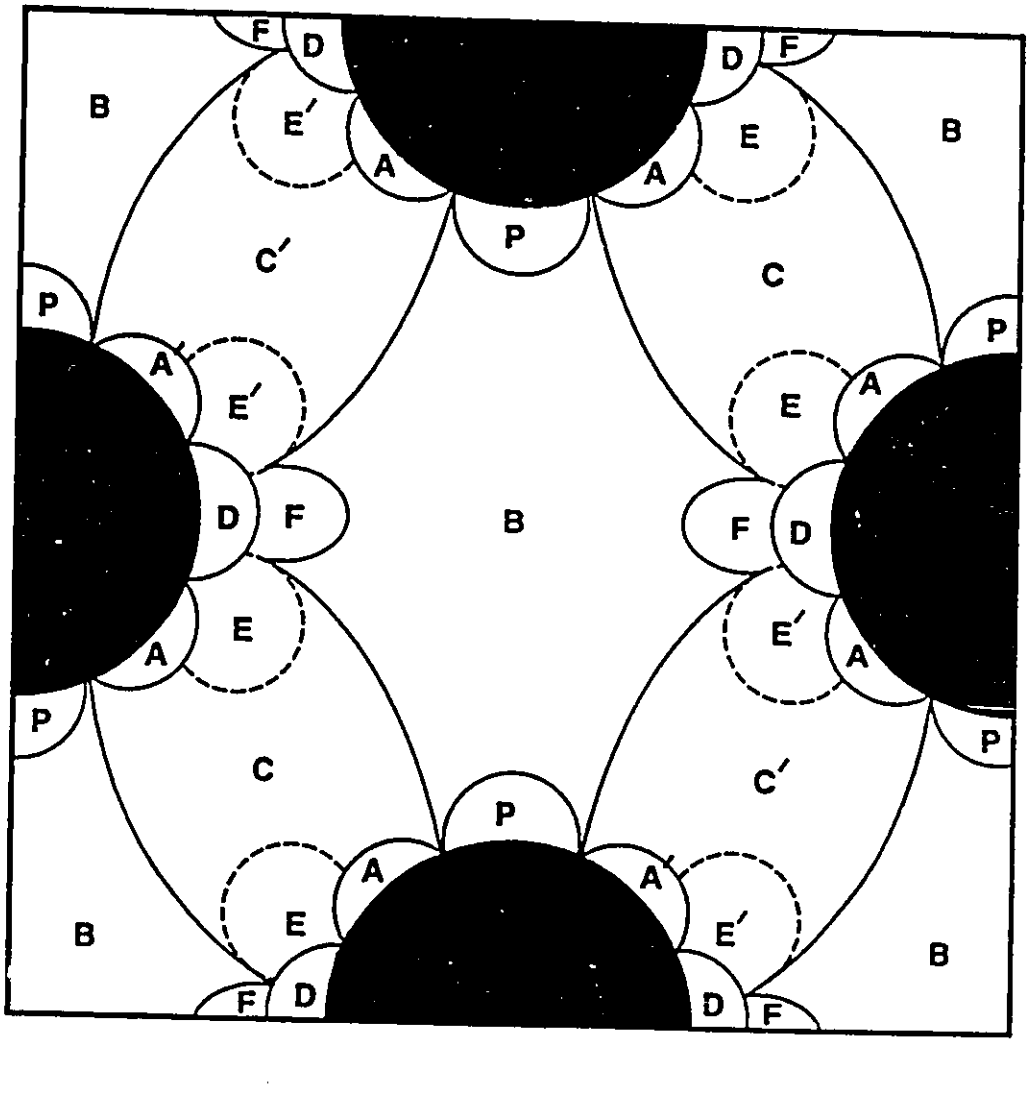

Figure 2.25 - Schematic diagram illustrating representative areas of matrix deformations. The primed regions have inverted signs from unprimed ones. (Bolmaro, 1993).

addition of the characteristic local textures. By summing different local textures the global texture development was observed to be greatly reduced. They also point that the general results of this work could be applied to an understanding of texture development in other two-phase systems such as particulate reinforced materials. It is useful to point out that this work was an impetus for the present work and some of the important results will be directly compared with the experimental results of the present work.

2.6 - Recrystallization in Two-Phase Materials

Many observations of recrystallization behaviour in two-phase materials have been reported. The recrystallization behaviour of two-phase materials has been reviewed by Cotterill and Mould (1976), R.D. Doherty (1980), Humphreys and Juul Jensen (1986). This work has primarily concerned with low volume fractions of micron and sub-micron particles. As in single-phase materials, recrystallization occurs only when there is sufficient stored energy to provide a driving force and there is the presence of high angle boundaries (i.e. mobile boundaries). Both of these criteria can be effected by the presence of a non-deformable second phase.

Humphreys (1980) has stressed the importance of particle size on recrystallization behaviour. As shown in Figure 2.26, second phase particles can enhance or retard recrystallization behaviour depending on the level of deformation and the particle size. Humphreys has related this to the detailed interactions of dislocations with the particle and the scale dependent relaxation process which can occur. Essentially, large misorientation which may act as nuclei for the recrystallization process

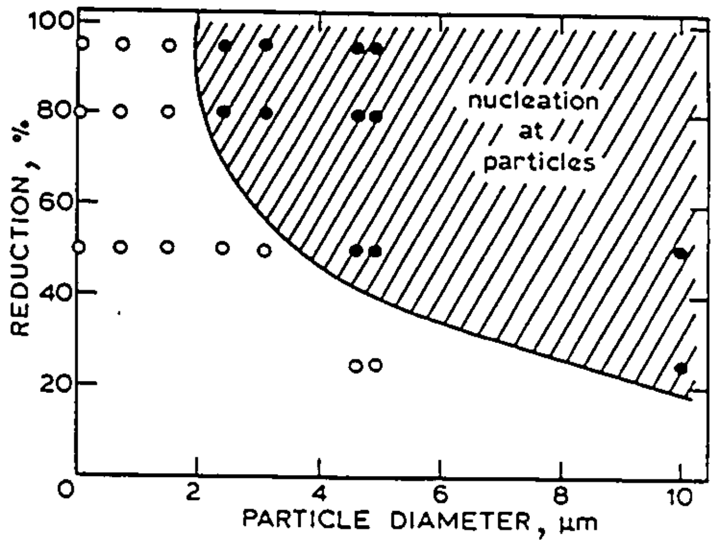

Figure 2.26 - Conditions of deformation and particle size for which nucleation is observed to occur at particles of Si in rolled aluminum, (Humphreys, 1980).

are produced in systems with large particles (greater than 1 μm). Herbst and Huber (1978) have observed strong particle shape and particle-particle interactions relating to the development of matrix misorientations near second phase particles in AlMgSi alloys. Figure 2.27 is a schematic diagram showing the misorientation angles (measured by selected area diffraction patterns in TEM) adjacent to and around a second phase particle. Misorientations of greater than 20° were reported. These were found to be potent sites for initiation of the recrystallization process. Recently some observations have been made on the kinetics of recrystallization in metal matrix composites. For example, Ferry et al. (1991) have reported that the recrystallization temperature is lowered for the MMC compared to the unreinforced alloy and the kinetics of recrystallization as measured by hardness values are increased (for example, see Figure 2.28).

The presence of second phase particles not only affects the process of dislocation storage and arrangement but can also affect the final recrystallized grain size. Humphreys et al. (1990) have suggested that the final grain size is dependent on particle diameter and particle spacing. The basis of this analysis is the assumption that each particle produces one nucleus and the nucleus from each particle will grow until they impinge. Humphreys et al. (1990) has also suggested that the particles can effect the amount of grain growth by a Zener pinning mechanism. This will also limit the final grain size in the composite. These two effects produce different dependencies on particle size and volume fraction but the experimental evidence is not conclusive to determine which relationship, if either, provides a better description of the experimental results.

Finally, it is worth noting that very little information is available for massive

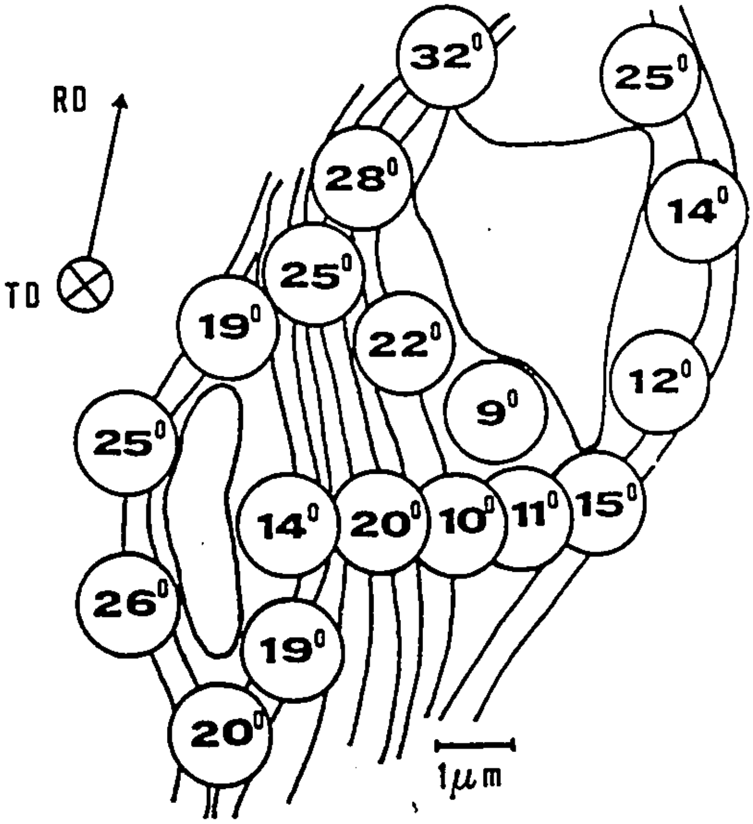

Figure 2.27 - Schematic diagram illustrating the amount of lattice misorientations around particles after 90 % rolling reduction. Misorientations measured by selected area diffraction patterns in TEM, (Herbst and Huber, 1978).

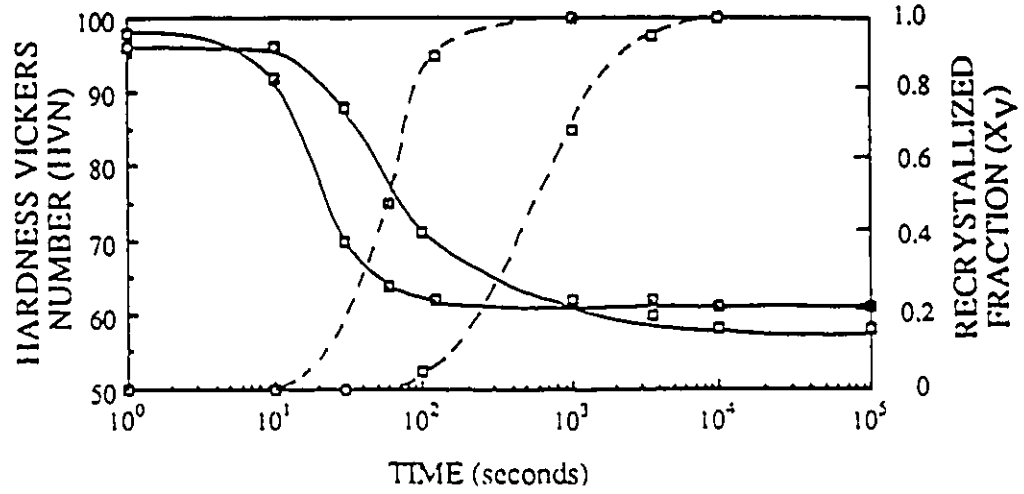

Figure 2.28 - Hardness values and fraction recrystallized as a function of time during annealing at 360 °C for the composite (solid symbols) and the monolithic alloy, (Ferry et al., 1991).

second phases at high volume fractions (Cotterill and Mould, 1976) and the majority of materials investigated have had grain sizes comparable to or smaller than the scale of the reinforcement.

CHAPTER 3

EXPERIMENTAL PROCEDURE

3.1 - Introduction:

This section describes the techniques used for fabrication, mechanical testing and characterization of copper-tungsten composites. The compression samples were cast, mechanically worked and recrystallized, and then a fiducial grid was prepared on the sample surface prior to the final compression tests.

3.2 - Sample Preparation

These composites were prepared by a modified liquid metal infiltration technique in vacuum induction furnace using oxygen free electrolytic (OFE) copper[1] with a purity of 99.99 % and commercial as-drawn 1 mm tungsten wire[2]. The chemical analysis for the as-received copper and tungsten are shown in Table 3.1 and 3.2. The tungsten fibres were held in place during casting by high density graphite[3] spacers. The distribution of the fibres was controlled by drilling holes in the graphite spacers on a milling machine. Figure 3.1 shows a schematic summary of the four sample geometries used in this work. This fabrication route produced samples with final volume fractions of 20 and 30 % in

---

[1] supplied by Copper and Brass Sales, Etobicoke, Ont., M8W 4W3

[2] supplied by GTE/Sylvania, Towanda, Pa 18848

[3] POCO Graphite Inc., Decatur, Tx 76234

Table 3.1 - Chemical analysis impurities in as-received copper

Concentrations in parts per million (supplied by Copper and Brass Sales)

Bi	Cd	Pb	Hg	O_2	P	Se	S	Te	Zn
<1	<1	4	<1	3	2	<1	9	<1	<1

Table 3.2 - Chemical analysis of as-received tungsten fibres

Concentrations in parts per million (supplied by GTE-Sylvania)

Al	Ca	Cr	Cu	Fe	Mg	Mn	Ni	Si	Sn	Na	K	Mo	C
8	<1	2	<1	5	<1	<1	2	1	1	<5	62	<8	10

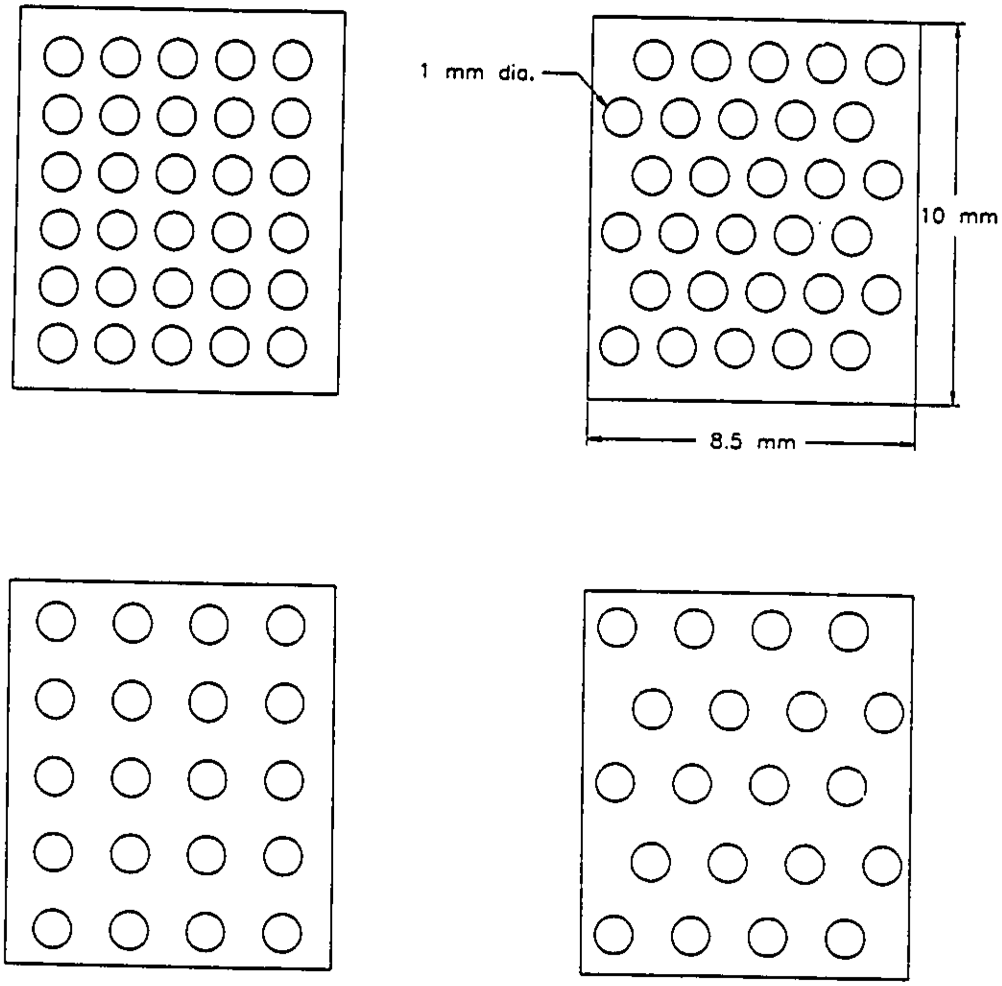

Figure 3.1 - Schematic of sample geometries and fibre arrangements

square and triangular fibre arrangements. Samples with a single tungsten fibre were also fabricated.

It was observed that the mechanical behaviour of the tungsten fibres was dependent on their thermal history during casting. Preliminary experiments had shown that the tungsten was susceptible to embrittlement when heated in the presence of the graphite mould. This effect had also been observed by Kelly and Tyson (1965) and Pederson (1990) when they fabricated copper-tungsten composites. The effect was examined by varying the thermal history of the tungsten fibres. The results can be summarized as follows: If the tungsten was heated above 900 °C in vacuum in a graphite crucible, embrittlement occurred. However, tungsten fibres heated to 1200 °C in a quartz tube embedded in a graphite susceptor showed no embrittlement. Samples of each were fractured under ultra-high vacuum and the fracture surfaces examined with a scanning Auger microscope with emphasis upon detecting levels of carbon, nitrogen and oxygen. The exact cause of the tungsten embrittlement was not determined by it was clear that the embrittlement of the tungsten depended on the heating environment (heating in graphite mould) and the degree of embrittlement was greater at higher temperatures and longer exposure times. This was the rationale for the casting procedure chosen.

The casting procedure was as follows:

1) a graphite crucible with a copper rod placed in it was melted under a vacuum of 10^{-5} torr while the tungsten fibres were held above the melt and away from the heating zone.

2) the melt was superheated to temperature of 1150 ° C

3) once the superheat temperature was reached and stabilized, the array of tungsten fibres, held in place by the graphite spacers, was submerged into the copper melt until fully immersed.

4) In order to ensure the absence of porosity in the casting , the graphite crucible was withdrawn from the induction coil at a rate of 3.8 mm/min resulting in a directionally solidified copper matrix.

The casting was observed to be comprised of several columnar copper grains approximately 5 mm in dia. and 50 mm in length. It was desirable to have a polycrystalline matrix where the regions between fibres contained 5-10 grains. This was important for both texture measurements (see section 3.6) and the ability to treat the matrix as a continuum (i.e. ignore single crystal anisotropies). It was also important to produce samples which were initially free from damage in the tungsten fibres. Preliminary tests had indicated some fibre cracking could occur during compression tests at room temperature. Finally, the geometrical arrangement of the fibres should be maintained during any processing steps. With these requirements established, the following procedure involving deformation of the sample and subsequent recrystallization was developed.

The casting was machined to a block of dimensions, 12 x 16 x 100 mm. This machining was done carefully so that the tungsten fibres were aligned and centred in the sample. This block was then wire cut on a electric discharge method machine into 9 pieces 12 x 16 x 10 mm. These samples were then deformed by channel die compression (fibres in direction of zero strain) at 250 °C to reduce the possibility of damaging the tungsten fibres (i.e. above the ductile-brittle transition of the tungsten fibres). The deformation was carried out in two steps. The first step was a compression to a true strain of 0.10 or 0.15 (0.10 for volume fractions of 30 % and 0.15 for volume fractions of 20 %). The sample was then rotated 90 degrees about the fibre axis and deformed a similar amount. This had the effect of introducing the required deformation for recrystallization and leaving the sample in the same geometric arrangement as in the initial casting without introducing damage to the tungsten fibres. The compression tests were conducted without lubrication and with a sample of pure polycrystalline copper on each side of the composite to ensure uniform deformation in the composite. The cast samples which were in effect multicrystals (3-4 grains in the cross-section) would otherwise have shown non-uniform deformation in the free direction of the channel die.

After the deformation process, the samples were recrystallized in a vacuum resistance furnace ($< 10^{-6}$ Torr) at 500 ° for 1 hour. An example of the resulting microstructure is shown in Figure 3.2a. It was concluded that a finer matrix grain size was desirable. Therefore, the deformation and recrystallization process was repeated and the microstructure shown in Figure 3.2b was produced. This resulted in samples with a polycrystalline matrix, tungsten fibres free of damage and regular geometric arrangements of tungsten fibres.

An important modification to this procedure was made for the samples with a square array of fibres with a 30 % volume fraction. These samples were machined from the casting as shown in Figure 3.3 and then processed. This was done to prevent the formation of a large zone at the centre of the square which had a low amount of

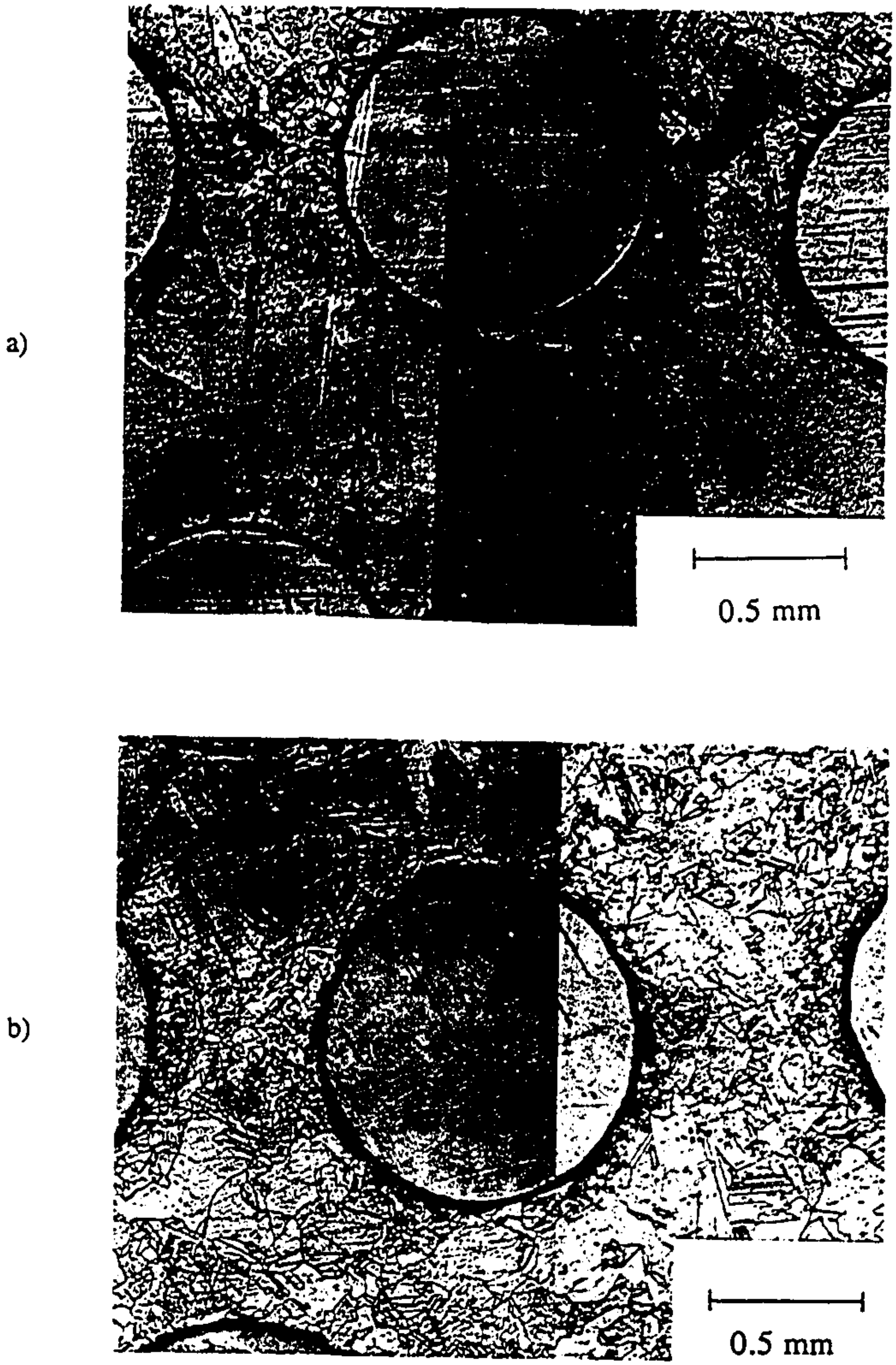

Figure 3.2 - Optical micrographs of matrix microstructure after a) first recrystallization and b) second recrystallization

deformation. Preliminary experiments had indicated that this region would not recrystallize and that a very heterogeneous microstructure would be the result (e.g. see Figure 3.4a). After the second recrystallization, the sample was machined to produce the samples schematically shown in Figure 3.3. Figure 3.4b shows an optical micrograph of the resulting microstructure.

Plane strain compression samples of unreinforced copper were also prepared by machining the samples from the as-received copper bar stock. The as-received material was in the form of an extruded bar in the cold worked condition. Samples were recrystallized at 500 °C for 1 hour and 700 °C for 3 hours producing grain sizes of 50 and 140 μm respectively. The resulting microstructures are shown in Figure 3.5a and Figure 3.5b.

3.3 - Metallography

It was required to metallographically prepare the composite surface perpendicular to the fibre direction for determination of the initial microstructure, measurement of matrix texture by x-rays and application of the fiducial grid. The grinding and polishing of these samples presented problems due to the large difference in hardness of tungsten fibres and copper matrix. In order to obtain as flat a surface as possible, special polishing films (i.e. polymer films embedded with diamond particles 1-6 μm[4]) were employed with a glass plate separating the polishing film from the brass polishing wheel.

---

[4] Allied High-Tech Products, Rancho Dominguez, Ca 90220

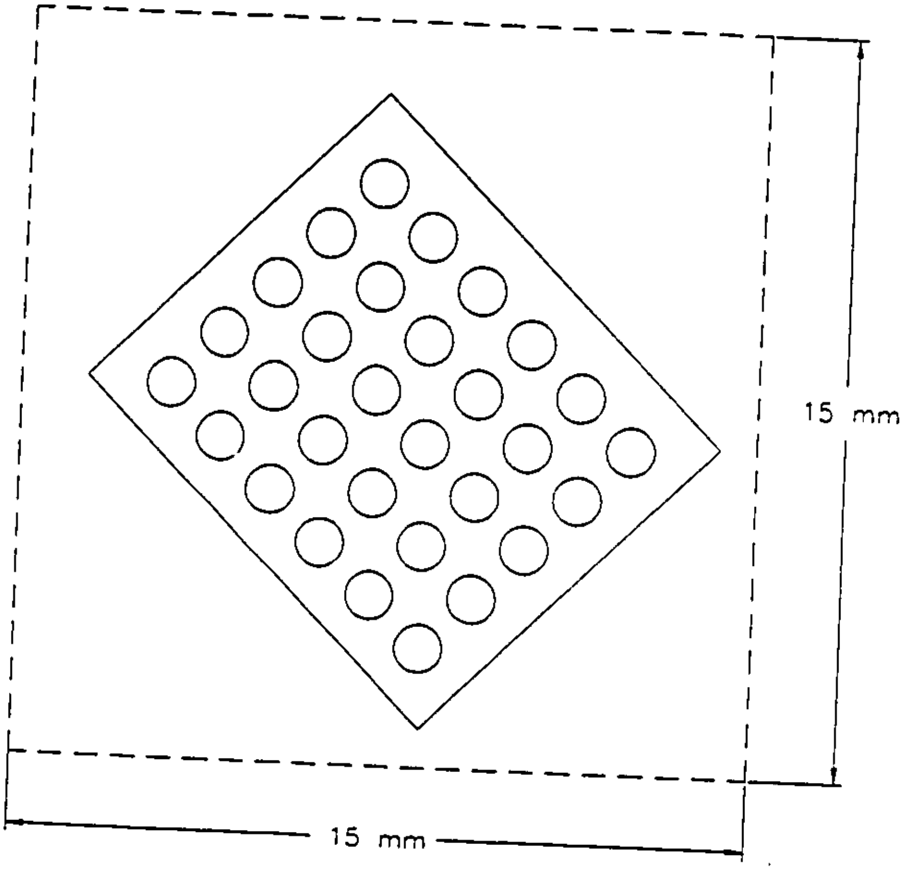

Figure 3.3 - Schematic diagram of geometry for preliminary deformation and recrystallization for 30 % volume fraction and square arrangement of fibres (see text)

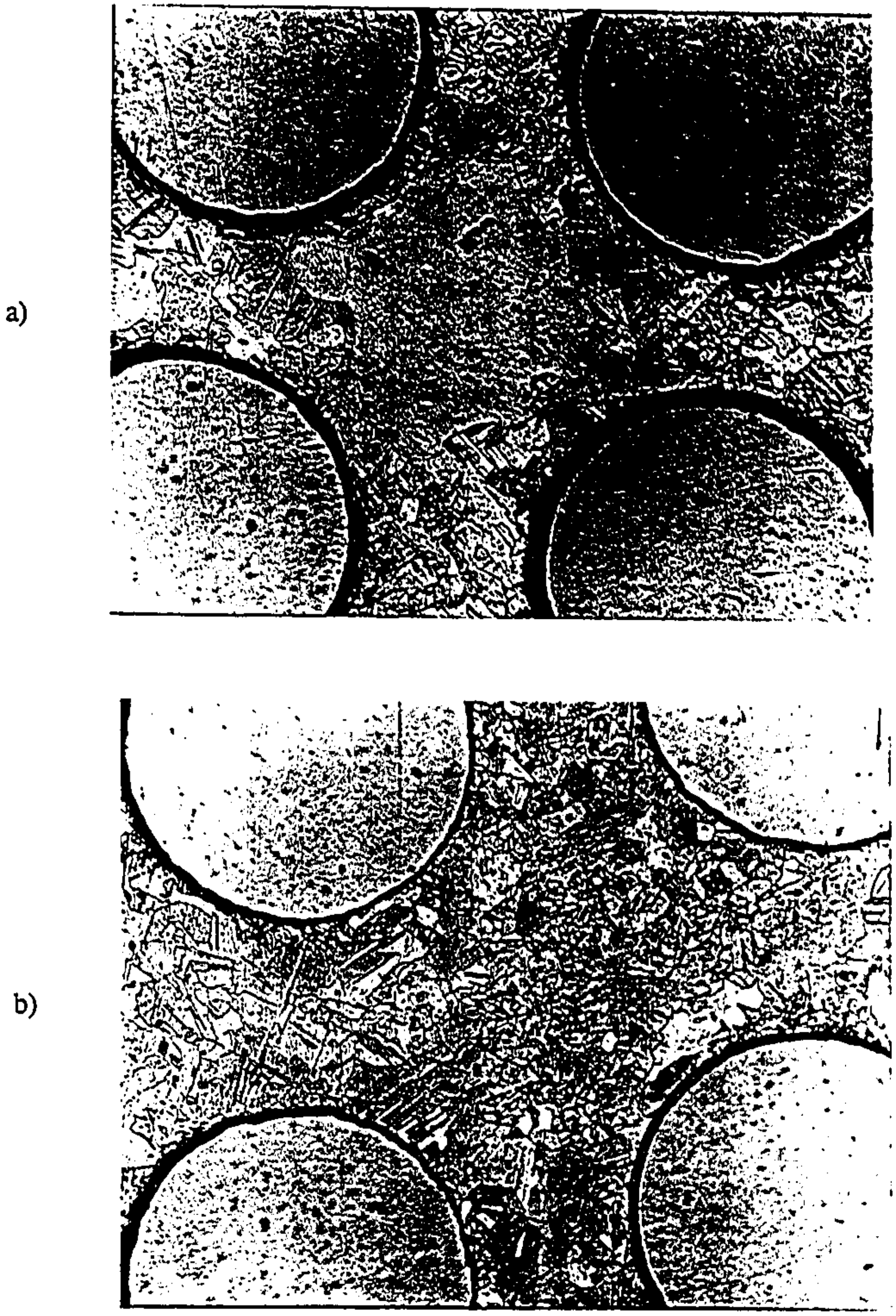

Figure 3.4 - a) original recrystallized structure with large grain at the centre of the fibres and b) recrystallized structure after modified deformation procedure. Note: tungsten fibres are 1 mm dia.

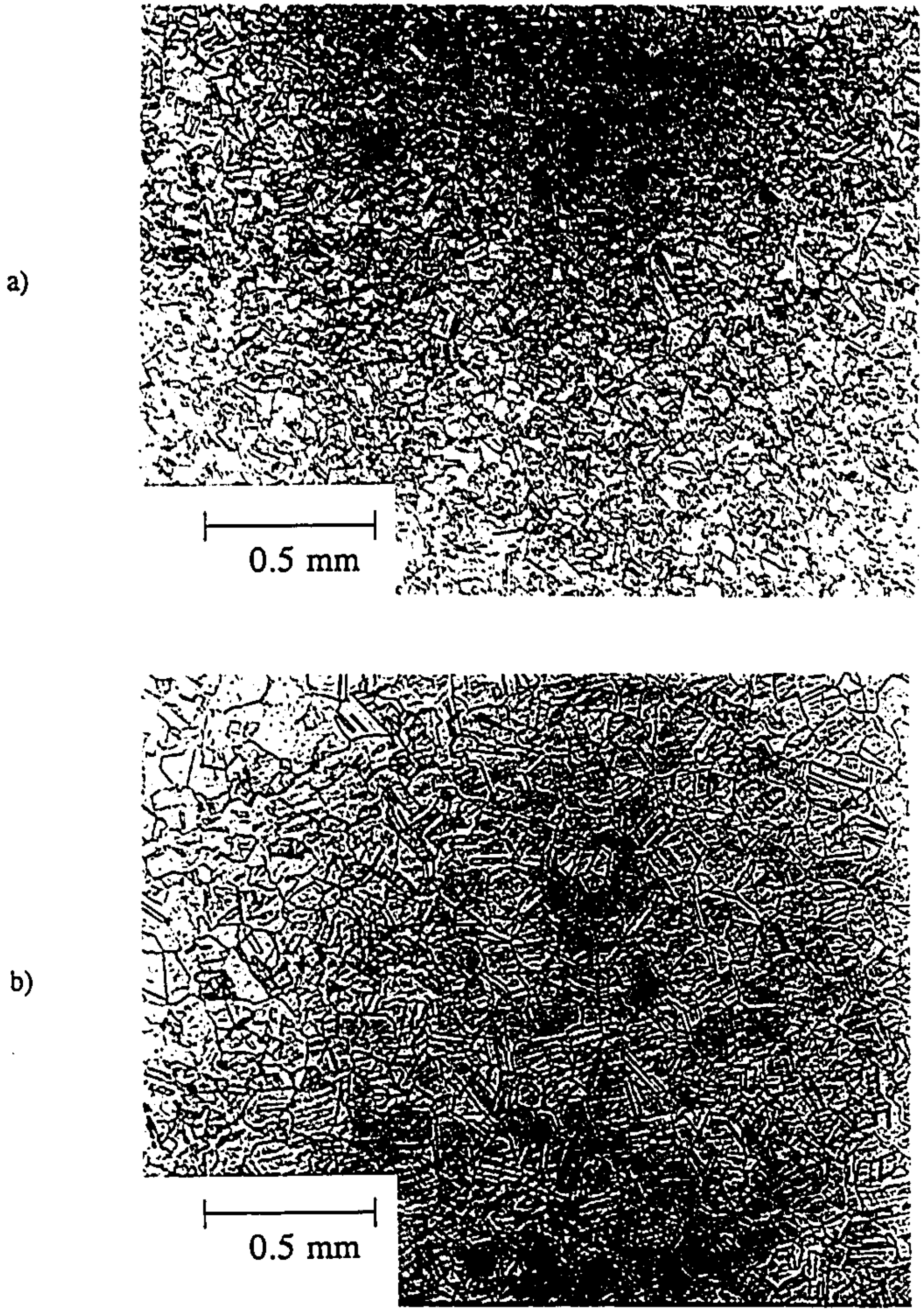

Figure 3.5 - Microstructure of unreinforced copper samples annealed at a) 500 °C and b) 700 °C.

The final polishing step was a traditional 0.3 μm alumina polish. Samples were etched with an ammonium persulphate solution (10 g ammonium persulphate in 100 ml distilled water) for 2-5 minutes.

3.4 - Preparation of Fiducial Grids

For the channel die compression samples, a fine gold grid was fabricated on the surface of the sample. This allowed for measurements of local strain based on the change in shape of the grid to be calculated. The grids were constructed by using an electron beam lithography technique (Attwood and Hazzledine, 1976). The procedure was as follows:

1) the sample faces to be gridded were metallographically prepared

2) samples were coated with a 6 w/o PMMA solution spin cast at 4000 rpm for 20 s in a class 100 clean room

3) sample with the PMMA film was baked at 175 ° for 1 hr

4) sample was exposed to an electron beam in a Cambridge Instruments scanning electron microscope (SEM) under the following conditions: accelerating voltage of 25 KV, absorbed current 1×10^{-9} Amperes, magnification of 10 X, 400 scan lines/per frame, 6s for full frame scan, 50 full frame scans and maximum spot size (approx. 1 μm)

5) sample was rotated 90 ° and exposed again to create a series of vertical and horizontal lines

6) sample was developed in PMMA developer (3 parts methyl ethyl

ketone, 1 part ethyl alcohol) for 120 seconds

7) sample was etched in Fe_3Cl solution for 10 s (10g Fe_3Cl, 100 ml H_20)

8) gold film was thermally evaporated on to surface in 10^{-5} vacuum to thickness of approximately 500 nm

9) sample was place in Chlorobenzene solution to remove remaining PMMA and attached gold

The main steps in the process are shown schematically in Figure 3.6. The grided area was 6 x 6 mm with line spacings of 20 μm and line widths of 2-3 μm. The quality of the grid was determined by :

i) the continuity of the gold lines. The uniformity of the spun PMMA film and the proper film exposure and development were the important criteria.

ii) the degree of orthogonality of the grid. This was controlled by the rotation of the sample in the SEM in between exposure steps. The horizontal and vertical lines were perpendicular within ± 2.5°.

iii) the line width which was determined by the electron beam spot size used (i.e. in this case 1 μm)

iv) the long range reproducibility of the grid line spacings. The important consideration was the ability of the SEM to rassister the electron beam on the surface of the sample repeatedly.

The gold grid in the deformed and undeformed states was examined using backscattered electron images in the scanning electron microscope since there is good atomic number contrast (i.e. $Z_{Cu} = 29$, $Z_{Au} = 79$) between gold and copper. A

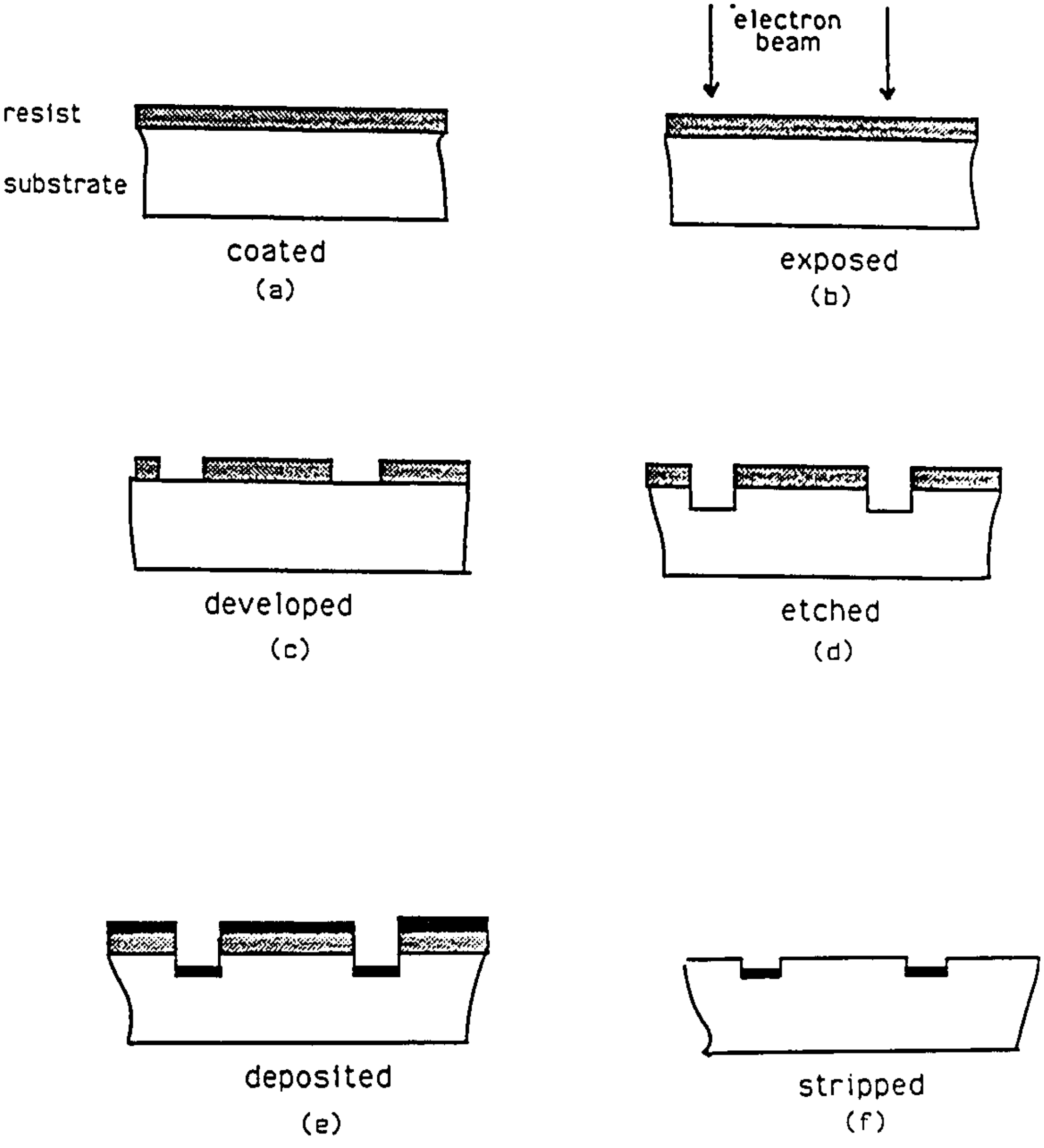

Figure 3.6 - Schematic diagram illustrating main steps in preparation of gold grids

representative example of the starting grid is shown in Figure 3.7.

3.5 - Calculation of Strain from Fiducial Grids

The calculation of strain from deformed grids is a problem which has received attention from investigators interested in measuring strains experimentally in metal stampings (e.g. Sowerby (1982)) and researchers analyzing deformed meshes in finite element method (FEM) calculations (Dawson (1992)). The approach taken here is to calculate the deformation gradient tensor, F, from the coordinates of the initial and final corners of a single grid element.

$$F_{ij} = \partial x_i / \partial X_j$$

In this work, the method for calculating F was taken from Dawson (1992) and essentially involved calculating an average value of F from the coordinates of a square element before and after deformation. Consider the following example for calculation of the term F_{11} having undergone plane strain compression as illustrated in Figure 3.8 . In this case:

$$F_{11} = [(\Delta x' + \Delta x'')/2]/\Delta X$$

where: $\Delta x'$, $\Delta x''$ are the length of the top and bottom of the element after deformation. Since in practice, the values of $\Delta x'$ and $\Delta x''$ will be different due to non-uniform deformation in a given element (see Figure 3.8), an average value for F_{11} at the centre of the element will be calculated.

Once the deformation gradient tensor has been calculated, it is useful to symmetrize the matrix. This can be accomplished by taking FF^T which yield the following matrix, Green's deformation tensor:

$$C_{xx} = F_{11}^2 + F_{12}^2$$

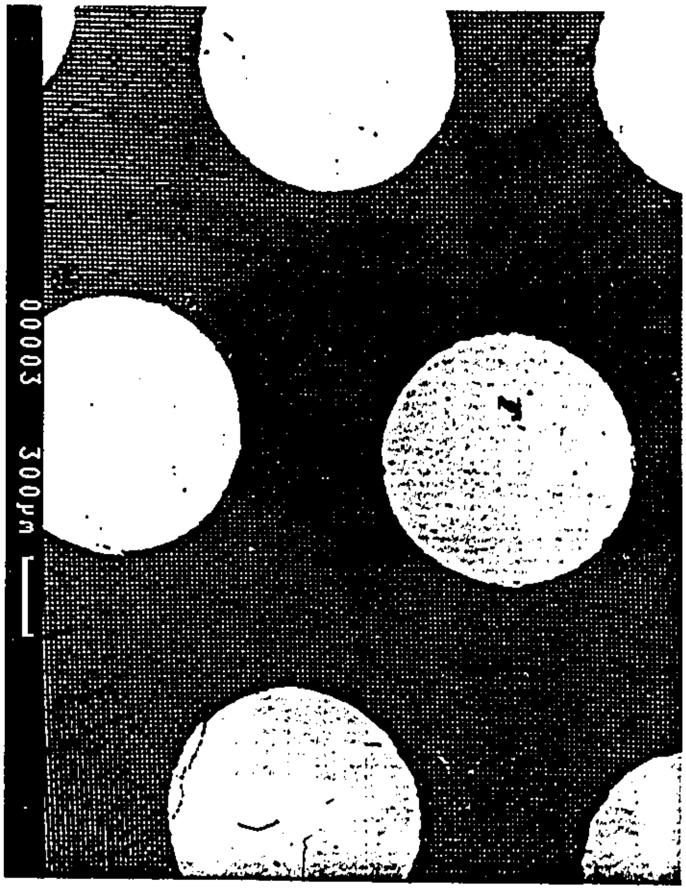

Figure 3.7 - Back-scattered electron image of initial gold grid

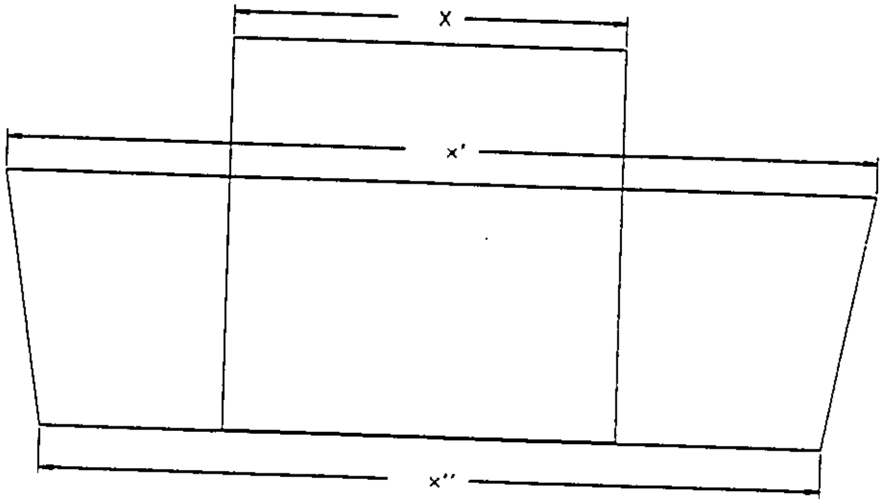

Figure 3.8 - Schematic diagram of deformed grid element

$$C_{xy} = C_{yx} = F_{11}F_{21} + F_{12}F_{22}$$

$$C_{yy} = F_{21}^2 + F_{22}^2$$

From this symmetric matrix, the principal values of the squares of the elongation ratios, λ_{ii}, can be calculated as:

$$\lambda_{11}^2, \lambda_{22}^2 = (C_{xx} + C_{yy})/2 \pm 1/2 \surd\{(C_{xx} - C_{yy})^2 + 4C_{xy}^2\}$$

Finally, the values of the principal true strains are given by:

$$\epsilon_{11} = \ln(\lambda_{11})$$

$$\epsilon_{22} = \ln(\lambda_{22})$$

The procedure for calculating local strains was to digitize the nodal points of the gold grid after deformation. The region of the sample to be digitized was chosen from the centre of the sample to avoid edge effects. A short computer program was written to take the corners of each quadrilateral and calculate *F*. The program then applied the formulae above to produce the values of principal strain.

An important aspect of this analysis is a consideration of the errors which arise during the calculation. These errors can be divided into i) errors arising from experimental measurements (i.e. grid line spacings, deviations from orthogonality in original grids, digitizing errors, etc.) and ii) errors arising from plastic heterogeneity due to grain to grain variations, macroscopic strain gradients and local deviations from plane strain. In order to quantify both types of errors, it is useful to consider two cases. The first is the digitization of an initially square undeformed grid and second, the digitization of a single phase polycrystalline sample after a given amount of strain. This approach allows one to allows for an assessment of errors developed in the analysis as follows:

1) an initially undeformed grid was digitized and analyzed using the technique described above. The variation in the measurements was quantified by calculating the average and standard deviation of the Von Mises strain. As expected, the average was close to zero (i.e. 0.005 strain) for 100 grid elements. The standard deviation of the strain was a strain of 0.025.

2) a polycrystalline copper sample was deformed to 40 % by channel die compression. The deformed grid (see Figure 3.9) was digitized and analyzed by the grid analysis program. Figure 3.10 is a histogram of the von Mises strain for a sample deformed to a true strain of 0.4. In this case the mean value of von Mises strain was 0.39 with a standard deviation of 0.09.

Having established that the majority of the error arises from heterogeneities in local deformation, a criterion was established to examine the data. The area of each grid element would be calculated from the determinate of the F , i.e.

$$\text{area} = F_{11}F_{22} - F_{12}F_{21}$$

It was decided that if the area of a deformed grid element was 15 % greater or 15 % smaller than the area of an undeformed grid element, this element would be removed from the analyzed data. This typically resulted in the removal of approximately 10 % of data. The data which was removed was usually in regions of high strain gradients.

The important conclusion of this section is that due to inhomogeneity of plastic flow in polycrystalline samples, a large error is expected for the analysis of a single grid element. However, these locals effects are cancelled when a larger area is examined. the local effects therefore represent a background noise level in the data.

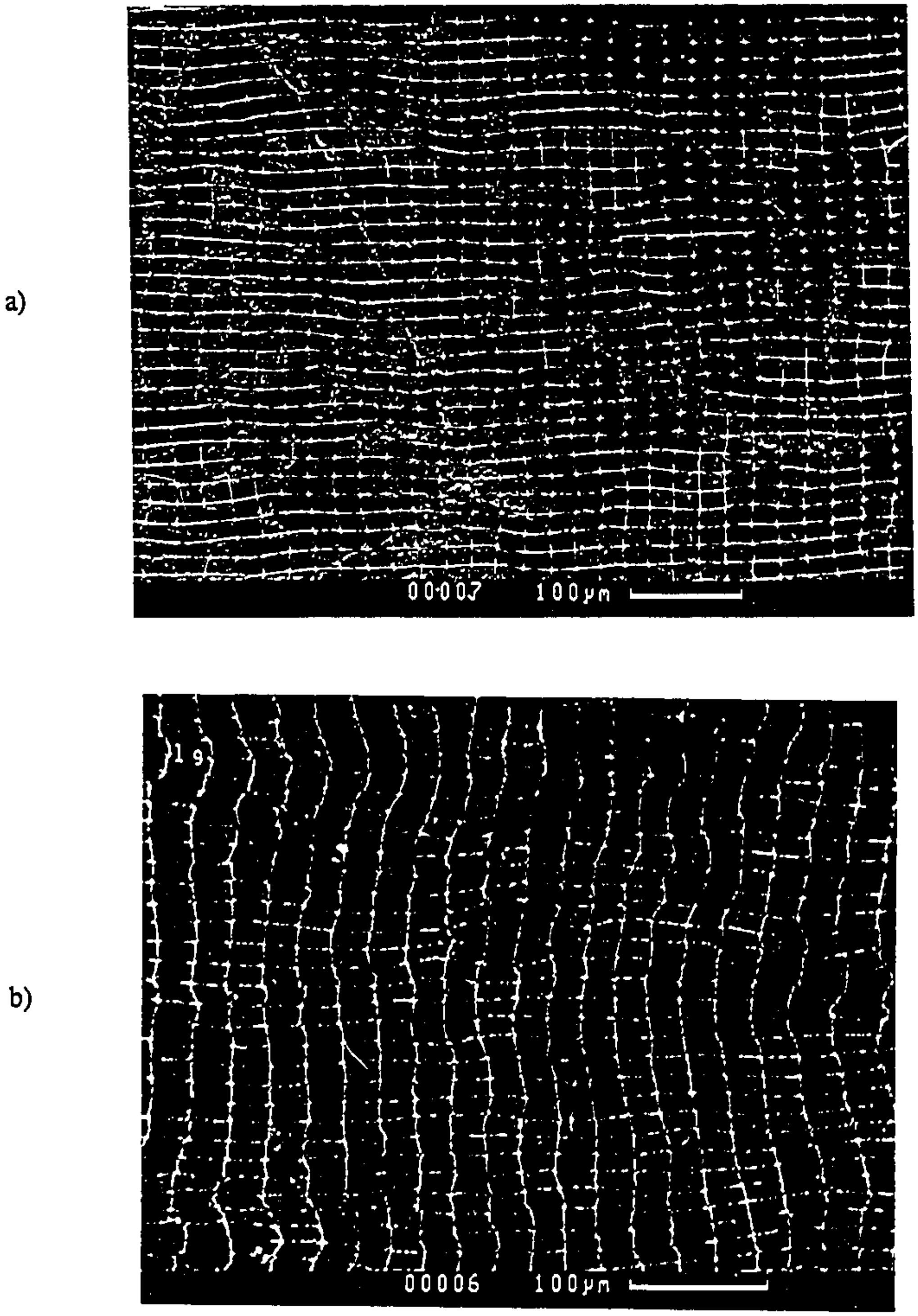

Figure 3.9 - Backscattered electron image of deformed grids for unreinforced copper after deformations of a) 0.2 and b) 0.4

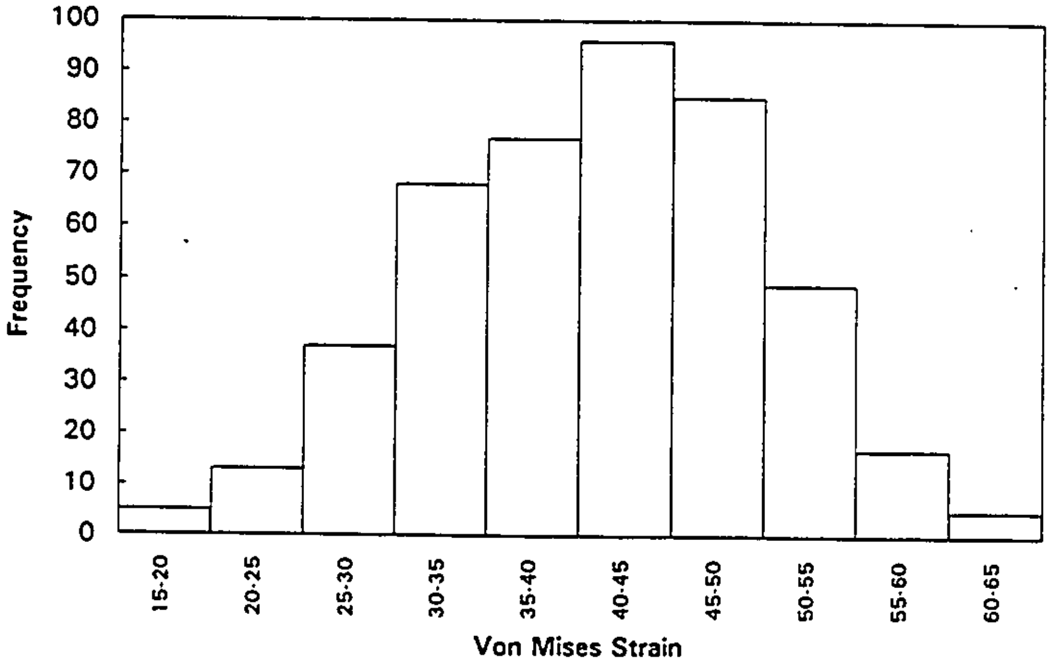

Figure 3.10 - Histogram of distribution of von Mises strain from grid calculations for unreinforced copper after deformation of 0.4.

3.6 - Texture Measurements

In considering the experimental determination of textures in metals it is useful to consider the nature of the measurement. A major consideration in determining the reliability of the measurements is the volume of material being sampled and how this changes as the orientation of the sample is changed. A combination of the x-ray spot size, the penetration depth of the x-rays, the grain size and orientation of the sample in the goniometer cradle determines how many grains are being sampled. In this case the penetration depth is much smaller (i.e. 50 μm) than the grain size so that only surface grains are being sampled. In composite materials, it is important to consider shadowing effects of the reinforcing phase (Bunge, 1985). The presence of the tungsten fibres prevents the incident x-rays from sampling a region of the matrix adjacent to the fibre. The volume of matrix material affected depends on the angle of incidence, λ. However, as the azimuthal angle is changed the volume of material which is not sampled changes. This will cause problems when trying to construct complete pole figures which are self-consistent. In order to reduce this effect, the maximum value of λ used in the calculations was 70° instead of the normal 80°.

Experimental pole figures were measured using a Scintag texture goniometer using CuK_α x-ray radiation. Figure 3.11 shows the definition of the angles for the goniometer cradle and the corresponding angles on a standard stereographic projection. Measurements were made for the copper on the (111), (200) and (311) poles which have 2θ values of 43.4, 50.5 and 90.0 degrees respectively. The copper (220) pole figure

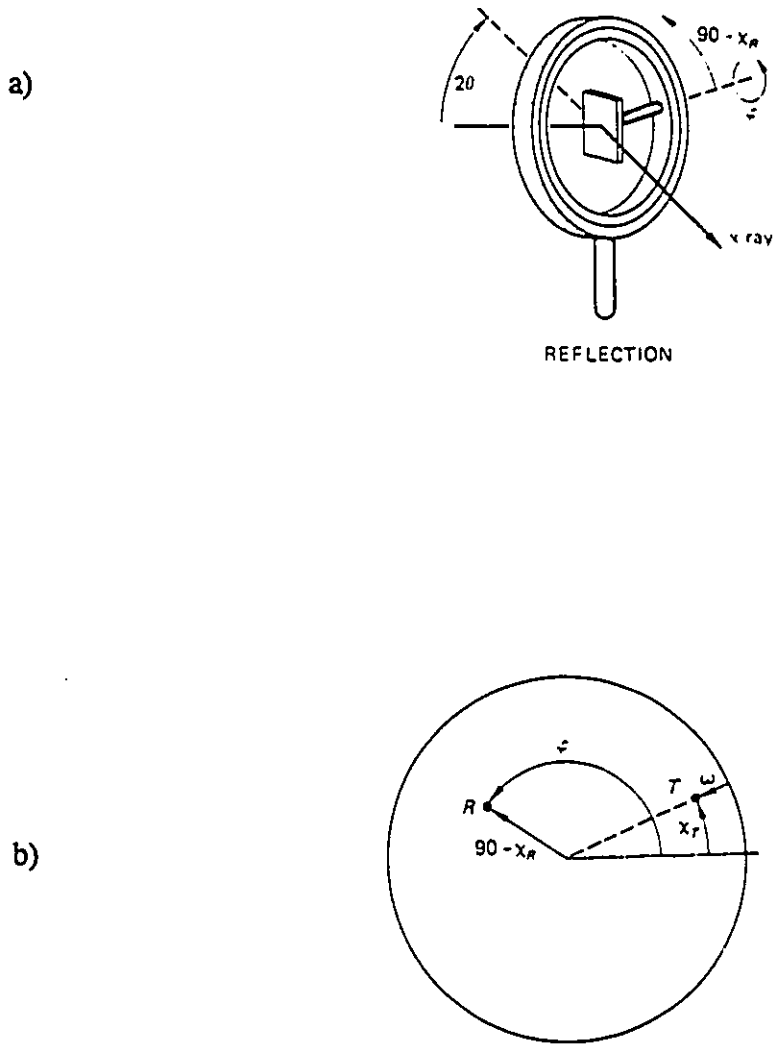

Figure 3.11 - Definition of angles for x-ray texture measurements a) for goniometer and b) on corresponding projection (H.R. Wenk, 1985).

could not be measured due to overlap with the tungsten (211) pole. The values of azimuth and angle of incidence were incremented by 5 degrees stepwise from 0-360 and 0-80 respectively. At each position, x-rays were counted for 1 second. The input slit for the x-ray detector was set at 1 mm. All pole figures shown in this work will be equal-area projections. The equal-area projection has the advantage that the intensity of poles for a random sample is uniform over the entire projection (e.g. compare equal area projection and stereographic projection for an initially random sample shown in Figure 3.12). The experimental textures were corrected for defocusing and background effects based on experimental correction files from a random copper sample. The incomplete pole figures (corrected for defocusing and background) were processed on a PC-based software package (Kocks, 1989 , Kallend et al., 1991). This allowed for the generation of fully normalized and complete pole figures using the WIMV algorithm.

Texture measurements were performed in two ways. Firstly, global texture measurements were made on the surface adjacent to channel die wall. These measurements sampled all the various regions of the matrix and thus, generated data on the development of the average texture. In order to obtain information on local texture development samples were sectioned as shown in Figure 3.13. In this case, regions of similar deformation path and magnitude could be examined. This was used to distinguish the various local texture components of the overall average texture. The resulting experimental textures were permuted so that the pole figures were oriented with the fibre axis at the centre of the projection and rolling direction pointing to the top.

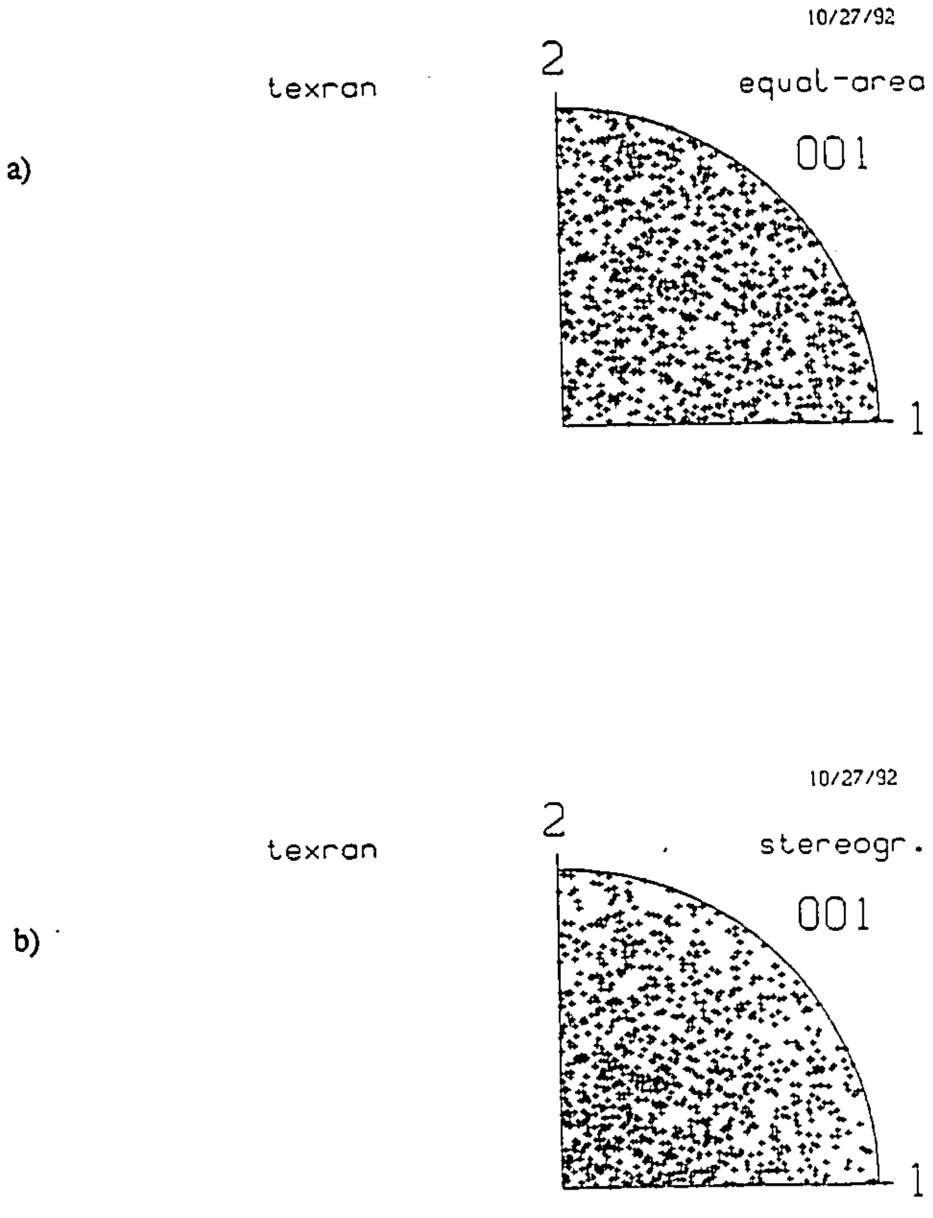

Figure 3.12 - Comparison of a) equal area projection and b) stereographic projection for a set of random orientations

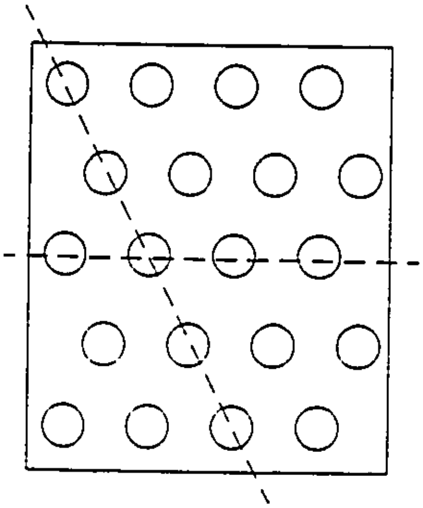

Figure 3.13 - Schematic illustrating sections used for texture measurements

3.7 - Mechanical Testing

3.7.1 Monotonic Channel Die Compression Tests

These tests were performed on a Model 880 MTS servo-hydraulic testing machine. The configuration of the channel die is shown in Figure 3.14. An important aspect of these tests was to reduce the effect of friction between the sample and the channel die. This involved careful machining of the samples to fit the channel die and the selection of appropriate lubrication conditions. At all times the height to width ratio (i.e aspect ratio) of the samples was kept between 1.4 and 0.7. This represents a compromise between reducing the contact area between the sample and the compression punches (high aspect ratio) and the requirement to avoid sample buckling (e.g. if the aspect ratio was too large). In order to reduce the effects of friction, 3 mil teflon tape was placed between the sample and die walls. The side of the teflon tape in contact with the sample was coated with Molykote lubricant. The deformation was carried out in strain increments of 0.1. After each increment of strain, textures were measured, the gold grid on the surface was photographed and the teflon tape was replaced prior to subsequent deformations. The analog data from the load cell and extensometer was recorded and converted to digital values using a 14 bit analog to digital converter. The resulting digital load-extension curves were converted to true von Mises equivalent stress and true von Mises strain following the test. The following relationships were used:

$$\epsilon_{\text{channel die}} = \ln(A/A_o)$$

$$\sigma_{\text{channel die}} = (F/A)$$

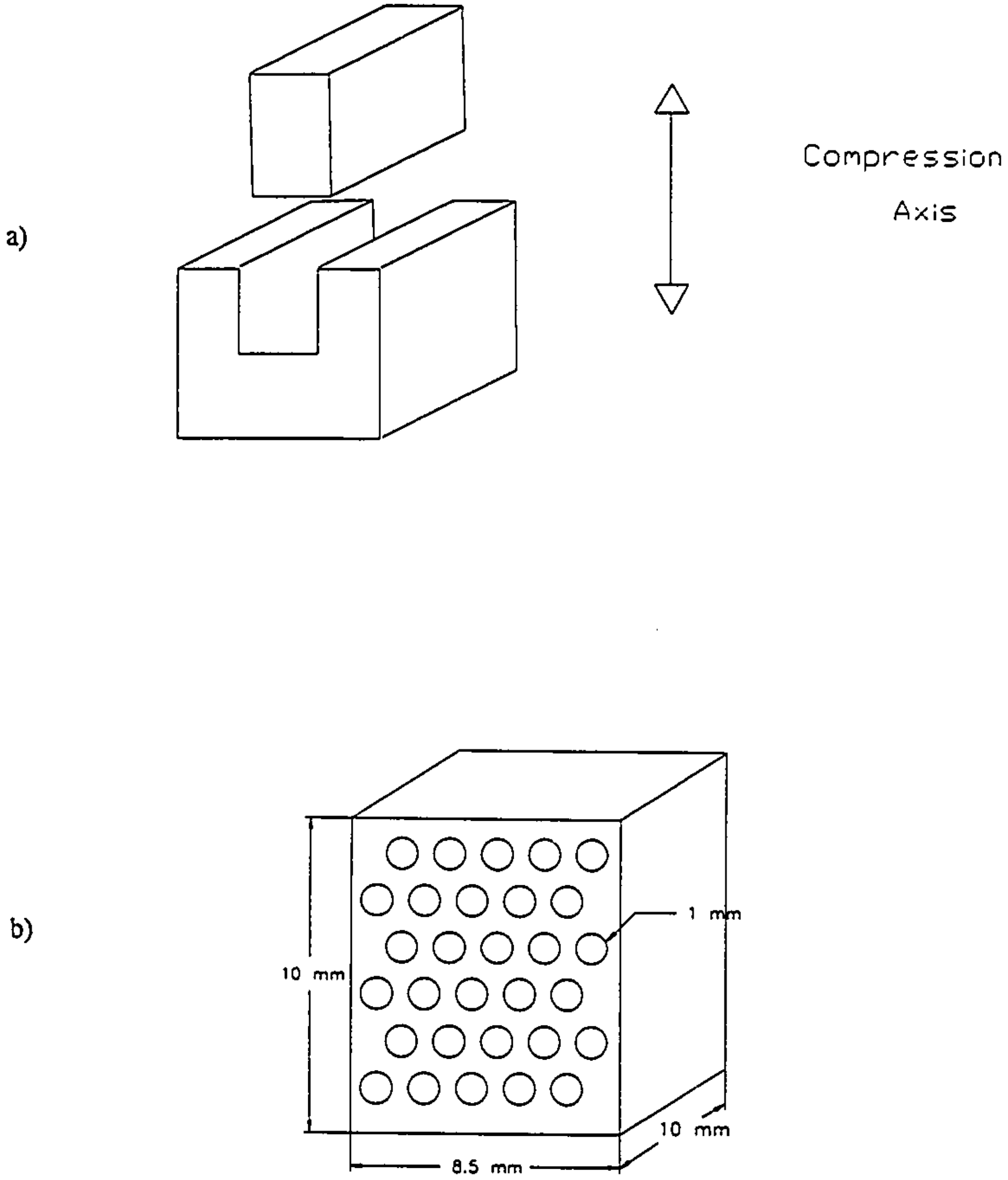

Figure 3.14 - Schematic diagram of a) channel die used for plane strain compression tests and b) sample including dimensions

where:

A = instantaneous cross-sectional area

A_o = initial cross-sectional area

F = force from the load cell

for plane strain:

$$\sigma_{\text{Von Mises}} = (\sqrt{3}/2)\sigma_{\text{channel die}}$$

$$\epsilon_{\text{Von Mises}} = (2/\sqrt{3})\epsilon_{\text{channel die}}$$

The sources of errors in these tests arose from the measurements of load and displacement. The load readings were determined from a calibrated load cell with errors of less than or equal to 0.5 %. The displacement was measured using a calibrated extensometer. However, in this case the displacement measured was that of the hydraulic ram which included elastic displacements in the load frame, the channel die and most importantly the teflon lubrication. It was typically observed that for an imposed deformation of 1 mm on a sample of 10 mm in height, the actual measured displacement on the sample after the test would be 0.9 mm. It should be noted that the discrepancy between the imposed displacement and the measured displacement is 5-10 times greater than the elastic strains generated in the sample. The largest contribution arises from flow in the teflon lubrication. As a consequence of these factors the low strain behaviour (i.e. elastic modulus and yield point) cannot be accurately measured with this type of test. In order to ensure the reproducibility of these tests a large strains, at least two tests were performed at each condition for the different samples.

3.7.2 Large Strain Bauschinger Tests

For the 20 % volume fraction samples with triangular fibre arrangements, strain path reversal experiments were conducted after 15 and 30 % forward strain. The forward deformation was conducted as described in the previous section. A reversal of the strain path was achieved by rotating the compression axis 90 ° about the sample fibre axis. The sample was carefully re-machined by EDM before the reverse deformation was imposed.

3.7.3 Diametral Compression Tests of Tungsten Fibres

Due to the degradation in mechanical properties of the tungsten fibres during casting, it was useful to determine the fracture stress of the tungsten fibres after casting. The tungsten fibres were recovered from the composite by dissolving the copper matrix in concentrated nitric acid. The resulting fibres were 1 mm in diameter in 10 mm in length. These fibres were then compressed between tool steel platens with the long direction of the fibre perpendicular to the loading direction as shown schematically in Figure 3.15. A detailed description of this test is given by Jaeger and Cook (1976). The stresses generated in the particle along the loading axis can be summarized as:

$$\sigma_x = -W/\pi R$$

$$\sigma_y = W(3R^2+y^2)/\pi R(R^2-y^2)$$

where: W is the applied load, R is the radius of the cylinder and y is the distance from the centre of the sample along the loading axis. These formulae are derived from an elastic solution for a point load between the platen and cylinder. Experiments where the

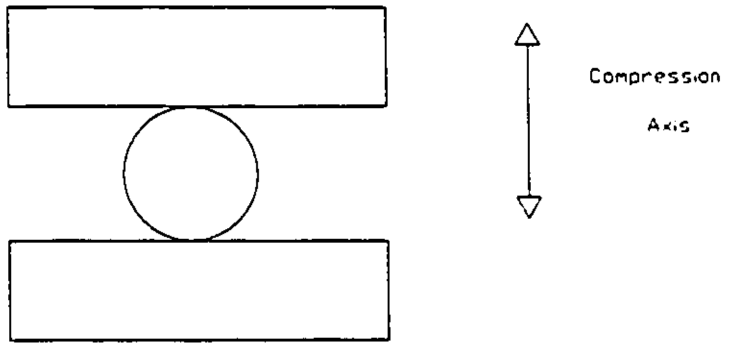

Figure 3.15 - Loading arrangement for diametral compression tests

load is distributed over a narrow arc (typically 15°) produce tensile fracture stresses which do not differ substantially from point loading experiments (Jaeger and Cook, 1976). This occurs since the largest tensile stresses are generated at the centre of the sample which is far away from the loading points.

The compression tests were conducted on a MTS servo-hydraulic testing machine. A short computer program was written to compress the sample in stroke control and monitor the applied load (10 KN full scale). Load readings were recorded digital using a 14-bit digital to analog converter. The test was stopped when the applied load fell below ten percent of the maximum previous load (i.e. when the sample fractured). After the test the maximum load (i.e. the fracture load) measured from the load cell was recorded. At least 5 tests were performed at each condition.

3.8 Finite Element Method Calculations

A series of finite element method (FEM) calculations were conducted at Alcan International's Kingston Research and Development Centre. The purpose of this work was perform a computer simulation of the experimental composite compression tests.

The procedure for generating a FEM model was as follows:

1) creation of a model geometry - this involves the creation of the geometric frame for the particular composite to be modelled. The outer dimensions of the sample the location of the tungsten fibres within the body were specified. For these models, the geometries were chosen to be the same as the actual composites (i.e. Figure 3.1) with the exception that a horizontal symmetry plane was placed at the centre of the sample. The creation

of the model geometry was conducted using the IDEA-S computer program on a Silicon Graphics workstation.

2) assignment of material groups - the various features of model geometry were assigned to material groups which would later have materials properties assigned to them. In this case, the fibres were assigned to one group and the remaining material inside the frame (i.e. the matrix) was assigned to another group.

3) generation of nodes and mesh elements - this was an important step which would have a large effect on the quality of the results. For this work, quadrilateral plane strain elements were chosen. The mesh generation algorithm within IDEA-S was used. The criterion that were applied to judge the quality of the mesh were as follows:

i) there should be more mesh elements where the largest gradients of stress and strain are expected.

ii) adjacent mesh elements should not vary in dimension by more than a factor of two

iii) aspect ratio of mesh elements should be close to 1

iv) the total number of mesh elements should be a minimized so that the model will execute in a reasonable amount of time

There were various methods possible to control the mesh generation in IDEA-S. After several attempts a satisfactory mesh was constructed. In this case, mesh was generated in two steps. The matrix mesh was generated by specifying the number of nodal points on the diameter of each fibre (40) and on the sides of the sample (25 on the sides and 50 across the top). The fibre meshes were generated by specifying the number of nodes on on the diameter (40). An example of the geometry and mesh used for 20 % volume fraction sample with square arrangement of fibres is shown in Figure 3.16.

Following the mesh generation, a nodeset (a list of nodal points) consisting of all nodal points on the top surface of the geometry was created for later use in applying the boundary displacement conditions. Finally, a symmetry condition was imposed on all the nodal points at the bottom of the geometry. This restricted the degrees of freedom on these nodal points. These nodes were allowed no translation in the vertical direction and no rotational motion (i.e. the nodes could only move in the horizontal direction).

The ABAQUS input file was comprised of a series of lists shown schematically in Table 3.3. The material properties in the ABAQUS input file were manually edited. The elastic properties used were: E=400 GPa, ν=0.28 for tungsten and E=110 GPa, ν=0.3 for copper. The tungsten was assumed to be elastic and was therefore not assigned plastic properties. The copper's plastic properties were represented by a piece-wise linear representation of the copper experimental plastic stress-strain behaviour (see Figure 3.17)

The final steps in producing the model were specifying the displacement boundary conditions and output options. The displacement boundary conditions were specified by the total vertical displacement of the top surface of the geometry. For example, a macroscopic strain of 0.2 required the top surface to be displaced by 1.81 mm. The output options specified were that the complete results were printed to a file every 5 increments and the sum of reaction forces and displacements on the top surface were printed every increment.

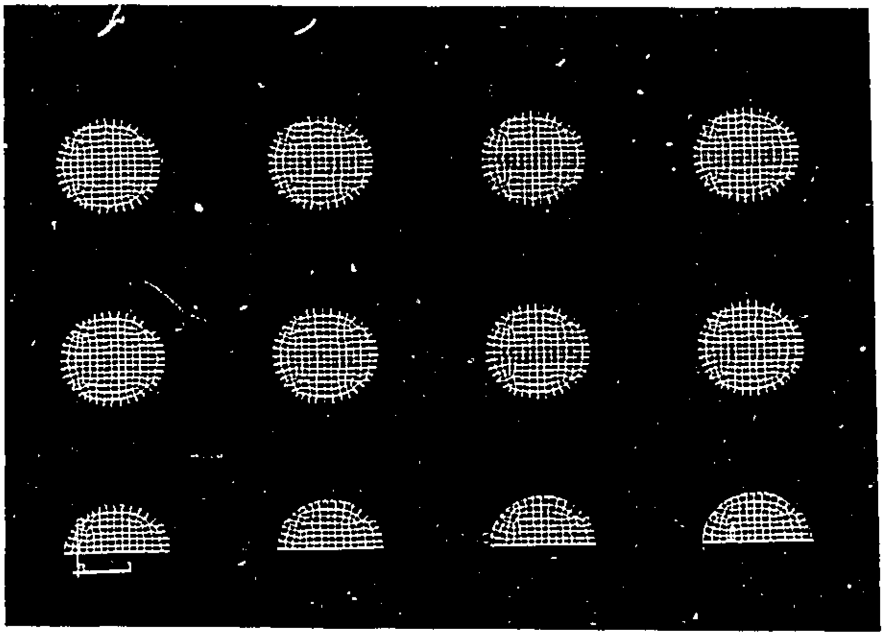

Figure 3.16 - Mesh used for FEM calculations for 20 % volume fraction with square arrangement of fibres.

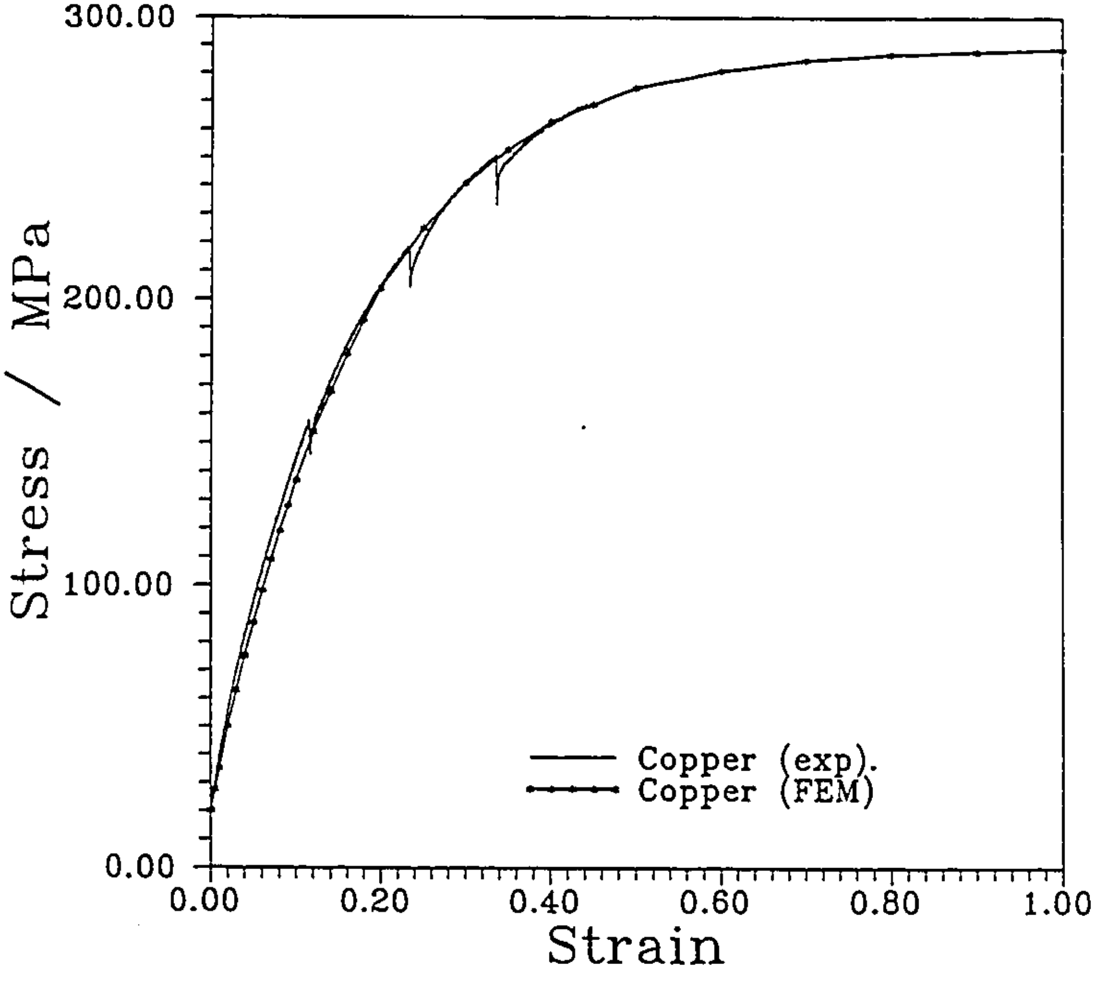

Figure 3.17 - Plastic stress-strain curve used in FEM calculations

Table 3.3 - Organization of Abaqus input file

Title and comments
Nodal point numbers   x,y,z coordinates
Elements numbers   4 nodal points numbers/elements
Material Groups   Element numbers
Material Properties Elastic and Plastic Properties
Boundary Conditions   Nodal point number Restraints
Execution Statements Displacement Specifications Step sizes and increment limits Output options

The completed model was submitted to create an ABAQUS executable file which was subsequently executed on the Silicon Graphics workstation. The models in this work typically required 4-10 hours to complete. After models were completed, the results could be observed using the ABAQUS post-processor. This allowed the generation of colour contour plots for the parameters of interest (e.g. von Mises stress and strain, hydrostatic pressure ...) from the area of interest. All contour plots in this work were taken from the central region of the model geometry. These plots could then be printed using a Tektronix colour printer. The data generated for the reaction forces and displacements on the top surface were analyzed in exactly the same way as force displacement data from the mechanical tests (see Section 3.7).

CHAPTER 4

RESULTS - PLANE STRAIN COMPRESSION TESTS

4.1 Introduction

This section describes the results of the experimental and modelling work for the plane strain compression tests. It is divided into i) macroscopic measurements such as stress-strain behaviour and texture development and ii) local behaviour including fibre fracture and the distributions of recrystallization events. The results for triangular and a square arrangements of fibres at two different volume fractions will be presented.

4.2 Mechanical Behaviour

4.2.1 - Monotonic Plane Strain Compression Tests

The results of mechanical behaviour include i) measurements of stress-strain behaviour from channel die compression tests and comparison with FEM calculations and ii) examinations of the macroscopic shape change of the sample during the compression tests. The observations of damage which may be seen in some of the composite samples will be presented in the Section 4.2.2.

The true stress-strain curves from the channel die compression tests for unreinforced copper of two grain sizes (i.e. 50 and 140 μm) are shown in Figure 4.1. In this work, the stress-strain curves presented are expressed as von Mises equivalent stress-strain curves as defined in Section 3.7.1. The discontinuities in the curves arise

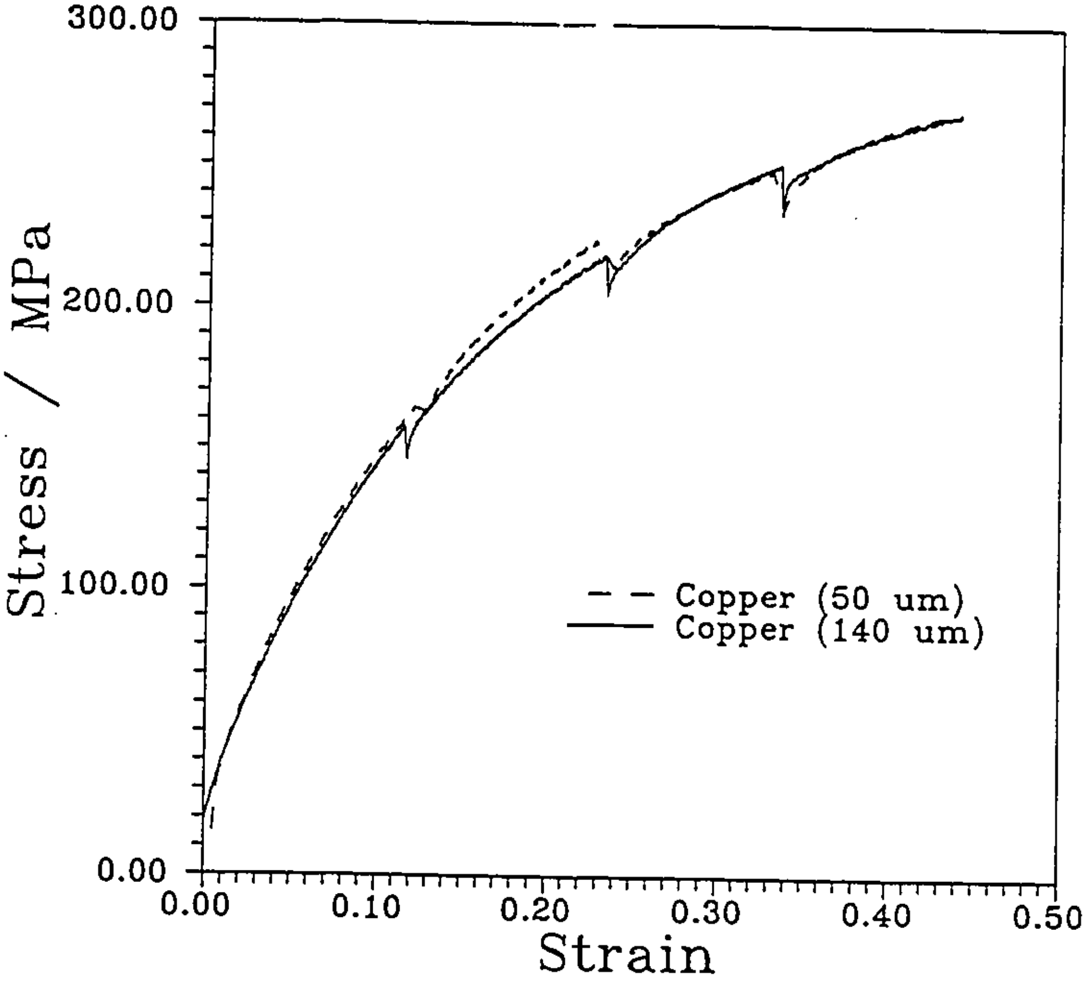

Figure 4.1 - Stress-strain curves for unreinforced copper of grain size 50 and 140 μm

when the compression tests are stopped and the lubrication replaced. The unloading and reloading sections of the curves have been removed from the data to make interpretation of the stress-strain behaviour easier. The copper samples with 50 μm grain size show slightly higher strength levels for true strains less than 0.2. Above true strains of 0.2, there is little difference in stress-strain behaviour for the two grain size materials. However, due to the nature of the channel die compression (see description of sources of errors in Section 3.7.1), the differences in the stress-strain curves at low strains are most likely not significant. This is in agreement with literature values for grain size effects on the yield stress for copper (e.g. Meyers and Chawla, 1984). In the following sections, the results of the large grain size material behaviour will be used for comparison with the composites.

The experimental von Mises stress-strain curves for the samples with triangular arrangements of fibres at 20 and 30 % volume fraction are shown in Figure 4.2. The following observations from this figure can be made: i) at true strains below 0.2 the strength level of the composite scales with volume fraction of tungsten (i.e. strength level for a given strain increases with volume fraction) and ii) at true strains above 0.2, the stress-strain curves from the composites and the unreinforced copper are converging.

The macroscopic shape and spatial distribution of the tungsten fibres for the 20 % volume fraction sample, before and after 30 % deformation, are illustrated in Figure 4.3. While the sides of the sample show substantial deviations from parallelism especially close to the tungsten fibres, there is no indication of barrelling in the sample.

Figure 4.4a, b and c are micrographs of the 30 % volume fraction sample after

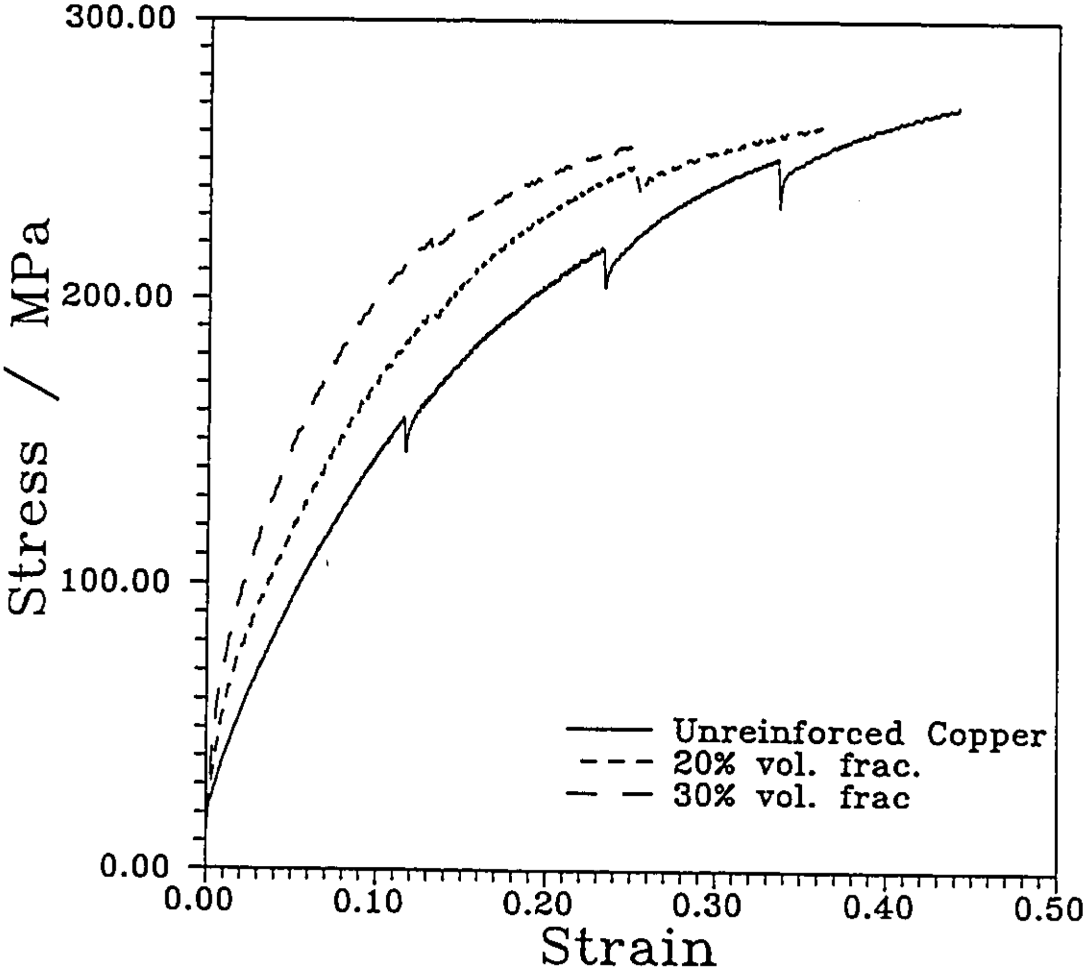

Figure 4.2 - Stress-strain curves for composites with triangular arrangements of fibres

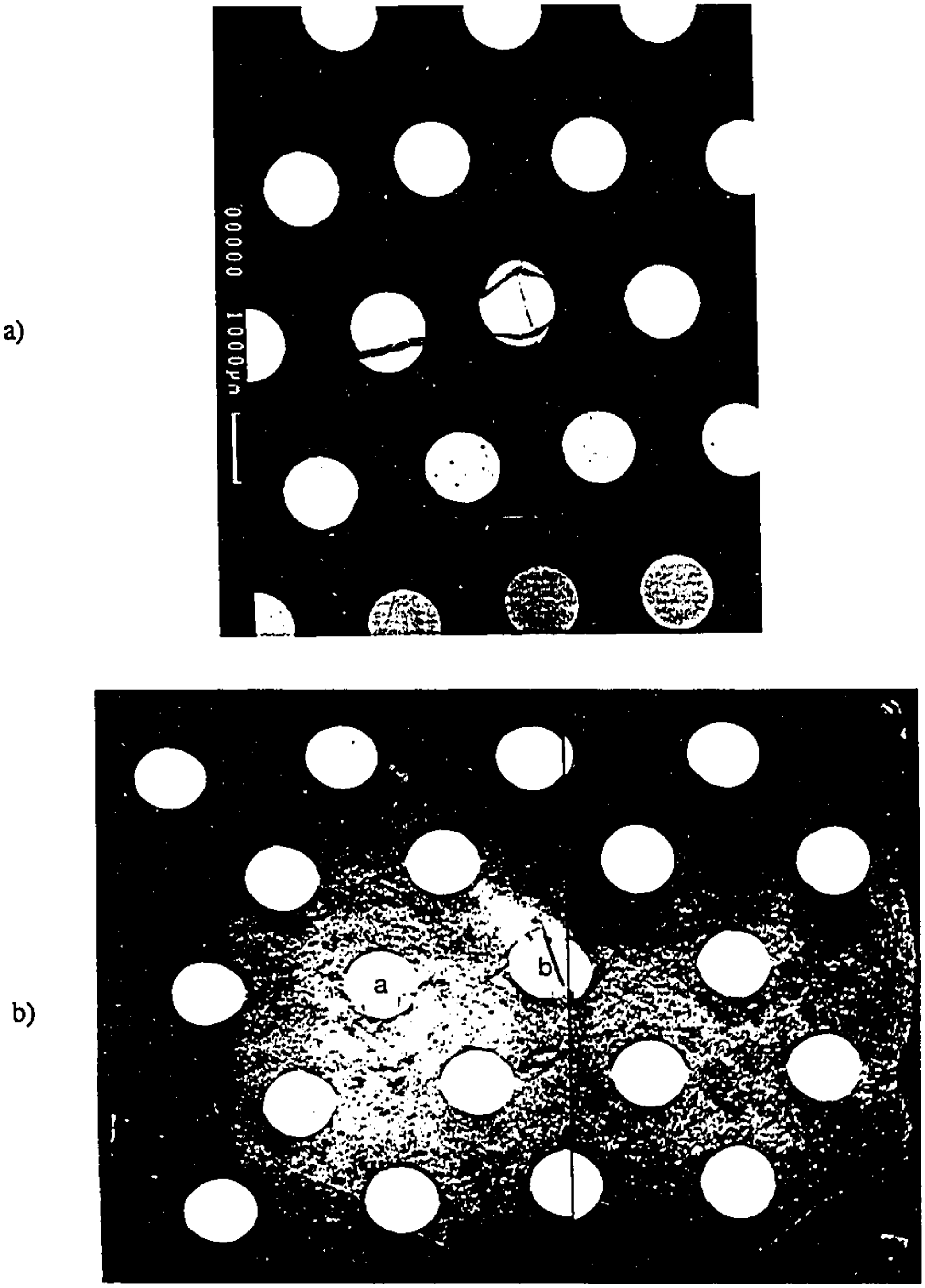

Figure 4.3 - Back-scattered electron images of 20 % volume fraction sample with triangular arrangement of fibres a) before deformation and b) after an imposed deformation of 0.3. Note: tungsten fibres are 1 mm dia.

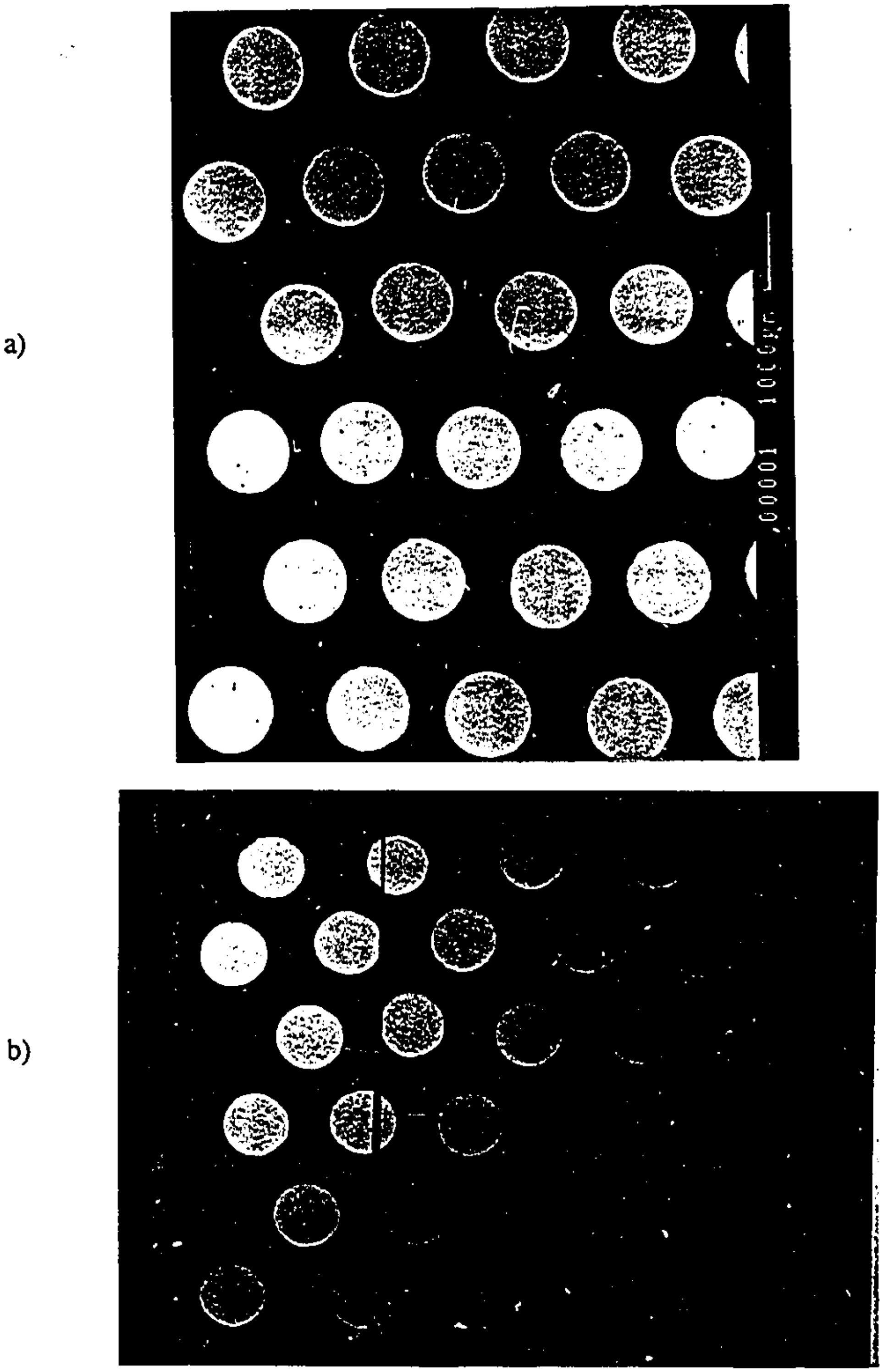

Figure 4.4 - Back-scattered electron images of the 30 % volume fraction sample a) before deformation, b) after an imposed deformation of 0.2 and c) 0.3. Note: tungsten fibres are 1 mm dia.

c)

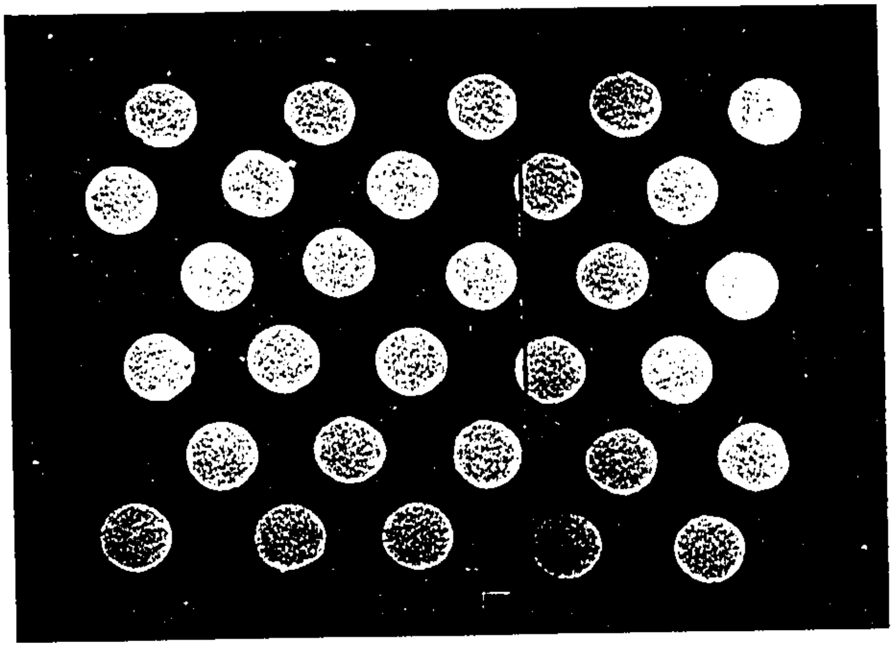

imposed deformation of 0, 0.2 and 0.3 respectively. The macroscopic shape change as the sample is deformed can also be observed in this sequence of micrographs. Once again, there are large local deviations from parallelism for the sides of the sample. The undulations of the surface are related to distribution of fibres. The matrix material in regions between the fibre rows has been pushed outward while the matrix material along the fibre rows was constrained from deforming.

The von Mises equivalent stress-strain curves for the composites with a square arrangement of fibres are shown in Figure 4.5. At low true strains (i.e. < 0.2), the strength level for a given value of strain increases with the volume fraction of tungsten fibres. At true strains greater than 0.2, there is a large decrease in the level of stress for the 30 % volume fraction sample.

Figure 4.6 is a back-scattered electron micrograph of the 20 % volume fraction sample after deformation of 0.3. The sides of the sample have an irregular shape but there is no evidence of barrelling in the sample.

Figure 4.7a-d illustrate the macroscopic shape of the 30 % volume fraction samples after a true strain of 0, 0.1, 0.2 and 0.3, respectively (note: d is a different sample from a,b and c). The 30 % volume fraction sample shows some reverse barrelling and damage at a true strain of 0.2. At a true strain of 0.3, this sample had developed macroscopic instabilities accompanied by a the formation of large shear bands and damage in the sample illustrated in Figure 4.7d. The development of these instabilities coincides with the drop the stress-strain curve for this sample (see Figure 4.5). A detailed description of the damage evolution will be presented in Section

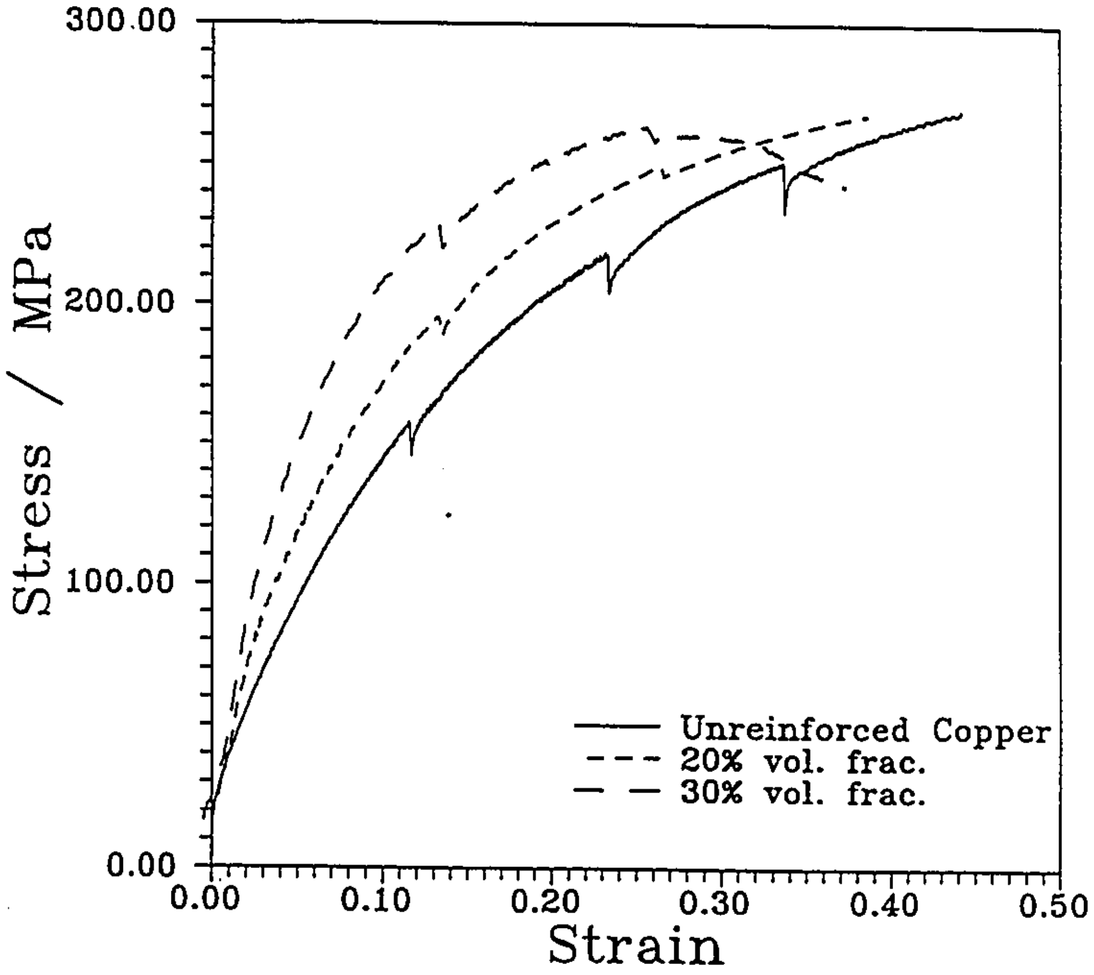

Figure 4.5 - Equivalent stress-strain curves for samples with square arrangements of fibres

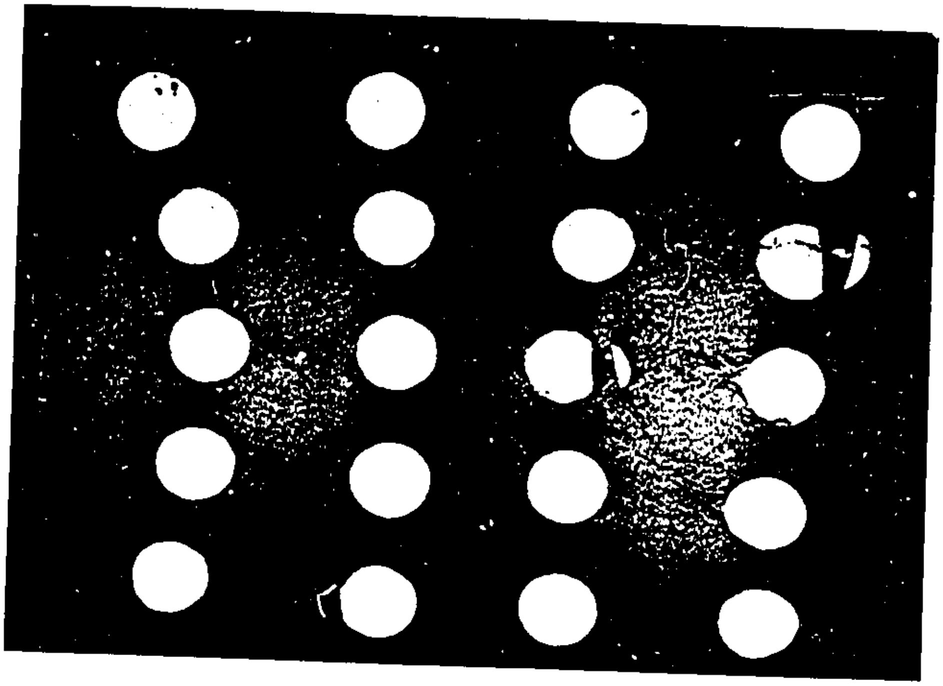

Figure 4.6 - Back-scattered electron micrograph of 20 % volume fraction sample after an imposed deformation of 0.3. Note: tungsten fibres are 1 mm dia.

a)

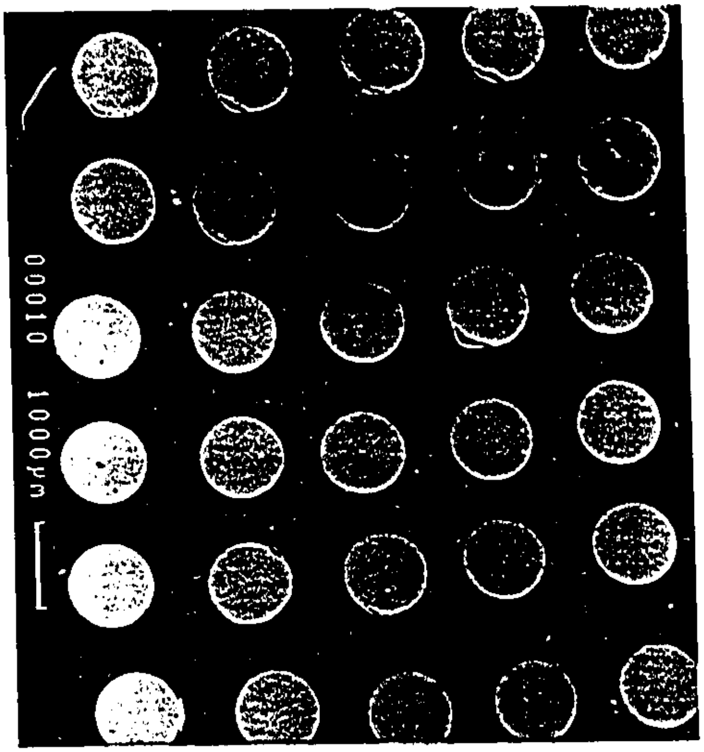

b)

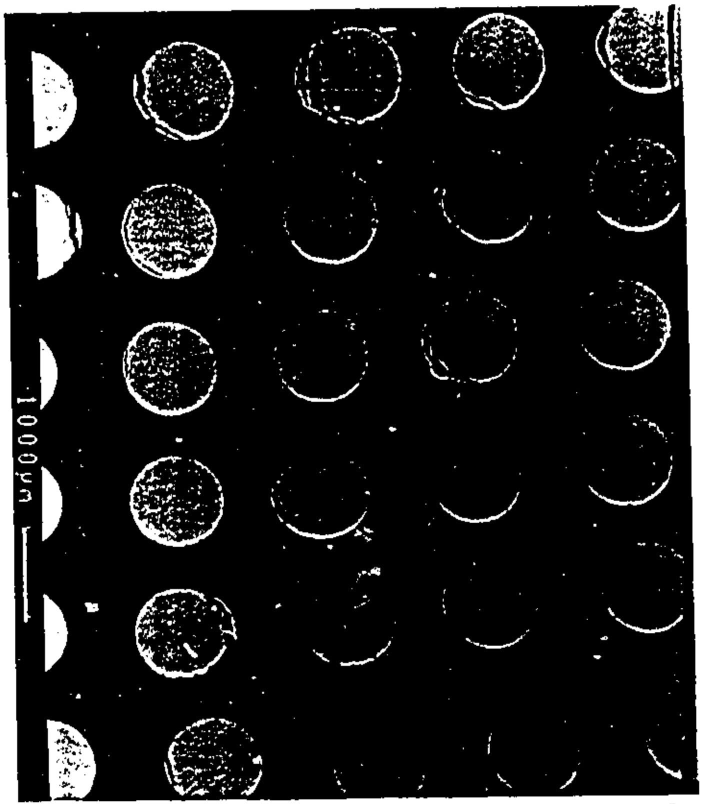

Figure 4:7 - Back-scattered electron image of the 30 % volume fraction sample after imposed deformation of a) 0, b) 0.1, c) 0.2 and d) 0.3. Note: tungsten fibres are 1 mm dia.

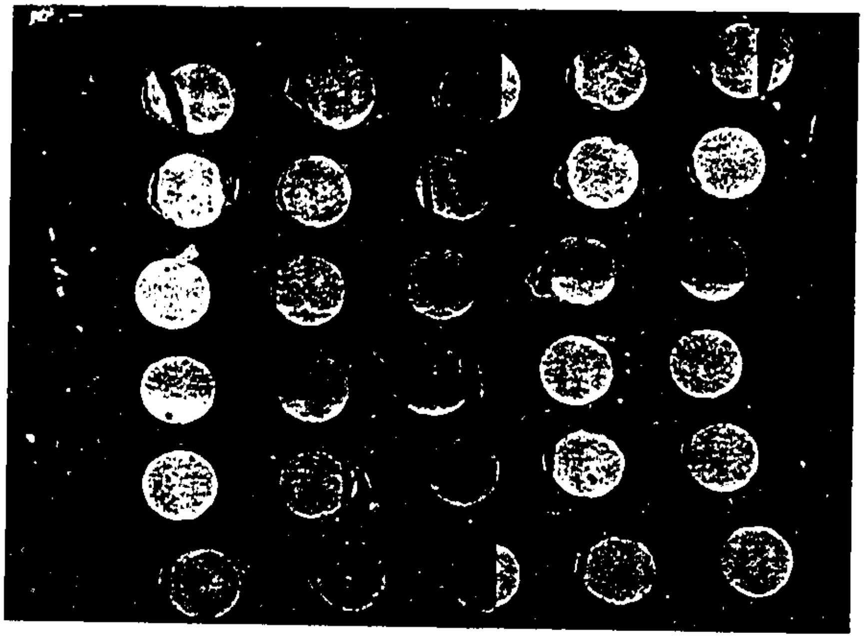

c)

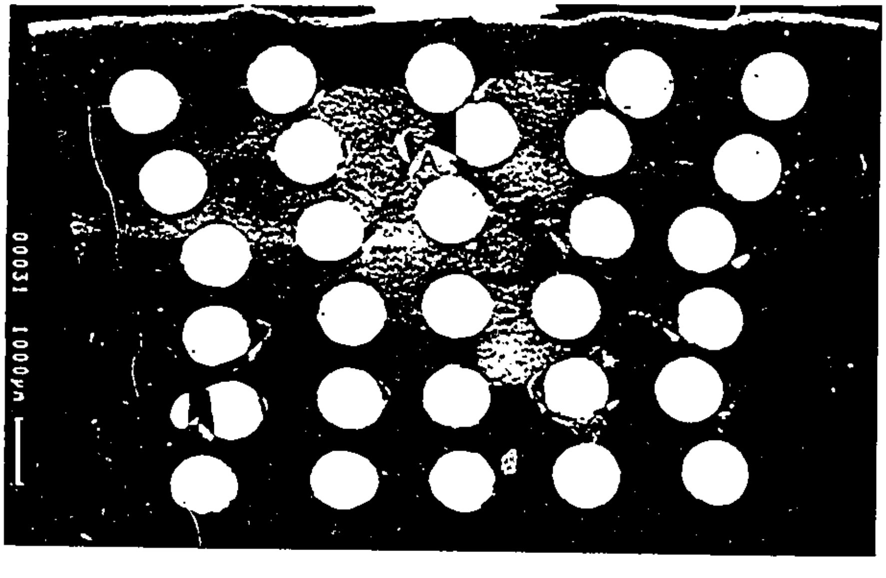

d)

4.5.

For the square arrangement of fibres (deformation axis parallel to edge of the square), stress-strain curves calculated from the results FEM simulation can be compared to the experimental results as shown in Figure 4.8. The agreement between the experimental results and the FEM calculations is good at true strains below 0.10. Above a true strain of 0.10 the stress values from the FEM calculations are higher than the experimental values. The macroscopic shape change of the sample can also be compared. Figure 4.9 and Figure 4.10 illustrate the FEM calculated prediction for the macroscopic shape change. The 20 % volume fraction sample shows uniform deformation with little deviation from parallelism of the sample sides (see Figure 4.9). The experimental shape change shown in Figure 4.6 is in fair agreement with this observation. The 30 % volume fraction sample (e.g. Figure 4.10) shows reverse barrelling similar to the experimentally observed sample shape (see Figure 4.7).

4.2.2 - Damage Observations

Some comments on damage have been noted in Section 4.2.1. It is useful to have a more complete description of these observations. In the triangular arrangements of fibres, the level of damage in the fibres is low and consists of interfacial debonding and particle cracking . In the case of the samples with a square arrangement of fibres, the level of damage increases with strain and is at greater level for the higher volume fraction samples.

In the 20 % volume fraction samples with triangular arrangement of fibres some

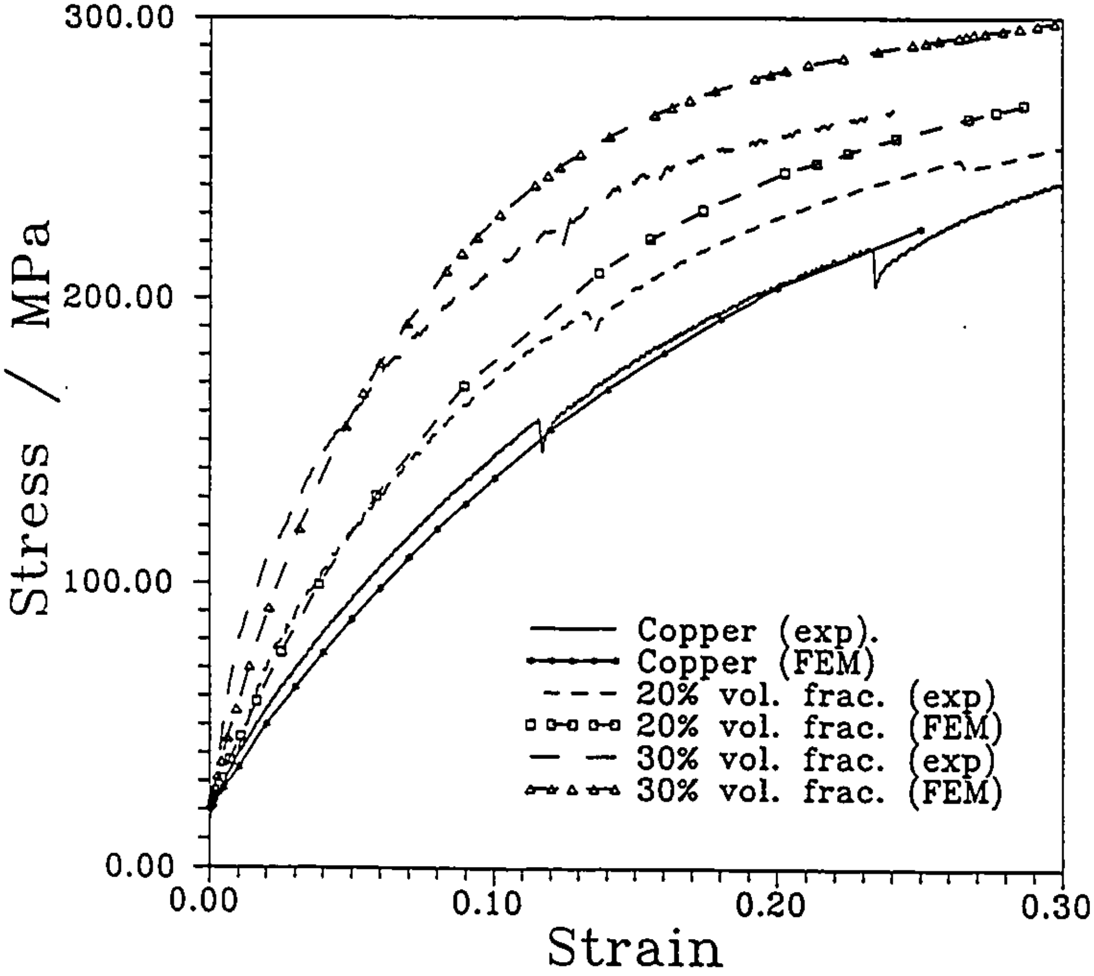

Figure 4.8 - Stress-strain curves for copper-tungsten composites with square arrangement of fibres (deformation axis parallel to the edge of the square).

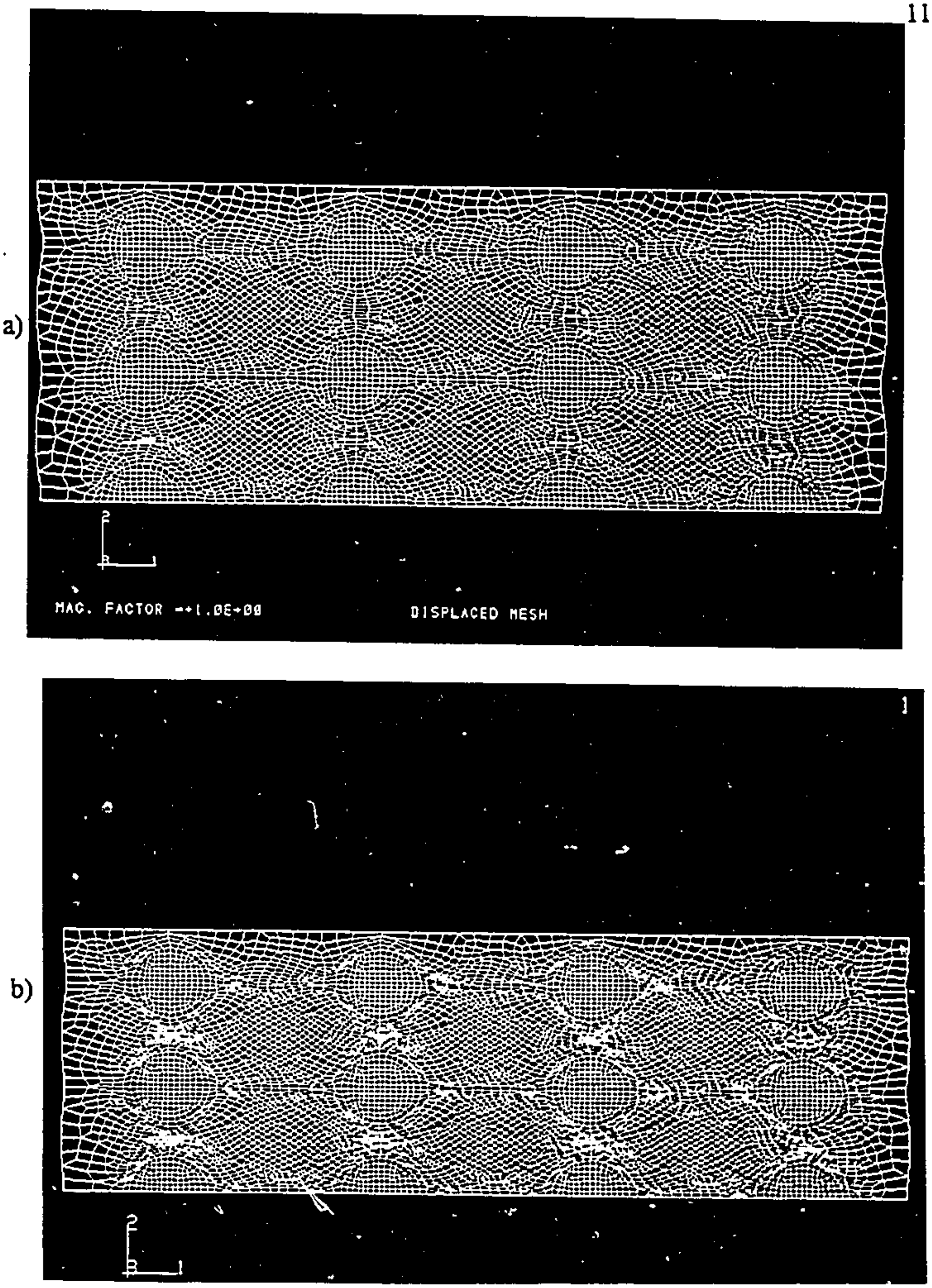

Figure 4.9 - Macroscopic shape change from FEM calculations for 20 % volume fraction sample with square arrangement of fibres, after an imposed deformation of a) 0.20 and b) 0.30

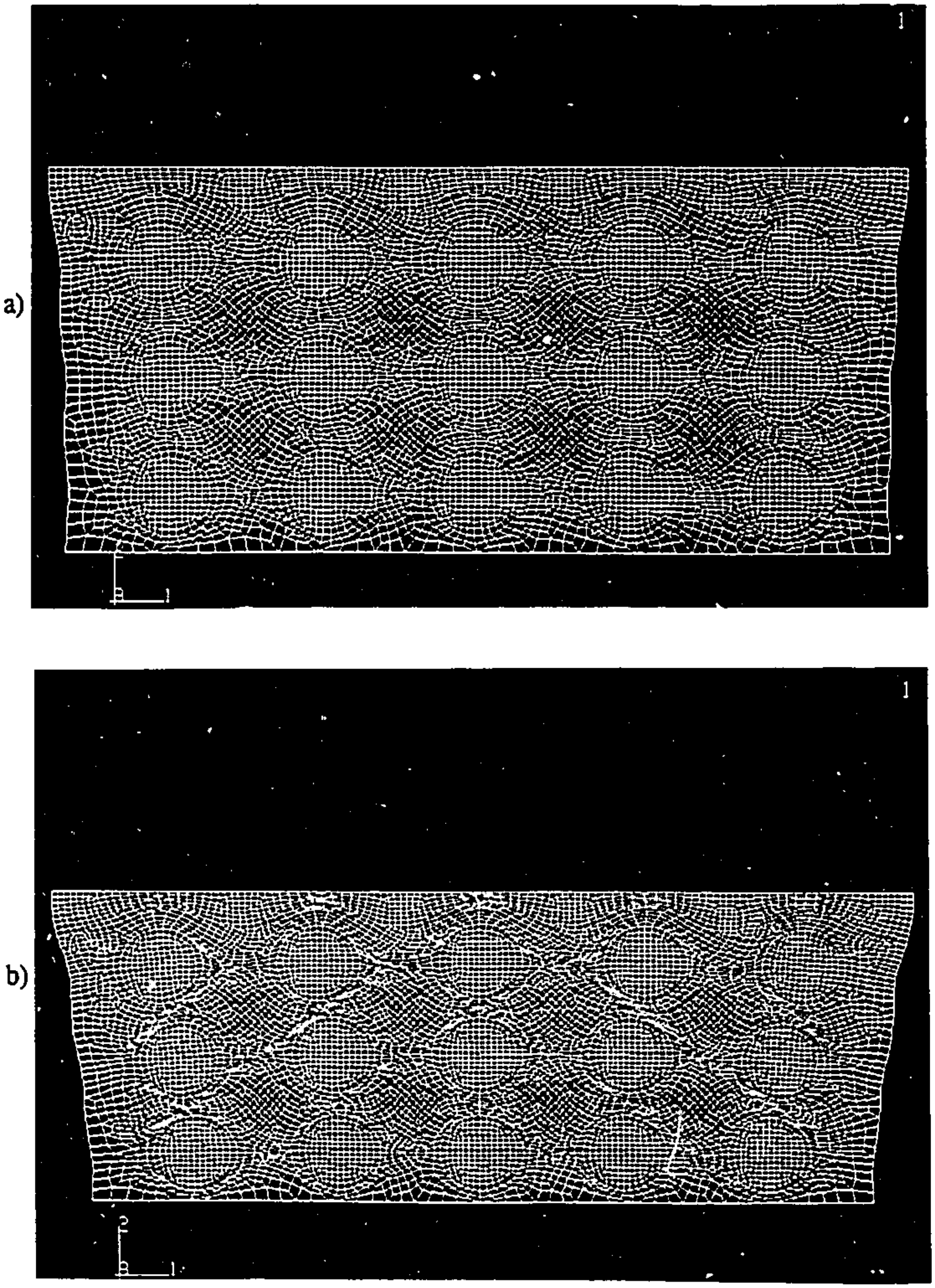

Figure 4.10 - Macroscopic shape change from FEM calculations for the 30 % volume fraction sample with square arrangement of fibres, after a strain of a) 0.10 and b) 0.20.

damage was present in the initial sample due to prior processing (Figure 4.3). No additional damage was introduced during the subsequent deformation, however, some modification of the existing damage was observed such as the closing of cracks (marked by "a" in Figure 4.3) and the opening of cracks (marked by "b" in Figure 4.3).

For the 30 % volume fraction with triangular arrangement of fibres, no damage was introduced during prior processing as seen Figure 4.4a. After a deformation of 0.2, a small amount of damage (i.e. interfacial debonding) has been introduced into the sample as shown by the arrows in Figure 4.4b. Upon further deformation, the number of debonds has increased (8 out of 30 fibres show some debonding) and the size of the previous debond voids has enlarged (Figure 4.4c). The debonds are all found at fibres close to the sample surface.

There are some examples of particle fracture indicated by arrows for the 20 % volume fraction samples with square fibre packing (Figure 4.6). It is likely that the cracks parallel to loading direction were introduced during the deformation while the crack perpendicular to loading axis was created during prior processing. Unfortunately, there is no information available on the starting level of damage for this sample.

Figure 4.7 illustrates the evolution of damage as a function of increasing imposed deformation for the 30 % volume fraction with square arrangement of the fibres. Figure 4.7a is a micrograph of the initial sample showing that some damage was introduced into the sample during prior processing. Figure 4.7b and Figure 4.7c are micrographs of the sample taken after imposed deformation of 0.1 and 0.2. Upon examination of Figure 4.7 the following observations may be made:

i) prior to deformation 30 % of the fibres (i.e. 9 of 30 fibres) have cracks which are predominately perpendicular to the loading direction

ii) after a deformation of 0.1, 35 % of the fibres (i.e. 11 of 30 fibres) have cracks parallel to the loading direction. Of the fibres with cracks, 7 of 11 had no cracks prior to deformation and 4 of 11 had prior cracks (although in a different orientation)

iii) after a deformation of 0.2, 70 % of the fibres (i.e. 21 of 30 fibres) had cracks parallel to the loading direction

The distribution of cracks is roughly uniform throughout the sample, although cracks that have occurred near the surface of the sample show larger crack opening displacements.

4.2.2 - Large Strain Bauschinger Tests

Figure 4.11a and b are examples of a strain path reversal experiment at 15 and 30 % strain respectively, for a 20 % volume fraction sample with triangular arrangement of fibres. There is no large effect due to the strain reversal in either case. There is no evidence of permanent softening in these composites. Due to the nature of the test, the low strain region of the stress-strain curve is not reliable (see Section 3.7.1) and therefore no comments can be made on transient softening phenomenon. It is important to point out the large difference between these test and the results of Lilholt (1977a and b) where the fibres were aligned with the loading axis (see Section 2.2).

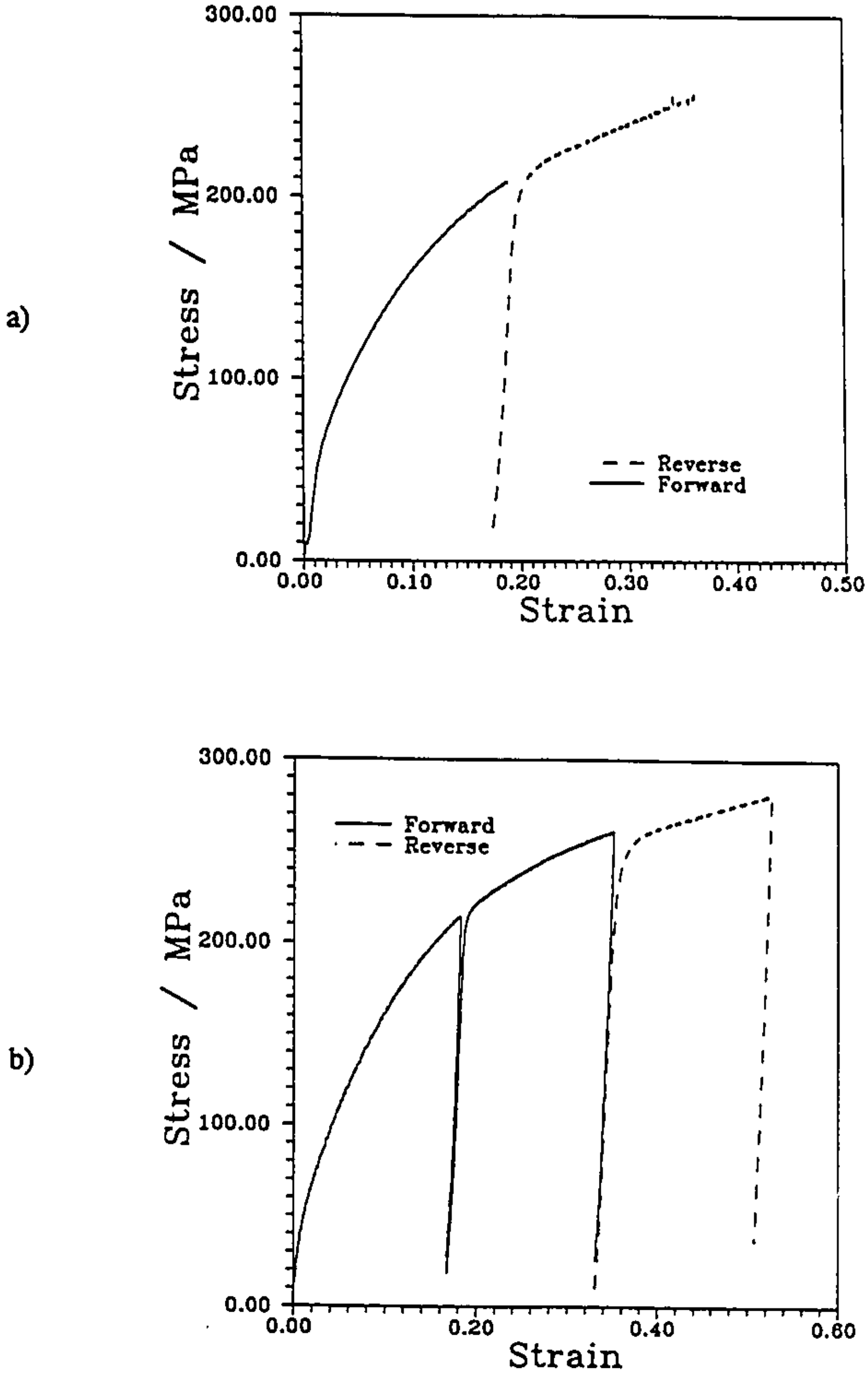

Figure 4.11 - Large strain Bauschinger tests for 20 % volume fraction samples with triangular arrangement of fibres a) reverse after forward deformation of 0.15 and b) reverse after forward deformation of 0.3

4.2.3 - Diametral Compression of Tungsten Fibres

Diametral compression tests were performed on tungsten fibres retrieved from the 30 % volume fraction samples with both square and triangular arrangements of fibres. For each case, 10 tests were performed. The stresses at the centre of the sample were calculated using the linear elastic solution presented in Section 3.7.3. A summary of the stresses at failure is presented in Table 4.1.

Both sets of samples failed in a brittle mode with the sample fracturing into with a crack propagating down the centre of the fibre parallel to the loading direction. The fracture surface for a typical fibre is shown at two different magnifications in Figure 4.12. The fracture surface is essentially flat and showed evidence of a fibre structure in the tungsten.

4.2.4 - Tensile Tests of Tungsten Fibres

The tungsten fibres were electropolished in a NaOH solution and then tested in tension. Unfortunately, the fibres pulled out of the grips before the fracture stress was reached. However, the maximum stress obtained before fibre pullout was 500 MPa.

a)

b)

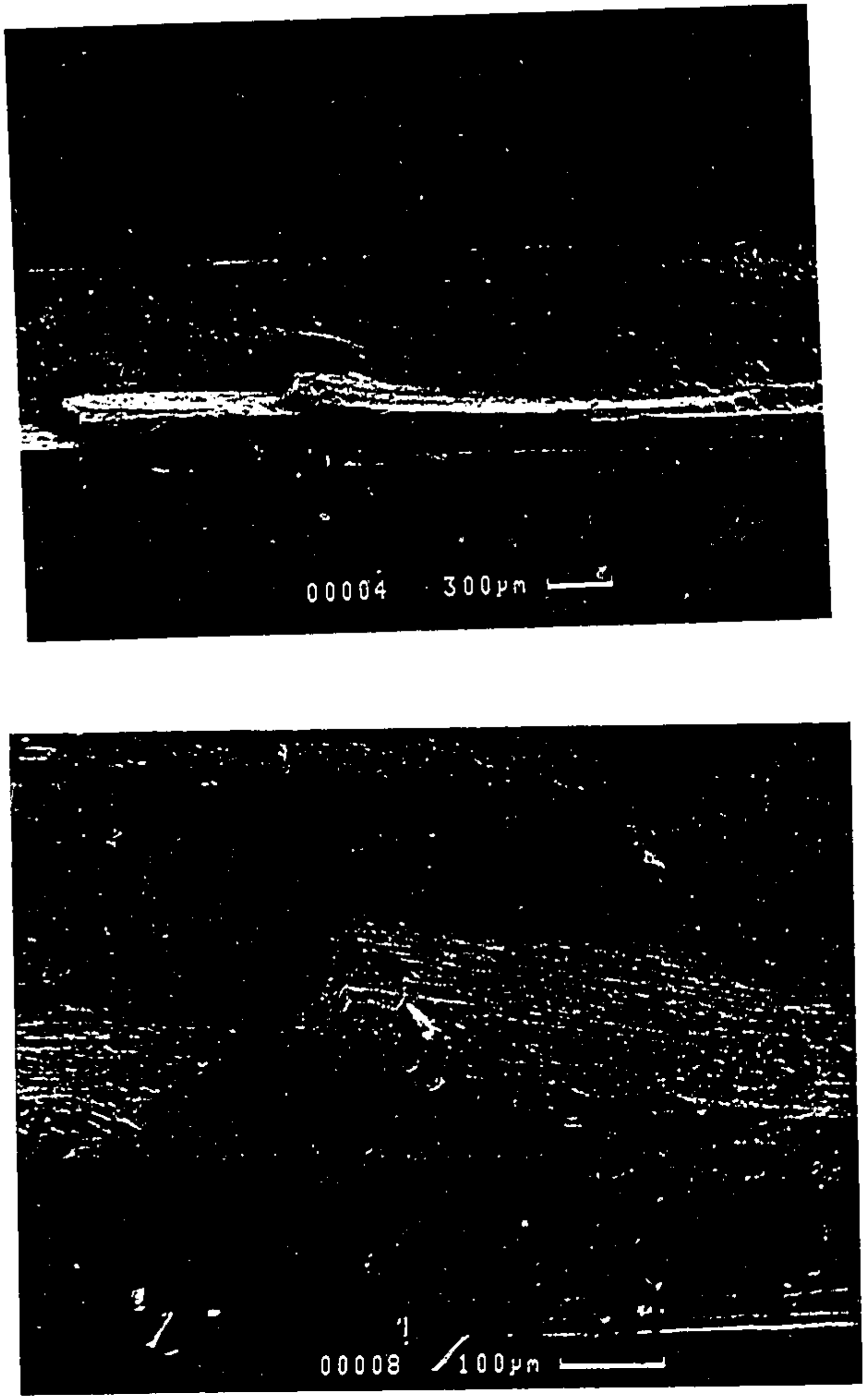

Figure 4.12 - Secondary electron images of fracture surface of tungsten fibres after with diametral compression test a) low mag. and b) high mag.

Table 4.1 - Results of Diametral Compression Tests on

Tungsten Fibres Dissolved from Composites

Sample	σ_x/MPa	σ_y/MPa	Standard Deviation for σ_x / MPa	Number of Samples
30 % v.f. Triangular	323.8	-970.2	40.6	10
30 % v.f Square	230.3	-690.9	35.8	10

4.3 - Local Strain Measurements

In this section, a detailed description of the spatial distribution of strain for the different fibre arrangements and volume fractions (including single fibre samples) studied in this work will be described. In each case, a back-scattered electron micrograph of the deformed grid, the experimental von Mises strain distribution and the FEM calculated von Mises strain distribution will be presented. The description of the strain distribution may be divided in to two groups. The first group represents the region adjacent to the fibres. The behaviour of this region is common to all the volume fractions and geometric arrangements studied in this work. The second group includes the regions in between the fibres (or away from the fibre in the single fibre case) where the local behaviour is very dependent on the geometric arrangement and spacing of the fibres.

4.3.1 - Single Fibre

Figure 4.13 is a back-scattered electron image of a grided sample with a single tungsten fibre embedded in a polycrystalline matrix after an imposed deformation of 0.3. The distribution of the local strain can be quantified by a contour plot of the von Mises strain calculated from the change in shape of each grid element (as described in Section 3.5). Figure 4.14 is the corresponding experimental and the FEM von Mises strain contour plot. Important features of the strain distribution are marked as regions A-E.

The region adjacent to the fibre will be defined by a circular annulus of matrix material extending from the fibre to 1.1 times the fibre diameter. The behaviour of the material in this region is summarized by considering the three regions marked A-C in

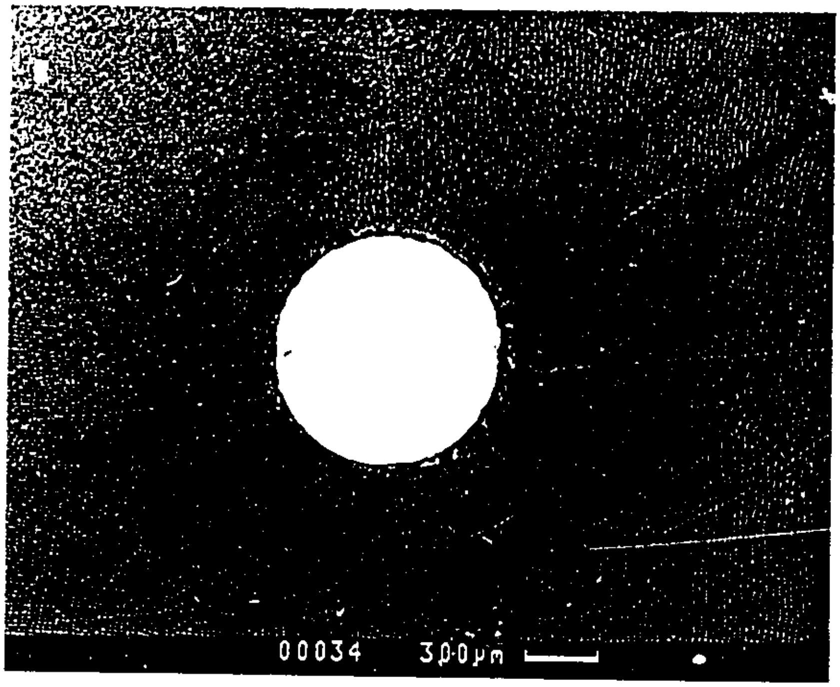

Figure 4.13 - Back-scattered electron image of single fibre sample after imposed deformation 0.30.

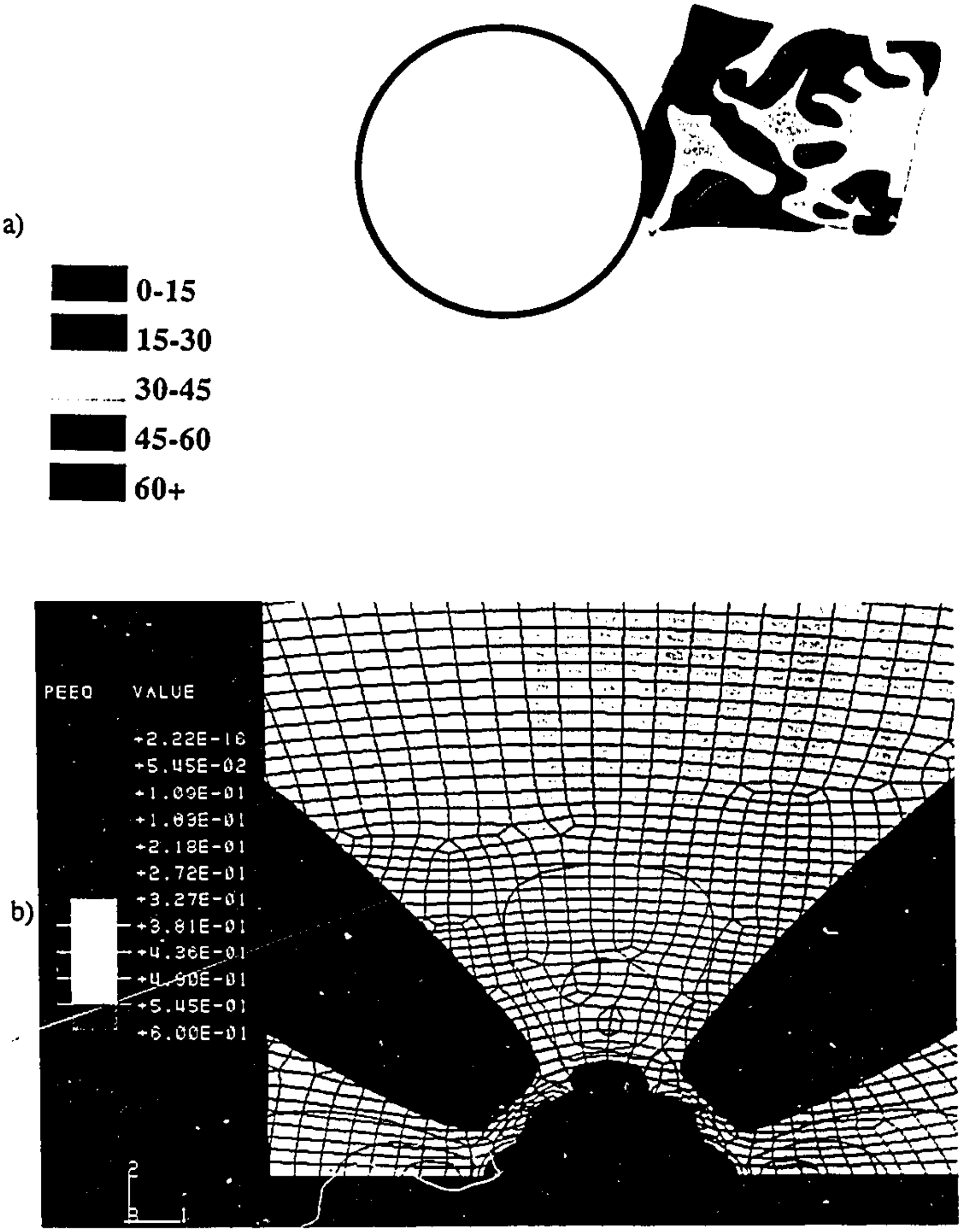

Figure 4.14 - Von Mises strain distribution for single fibre sample after imposed deformation of 0.3, a) experimental and b) finite element method calculated

Figure 4.13 (deformed grid) and the corresponding regions in Figure 4.14 (strain contour). Qualitatively, the behaviour of these representative areas can be observed in Figure 4.13. In region A and C the gold grid is relatively undistorted reflecting a low value of local strain. Region B is an area where a large shape change can be seen in the deformed gold grid. Quantitatively (as seen in the contour plots of von Mises strain), Regions A and C are areas where the deformation is lower than the imposed deformation (i.e. von Mises strain less than 0.2 for imposed deformation of 0.3). Region B is an area where the local deformation is greater than the imposed deformation. Finally, Region D and E represent an areas away from the fibre where the local amount of strain is greater than the imposed deformation.

4.3.2 - Triangular Arrangement, 20 % volume fraction

Figure 4.15a and b are a back-scattered electron images of the deformed gold grid after imposed deformation of 0.15 and 0.3, respectively. Figure 4.16 and Figure 4.17 are contour plots of the von Mises strain distribution from experimental measurements and FEM calculations for true strain deformation of 0.15 and 0.30, respectively. The observations of the deformed grid and the contour plots can be summarized by considering representative regions marked A-E. The results for regions A-C are similar to the single fibre case described in Section 4.3.1. In the region marked D (on a horizontal between the fibres) a large distortion of the gold grid is present. This region has received deformation similar to the macroscopic imposed deformation, however the magnitude of the deformation appears larger than the imposed deformation. Referring

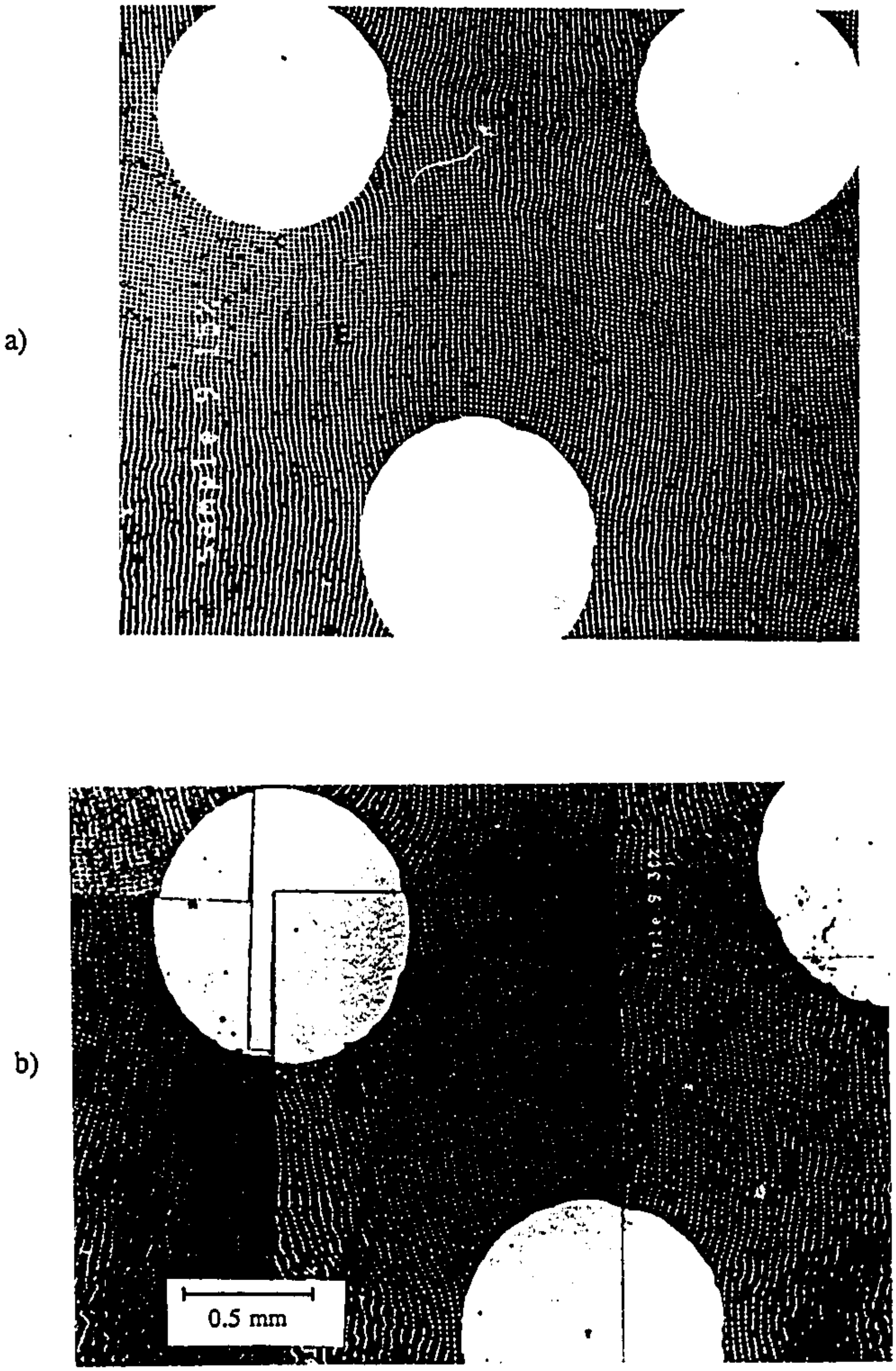

Figure 4.15 - Back-scattered electron image of 20 % volume fraction samples with triangular arrangement of fibres after imposed deformation, a) 0.15 and b) 0.3

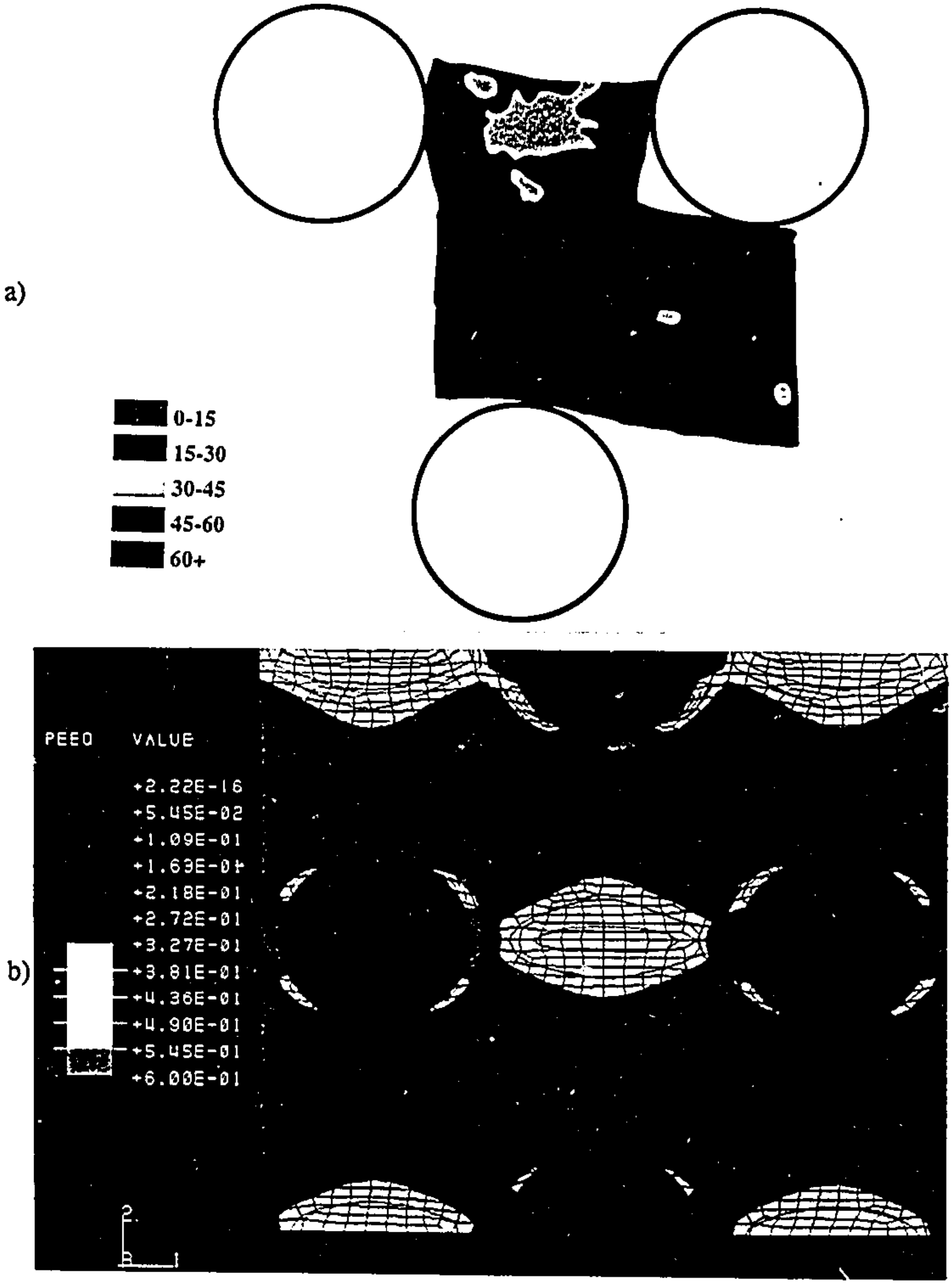

Figure 4.16 - Von Mises strain distribution for 20 % volume fraction sample with triangular arrangement of fibres, a) experimental (strain of 0.15) and b) FEM calculated (strain of 0.2)

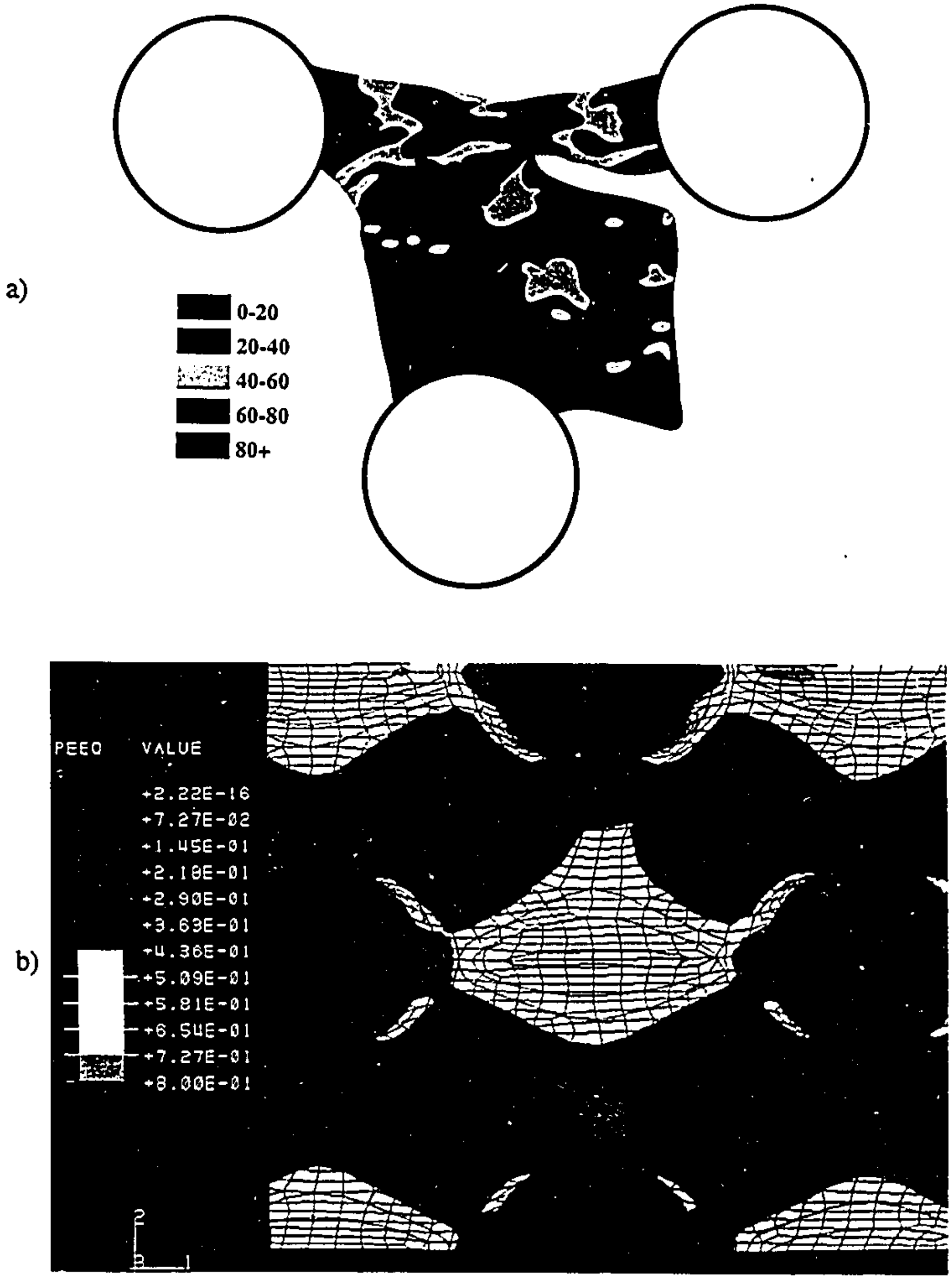

Figure 4.17 - Von Mises strain distribution for 20 % volume fraction sample with triangular arrangement of fibres for an imposed deformation of 0.3, a) experimental and b) FEM calculated

to Figure 4.16b, the value of von Mises strain in this region is 0.6-0.75 for imposed deformation of 0.3 (i.e. 2.5 times the imposed strain). In the region marked E, a more complicated mode of deformation has occurred as can be recognized by the rotation and shearing of grid elements in this area (see Figure 4.15). The magnitude of the deformation in Region E is similar amount to the imposed deformation.

4.3.3 - Triangular Arrangement, 30 % volume fraction

Figure 4.18 shows the back-scattered electron images of the deformed grid after a macroscopic strain of 0.1 and 0.2. The contour plots of the experimentally determined and FEM calculated von Mises strain for these levels of imposed deformation are shown in Figure 4.19 and Figure 4.20. Once again, it is useful to consider the representative regions A-E. Regions A-C are small areas close to the tungsten fibres where the behaviour is similar to the single fibre case described in Section 4.3.1. Region D is an area where the local shape change of the grids is similar to the imposed deformation but of a larger magnitude. The von Mises strain reaches 0.6 (or 3 times the imposed strain) for an imposed deformation of 0.2. Region E is an area where the von Mises strain level is similar to the imposed deformation but the type of deformation is a more complicated combination of shear strains and rigid body rotations.

A summary of the von Mises strains for the different regions in the composites is presented in Table 4.2. It is clear that the degree of strain amplification in the region along the horizontal between the fibres is a function of the volume fraction (i.e. fibre spacing). In the region along the diagonals between the fibres, a scalar quantity

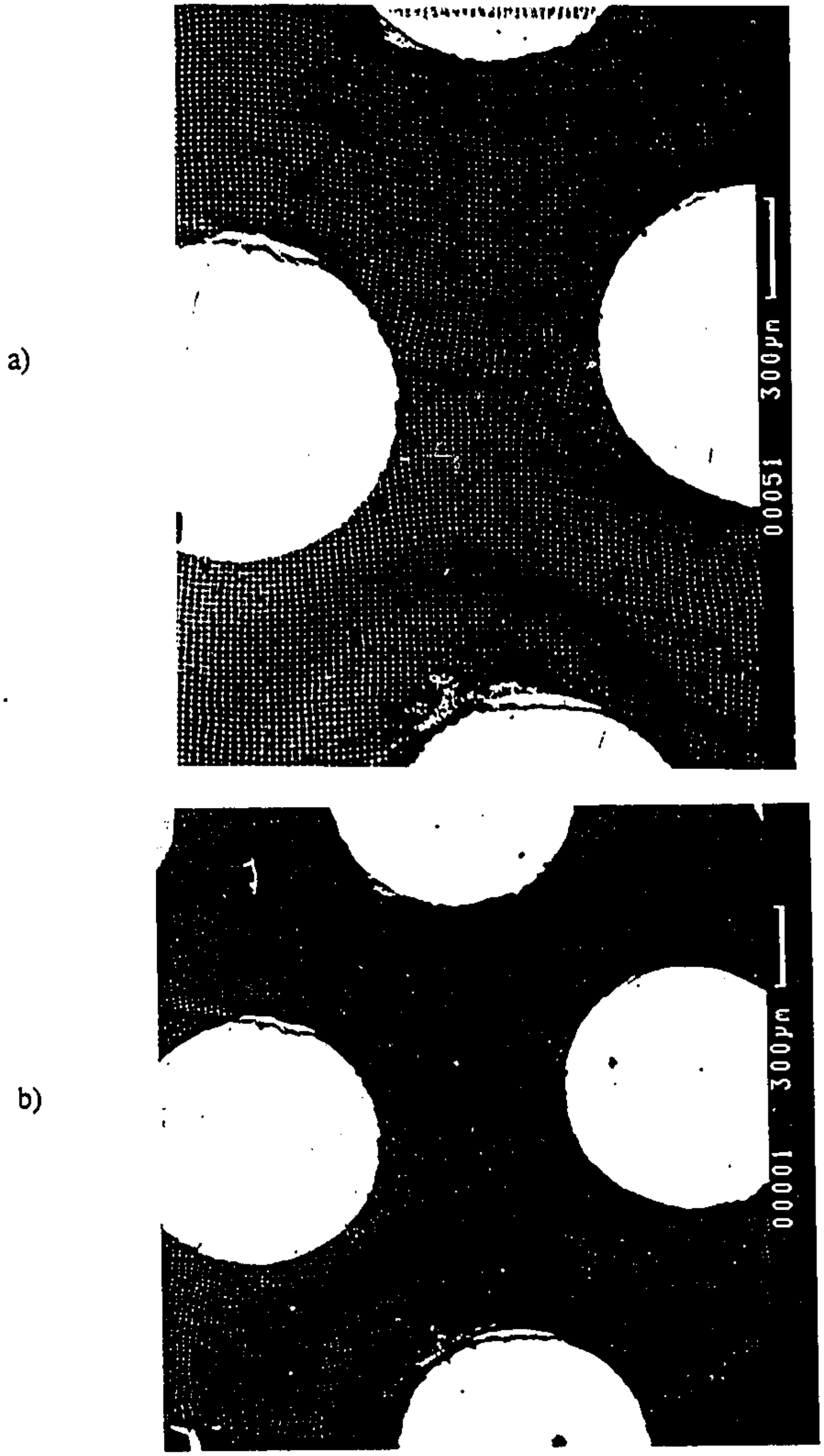

Figure 4.18 - Backscattered electron image of deformed grid for 30 % volume fraction with triangular arrangement of fibres, imposed deformation of a) 0.10 and b) 0.20.

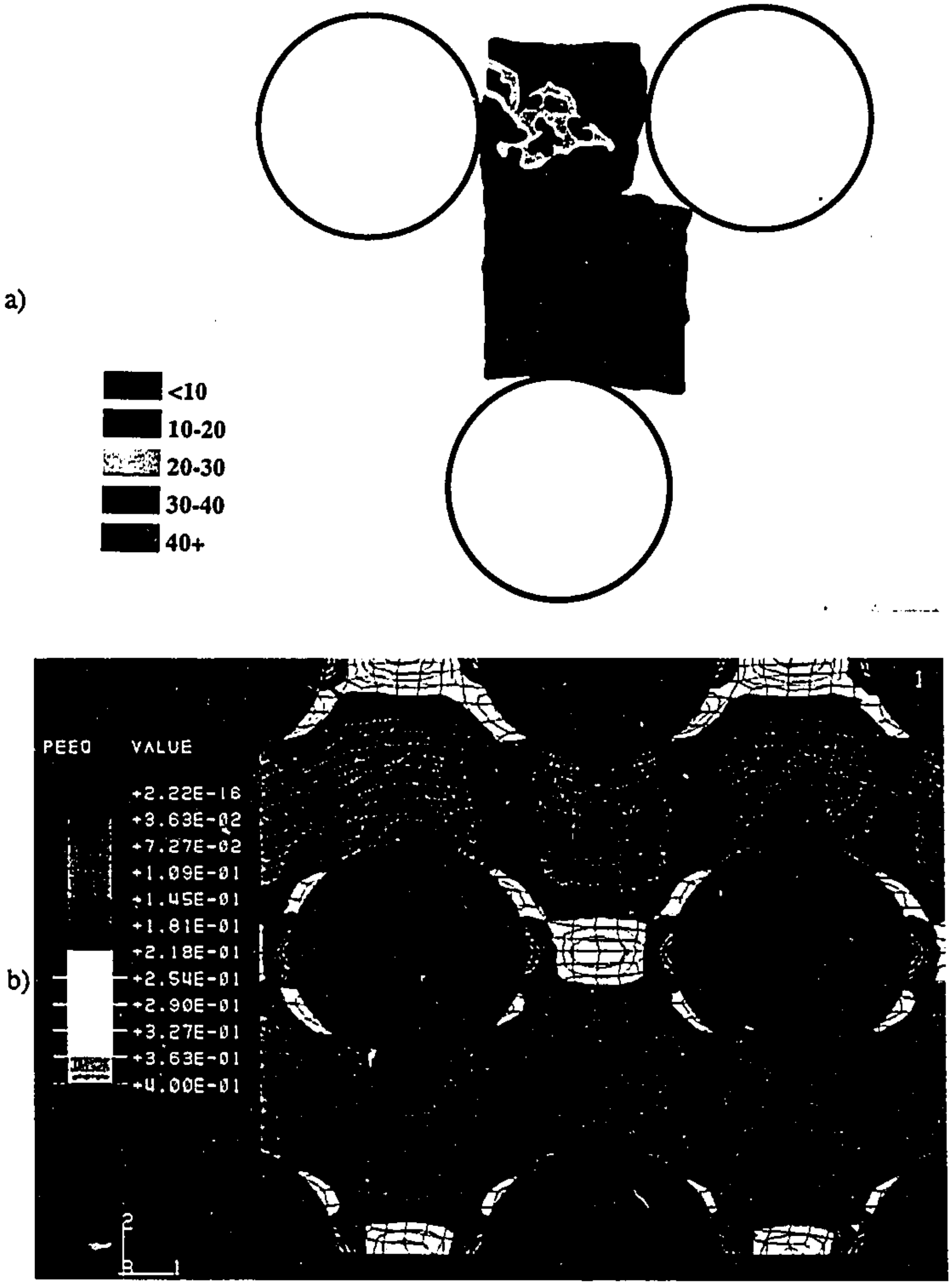

Figure 4.19- Von Mises strain distribution for 30 % volume fraction sample with triangular arrangement of fibres for an imposed deformation of 0.1, a) experimental and b) FEM calculated.

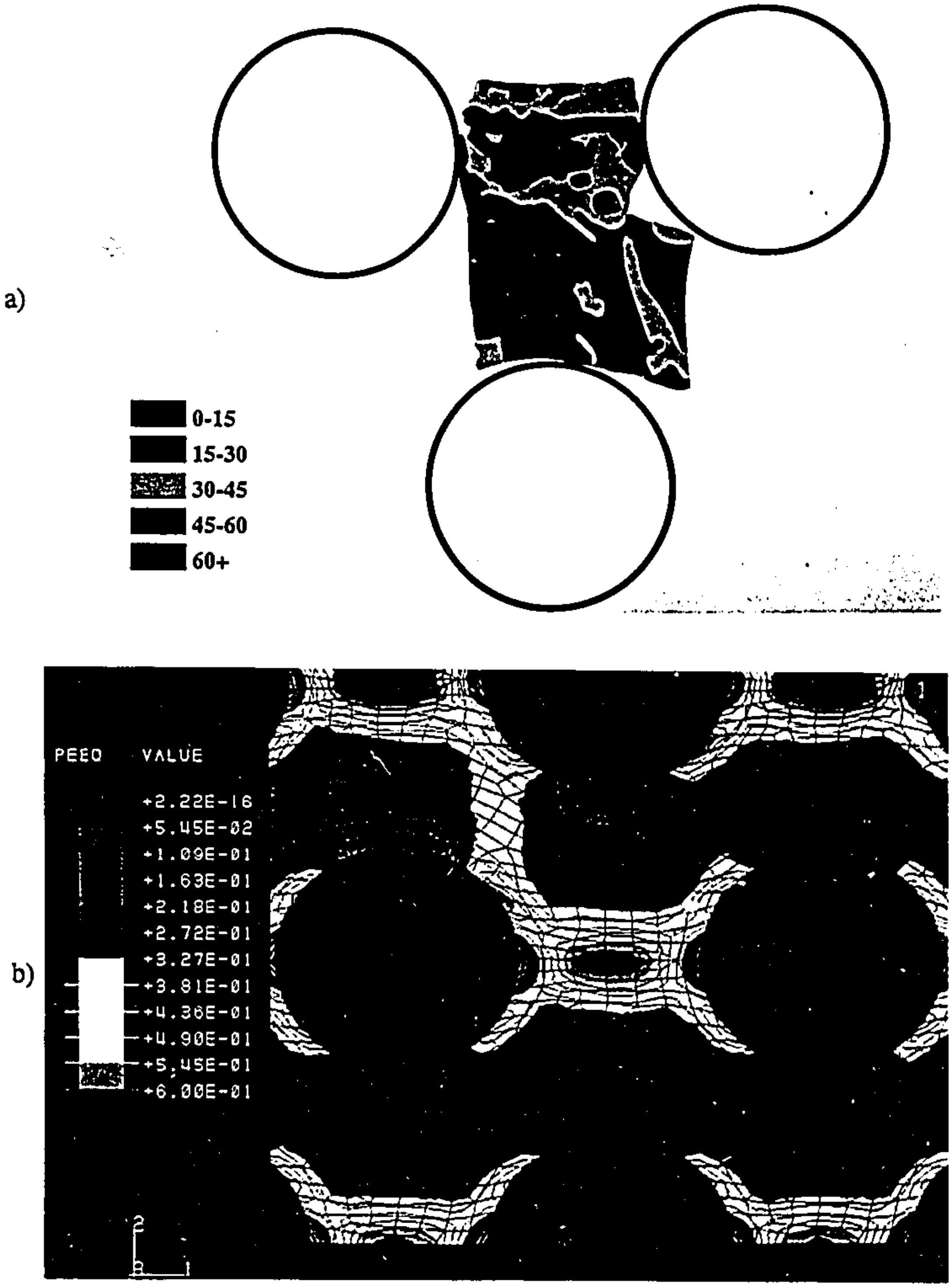

Figure 4.20 - Von Mises strain distribution for 30 % volume fraction sample with triangular arrangement of fibres for an imposed deformation of 0.20, a) experimental and b) FEM calculated

Table 4.2 - Von Mises strains for selected regions in composites with triangular arrangements of fibres (FEM calculations)

Sample	Von Mises Strain Region D (horizontal)	Von Mises Strain Region E (diagonal)
20 % v.f. tri deformation		
0.2	0.43-0.5	0.18-0.21
0.3	0.65-0.72	0.29-0.36
30 % v.f. tri deformation		
0.1	0.33-0.36	0.11-0.15
0.2	0.58-0.65	0.25-0.35

such as von Mises strain indicates that the level of deformation is close to the macroscopically imposed level. However, it is important to note that the use of a scalar measurement (i.e. von Mises strain) gives no information on the nature of the deformation.

4.3.4 - Square Arrangement, 20 % volume fraction

Figure 4.21 shows a back-scattered electron images of the deformed grid after a macroscopically imposed deformation of 0.2 and 0.3. It is clear that in this sample some interfacial debonding has occurred (see Figure 4.21b). Experimentally determined and FEM calculated contour plots of von Mises strain are shown in Figure 4.22 and Figure 4.23 for the two levels of deformation. For the square arrangements of fibres, it is useful to consider five representative areas marked on the micrographs as A-F. The behaviour of the matrix material adjacent to the fibres (regions A-C) is similar to the single fibre case described in Section 4.3.1. Regions D and E are areas where the strain is similar in type but of greater magnitude than the imposed deformation (i.e. in region D, the von Mises strain is greater than 0.80 for an imposed deformation of 0.30). Region F is an area where the gold grid appears undistorted and this is reflected in the low level of von Mises strain for this area (see Figure 4.21).

4.3.5 - Square Arrangement , 30 % volume fraction

Figure 4.24 area back-scattered electron images of the gold grid after imposed deformations of 0.1 and 0.2, respectively. The corresponding

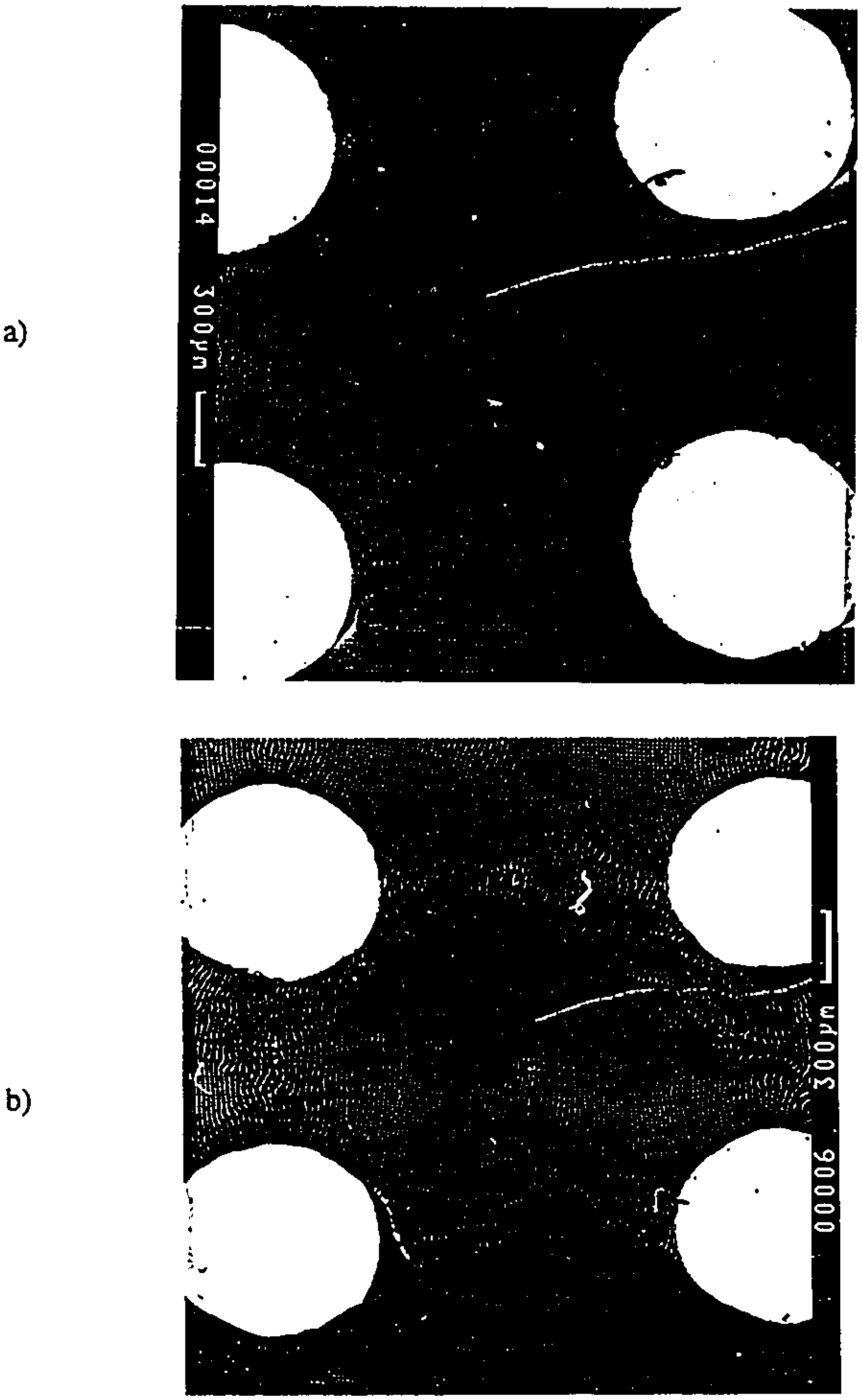

Figure 4.21 - Back-scattered electron images of 20 % volume fraction sample with square arrangements of fibres after imposed deformations of a) 0.2 and b) 0.3.

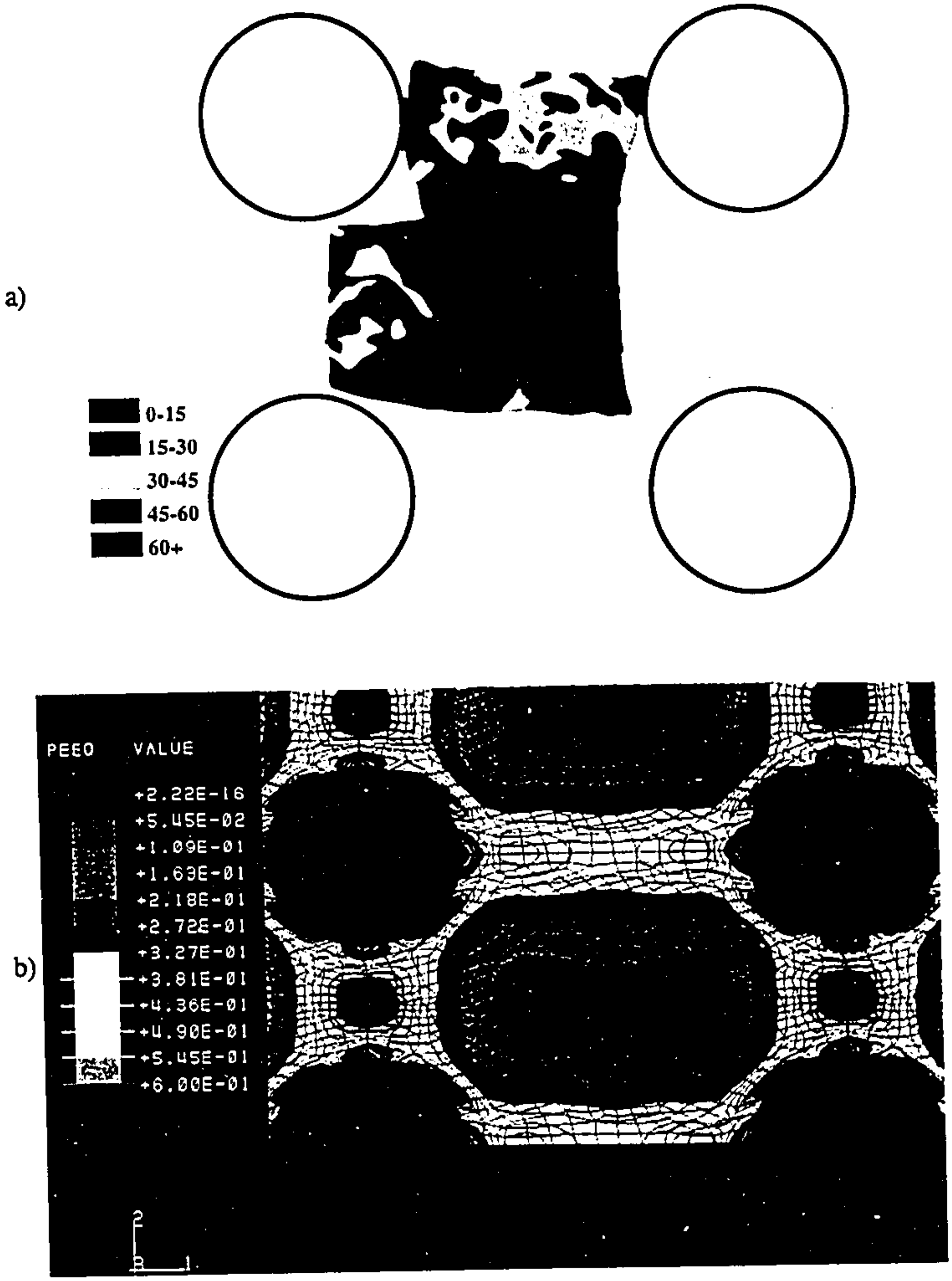

Figure 4.22 - Von Mises strain distribution for 20 % volume fraction sample with square arrangement of fibres for an imposed deformation of 0.20, a) experimental and b) FEM calculated.

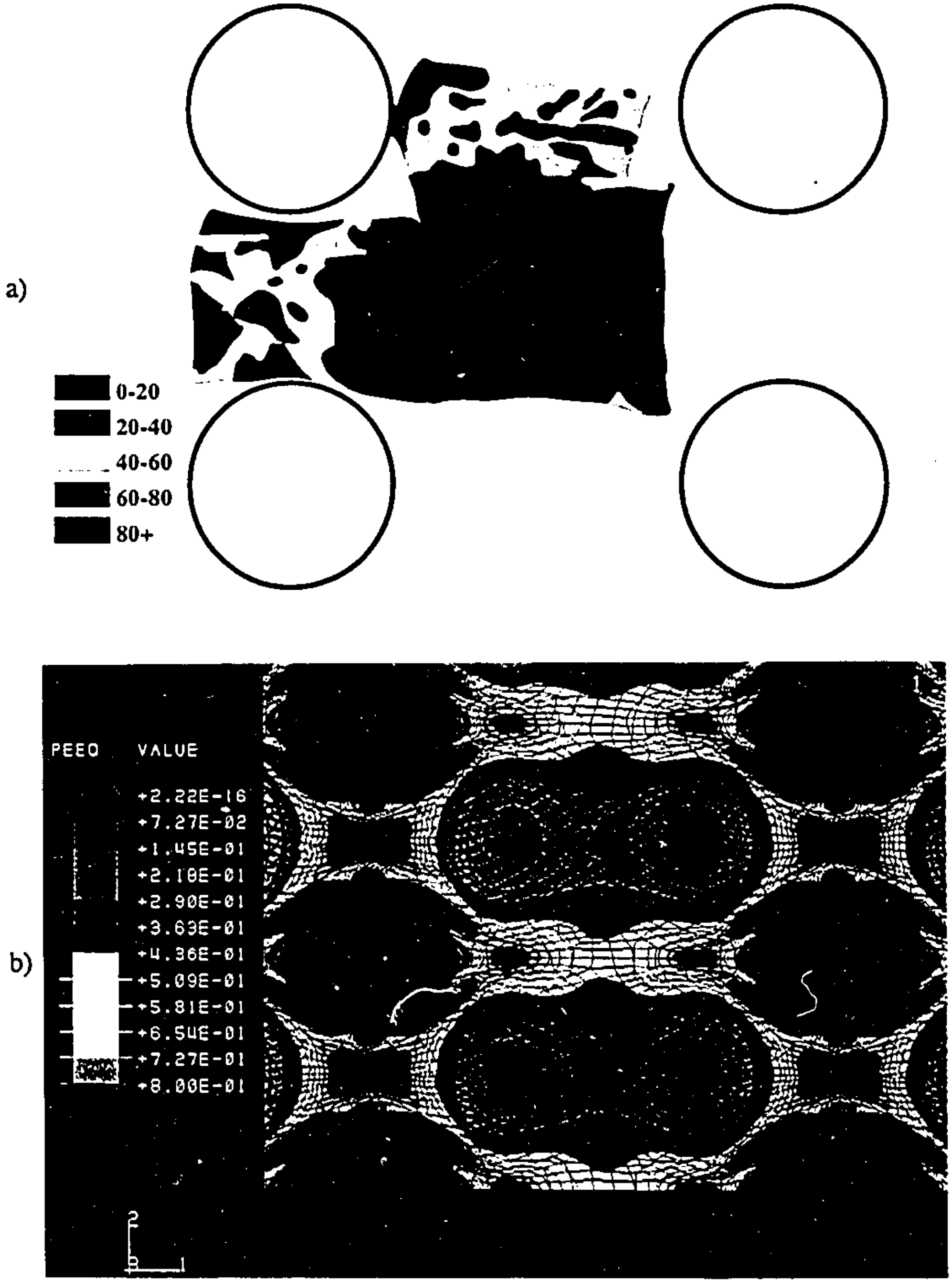

Figure 4.23 - Von Mises strain distribution for 20 % volume fraction sample with square arrangement of fibres for an imposed deformation of 0.30, a) experimental and b) FEM calculated

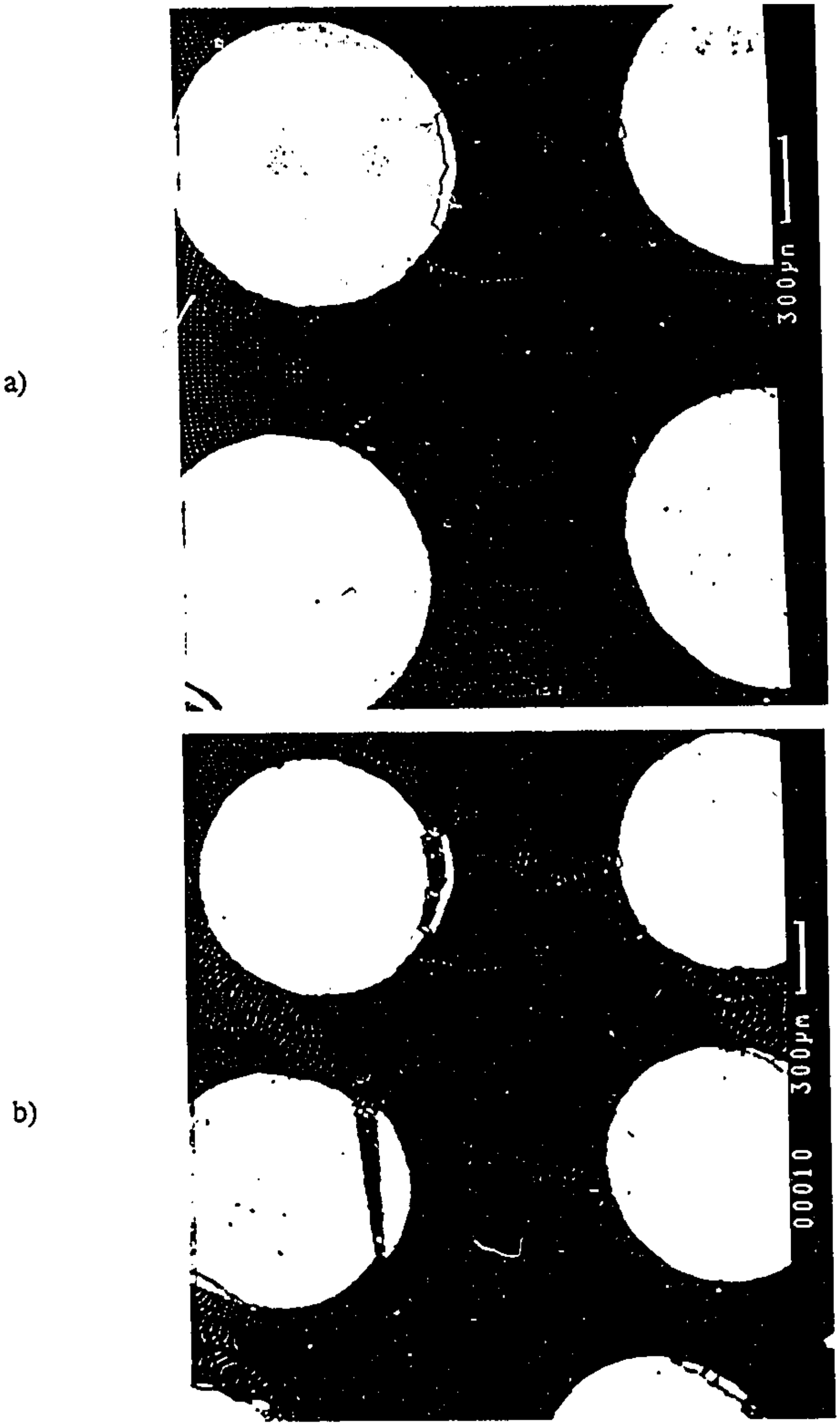

Figure 4.24 - Back-scattered electron image of 30 % volume fraction sample with square arrangement of fibres for imposed deformation of a) 0.10 and b) 0.2.

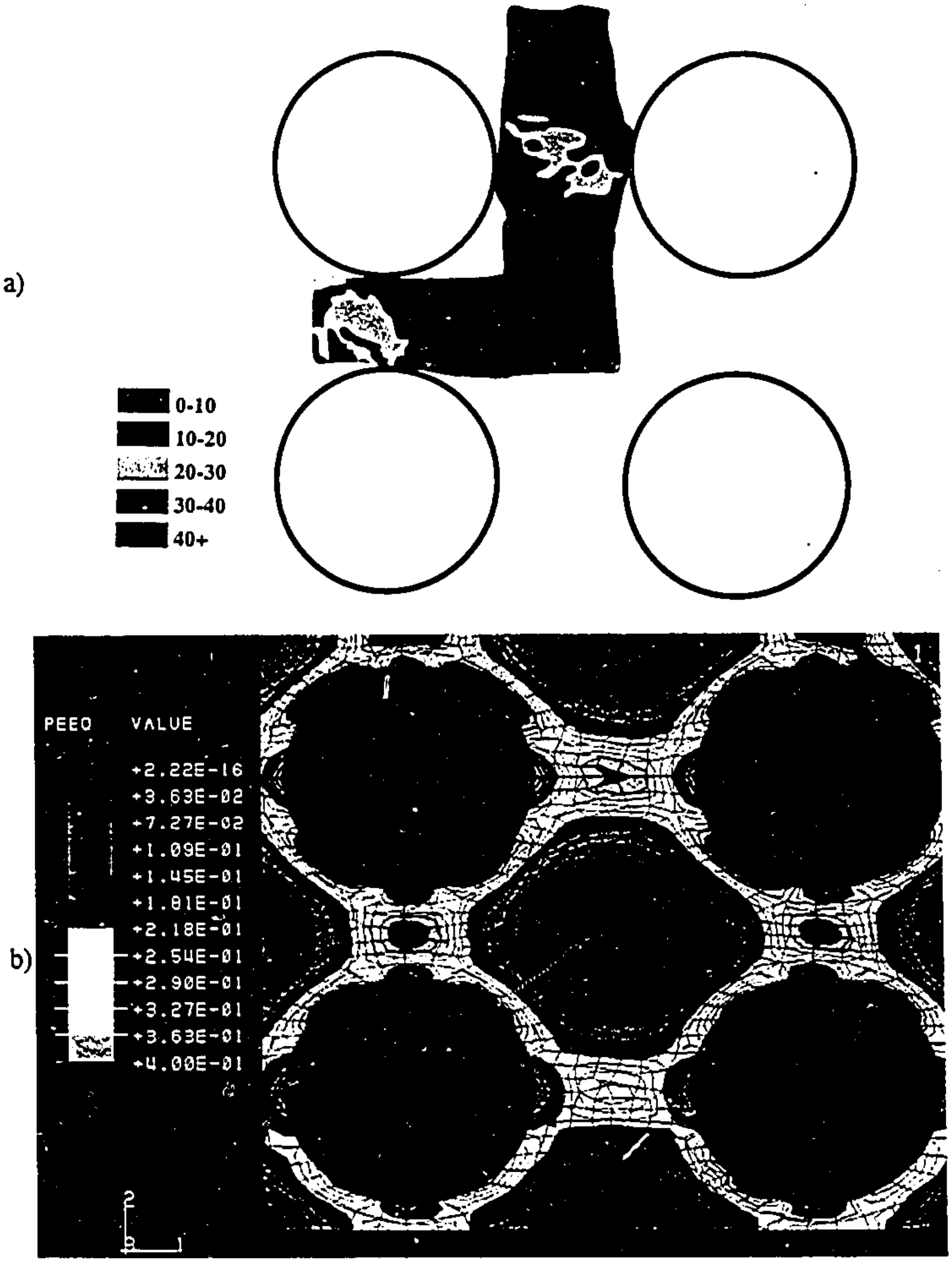

Figure 4.25 - Von Mises strain distribution for 30 % volume fraction sample with square arrangement of fibres for an imposed deformation of 0.10, a) experimental and b) FEM calculated

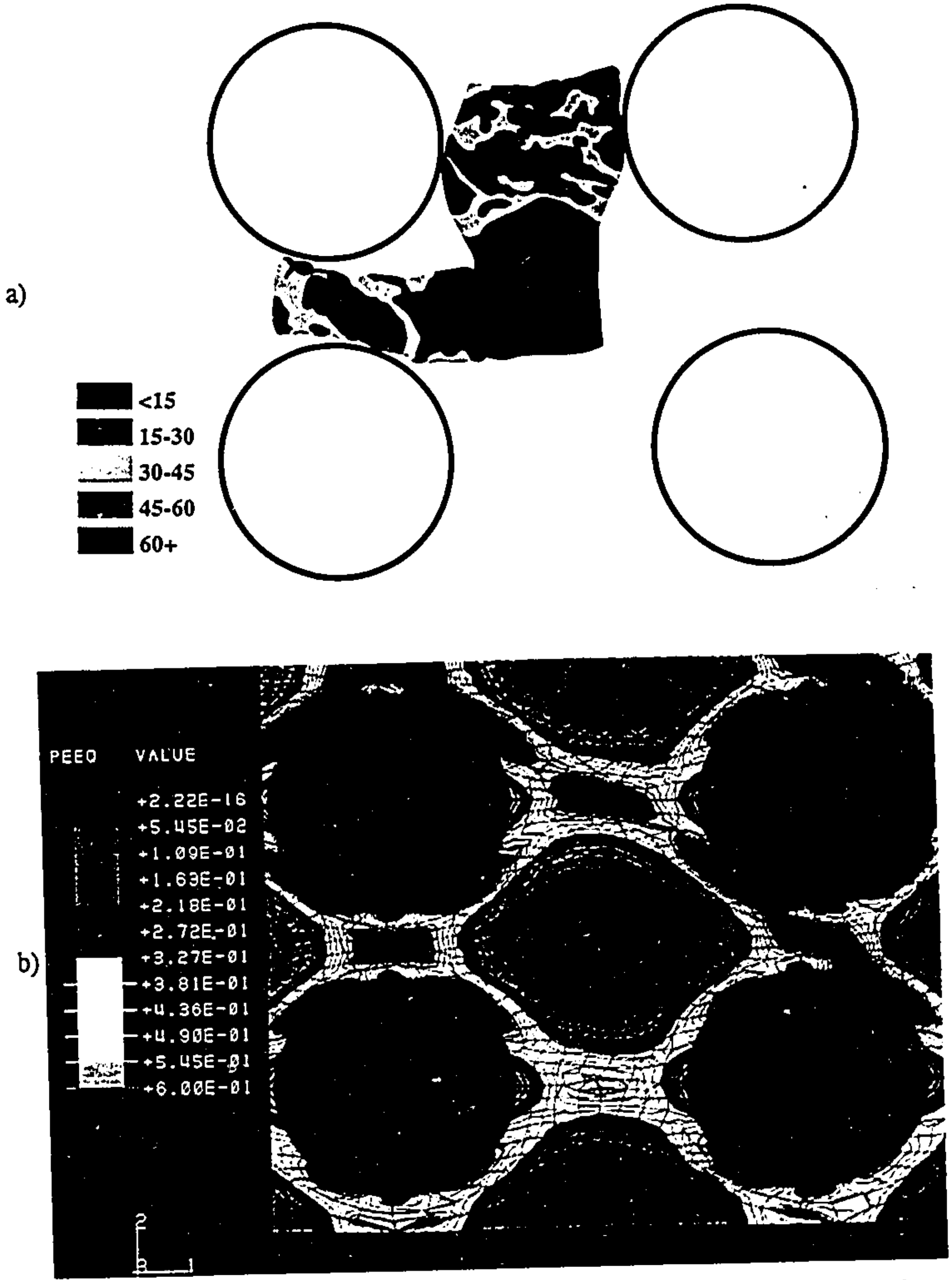

Figure 4.26 - Von Mises strain distribution for 30 % volume fraction sample with square arrangement of fibres for an imposed deformation of 0.20, a) experimental and b) FEM calculated

experimental and FEM calculated von Mises strain distributions are shown in Figure 4.25 and Figure 4.26. Some fibre cracking has occurred in these samples as marked by the arrows in Figure 4.24a and Figure 4.24b. It is clear that the crack in the fibre (marked in Figure 4.24) has opened further at the higher strain and that this has effected the flow pattern in the matrix. The strain distributions can be summarized by considering the regions marked A-F. In the regions near, A-C the results are similar to the single fibre case described in Section 4.3.1. Regions D and E have similar types of strain but at a higher level of strain than the imposed deformation. Finally region E, at the centre of the arrangement of the fibres, has undergone a relatively small amount of deformation as can be seen in the Figure 4.24 or Figure 4.26.

The results for the various regions between the fibres for the samples with square arrangements of fibres are summarized in Table 4.3. The following general observations can be made:

i) the heterogeneity of strain in the matrix is greater at the larger volume fractions

ii) the levels of strain are higher in region E and than in region D

iii) the level of strain at the centre of the four fibres is much lower than the imposed deformation in all cases

Table 4.3 - Von Mises strains for selected regions in composites with square arrangements of fibres (FEM calculations)

Sample	Von Mises Strain Region D	Von Mises Strain Region E	Von Mises Strain Region F
20 % v.f. - Sqr			
Deformation			
0.2	0.38-0.49	0.6+	0-0.1
0.3	0.51-0.65	0.8+	0.07-0.22
30 % v.f. - Sqr			
Deformation			
0.1	0.35-0.4	0.4+	0-0.07
0.2	0.6+	0.6+	0-0.1

4.4 - Finite Element Calculations of Stress Distributions

Figure 4.27 to Figure 4.35 illustrate the distribution of stresses for the various combinations of volume fraction, geometric arrangement and imposed deformation. The description of the results will be divided into observations of stress distribution in the tungsten fibres and in the matrix.

The results for the stresses inside the tungsten fibres are summarized in Table 4.4. The observations can be summarized as follows:

i) The compressive stresses in the fibres parallel to the loading axis increase as:

  a) level of deformation increases

  b) the volume fraction of tungsten increases

  c) as the fibre arrangement changes from triangular to square

ii) the tensile stresses in the fibre perpendicular to the loading axis increase as:

  a) the volume fraction increases

  b) as the fibre arrangement changes from triangular to square

It is clear that the levels of stresses in the fibres are a function of the geomtric arrangement of the fibres.

The stresses in the matrix tend to be at lower levels than in the fibres as expected. The nature of the stresses in the horizontal direction (i.e. σ_{xx}) varies spatially with some tensile and compressive regions. The disribution of the stresses is particularly inhomogeneous for the case of square arrangements of fibres. For example, Figure 4.35 shows a fibrous distribution of stresses with bands of streses traversing the sample at different levels.

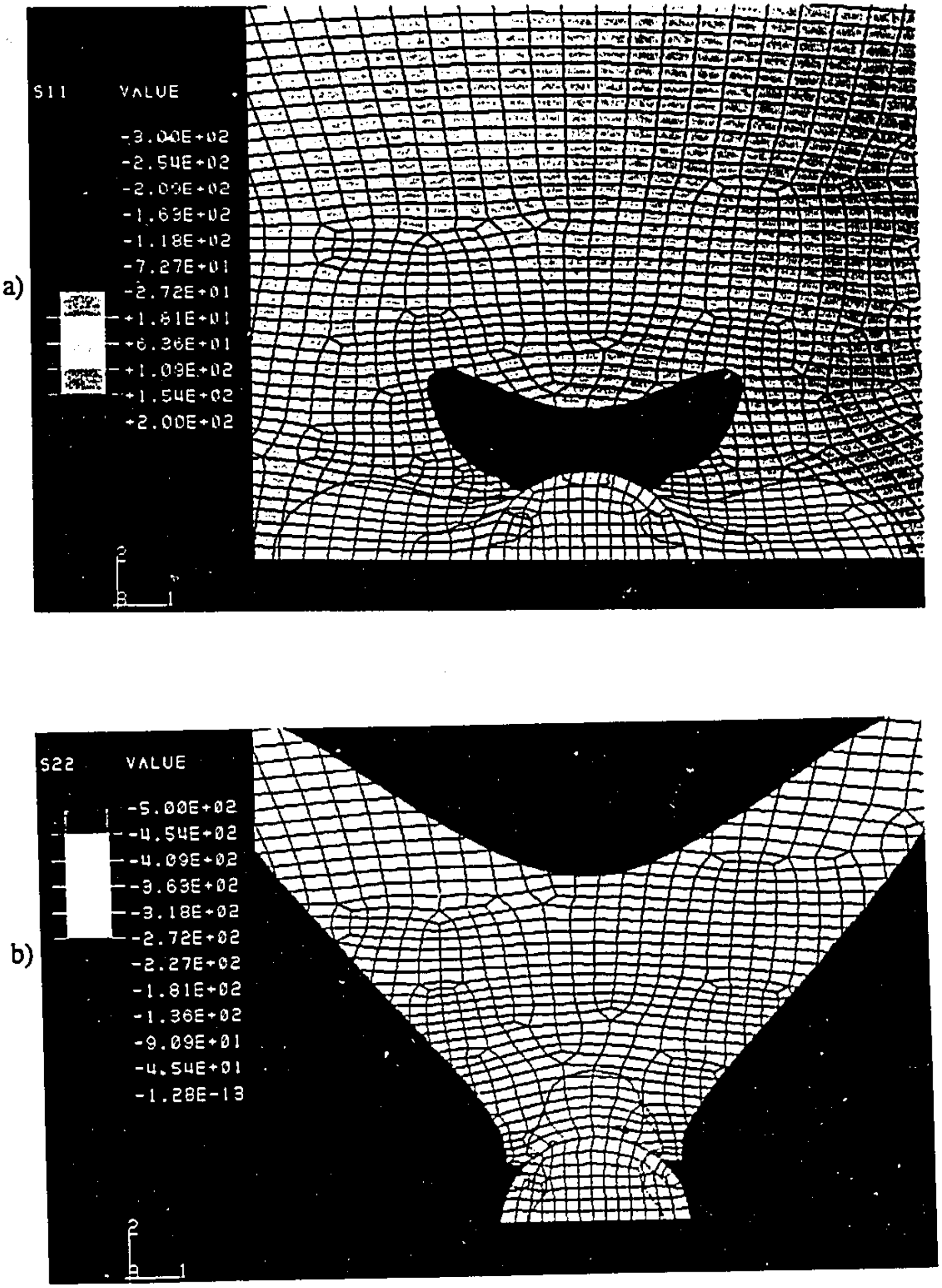

Figure 4.27 - Stress distributions from FEM calculations for sample with single fibre after an imposed deformation of 0.30, a) σ_{11}, b) σ_{22} , c) σ_{12} and d) hydrostatic pressure

c)

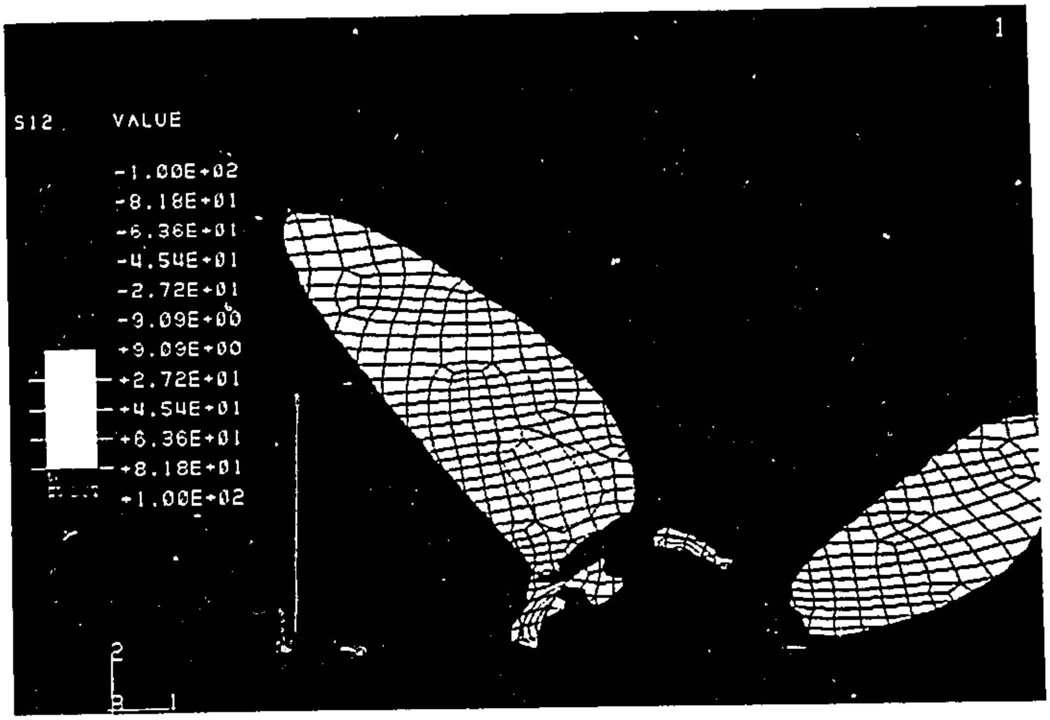
1
S12 VALUE
-1.00E+02
-8.18E+01
-6.36E+01
-4.54E+01
-2.72E+01
-9.09E+00
+9.09E+00
+2.72E+01
+4.54E+01
+6.36E+01
+8.18E+01
+1.00E+02
2
3
1

d)

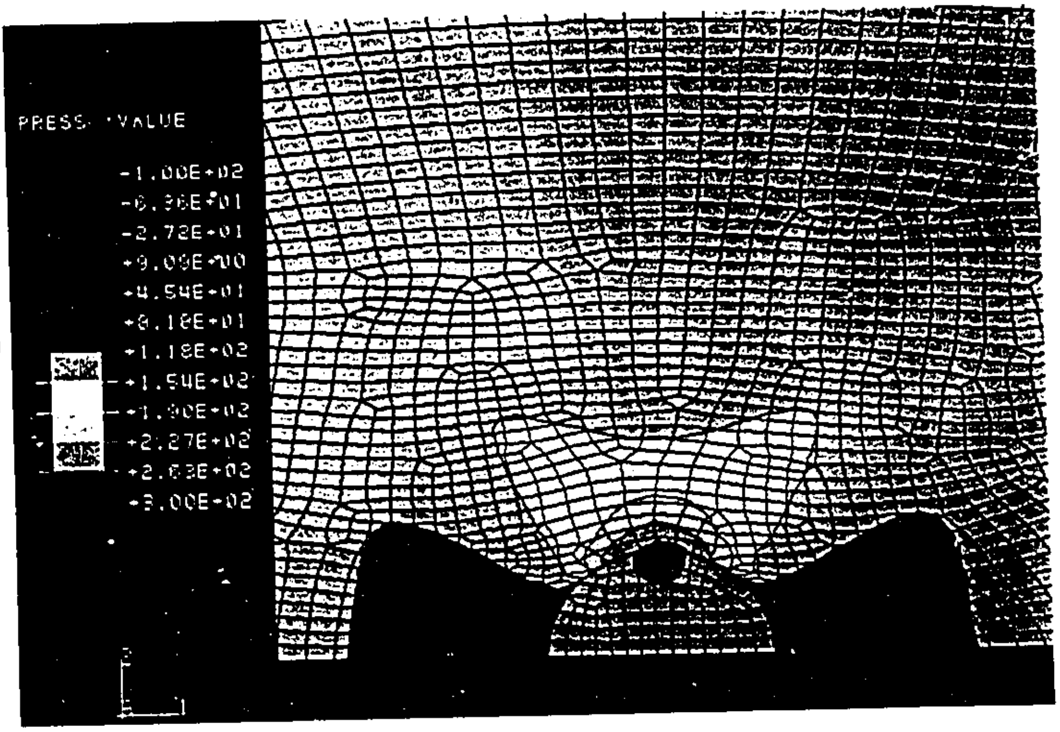
PRESS VALUE
-1.00E+02
-6.36E+01
-2.72E+01
+9.09E+00
+4.54E+01
+8.18E+01
+1.18E+02
+1.54E+02
+1.90E+02
+2.27E+02
+2.63E+02
+3.00E+02
2
1

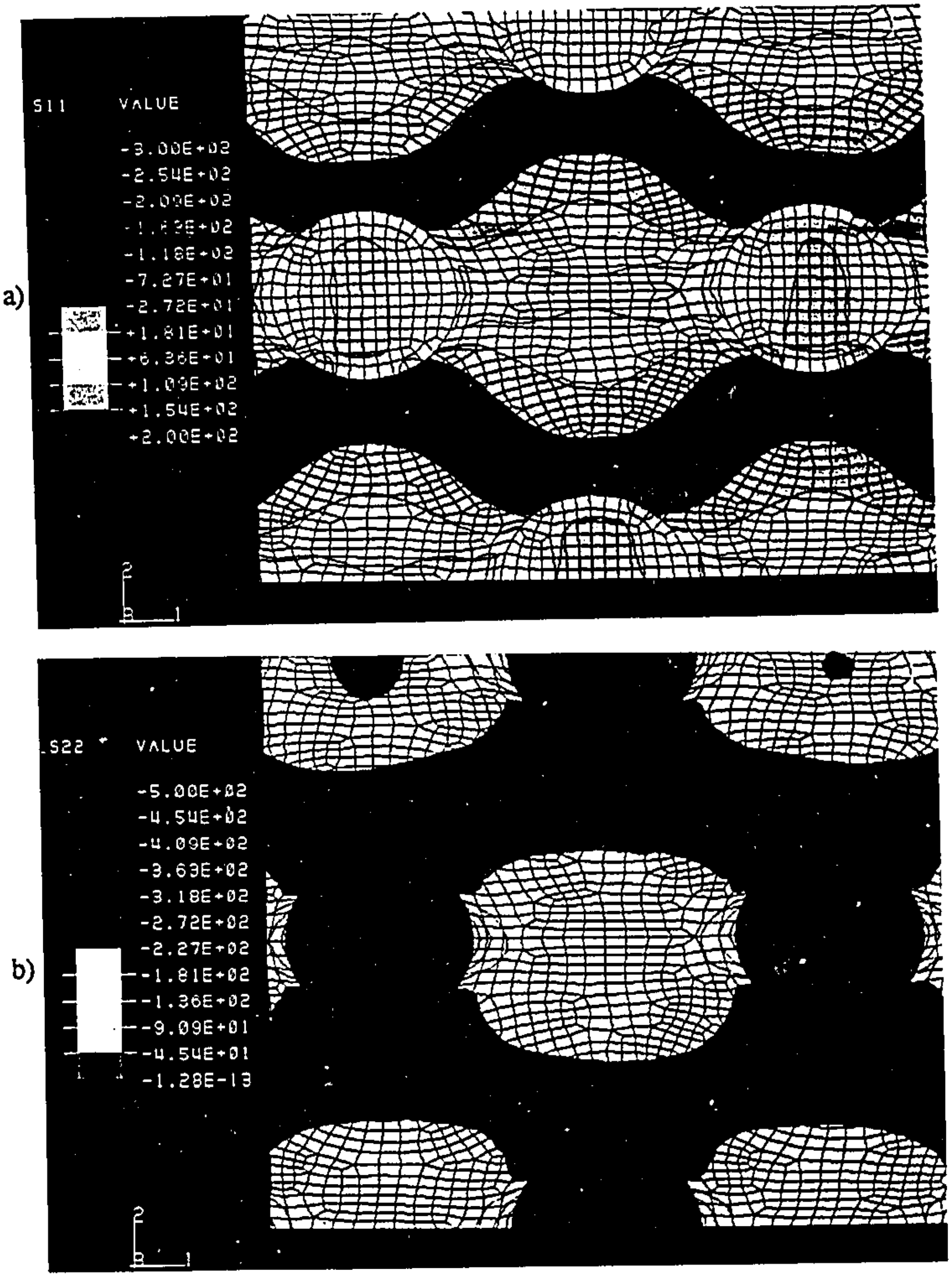

Figure 4.28 - Stress distributions from FEM calculations for 20 % volume fraction sample with triangular arrangement of fibres after an imposed deformation of 0.20, a) σ_{11}, b) σ_{22} , c) σ_{12} and d) hydrostatic pressure

c)

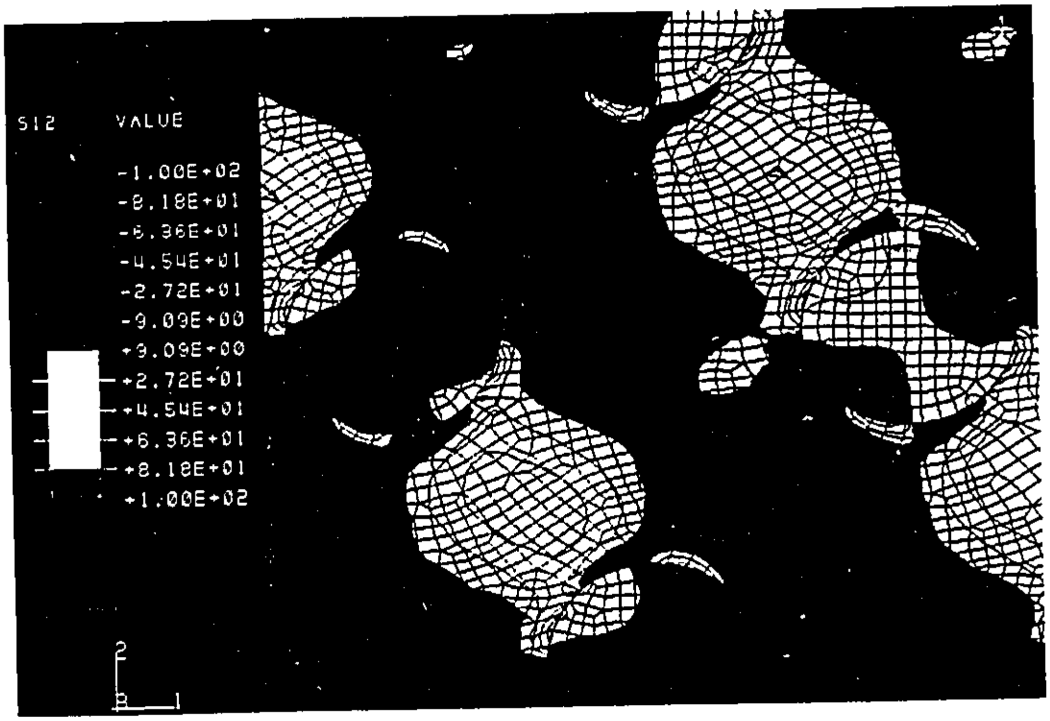

S12 VALUE
-1.00E+02
-8.18E+01
-6.36E+01
-4.54E+01
-2.72E+01
-9.09E+00
+9.09E+00
+2.72E+01
+4.54E+01
+6.36E+01
+8.18E+01
+1.00E+02
2
3
1
1

d)

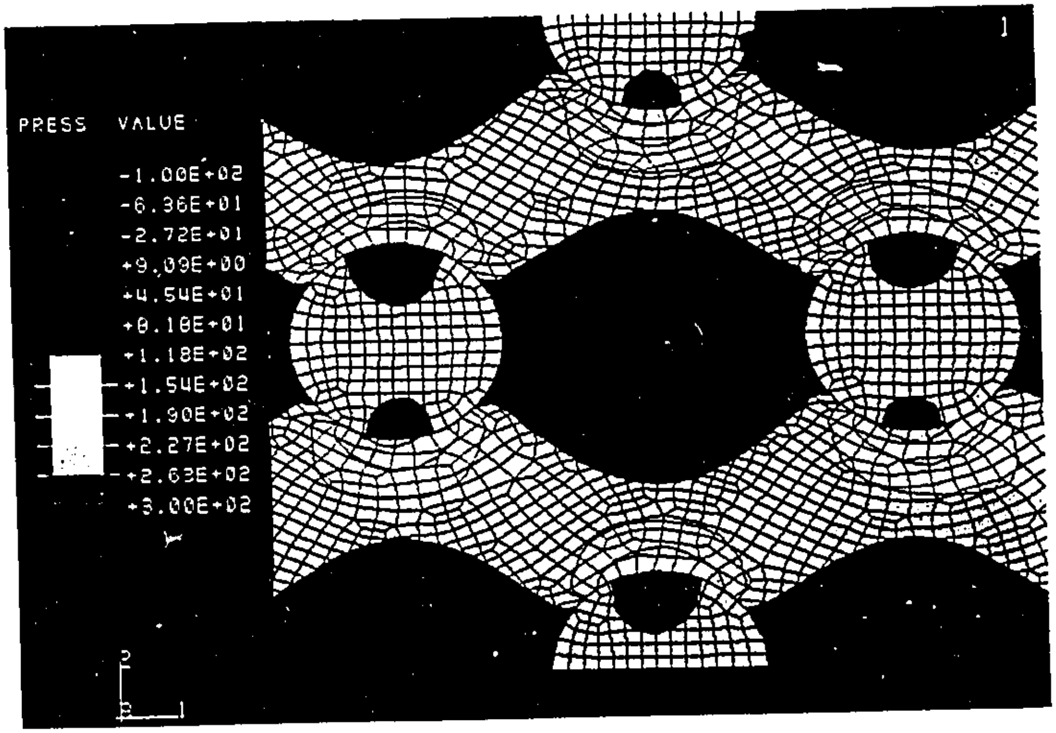

PRESS VALUE
-1.00E+02
-6.36E+01
-2.72E+01
+9.09E+00
+4.54E+01
+8.18E+01
+1.18E+02
+1.54E+02
+1.90E+02
+2.27E+02
+2.63E+02
+3.00E+02
2
3
1
1

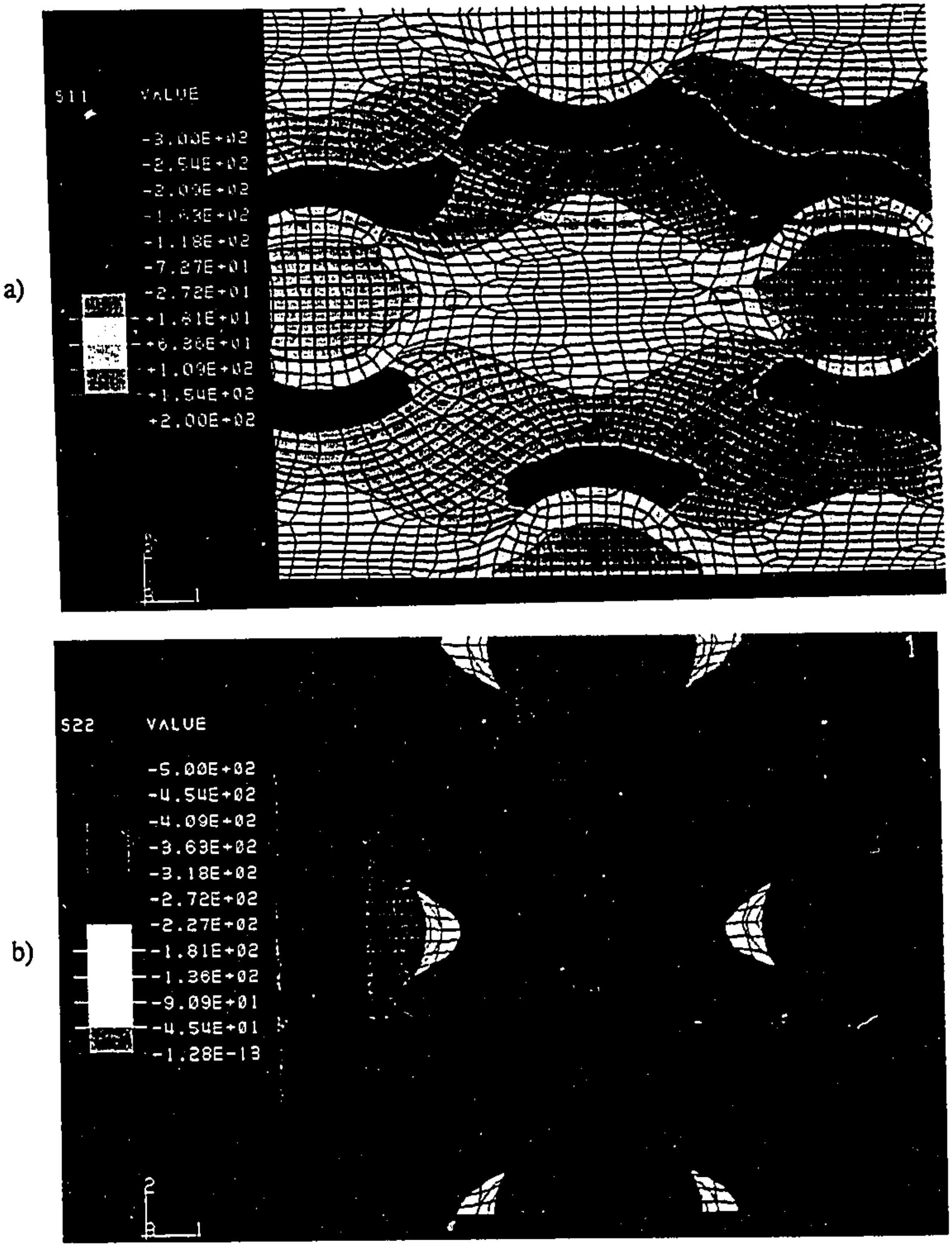

Figure 4.29 - Stress distributions from FEM calculations for 20 % volume fraction sample with triangular arrangement of fibres after an imposed deformation of 0.30, a) σ_{11}, b) σ_{22} , c) σ_{12} and d) hydrostatic pressure

c)

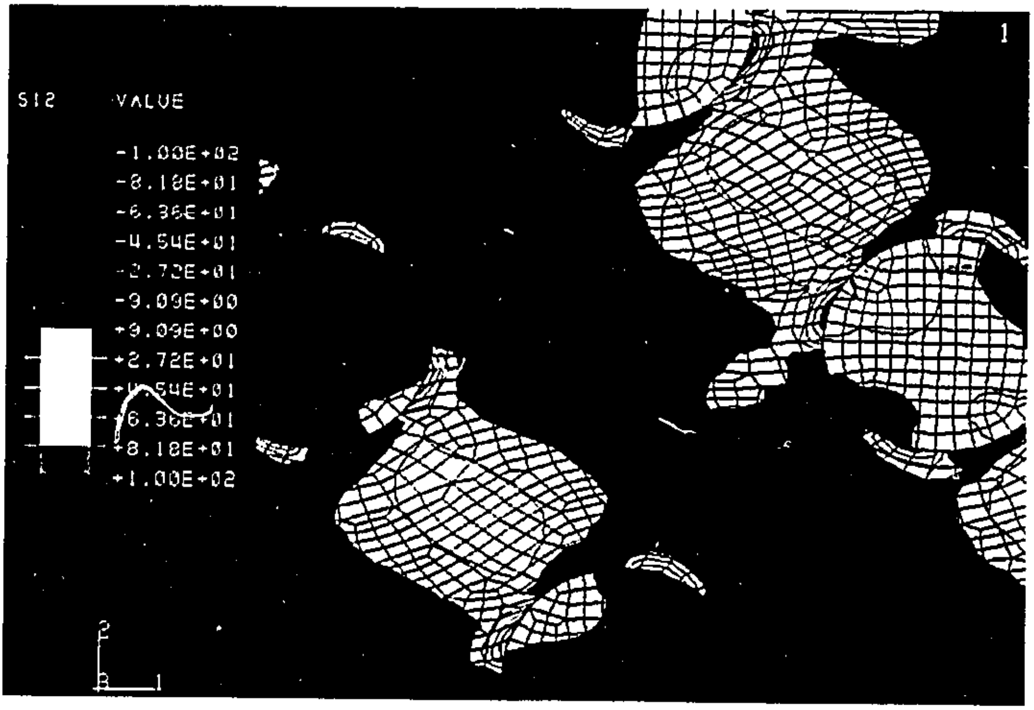
1
S12 VALUE
-1.00E+02
-8.18E+01
-6.36E+01
-4.54E+01
-2.72E+01
-9.09E+00
+9.09E+00
+2.72E+01
+4.54E+01
+6.36E+01
+8.18E+01
+1.00E+02
2
3
1

d)

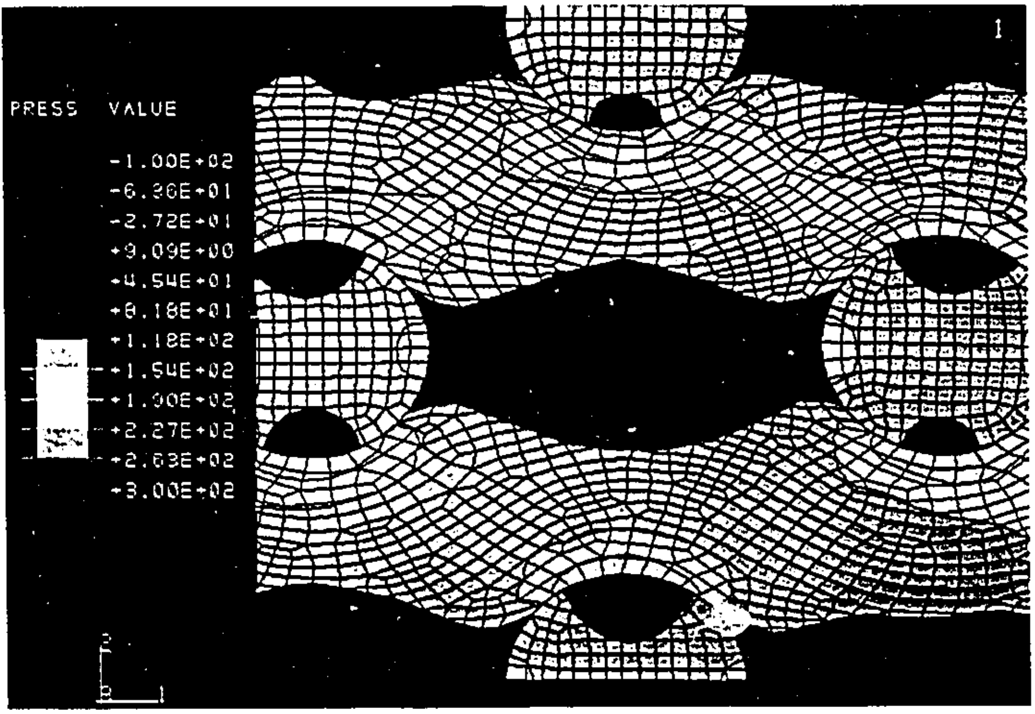
1
PRESS VALUE
-1.00E+02
-6.36E+01
-2.72E+01
+9.09E+00
+4.54E+01
+8.18E+01
+1.18E+02
+1.54E+02
+1.90E+02
+2.27E+02
+2.63E+02
+3.00E+02
2
3
1

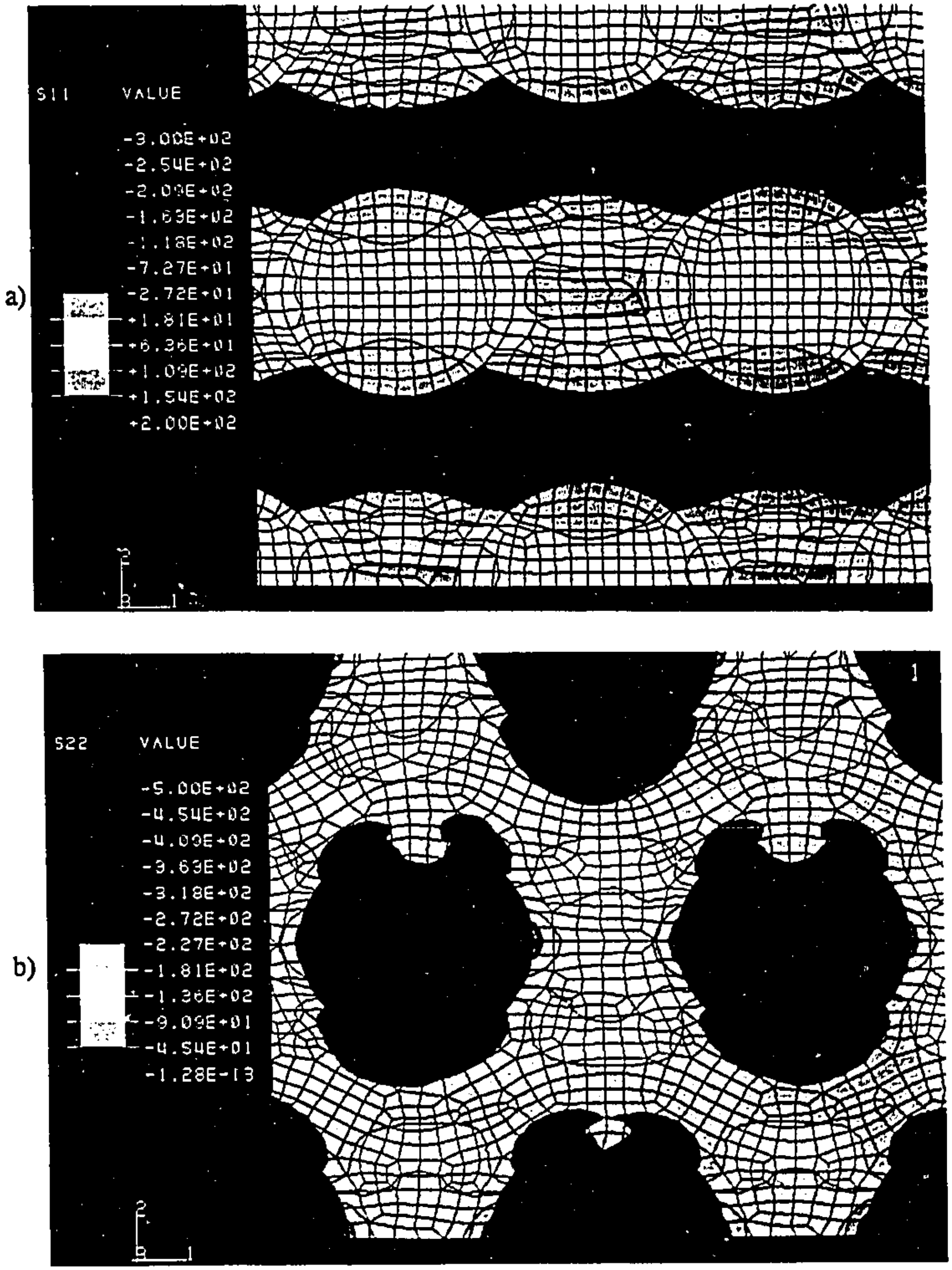

Figure 4.30 - Stress distributions from FEM calculations for 30 % volume fraction sample with triangular arrangement of fibres after an imposed deformation of 0.10, a) σ_{11}, b) σ_{22} , c) σ_{12} and d) hydrostatic pressure

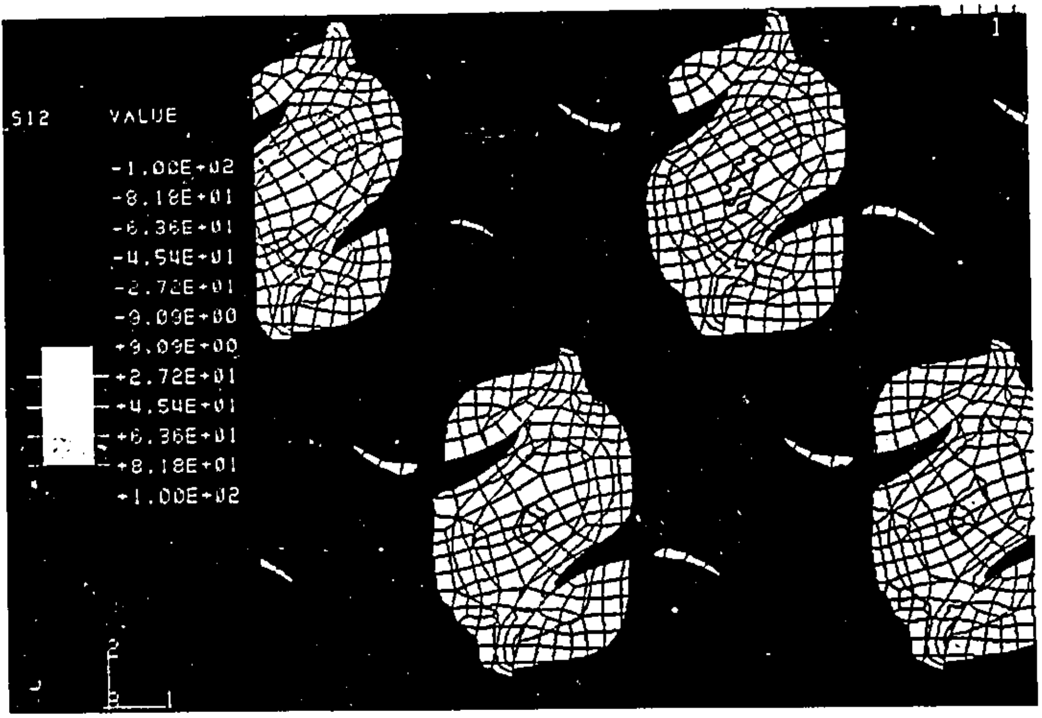
1
S12
VALUE
-1.00E+02
-8.18E+01
-6.36E+01
-4.54E+01
-2.72E+01
-9.09E+00
+9.09E+00
+2.72E+01
+4.54E+01
+6.36E+01
+8.18E+01
+1.00E+02
2
3
1

c)

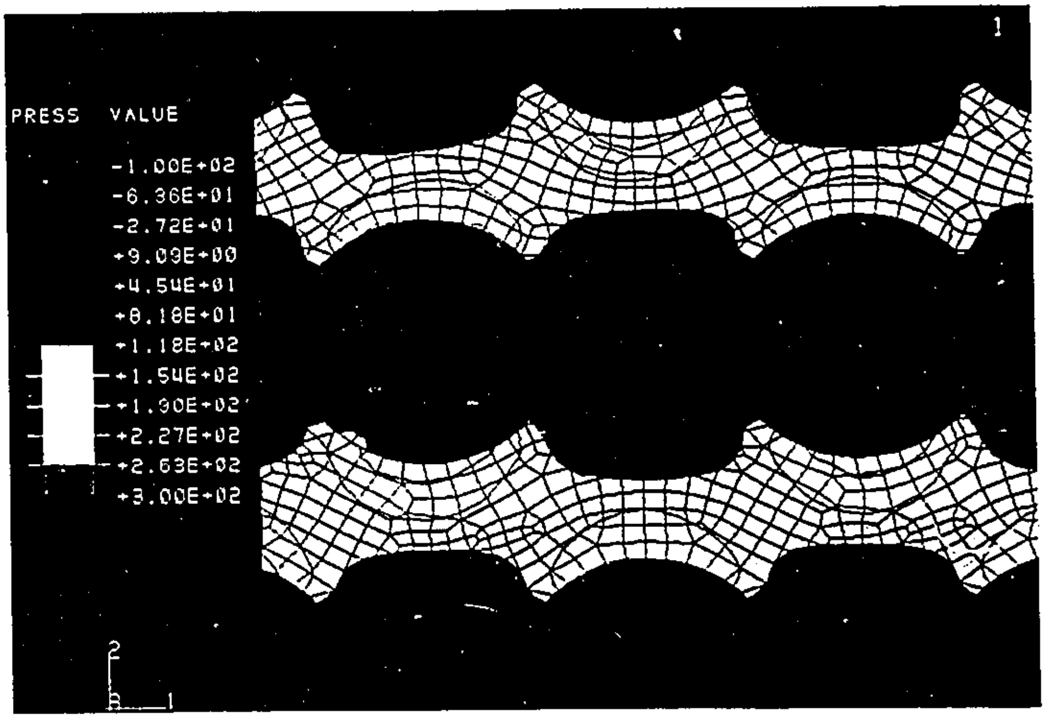
1
PRESS
VALUE
-1.00E+02
-6.36E+01
-2.72E+01
+9.09E+00
+4.54E+01
+8.18E+01
+1.18E+02
+1.54E+02
+1.90E+02
+2.27E+02
+2.63E+02
+3.00E+02
2
3
1

d)

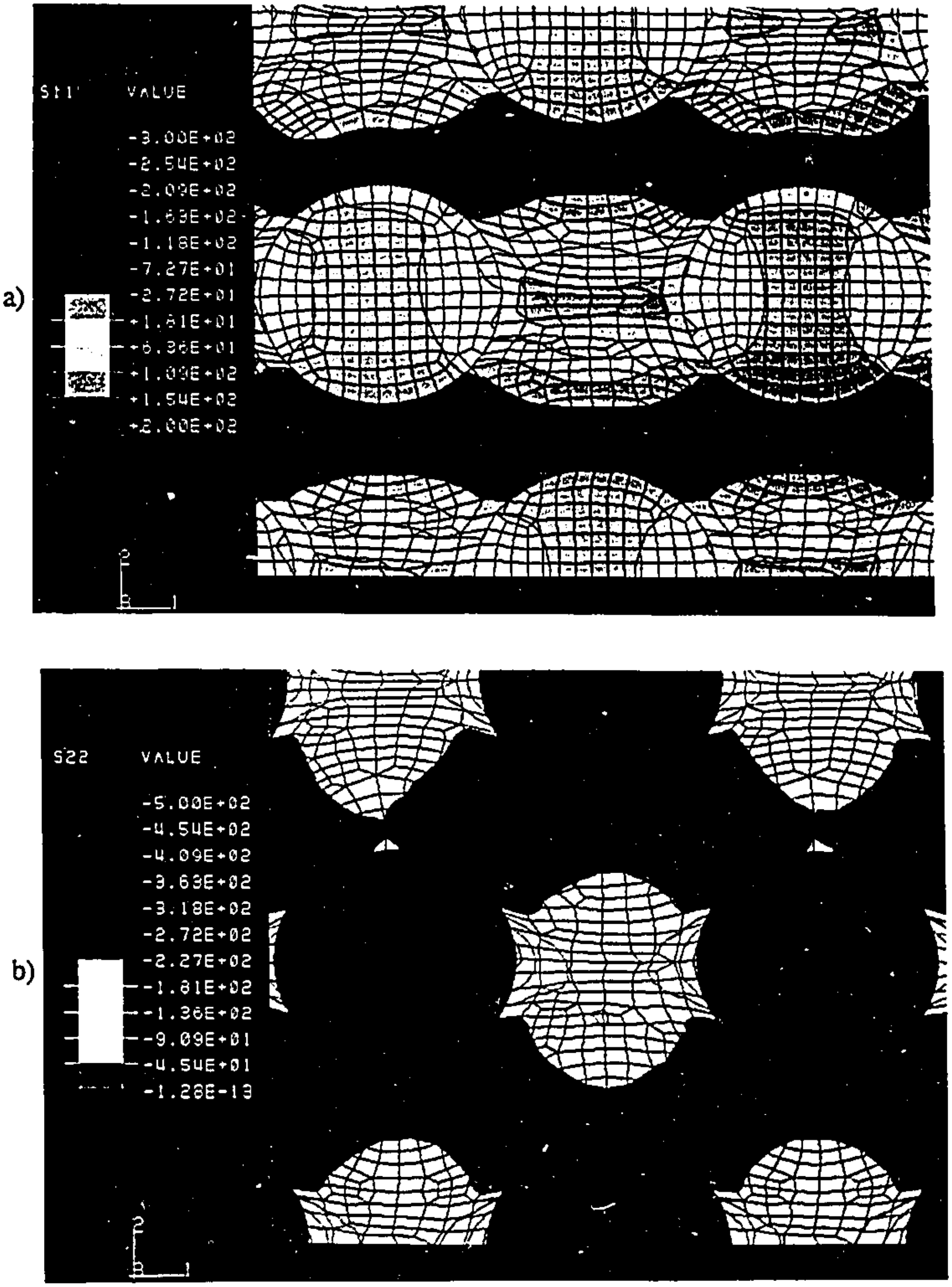

Figure 4.31 - Stress distributions from FEM calculations for 30 % volume fraction sample with triangular arrangement of fibres after an imposed deformation of 0.20, a) σ_{11}, b) σ_{22} , c) σ_{12} and d) hydrostatic pressure

c)

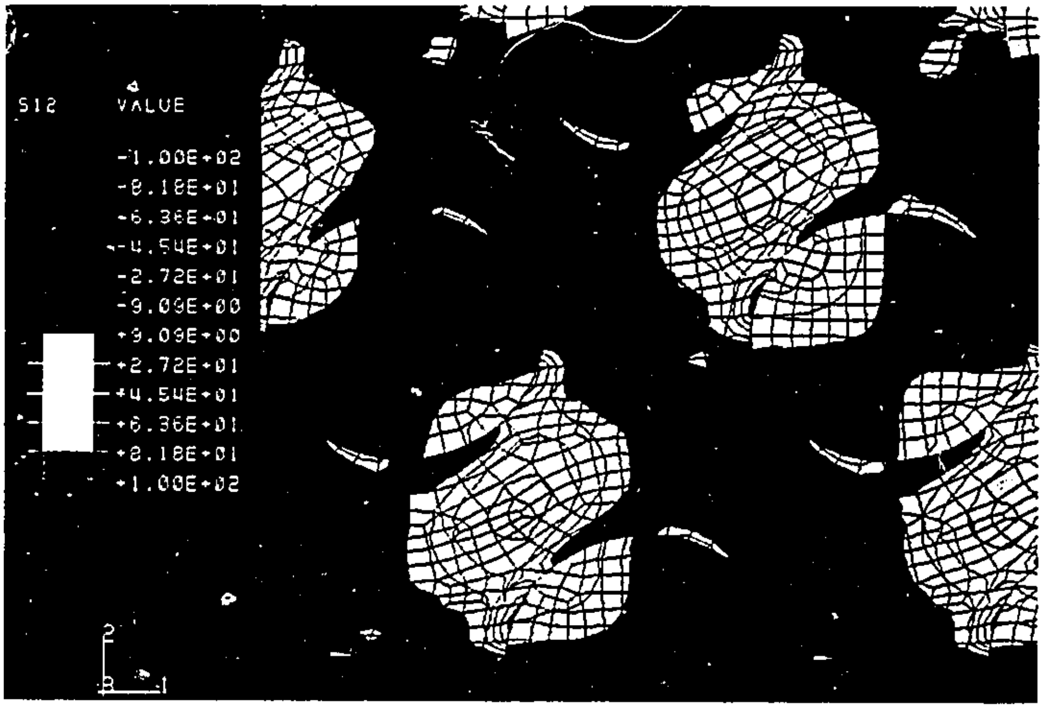
S12 VALUE
-1.00E+02
-8.18E+01
-6.36E+01
-4.54E+01
-2.72E+01
-9.09E+00
+9.09E+00
+2.72E+01
+4.54E+01
+6.36E+01
+8.18E+01
+1.00E+02
2
3
1

d)

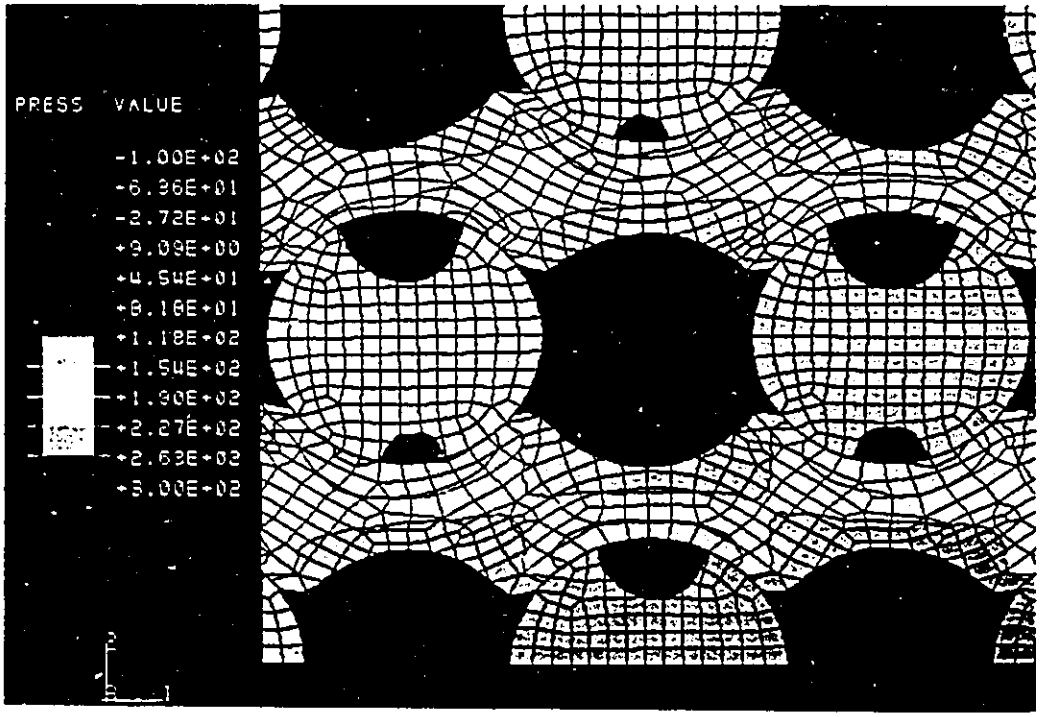
PRESS VALUE
-1.00E+02
-6.36E+01
-2.72E+01
+9.09E+00
+4.54E+01
+8.18E+01
+1.18E+02
+1.54E+02
+1.90E+02
+2.27E+02
+2.63E+02
+3.00E+02
2
3
1

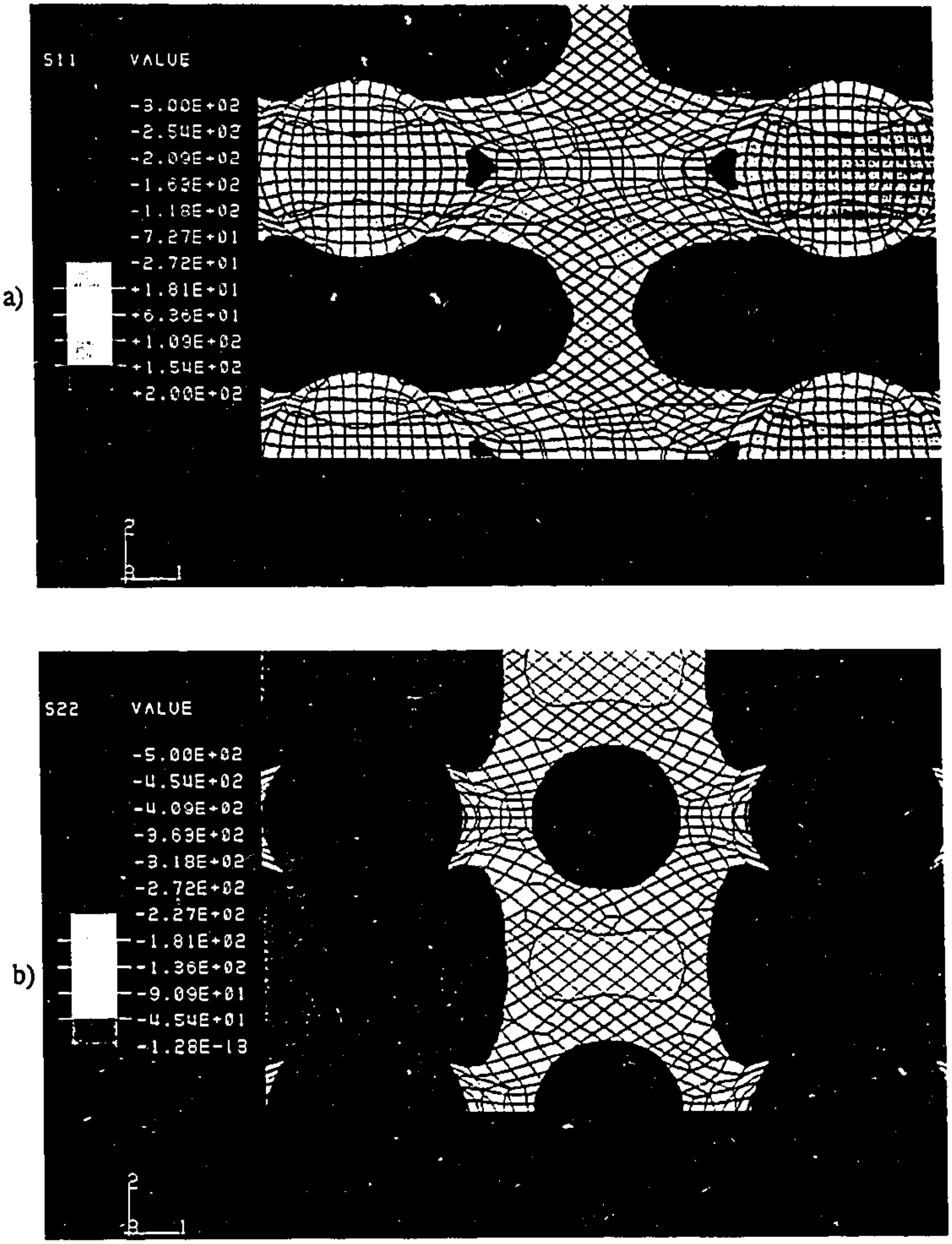

Figure 4.32 - Stress distributions from FEM calculations for 20 % volume fraction sample with square arrangement of fibres, imposed deformation of 0.20, a) σ_{11}, b) σ_{22} , c) σ_{12} and d) hydrostatic pressure

c)

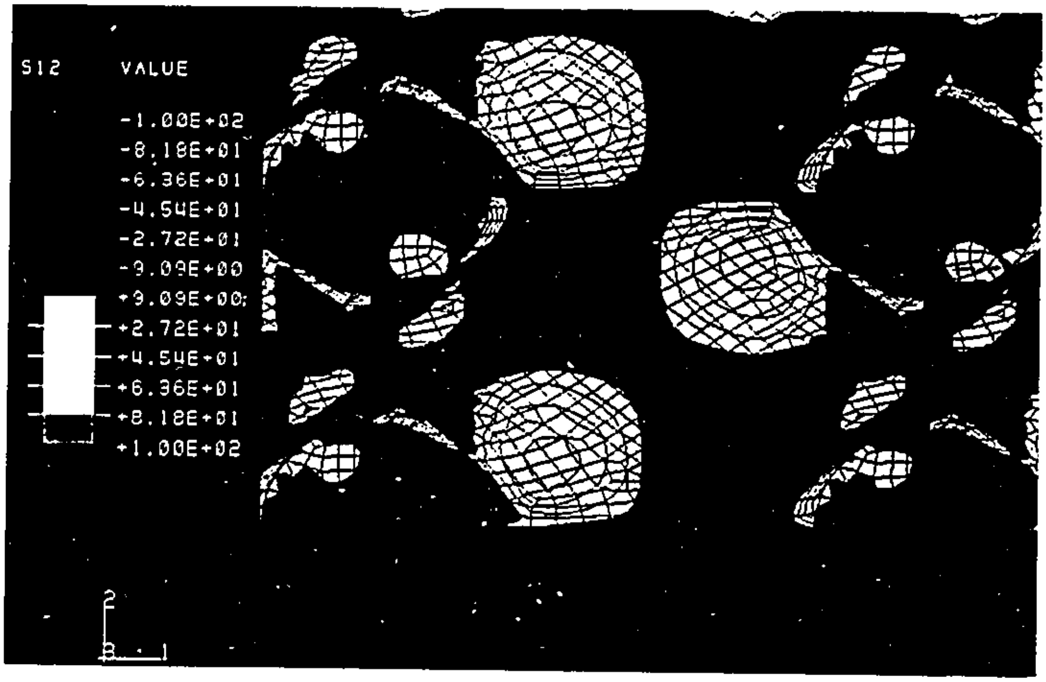
S12 VALUE
-1.00E+02
-8.18E+01
-6.36E+01
-4.54E+01
-2.72E+01
-9.09E+00
+9.09E+00
+2.72E+01
+4.54E+01
+6.36E+01
+8.18E+01
+1.00E+02
2
3
1

d)

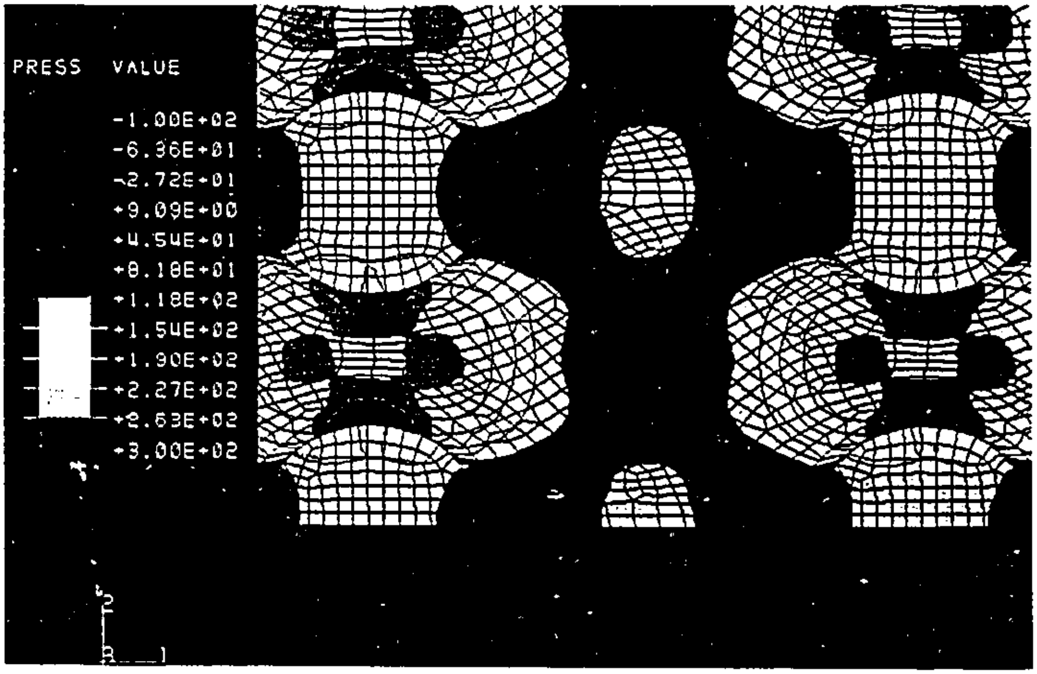
PRESS VALUE
-1.00E+02
-6.36E+01
-2.72E+01
+9.09E+00
+4.54E+01
+8.18E+01
+1.18E+02
+1.54E+02
+1.90E+02
+2.27E+02
+2.63E+02
+3.00E+02
2
3
1

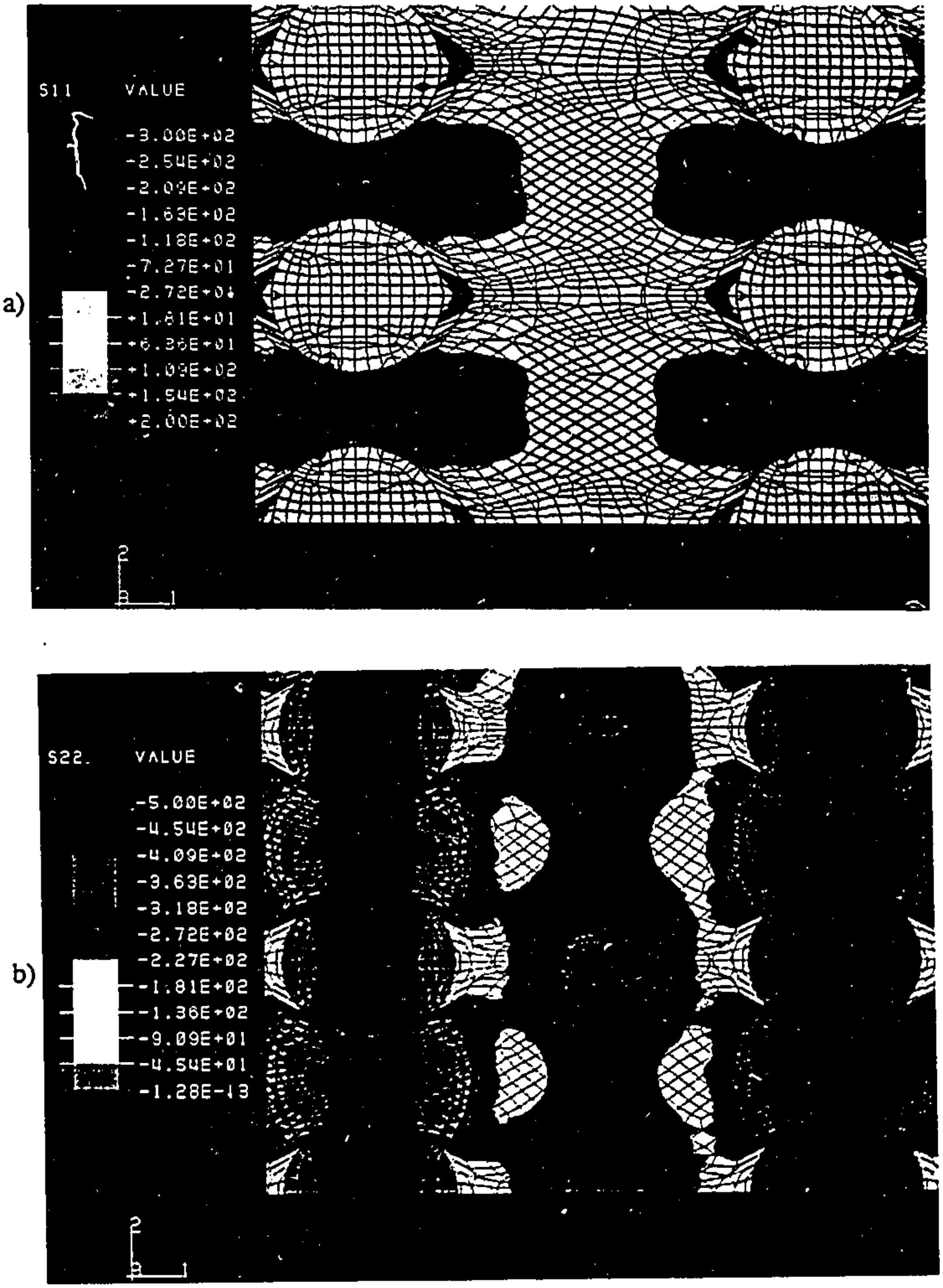

Figure 4.33 - Stress distributions from FEM calculations for 20 % volume fraction sample with square arrangement of fibres, imposed deformation of 0.30, a) σ_{11}, b) σ_{22} , c) σ_{12} and d) hydrostatic pressure

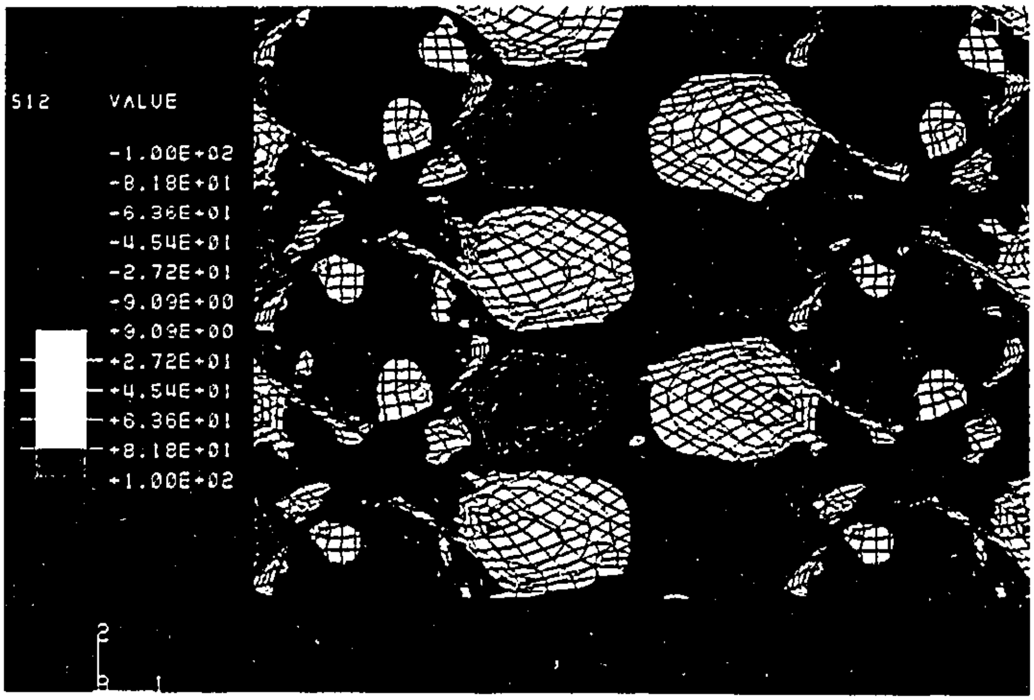
S12
VALUE
-1.00E+02
-8.18E+01
-6.36E+01
-4.54E+01
-2.72E+01
-9.09E+00
+9.09E+00
+2.72E+01
+4.54E+01
+6.36E+01
+8.18E+01
+1.00E+02
2
3
1

c)

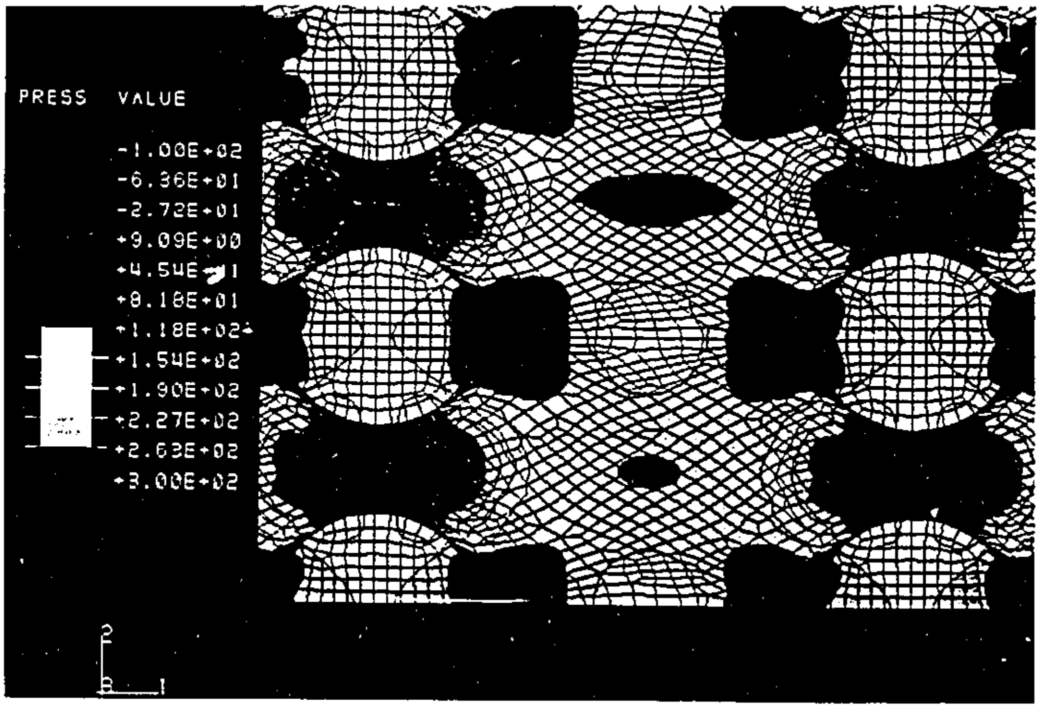
PRESS
VALUE
-1.00E+02
-6.36E+01
-2.72E+01
+9.09E+00
+4.54E+01
+8.18E+01
+1.18E+02
+1.54E+02
+1.90E+02
+2.27E+02
+2.63E+02
+3.00E+02
2
3
1

d)

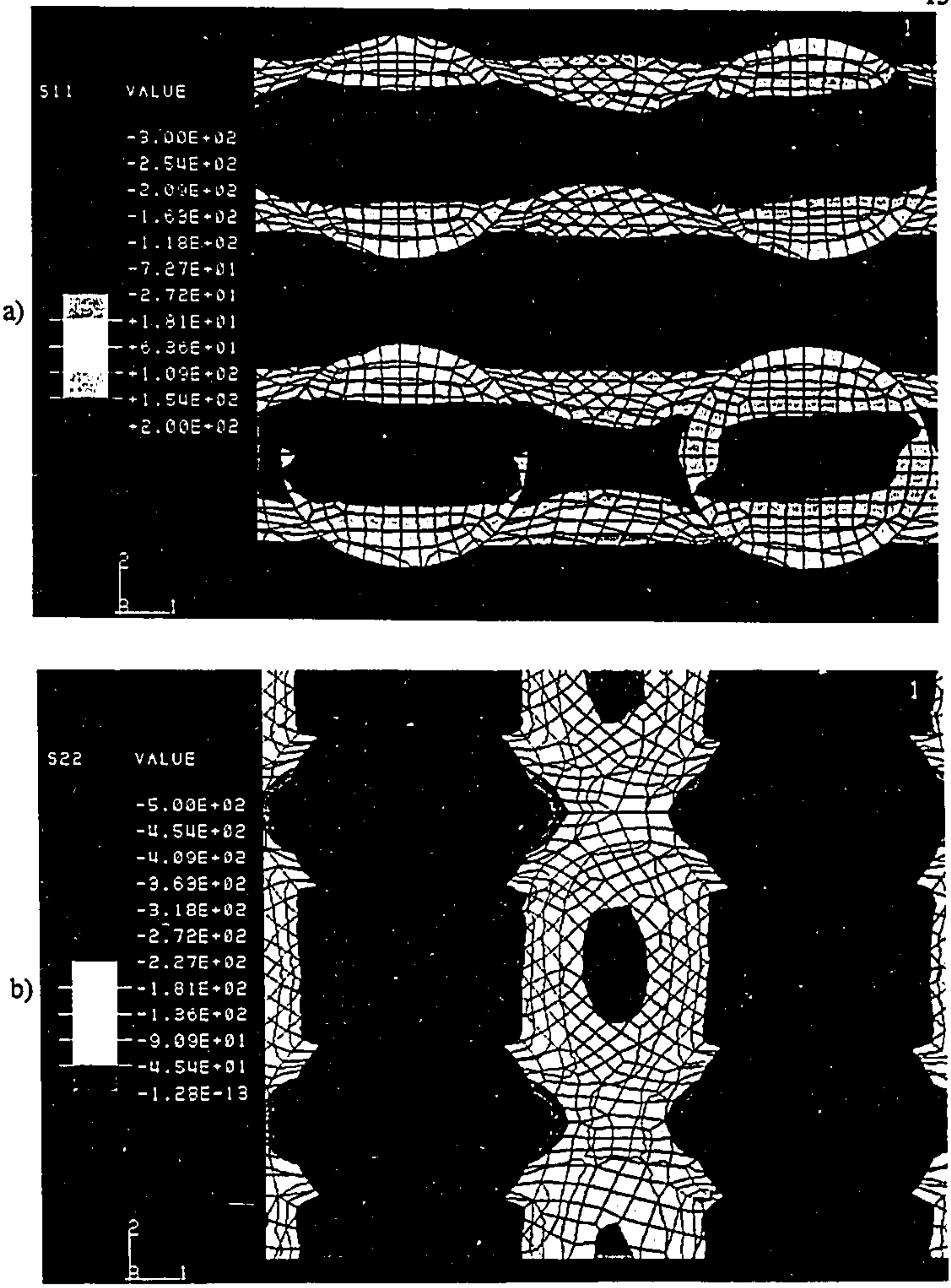

Figure 4.34 - Stress distributions from FEM calculations for 30 % volume fraction sample with square arrangement of fibres, imposed deformation of 0.10, a) σ_{11}, b) σ_{22} , c) σ_{12} and d) hydrostatic pressure

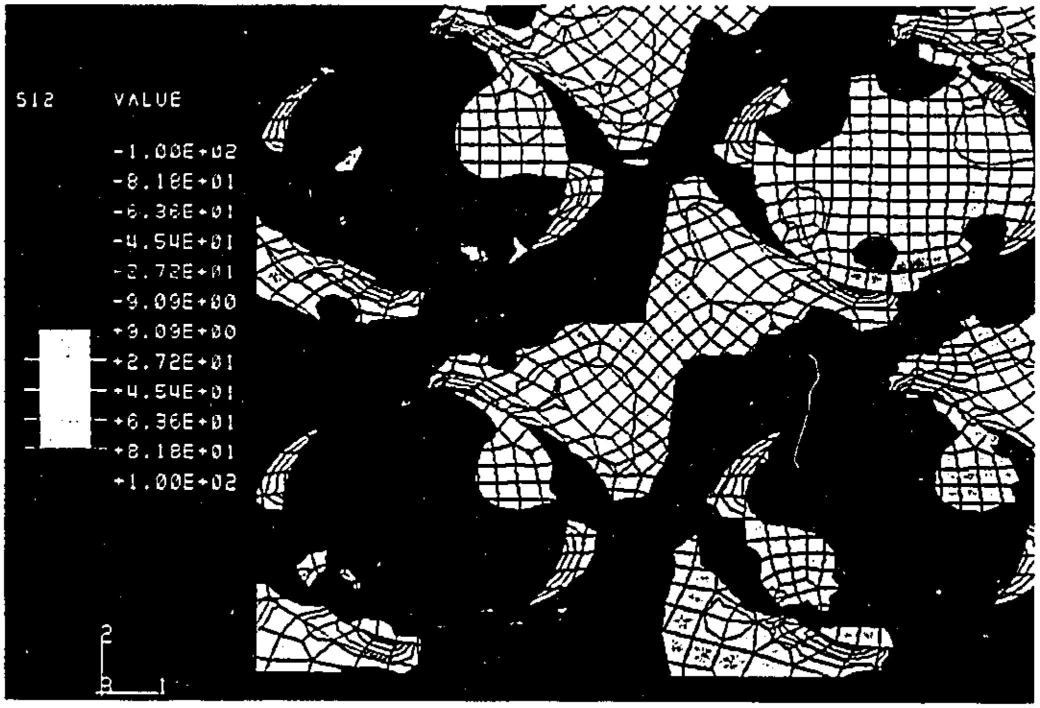
S12 VALUE
-1.00E+02
-8.18E+01
-6.36E+01
-4.54E+01
-2.72E+01
-9.09E+00
+9.09E+00
+2.72E+01
+4.54E+01
+6.36E+01
+8.18E+01
+1.00E+02
2
3
1

c)

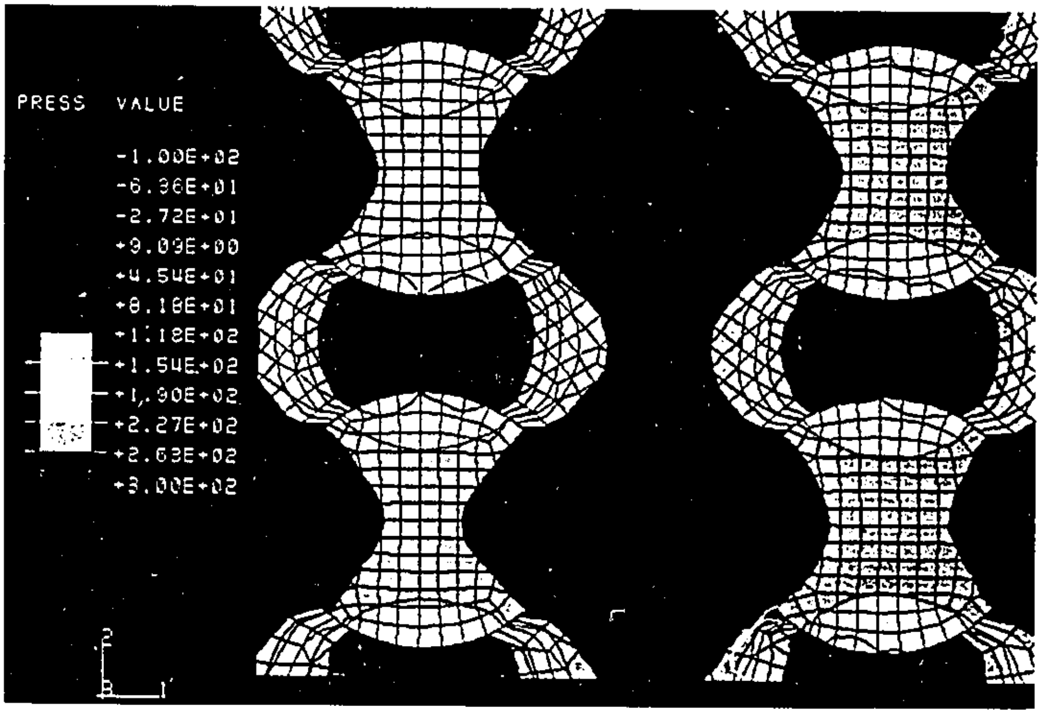
PRESS VALUE
-1.00E+02
-6.36E+01
-2.72E+01
+9.09E+00
+4.54E+01
+8.18E+01
+1.18E+02
+1.54E+02
+1.90E+02
+2.27E+02
+2.63E+02
+3.00E+02
2
3
1

d)

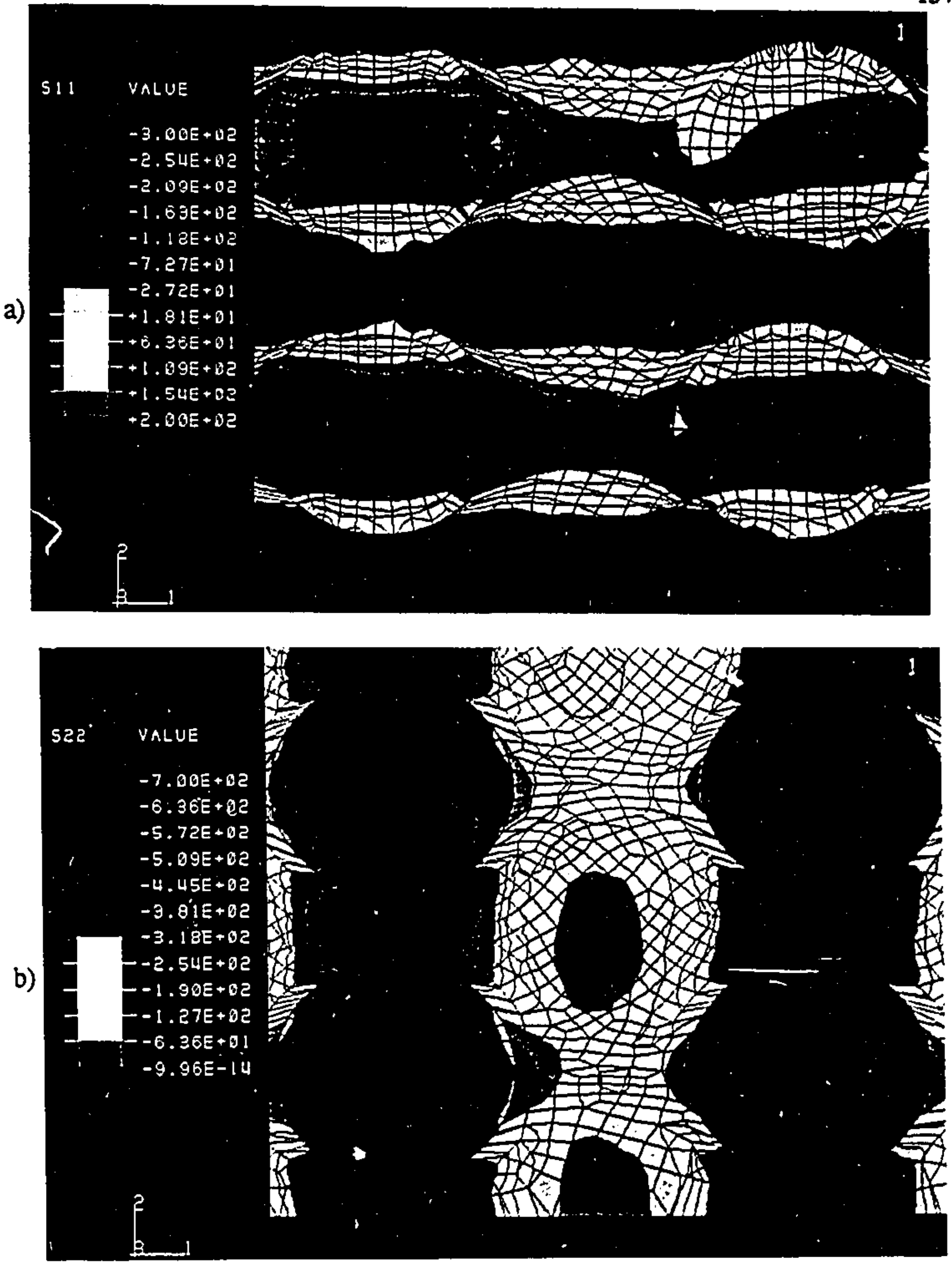

Figure 4.35 - Stress distributions from FEM calculations for 30 % volume fraction sample with square arrangement of fibres, imposed deformation of 0.20, a) σ_{11}, b) σ_{22} , c) σ_{12} and d) hydrostatic pressure

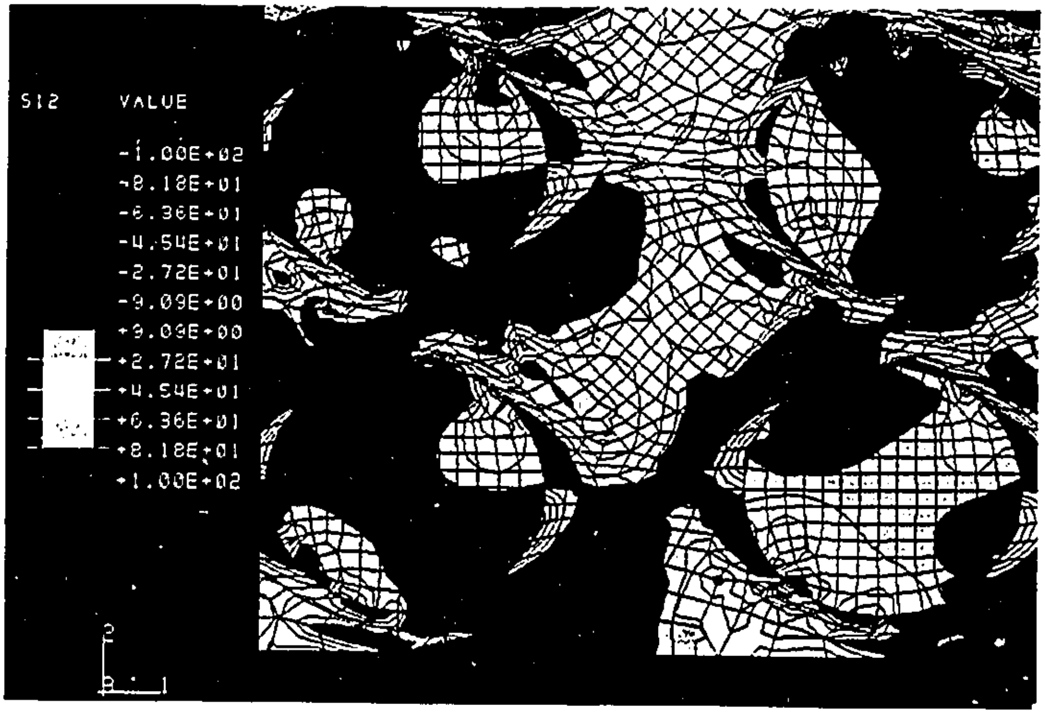
S12 VALUE
-1.00E+02
-8.18E+01
-6.36E+01
-4.54E+01
-2.72E+01
-9.09E+00
+9.09E+00
+2.72E+01
+4.54E+01
+6.36E+01
+8.18E+01
+1.00E+02
2
3
1

c)

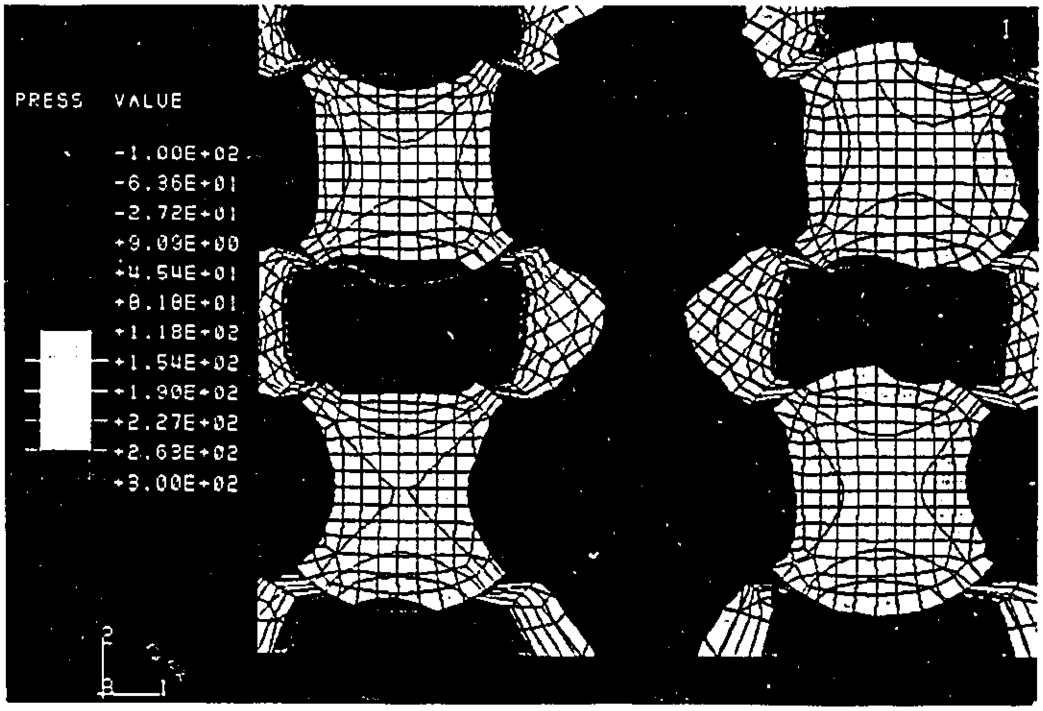
PRESS VALUE
-1.00E+02
-6.36E+01
-2.72E+01
+9.09E+00
+4.54E+01
+8.18E+01
+1.18E+02
+1.54E+02
+1.90E+02
+2.27E+02
+2.63E+02
+3.00E+02
2
3
1
1

d)

Table 4.4
Maximum and minimum stresses in the fibres from FEM calculations
(Tensile stresses positive, compressive stresses negative)

Sample Deformation Level	Maximun Tension $\sigma_{xx\text{-fibre}}$ / MPa	Minimum Tension $\sigma_{xx\text{-fibre}}$ / MPa	Maximum Compression $\sigma_{yy\text{-fibre}}$ / MPa	Minimum Compression $\sigma_{yy\text{-fibre}}$ / MPa
Single Fibre				
0.3	64-109	18-64	(-363)-(-409)	(-318)-(-363)
20 % v.f.-tri				
0.2	18-64	(-27)-18	(-318)-(-363)	(-227)-(-272)
0.3	64-109	(-27)-18	(-363)-(-409)	(-227)-(-272)
30 % v.f. -tri				
0.1	64-109	(-27)-18	(-272)-(-318)	(-181)-(-227)
0.2	109-154	18-63	-500+	(-363)-(-409)
20 % v.f. sqr				
0.2	109-154	18-63	(-409)-(-454)	(-363)-(-409)
0.3	109-154	18-63	(-454)-(-500)	(-318)-(-363)
30 % v.f. sqr				
0.1	200+	18-63	-500+	(-227)-(-272)
0.2	200+	(-27)-18	-700+	(-318)-(-381)

4.5 - Texture Measurements

In this section, (111) pole figures will be presented. The pole figures are oriented such that the transverse direction of the sample is in the centre, the normal direction is at the top and rolling direction is at the side of the pole figure. The grain sizes of the copper in the composites range from 50-200 μm.

Figure 4.36a illustrates the initial texture for unreinforced copper (i.e. 140 μm grain size material). There is a relatively strong fibre texture present in the starting material (i.e. note the presence of strong component in the bottom left corner of the pole figure with intensity four times random). Figure 4.36b is an experimental pole figure after a plane strain compression of 0.4. This texture is essentially a standard rolling texture with modifications arising from the non-random starting texture. The effect of the initial texture was investigated using the Los Alamos polycrystalline plasticity (LApp) code. The simulated textures after plane compression of 0.4 for an initial random texture and an initial fibre texture are shown in Figure 4.37 and Figure 4.38. Note the absence of a texture component at the bottom left corner of the pole figure in Figure 4.37.

The pole figures in Figure 4.39 are the experimentally measured starting texture and the texture after plane strain compression of 0.3 for the 20 % volume fraction sample with triangular arrangement of fibres. The starting texture (Figure 4.39a) is somewhat spotty (i.e. note the spots greater than 4 times and less .25 times random) due to the slightly larger than desirable initial grain size. The deformed texture (Figure 4.39b) can be described by a random background with larger than random intensity at points marked B and D and lower than random intensities at the points

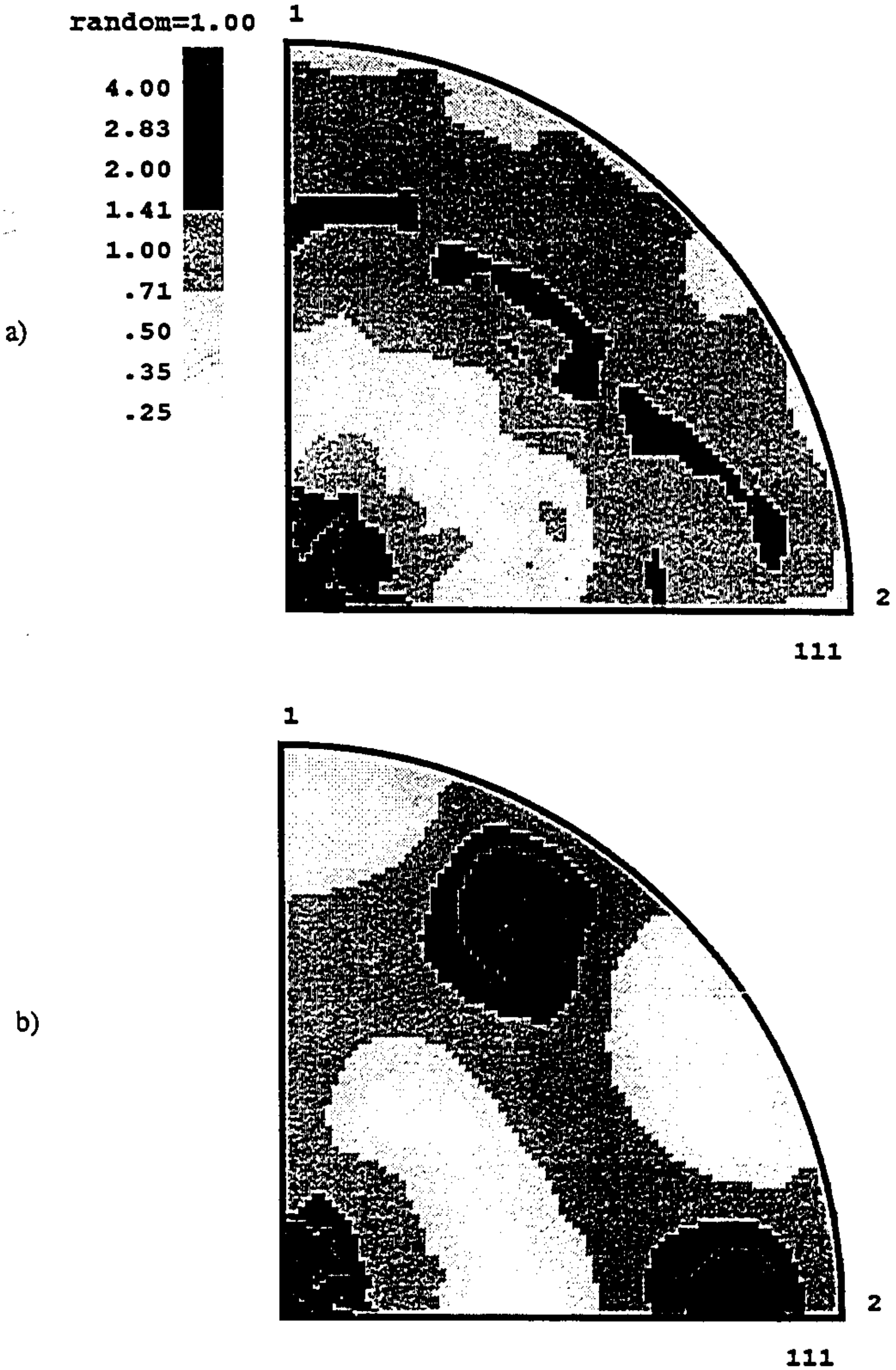

Figure 4.36 - Experimental (111) Pole figure for unreinforced copper illustrating, a) starting texture and b) texture after plane strain compression of 0.40

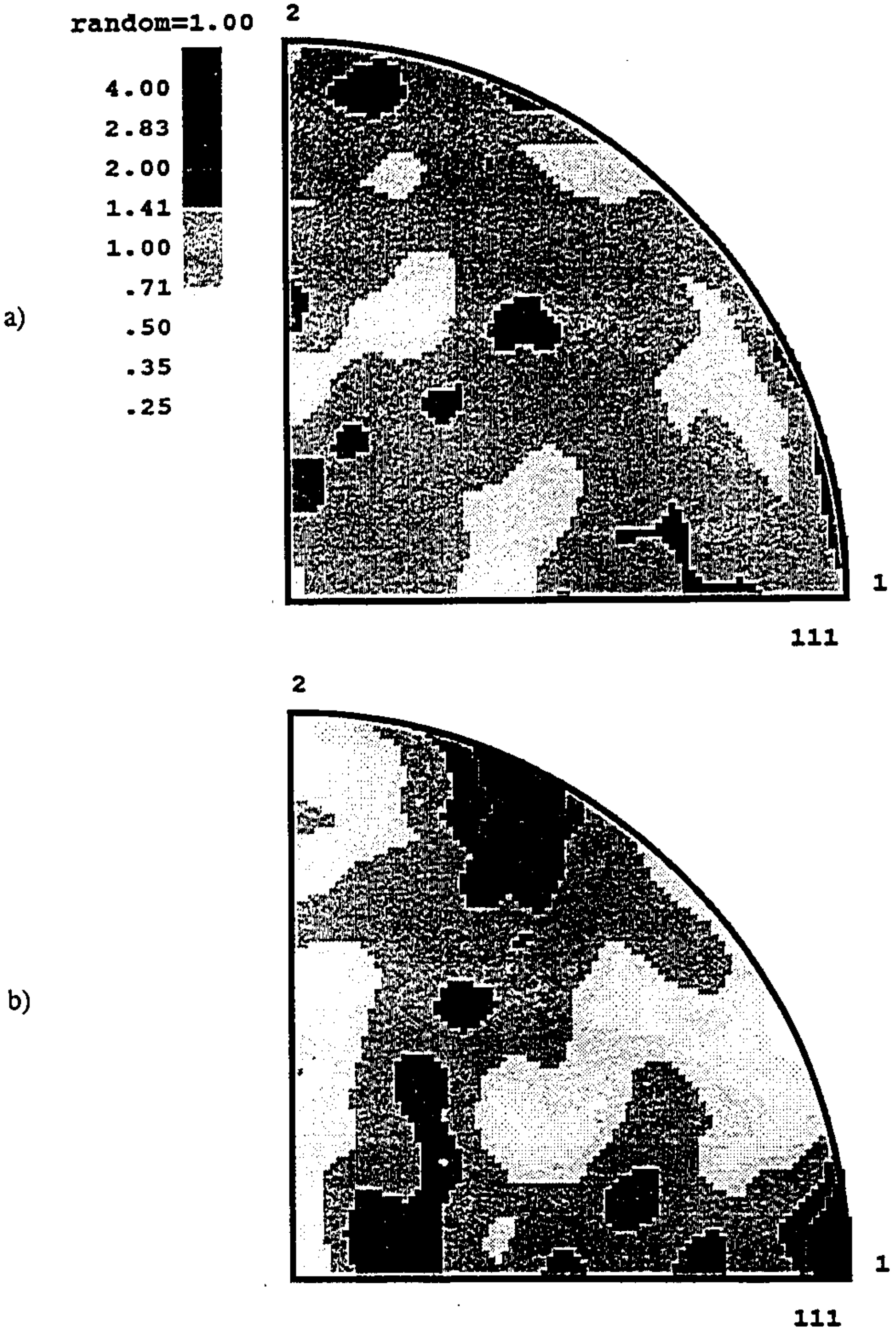

Figure 4.37 - Predicted (111) pole figures from LApp simulation (see text), a) starting texture (random) and b) after plane strain deformation of 0.40.

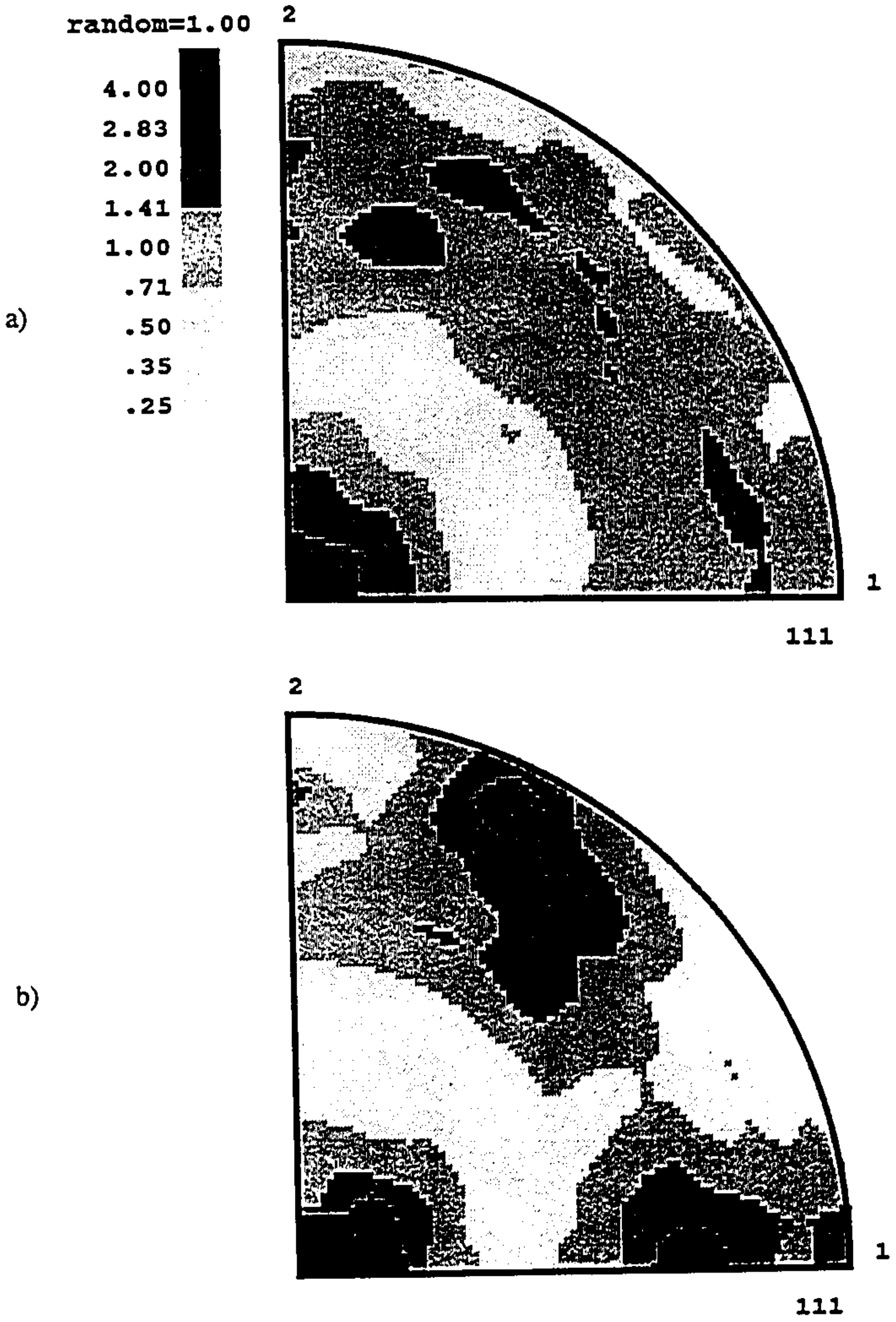

Figure 4.38 - Predicted (111) pole figure, a) starting texture for LApp (see text) and b) texture after plane strain compression of 0.40

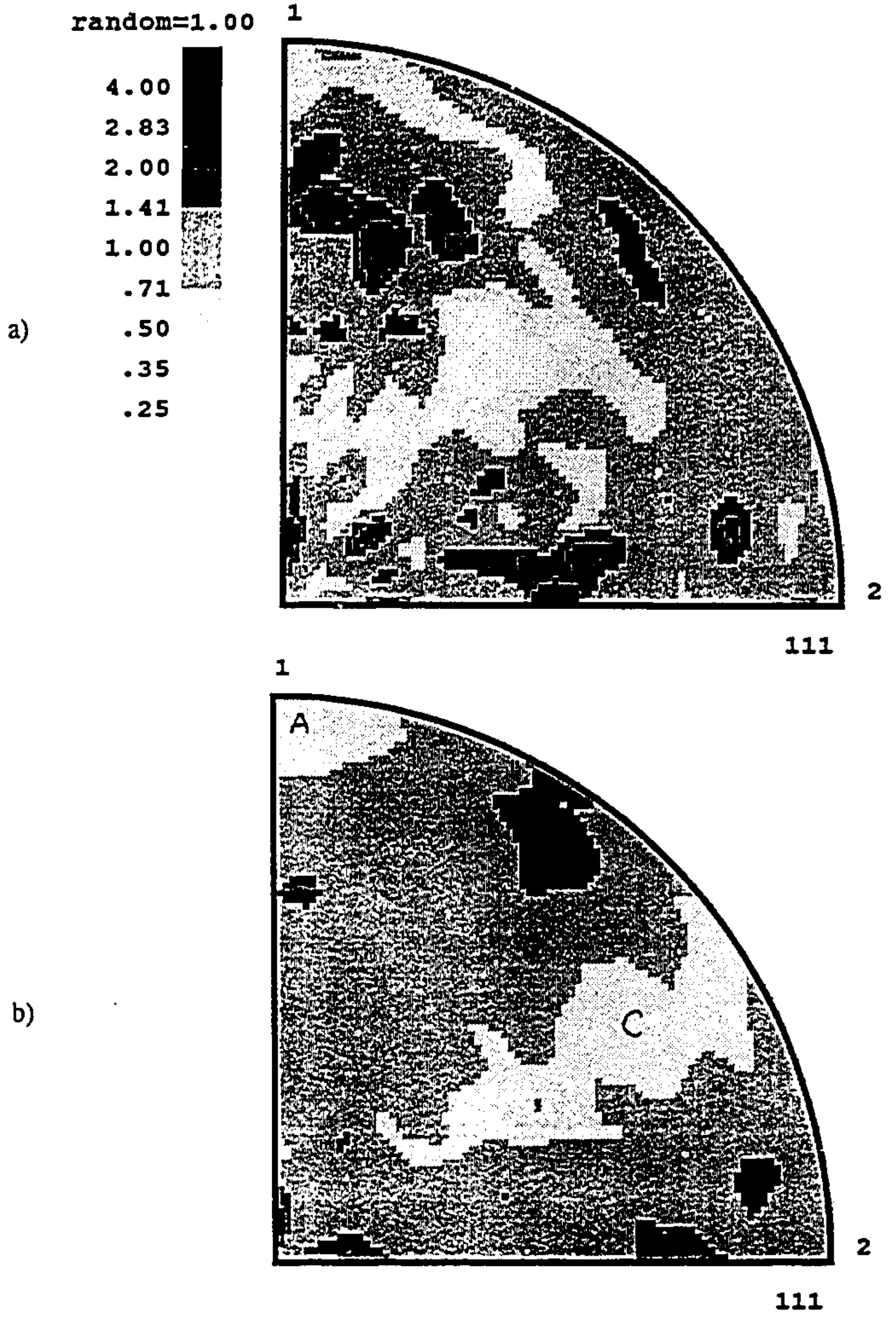

Figure 4.39 - Experimental (111) pole figures for 20 % volume fraction sample with triangular arrangement of fibres a) prior to deformation and b) after strain of 0.3 and c) predicted texture (Bolmaro et al., 1992)

c)

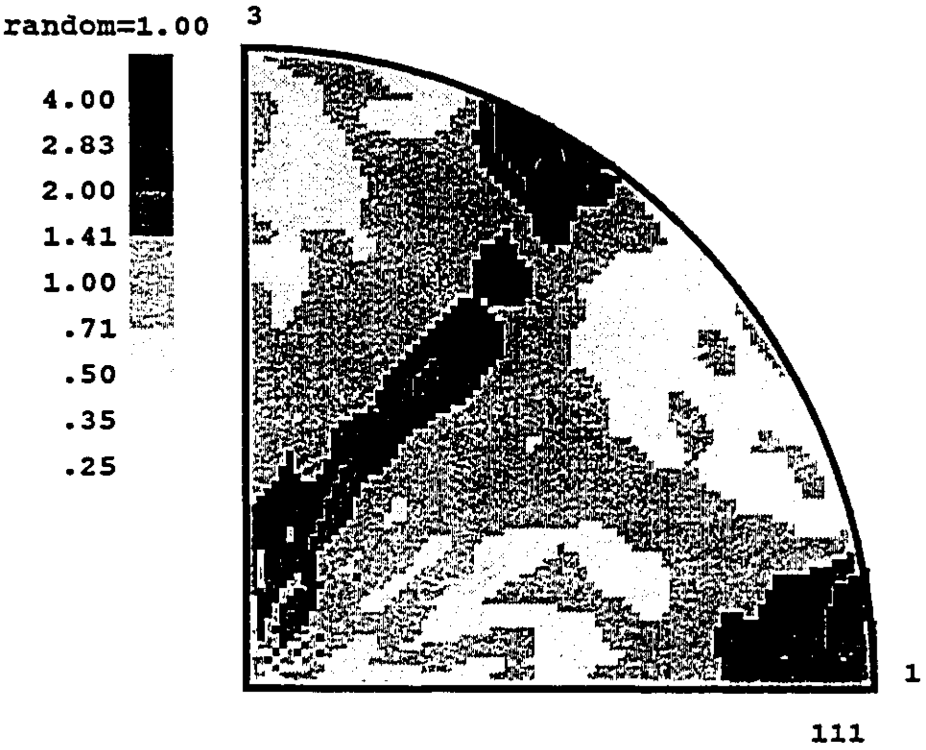

marked A and C. The prediction for the deformed texture from LApp (Bolmaro et al., 1992) is shown in Figure 4.39c. It is apparent that the same general features are present in both the experimental and simulated deformation textures, however the texture from the simulation is sharper (i.e. the intensities above random are higher and the intensities below random are lower).

In order to examine the local texture evolution, the samples were sectioned as described in Section 3.6. The resulting experimental pole figures are shown in Fig. Figure 4.40a and Figure 4.40b for the horizontal section and diagonal section, respectively. These can be directly compared to texture predictions from the work of Bolmaro et al. shown in Figure 4.41a and Figure 4.41b. The experimental textures are again weaker than the predictions from the polycrystalline plasticity code predictions.

Figure 4.42 and Figure 4.43 are experimentally measured pole figures for the 30 % volume fracture with triangular and square packing of fibres, respectively. The level of deformed textures in this case were measured after plane strain compression of 0.2. The features of the deformed textures are similar to the 20 % volume fraction sample with a triangular fibre arrangement.

4.6 - Recrystallization Observations

Figure 4.44a and Figure 4.44b are optical micrographs of the 20 % volume fraction sample with triangular arrangement of fibres after 30 and 60 minutes anneal at 300 °C, respectively. These samples had received an imposed deformation of 0.3 in the direction indicated prior to annealing. It is apparent that there are a large number of

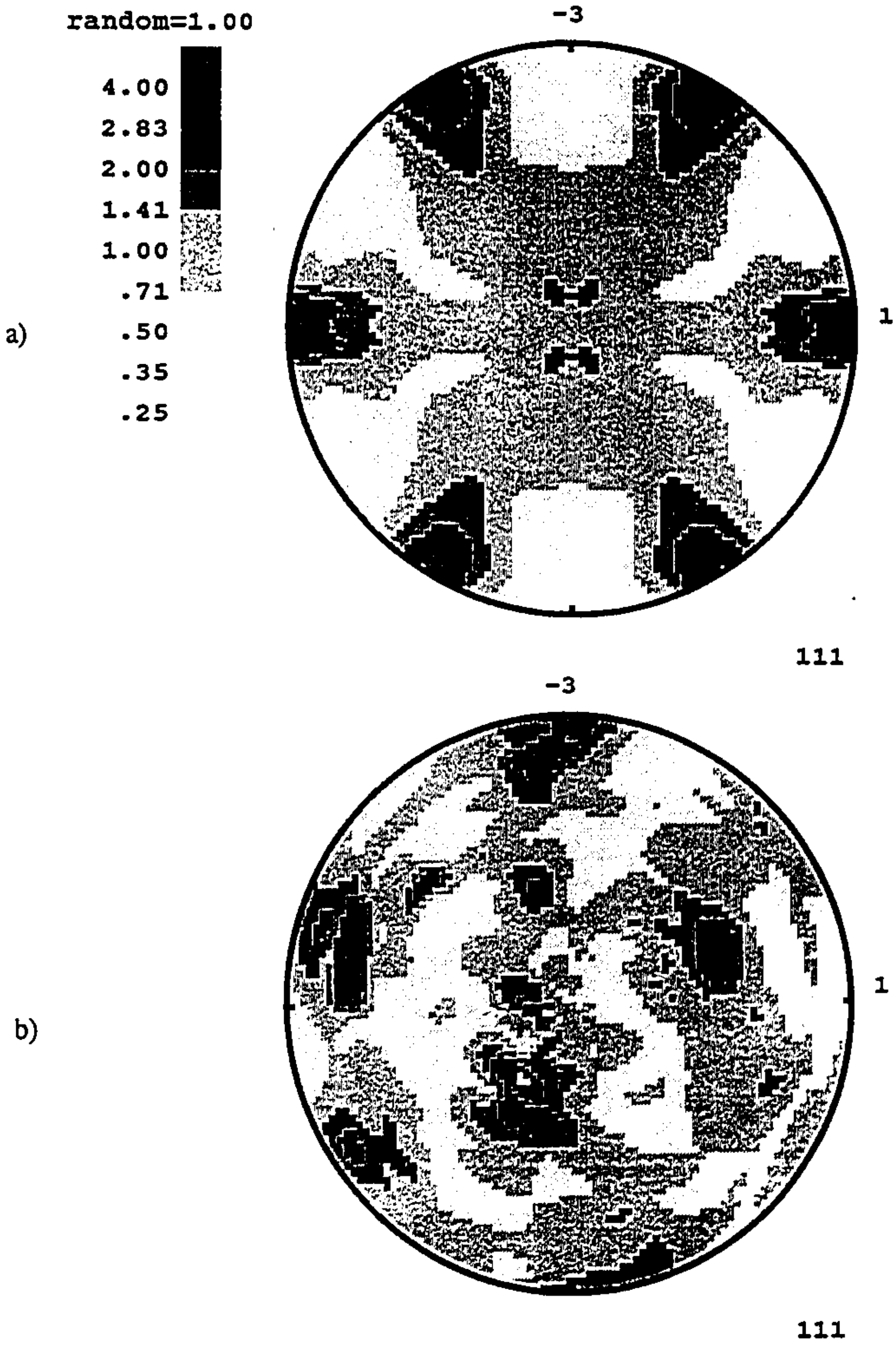

Figure 4.40 - Experimental (111) pole figures for samples sectioned as shown schematically, a) along horizontal and b) along diagonal. Note: pole figures have been permuted to the same sample reference frame as previous pole figures.

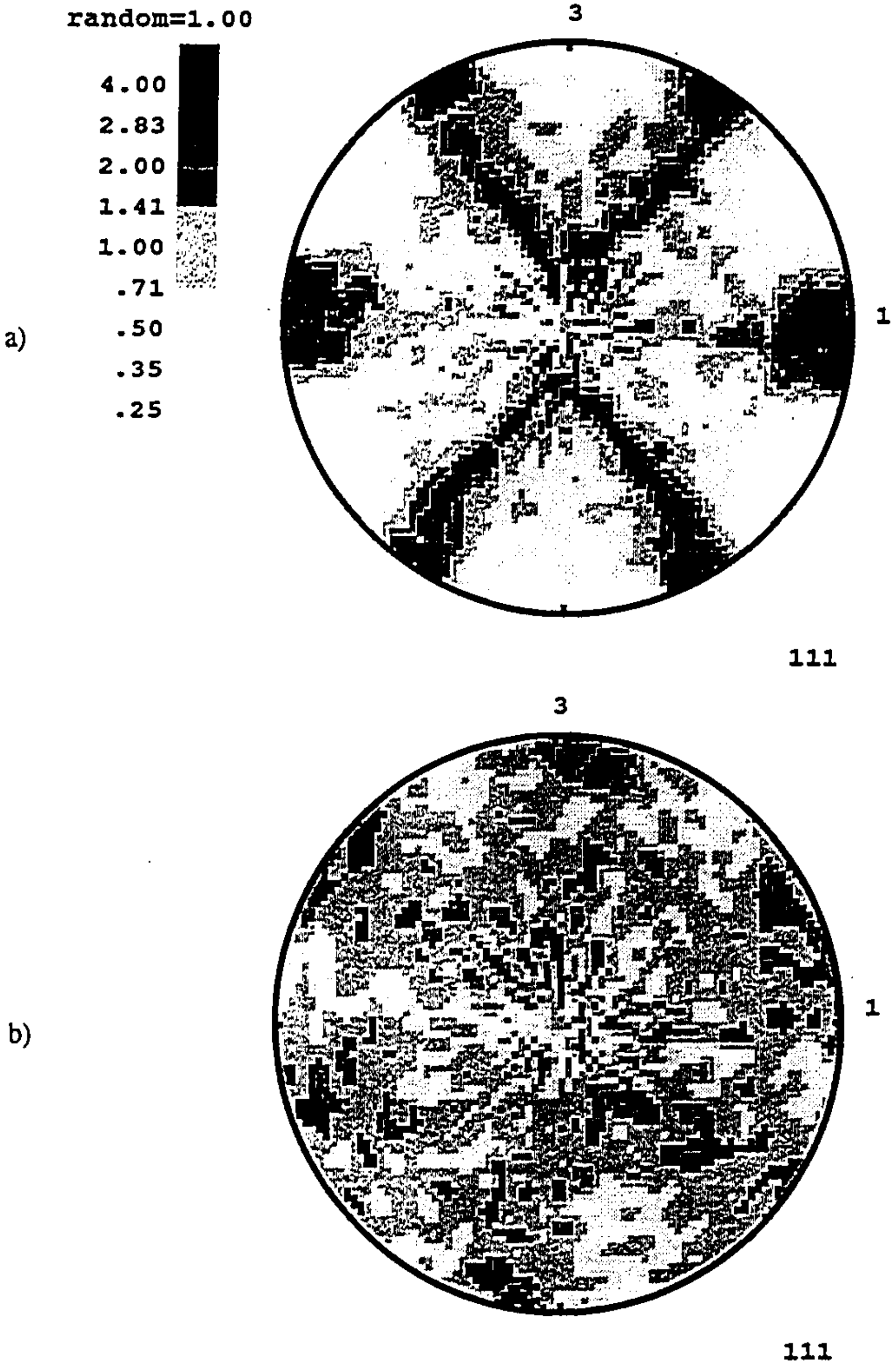

Figure 4.41 - Predicted (111) pole figures from points shown schematically a) on horizontal between fibres and b) on diagonal between fibres. (Bolmaro et al., 1992).

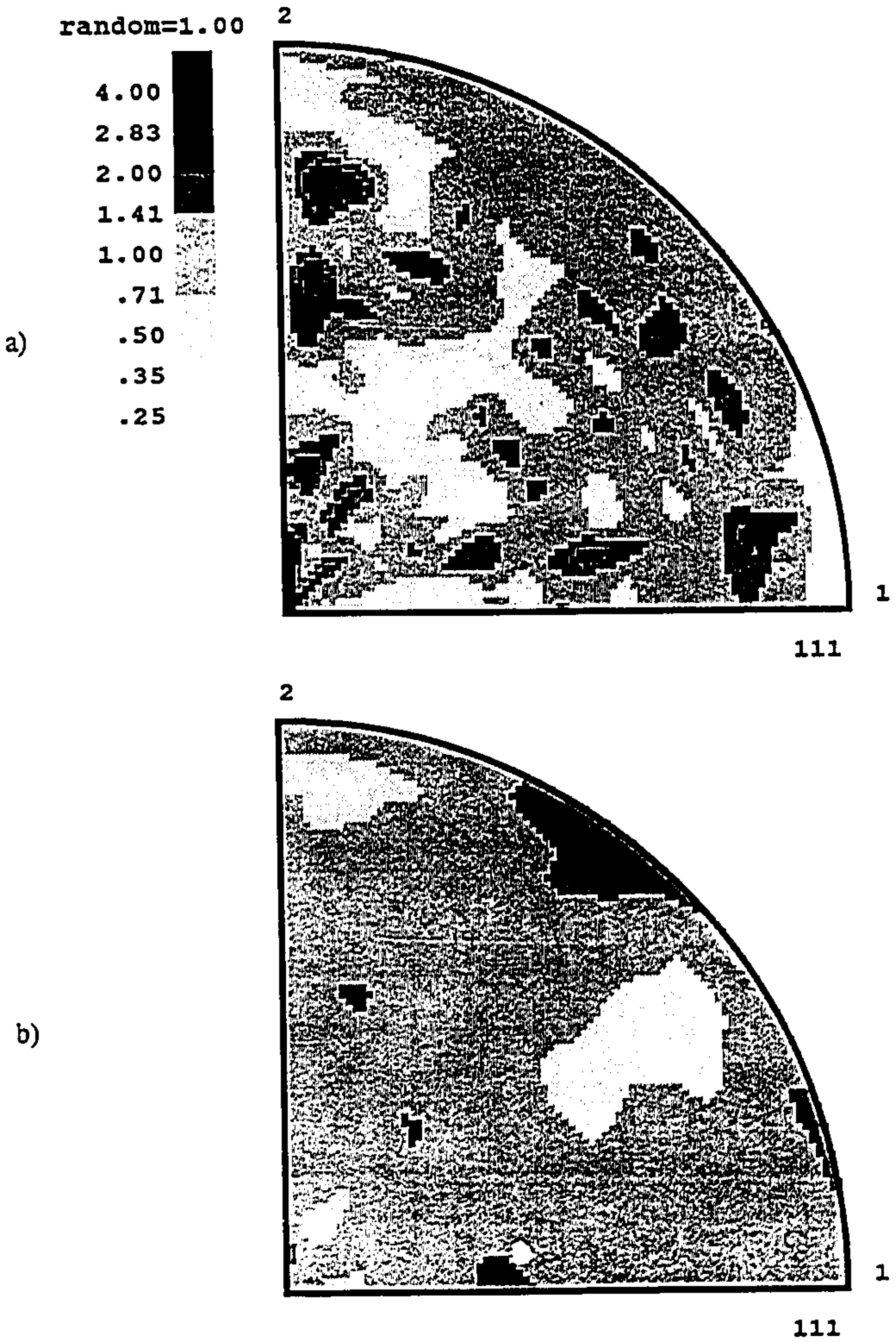

Figure 4.42 - Experimental (111) pole figures for 30 % volume fraction sample with triangular arrangement of fibres, a) initial texture and b) texture after deformation of 0.2.

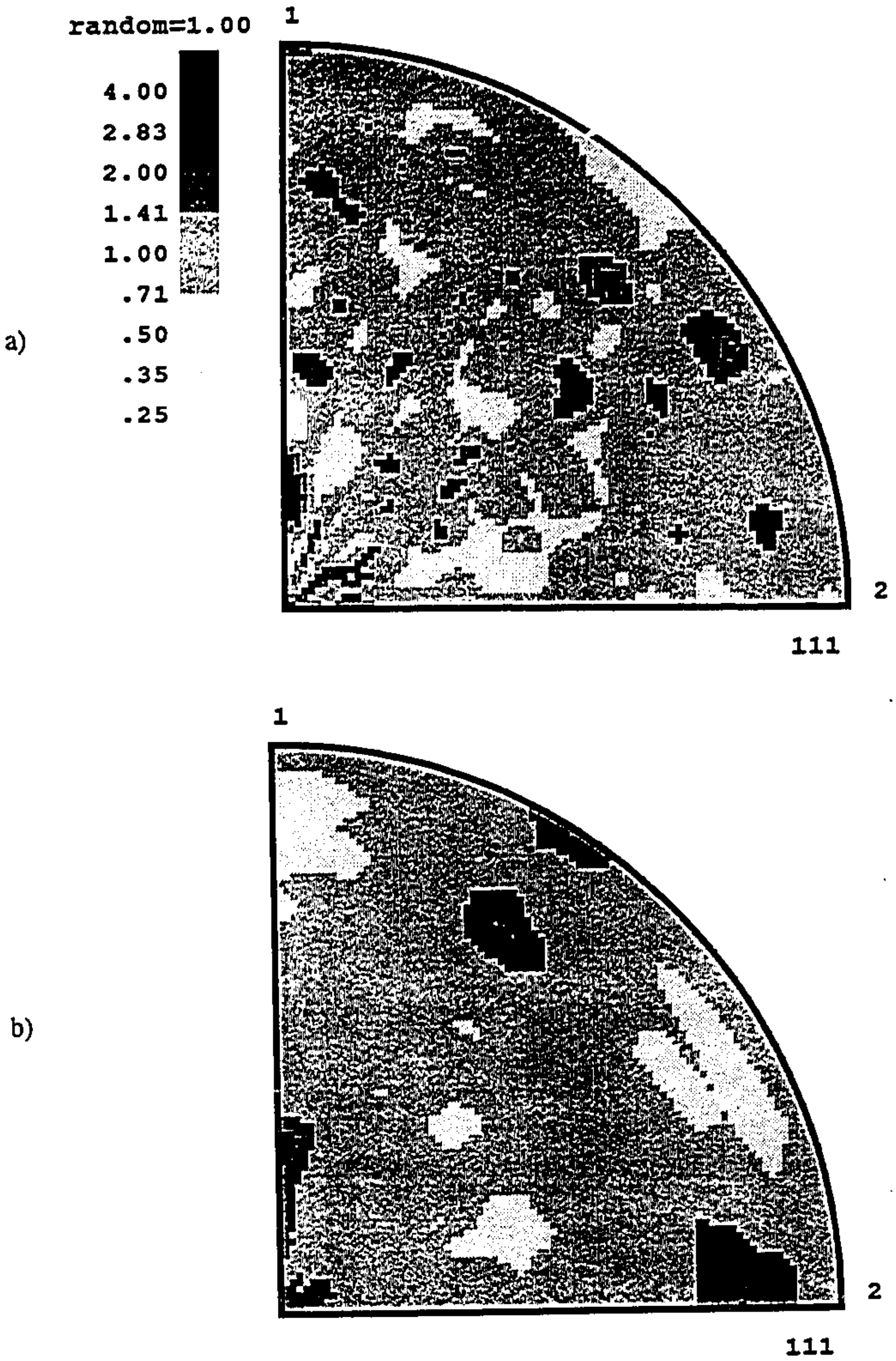

Figure 4.43 - Experimental (111) pole figures for 30 % volume fraction sample with square arrangement of fibres, a) initial texture and b) texture after deformation of 0.2.

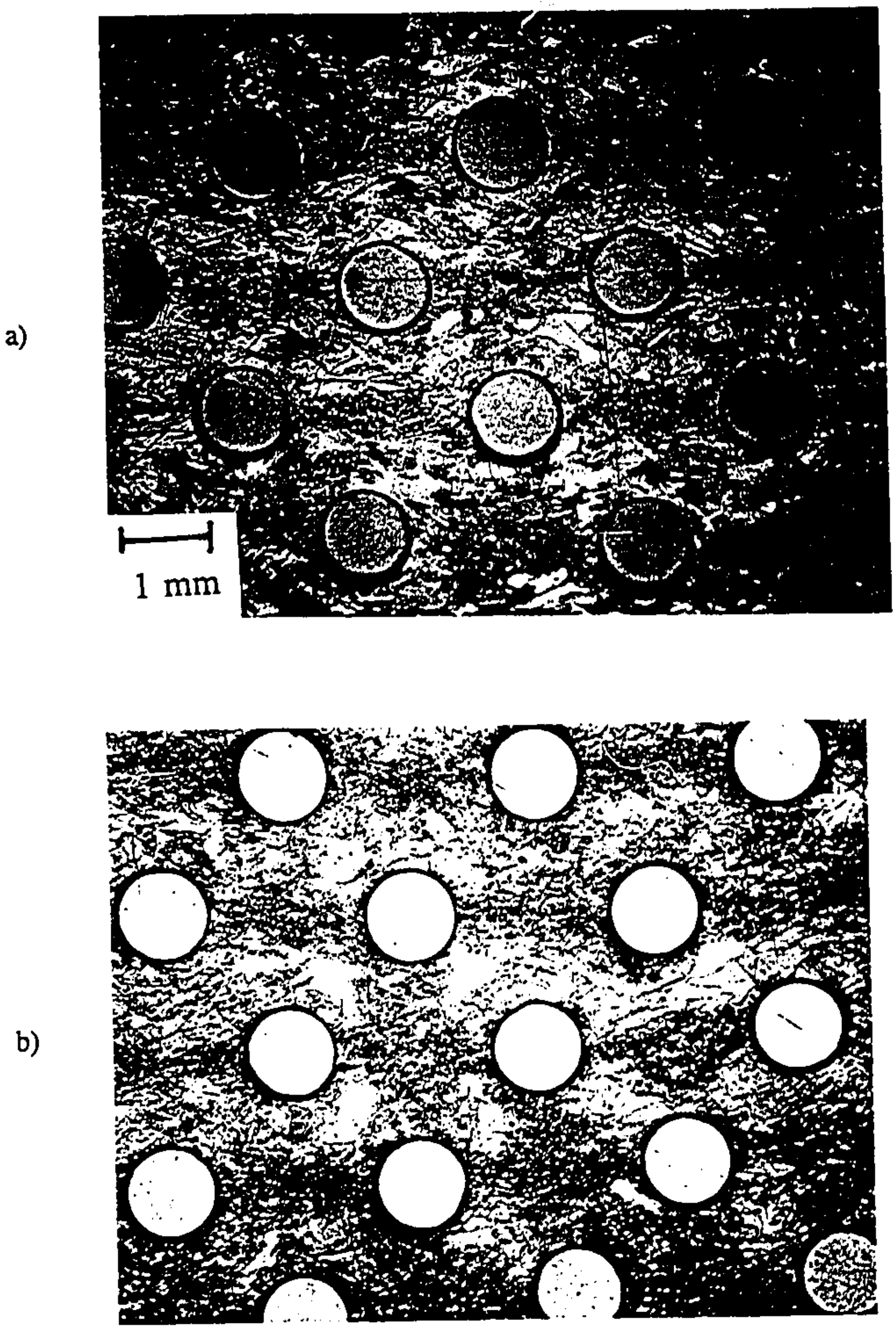

Figure 4.44 - Optical micrographs of 20 % volume fraction sample with triangular arrangement of fibres, deformed 30 % then a) annealed 30 min. at 300 °C and b) 1 hour at 300 °C. Note: tungsten fibres are 1 mm dia.

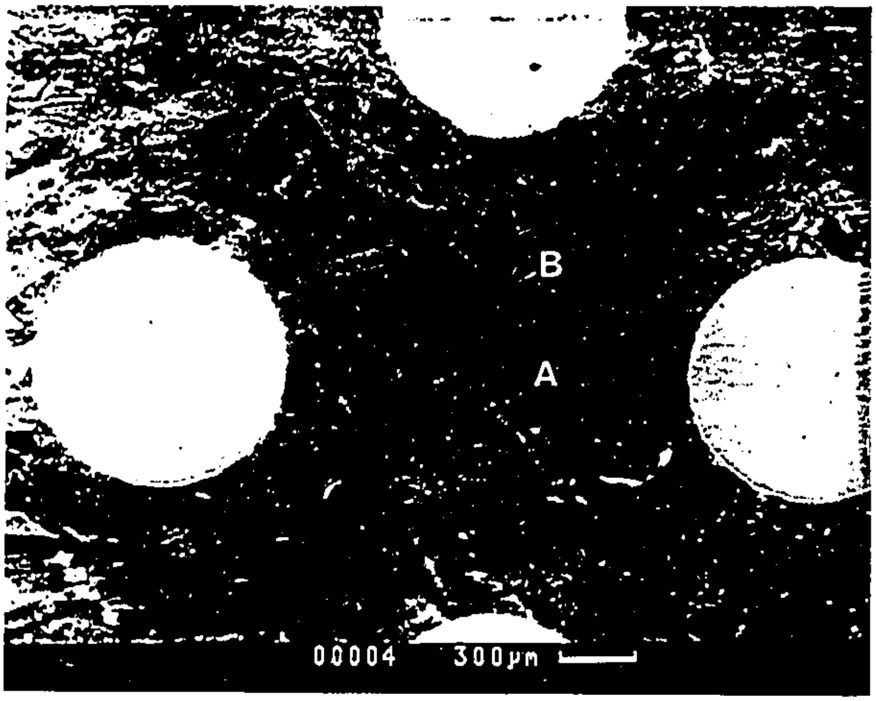

Figure 4.45 - Back-scattered electron image of 20 % volume fraction sample with triangular arrangement of fibres, imposed deformation of 0.3, annealed at 300 °C for 30 min. Note: tungsten fibres are 1 mm dia.

grains in the horizontal regions between fibres such as marked by A in Figure 4.44b. This is much clearer in the secondary electron image shown in Figure 4.45. In order to confirm that these grains were recrystallized grains, backscatter electron channelling images were taken in the region marked A and B in Figure 4.45. Figure 4.46a confirms that the grains in region A are recrystallized due to the presence of sharp image in the channelling contrast micrograph. The poor contrast in Figure 4.46 indicates that the grains in region B are unrecrystallized. This arises due to the disruption in the path of the channelling electrons as a result of the local disruptions in the lattice due to the presence of dislocations.

Figure 4.47 is an optical micrograph of the 30 % volume fraction sample with a triangular arrangement of fibres after a 30 minute anneal at 300 °C (note the sample had received a deformation of 0.3 prior to annealing). The important features of this micrograph are the presence of recrystallized grains in the regions marked "a" and "b" in Figure 4.47. The details of the distribution of recrystallized grains can be seen more clearly in secondary electron image shown in Figure 4.48.

The pattern of recrystallization in the samples with square arrangements of fibres are shown in Figure 4.49. In contrast to the triangular arrangements of fibres which were initially polycrystalline samples, these samples had a large grain size (2-3 mm) prior to deformation. The samples had been deformed by 0.1, then rotated 90° about the fibre axis and deformed another 0.1. It is clear that after recrystallization, large grains are present at the centre of each of the square fibre unit cells.

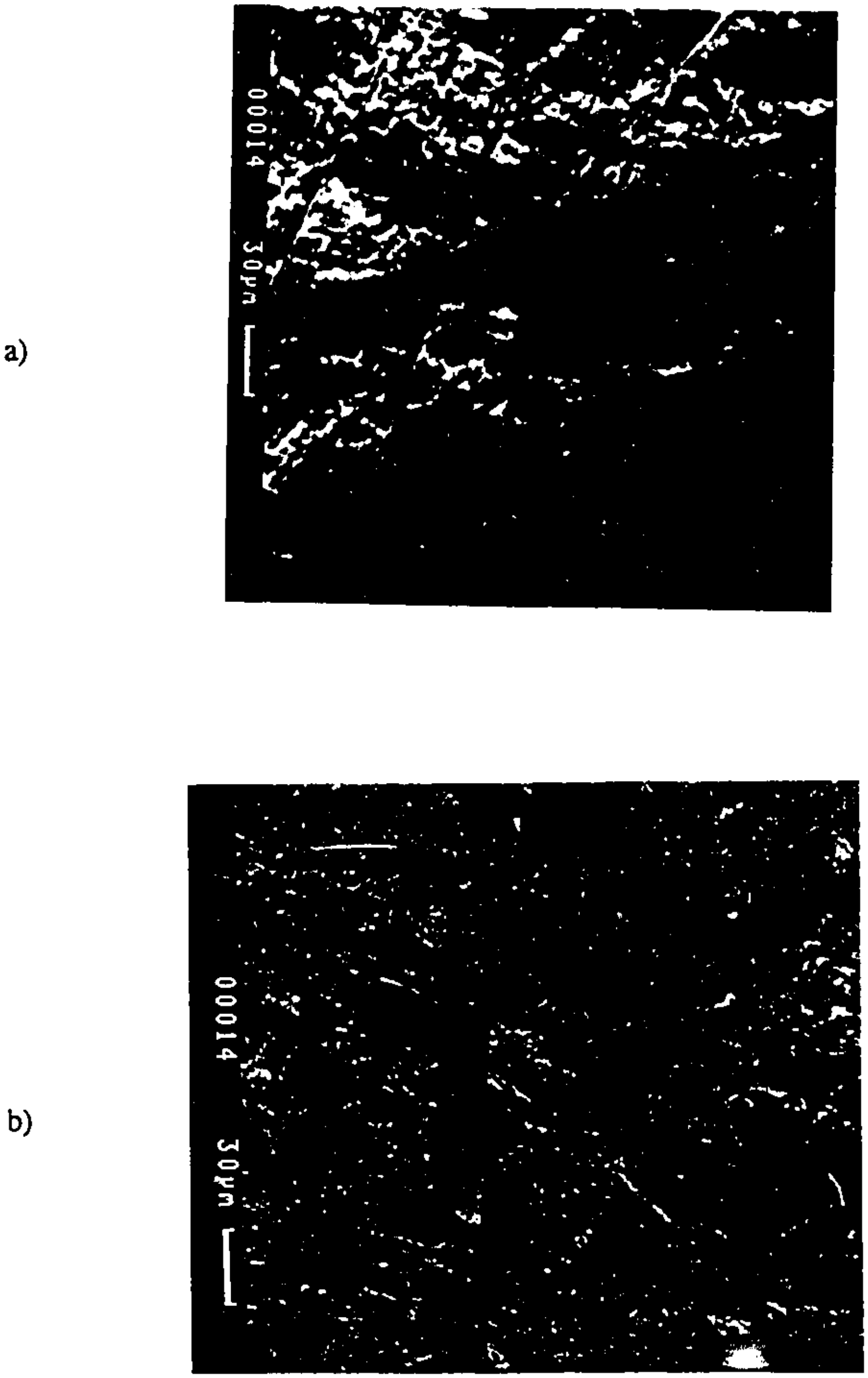

Figure 4.46 - Back-scatter electron channelling patterns for representative regions, a) horizontal between fibres and b) diagonal between fibres. Marked as A and B in Figure 4.45, respectively.

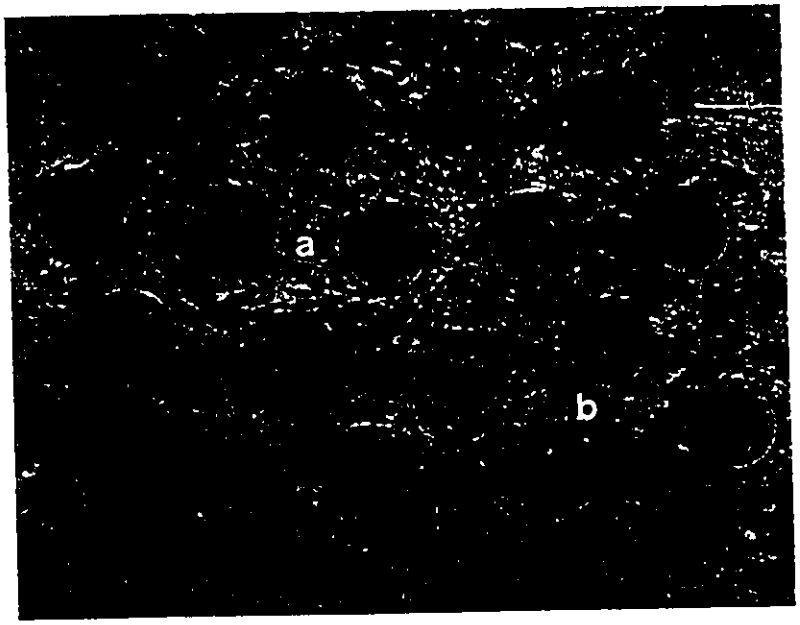

Figure 4.47 - Optical micrograph of 30 % volume fraction sample with triangular arrangement of fibres after 30 min. at 300 °C. Note: tungsten fibres are 1 mm dia.

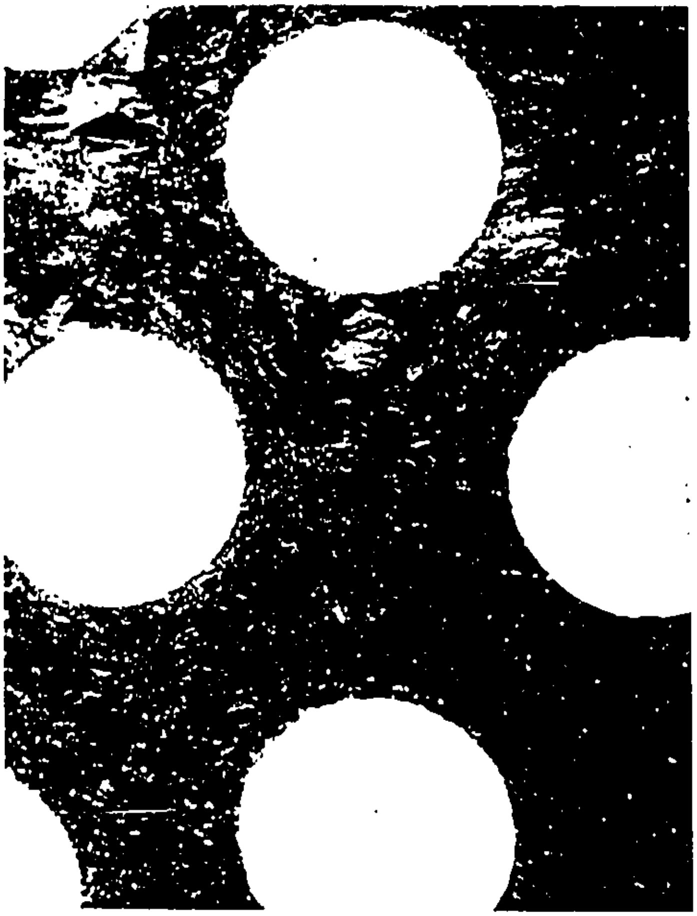

Figure 4.48 - Back-scattered electron image of 30 % volume fraction sample with triangular arrangement of fibres, imposed deformation of 0.2, annealed at 300 °C for 30 min. Note: tungsten fibres are 1 mm dia.

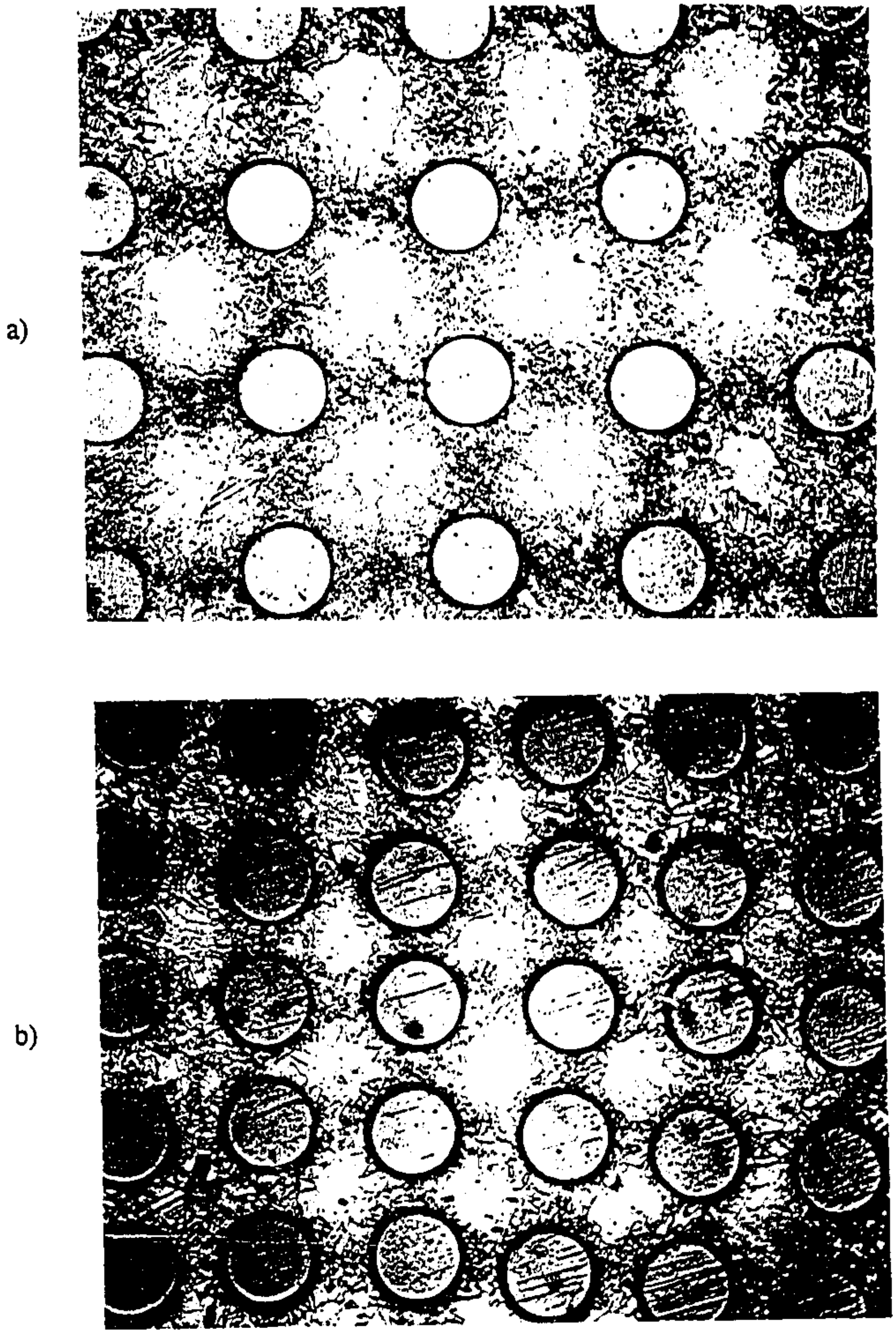

Figure 4.49 - Optical micrographs of samples with square arrangements of fibres after deformation (see text) and annealing at 500 °C, a) 20 % volume fraction and b) 30 % volume fraction. Note: tungsten fibres are 1 mm dia.

4.7 - Summary

A variety of experimental work ranging from measurements of macroscopic deformation behaviour to observations of local recrystallization has been performed. The results from finite element method calculations have been presented with experimental observations where possible. Some of the main results are :

a) the presence of the tungsten fibres causes an increase in the strength of the material.

b) deformation of the sample leads to damage (both fibre failure and interfacial debonding) in the composite.

c) there is a pattern of deformation in the matrix. The flow pattern near the fibres is always similar and the pattern in-between the fibres is a function of the geometric arrangement of fibres.

d) the finite element method calculations predict a large spatial distribution of stresses in the matrix and the fibres.

e) texture development in the matrix appears retarded when compared to the unreinforced material.

f) there is a pattern in the distribution of recrystallization events.

It is the goal of the next chapter to bring together the results from the various experiments and form a consistent understanding of the behaviour of this composite system under this loading path.

CHAPTER 5

DISCUSSION OF RESULTS

5.1 Introduction

This section will present a discussion of the results presented in the previous chapter. The objective of this section will be to describe a physical basis for the experimental results and to present these results in the context of previous work where appropriate.

5.2 - Mechanical Behaviour

The first point to emphasize is that the strengthening effect of the tungsten fibres is strongly dependent on the orientation of the fibres to the loading axis (Chawla, 1987). Figure 5.1 shows a comparison of experimental data for a composite deformed in uniaxial tension with the fibre axes aligned with the loading axis (13 % volume fraction, 250 μm fibres) and a composite with which was deformed in channel die compression with the fibres aligned perpendicular to the loading axis. The yield stress (as defined by 0.2% offset) in the composite with the fibre parallel to the loading axis is a factor of 10 higher than the samples with the fibre perpendicular to the loading axis. These loading paths represent the extremes of continuous fibre composite behaviour. As was pointed out in Section 2.2, the previous experimental work on copper-tungsten composites has been almost exclusively concerned with cases where the fibres are aligned with the

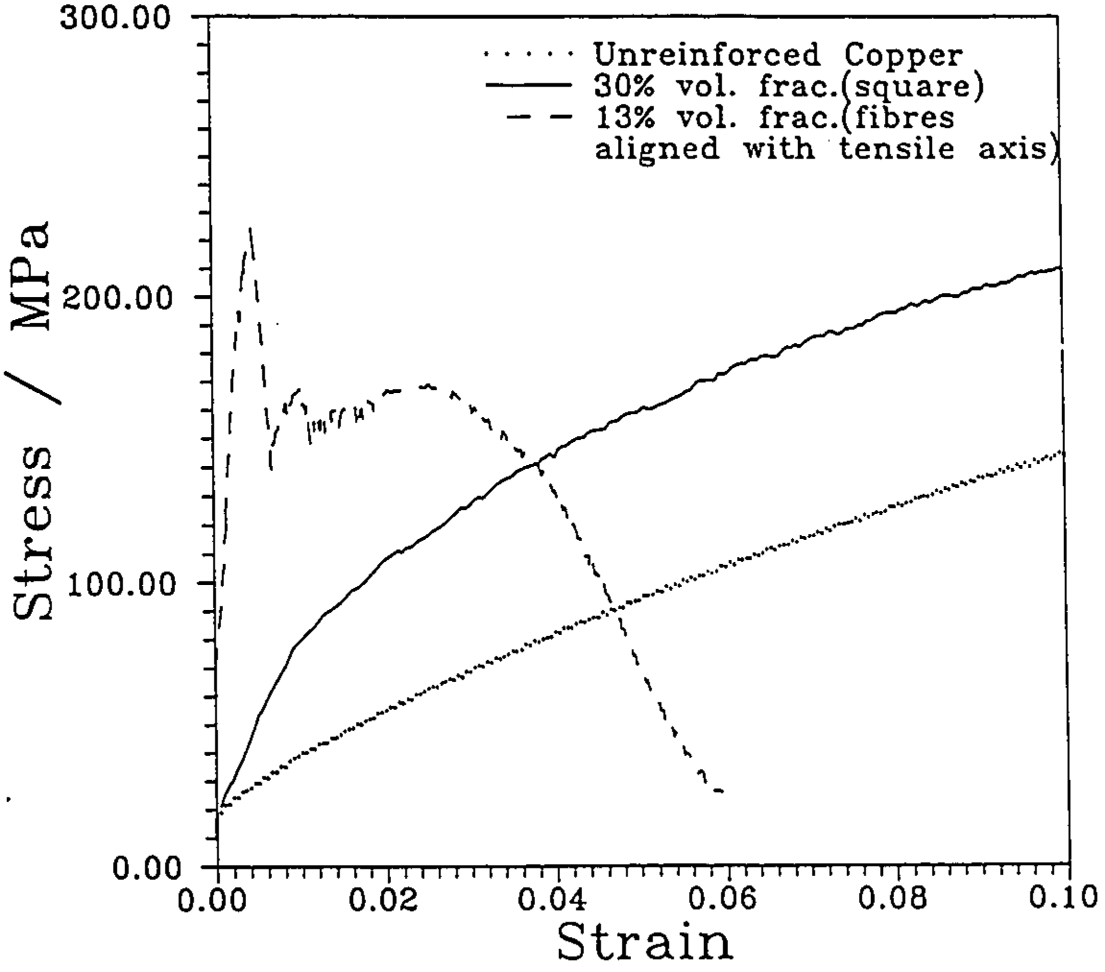

Figure 5.1 - Stress-strain curves for a) unreinforced copper (from channel die compression test) b) 30 % volume fraction tungsten (channel die compression, fibres perpendicular to loading axis), c) uniaxial compression (vol.frac of 13 % 250 μm fibres)

loading axis. The difference in mechanical response for these extremes at low strains has been modelled in detail by Brockenbrough et al. (1991). These authors concluded that the geometric arrangement of fibres had little effect on the behaviour of the composite when loaded parallel to the fibres but was important when the fibres were perpendicular to the loading axis. The present work has considered experimental and modelling studies for the case where the tungsten fibres are perpendicular to the loading axis.

5.2.1 - The effect of fibre volume fraction and spatial arrangement

It was observed in Section 4.2.1 that the stress-strain behaviour of the composite was a function of the volume fraction of reinforcing phase (see Figure 4.2 and Figure 4.5). A simple approach to understanding the effect of volume fraction on the stress-strain behaviour would be to assume that the strain is uniform in the matrix but that level must be modified due to the presence of the non-deforming tungsten fibres (Drucker, 1965). Effectively, this means that the strain in the matrix (i.e. $\epsilon_{corrected}$) is related to the macroscopic strain by:

$$\epsilon_{Corrected} = \frac{\epsilon_{macroscopic}}{(1-f)} \tag{5.1}$$

where:

f - volume fraction of tungsten

Figure 5.2 shows the results of making this correction. The 20 % volume fraction samples with square and triangular arrangements of fibres now show little difference

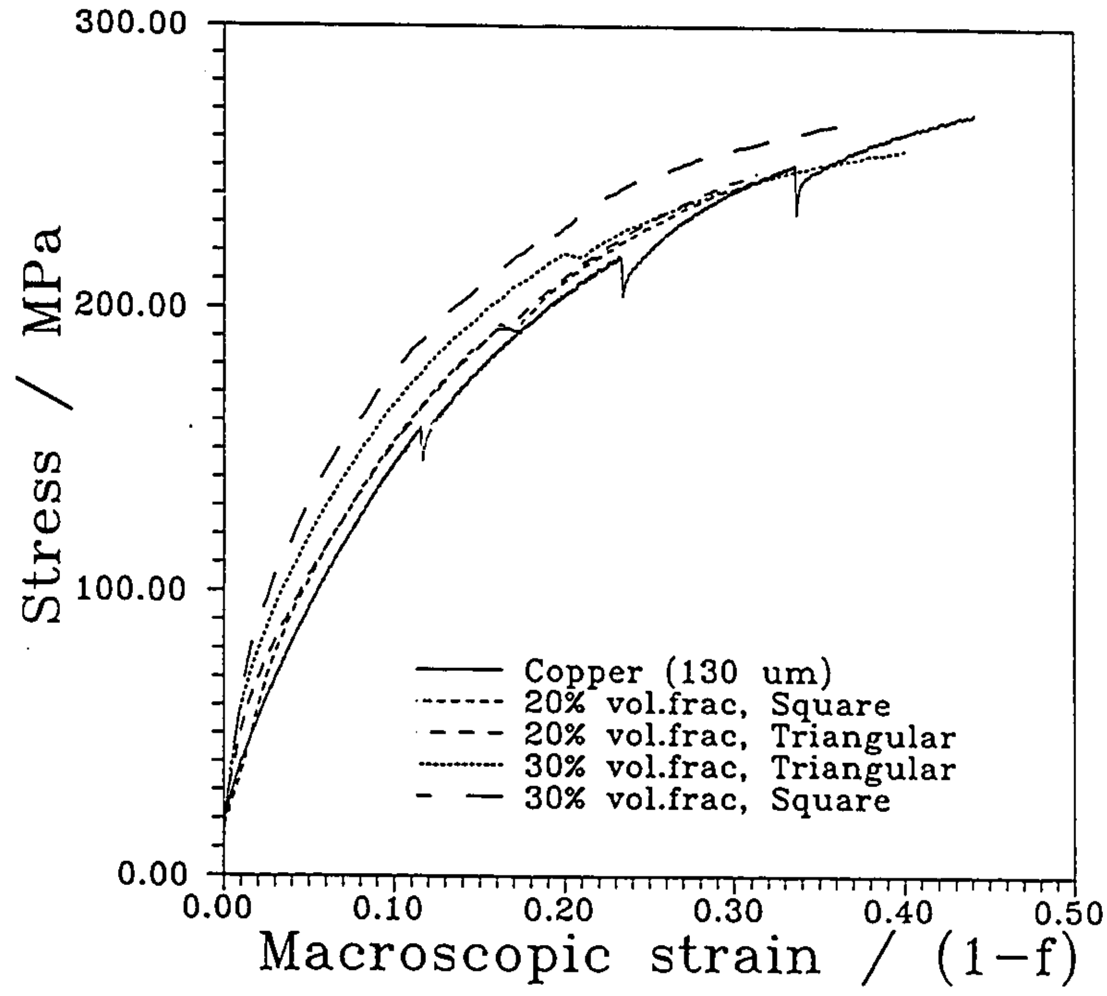

Figure 5.2 - Stress-strain curves corrected for non-deforming tungsten (see text)

from the unreinforced copper. The 30 % volume fraction samples show positive deviations at strains less than 0.2. Above this level, the composite with triangular arrangement of fibres square arrangement of fibres shows little difference from unreinforced copper. However, the 30 % volume fraction composite with square arrangement of fibres shows substantial deviations at all levels of strain.

The fact that this crude approximation works well for the 20 % volume fraction samples and the 30 % volume fraction sample with triangular arrangement of fibres at strains above 0.2 has the following consequences:

i) the level of load transfer to the fibres must be low in these cases since the contribution of the internal stress distribution has been considered

ii) the spatial distribution in the level and type of strain can be represented by an average value

The first point is in agreement with the results from the FEM calculations. For example in Figure 4.29 (i.e. 20 % volume fraction, triangular arrangement, strain of 0.3), the stresses parallel to the loading direction in the matrix are in the range of 227-318 MPa (compressive) while the stresses in the fibres are in the range 272-363 MPa. This observation is also consistent with observation that strain reversals at large plastic strains produced very little effect on the stress-strain behaviour for this material (see Section 4.2.2). The level of stress in the tungsten fibres relative to the matrix is lower than the elastic solution for a single fibre in a infinite medium given in Section 2.2. Upon substitution of the appropriate elastic constants for copper and tungsten, the stress in the fibre is found to be uniform and at a level 2.2 times the far-field stress (i.e. matrix stress away from the particle). It is clear that load transfer in the plastic region is a relatively inefficient process when compared to load transfer in the elastic region. Regarding the effect of the strain distribution on the macroscopic mechanical response, Figure 4.17 shows that there is a very large variation in the local amount of plastic deformation. The von Mises strain varies from below 0.1 to a high of 0.7. Of course, provided there is no damage in the sample the average of the local strains must average to reflect the imposed deformation (corrected for the non-deforming tungsten fibres). The observation that this variation in strain apparently has little effect on the stress-strain behaviour implies that while the local variation in strain is high, either a) the variation in the level of stress is low or b) the distribution of stresses above and below the mean stress tend to cancel each other out. As may be seen in Figure 4.29, the variation in stresses parallel to the loading direction (i.e. σ_{22}) is relatively small. The work-hardening rate in the copper matrix is relatively low at strains above 0.3. As a result, the local stress level varies by a relatively small amount as strain changes (see Figure 4.1). It is also clear in Figure 4.17 that the regions of much lower than average strain and stress adjacent to the particles form a small portion of the matrix material.

For the case of the 30 % volume fraction sample with square arrangement of fibres it was observed that the correction for the volume fraction of non-deforming tungsten fibres did not fully explain the deviation of the stress-strain curve from that of the unreinforced copper. Once again it is useful to look at the strain and stress distribution from the finite element method calculations to understand this effect. Figure 4.26 shows that for this case the variation in local levels of strain is larger than in the case of triangular arrangements of fibres and there are substantial volume fractions of matrix material that have lower that average amounts of deformation. Figure 4.35 shows that the stress distribution in the composite is much more complicated for this case. There are regions in the matrix and in the fibre where the local stresses are much higher than the macroscopic flow stress. The distribution of stresses in the composite is somewhat similar to what one would expect in a fibre composite where the fibres were aligned parallel to the loading axis. There are regions along the vertical columns of tungsten fibres where the stresses are high (i.e. 600-700 MPa) and adjacent to these columns are regions where the stresses are much lower (i.e. 50-200 MPa). It is therefore not surprising that the correction used here fails when there are such strong deviations from the assumptions used in justifying the correction. It is clear that in the case of square arrangements of fibres at 30 % volume fractions, fibre-fibre interactions are beginning to have an important effect on the mechanical response. Figure 5.3 reiterates this by showing that there is a substantial effect of the geometric arrangement of the fibres on the experimental macroscopic stress-strain behaviour for the samples with 30 % volume fraction. This would be in agreement with the general observations of Drucker (1965) who noted that, based on simple continuum plasticity models, plastic constraint factors would start to be noticeable as the volume fraction of the reinforcing phase rose above 30 %. The effect of volume fraction and geometric arrangement of fibres on elastic modulus and low-strain plasticity under similar loading conditions has been modelled by Brockenbrough et al. (1991, see Section 2.3.1). In this work the geometric arrangement of the fibres was found to have a small effect on this behaviour

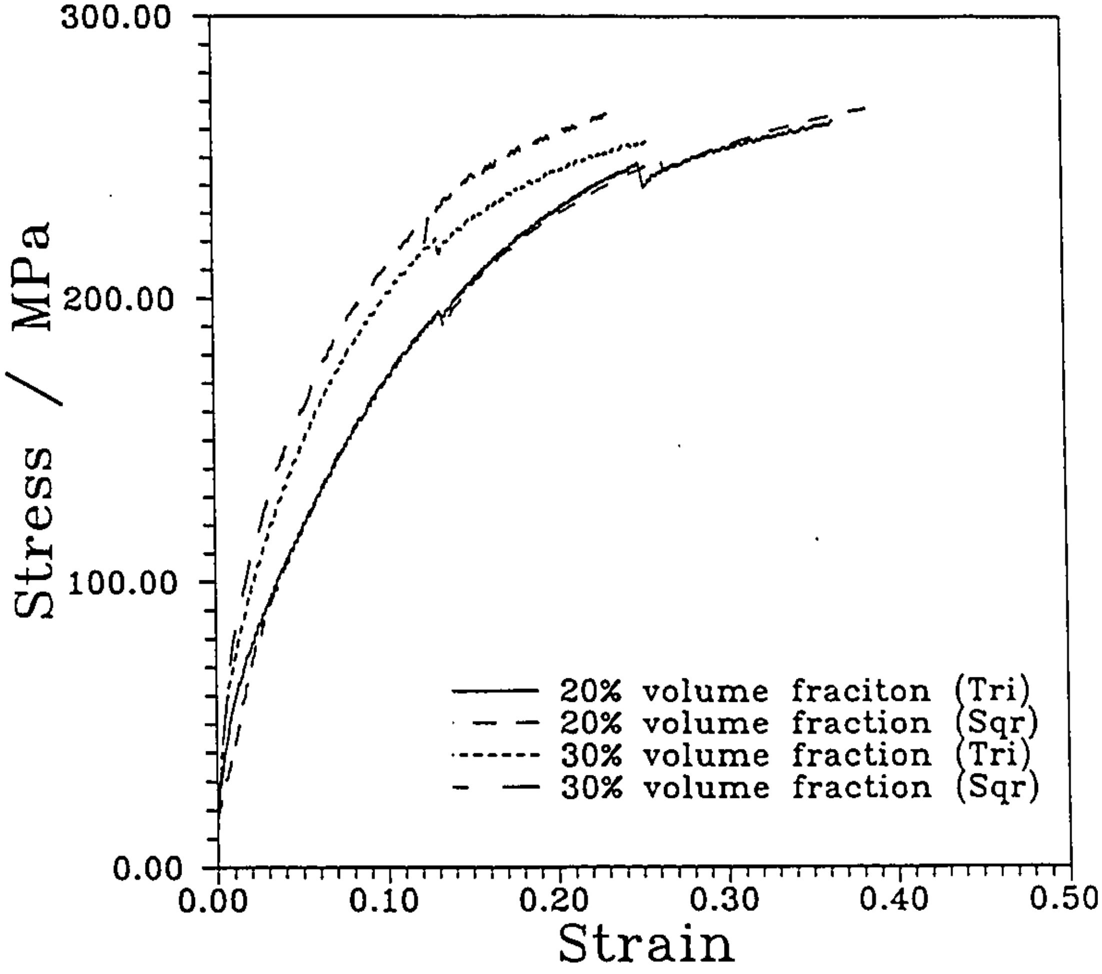

Figure 5.3 - Experimental stress-strain curves for 30 % volume fraction samples with square and triangular arrangements of fibres

at a volume fraction of 20 % but a large effect at a volume fraction of 46 %. This is consistent with the results from the present work.

The mechanical response of the composite can be summarized as follows: i) the level of load transfer to the fibres for samples with 20 % volume fraction is low at large plastic strains, ii) in the absence of substantial load transfer to the fibres the stress-strain response of the composite (after correction for the non-deforming tungsten) is essentially the same as the unreinforced copper and iii) the geometric arrangement of the second phase has an effect on the development of local stresses and local plastic constraint factors in composites with volume fractions greater than 30 %.

5.2.2 - Comparison of experimental and FEM calculated macroscopic behaviour

The macroscopic shape changes of the samples with 20 % volume fraction of tungsten fibres in a square arrangement from the experiment and the FEM calculations can be compared in Figure 4.6 and Figure 4.9. The results are in fair agreement although the experimental shape change is less uniform than the prediction from FEM calculations. This may have arisen due a) to the presence of initial deviations in the fibre arrangement after the processing to refine the grain structure of the matrix or b) local differences in the lubrication conditions in the channel die compression tests. Comparison of the macroscopic shape change for the samples with 30 % volume fraction of fibres with a square arrangement of fibres are shown in Figure 4.7a and Figure 4.10. In this case, the experimental sample and the FEM calculated prediction both show the presence of reverse barrelling. The reverse barrelling arose due to the fact that there is a region of the sample at the top and bottom which has no tungsten fibres present. The absence of tungsten fibres from this regions creates a lower flow stress in this region and the resulting larger deformation.

Figure 4.8 shows a comparison of the macroscopic flow curves from the experiment and calculated from the FEM analysis. As was pointed out in Section 4.2.1, the FEM calculated curves overestimate the stress-strain behaviour at strains above 0.10. This could arise for the following considerations:

i) the presence of damage in the experimental samples

ii) the assumption of isotropic strain hardening in the FEM model

iii) the presence of macroscopic instabilities in the experimental sample

The effect of fracture of the reinforcing phase can have a substantial effect on the load carrying capacity of composites (Hu, 1991). However, the effect of damage (i.e. particle or fibre failure) is strongly dependent on the orientation of the cracks as was described in Section 2.3. In the present work, the cracks in the fibres would be expected to have a small effect on the macroscopic stress-strain behaviour since a) the cracks in the fibres were parallel to the loading axis (see Section 2.3) and b) even after the fibres were cracked the majority of the fibre remained intact as a load carrying member.

The effect of straining path on stress-behaviour of various monolithic materials (i.e. copper, aluminum, iron, etc.) at large strains has been discussed by Gil Sevillano et al. (1981). There are two questions of importance here:

a) how is the strain hardening rate in the matrix (i.e. dislocation storage rate) effected by straining along different paths ?

b) how is the development of texture (i.e. the evolution of the Taylor factor) effected by the straining path ?

Gil Sevillano et al. have concluded that for copper the use of the von Mises equivalent stresses and strains as a method of comparing results from different straining paths gives reasonable agreement. However, Semiatin et al. (1985) have reviewed data (shown in Figure 5.4) that indicate that there can be differences between plane strain compression (i.e. pure shear) and torsion test results (i.e. simple shear) . It is clear in this case that the differences between the different loading paths has a relatively small effect on the flow stress in copper.

The final possible explanation for the differences between the FEM calculated and the experimental stress-strain behaviour is related to formation of macroscopic instabilities in the composites as shown in Figure 4.7. This breakdown in the mechanical stability of the sample was proceeded by cracking of the fibres and then the formation of macroscopic shear bands. It is also accompanied by a drop in the stress carried by the sample (see Figure 4.5). It is apparent that during this process, there is a strong interaction between the presence of damage in the sample and the formation of shear bands. The important factors involved in the process are i) the fracture of the fibres which causes a discontinuous change in the local stress state and ii) at large strains, the work-hardening rate in the matrix relative to the flow stress is low (i.e. above strains of 0.3). A complicated interaction between these two conditions leads to the formation of the observed macroscopic instabilities.

It, therefore, seems likely that the differences in the flow behaviour as predicted

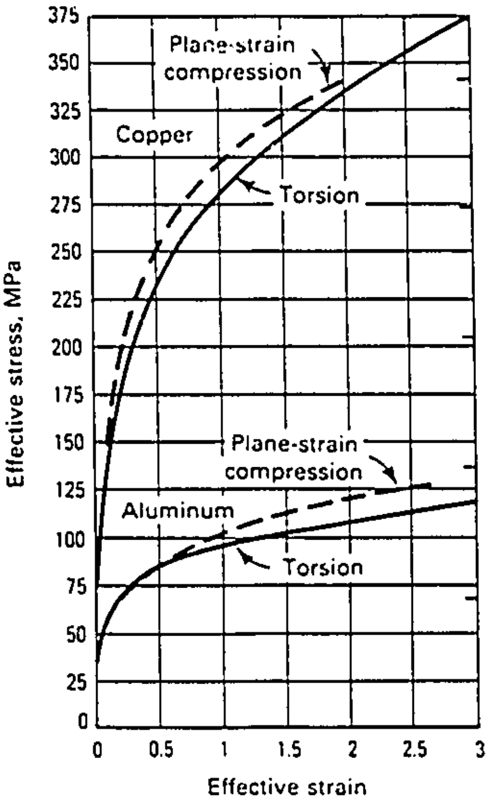

Figure 5.4 - Comparison of stress-strain behaviour from plane strain compression and torsion test (Hodierne, 1962).

by the FEM calculations arises due to the formation of macroscopic instabilities in the sample. These instabilities are a consequence of the presence of fibre damage and the relatively low work-hardening rate in the matrix.

5.3 Damage Observations

The discussion of damage in these composites can be divided into observations of fibre cracking and interfacial debonding. In the first case, the spatial distribution of stresses in the fibre will be important while in the second case the distribution of stresses at the interface is of primary interest. As has been pointed out by Goods and Brown (1979) it would be expected that these processes would be controlled by a criterion involving the maximum tensile stress in the particle or at the interface.

As was described in Section 4.2.2, substantial numbers of fibre failures occur only in the 30 % volume fraction sample with a square arrangement of fibres. This is consistent with the results from the FEM calculations which show that the largest tensile stresses in the fibres are found in this sample (see Figure 4.28 to Figure 4.35 or Table 4.4). However, when discussing fibre cracking it should be re-stated that the mechanical strength of the fibres in the composite was dependent on the processing of the composites during the casting procedure as described in Section 3.2.1. Table 4.1 shows that there is substantial difference in the tensile breaking stress of the fibres (as measured by the diametral compression test on the dissolved tungsten fibres) from the 30 % volume fraction with square and triangular fibres arrangements (i.e. 230 and 324 MPa, respectively). For the 30 % volume fraction sample with square arrangement of fibres, the tensile stress measured by the diametral compression test is close to the predicted stress in the fibre from the FEM calculations (i.e. 230 and 200 MPa respectively). The absence of substantial fibre cracking in the sample with 30 % volume fraction and a triangular arrangement of fibres is consistent with the results that i) the tensile stresses in the fibres (from FEM calculations) are lower than in the case of square arrangements and ii) the tensile failure stress of the tungsten fibres (as measured by diametral compression test) was higher for these fibres (Table 4.1).

Having shown that the cracking of the tungsten fibres is consistent with the prediction from the FEM calculations and the experimental diametral compression tests, the spatial distribution of the cracks must be considered. There is clearly a pattern of fibre cracking as seen in Figure 4.24. It is also apparent that the cracking of the fibres does not necessarily occur at the point of highest tensile stress (see Figure 4.35b). The location of fibre cracks, however, does relate closely to the region in the fibre of lowest hydrostatic pressure (see Figure 4.35d). This would be consistent with the observations of Zok (1988) who noted that the fracture stress of brittle materials was linearly dependent on the magnitude of the hydrostatic stress. This was based on the simple idea that in order to open up a crack (i.e. increase the volume of the sample) work must be done against the external pressure. However, the nature of crack nucleation must be an extremely complicated problem depending on the spatial distribution and shape of flaws in the tungsten as well as the applied stress state.

Figure 5.5 shows a secondary electron image of a fibre from the 30 % volume fraction sample with square arrangement of fibres after dissolving the matrix in nitric

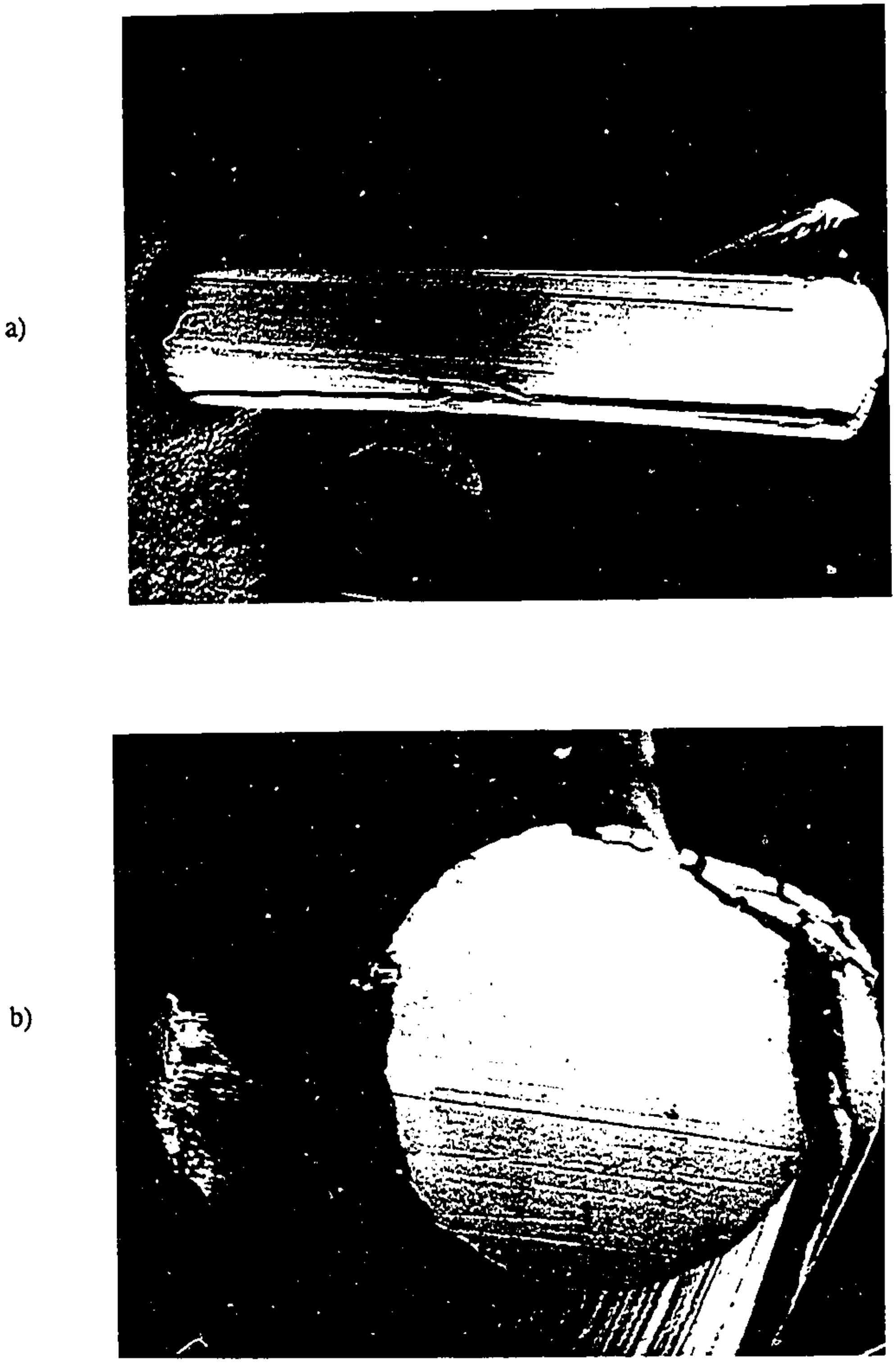

Figure 5.5 - Secondary electron images of cracks in fibres dissolved from matrix

acid. This is a representative example of the types of failure observed in the fibres after removal of the matrix material. In some case the cracks in the fibres extended throughout the entire length of the sample while other cracks traversed only a part of the length of the fibre. This observation would seem to indicate that the crack was initiated at the surface of the fibre adjacent to the channel die wall and then propagated along the length of the fibre. It would be expected that since there may be local deviations from plane strain conditions on the surface of the sample adjacent to the channel die wall, the stress state would also be somewhat different than in the interior of the sample (i.e. less constrained). This leads to more favourable conditions for nucleation of cracks at the surface.

The process of damage accumulation can also be followed in this sample (i.e. 30 % vol. frac, square arrangement of fibres). The level of the tensile stress in the fibre rises as the macroscopic strain is increased (see Table 4.4) and as a result there are a higher number of fibre failures as reported in Section 4.2.2. As was pointed out in the previous section, the process of damage accumulation can lead to macroscopic instabilities in the deformation pattern. Another interesting phenomenon can be seen in Figure 4.7d (marked by A) where as the deformation proceeds after a crack has formed the displacement of the crack opening is increased and at a certain point matrix material will start to be extruded into the cracked region. Ultimately, this process of matrix extrusion into the crack opening may effectively heal the particle fracture. This process has been described (Brechet et al., 1992) in a particulate reinforced aluminum composite deformed in tension under large hydrostatic pressure.

The presence of interfacial debonding after deformation is evident in Figure 4.4. Interfacial debonding has occurred in this sample due to lack of particle cracking which has occurred in this sample due to its higher fracture stress as measured by the diametral compression tests (i.e. $\sigma_{fracture}$ = 324 MPa). It is difficult to directly observe the normal stresses at the fibre-matrix interface due to the co-ordinate system used to display these results. It is certain however, that the region where interfacial debonding has occurred is an area where high tensile stresses in the horizontal direction are present (see Figure 4.35). A close examination of Figure 5.6 also indicates that the tensile stresses are largest for the fibres adjacent to the surface. This is in agreement with the experimental observations of the spatial distribution of debonding events in Figure 4.4. The observation that the tensile stresses are higher adjacent to the surface is a result of the boundary conditions present in the sample. This is a similar effect to the one described in Section 5.2.2 to explain the observations of reverse barrelling in the deformed samples. Figure 5.7 is an example of situation where the debond has not fully developed when the deformation was stopped. It is clear in this micrograph where the debonding is initiated and how it grows.

The damage observations in the present work can be summarized as follows. As the sample is deformed, the stresses in the tungsten fibres and at the interface rise due to work-hardening of the matrix. The detailed distribution of these stresses is a function of the volume fraction and geometric arrangement of the fibres. As the stresses rise in the particles, alternatives processes such as interfacial debonding or fibre cracking may intervene to lower the stresses in the particle (i.e. whichever process can occur at a lower

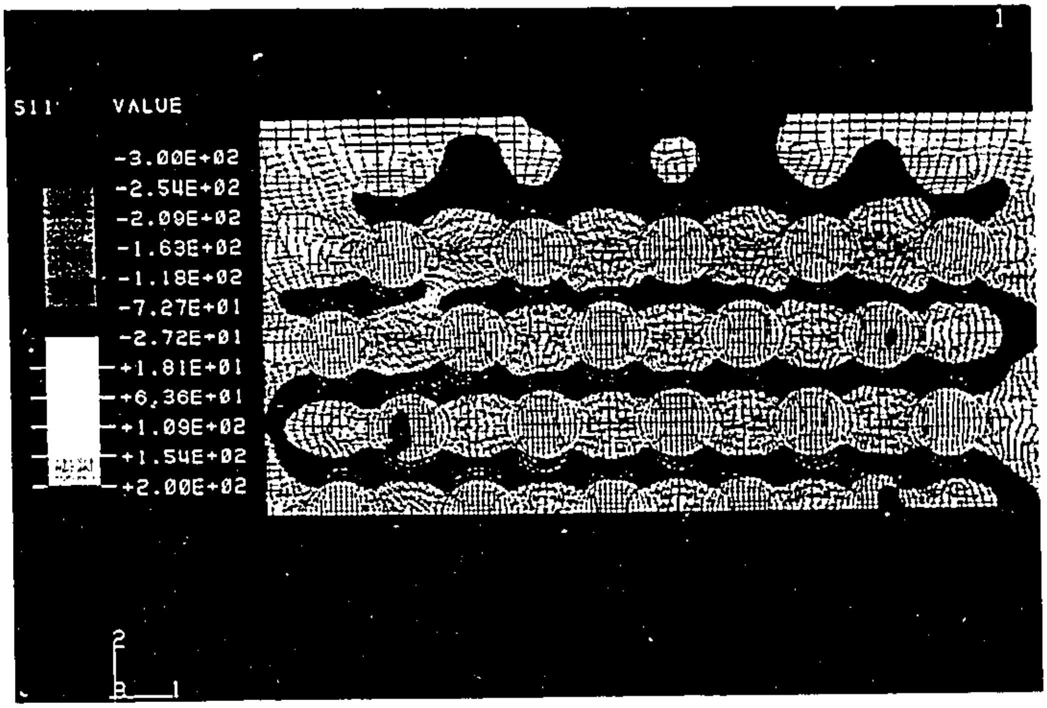

Figure 5.6 - FEM calculated distribution of horizontal stresses for 30 % volume fraction sample with triangular arrangement of fibres for an imposed deformation of 0.1.

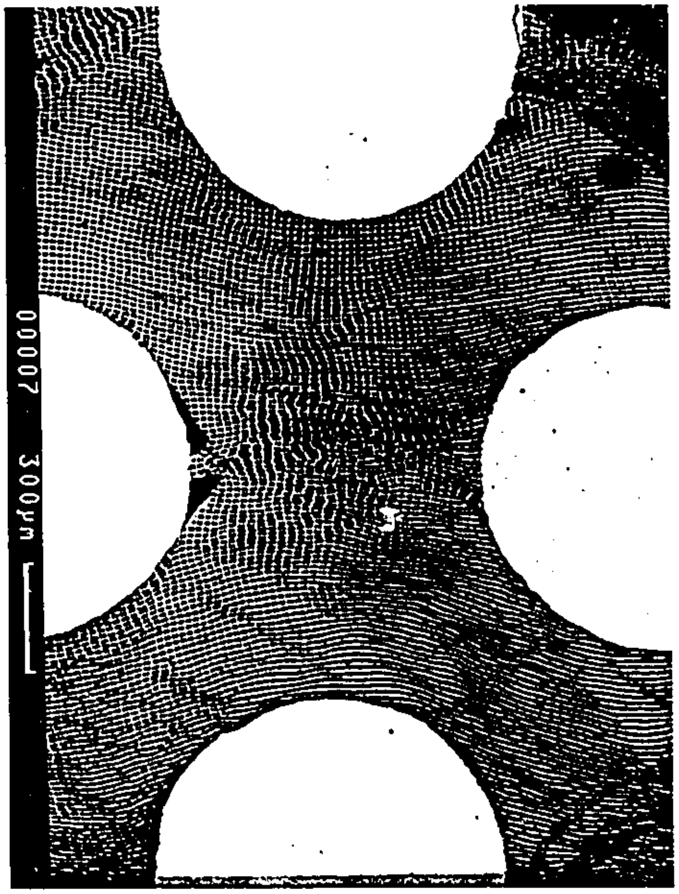

Figure 5.7 - Back-scattered electron image showing initiation of debonding event

stress). These processes are controlled by maximum tensile stresses (and perhaps hydrostatic pressure in the case of fibre cracking). The accumulation of damage events may then lead to a formation of macroscopic instabilities in the composite and reduction in the load carrying capacity of the composite.

5.4 Pattern of Deformation in the Matrix

As was observed in the Section 4.3, there is a clear pattern of non-uniform deformation in the matrix of the composite as a function of the applied deformation. Very good agreement was observed between the experimental measurements and the finite element method predictions of the local strain distribution (as measured by the scalar quantity of von Mises strain). The behaviour of the matrix can be summarized by two observations. First, there is region adjacent to the tungsten fibres extending a distance of approximately 1.1 times the fibre diameter where the deformation pattern is dominated by interactions between the matrix and the fibre (i.e. high levels of constraint in the matrix). The behaviour of the material in this region is common for all composites studied in this work. The second type of behaviour in the matrix encompasses the remainder of the matrix. It is important to consider the nature of the pattern of deformation in this region and how this is related to the geometric arrangement of the fibres.

The pattern of deformation in the matrix is controlled by the development of an kinematically admissible velocity field in the matrix. A simple approach to understanding the observed flow pattern for the square and triangular arrangements of fibres is shown in Figure 5.8a and b. The requirement made here is that as the sample

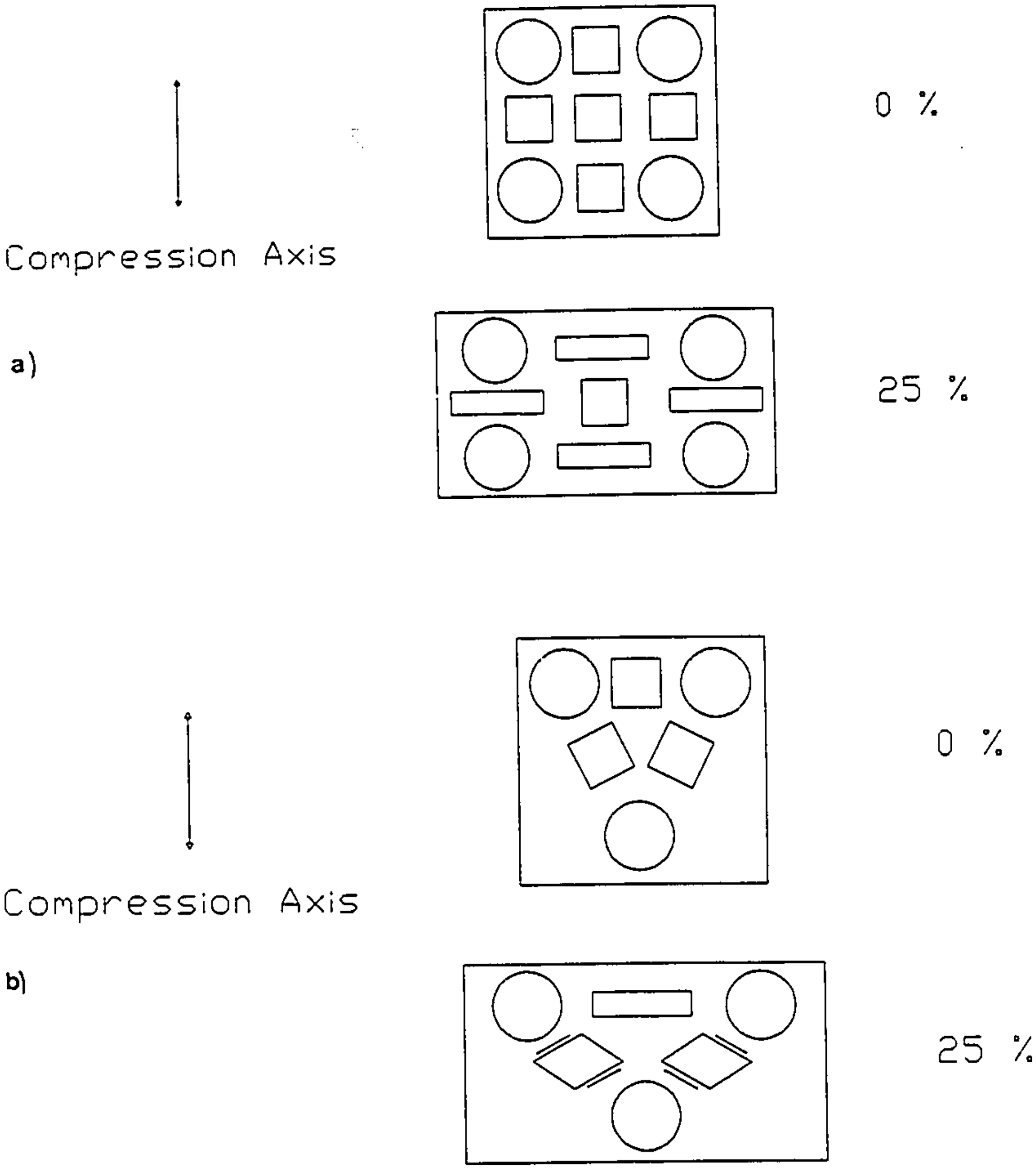

Figure 5.8 - Schematic diagram illustrating the matrix flow behaviour in samples with a) square and b) triangular arrangements of fibres.

deforms the tungsten fibres must translate in a manner to reflect the macroscopically imposed deformation.

For the square arrangement of fibres shown in Figure 5.8a, it may be seen that in order for continuity to be maintained in the sample three representative types of behaviour develop. In the region along the horizontal between fibres (marked by D) and the region along the vertical between the fibres (marked by E) the initially square element has been deformed in a manner similar to the applied strain but of a larger magnitude. This is a direct result of the presence of non-deforming fibres and to a first approximation the strain in this region could be obtained by assuming that the total horizontal displacement occurs in the region between the fibres. Invoking this assumption and the definition of strain, one obtains the following relationship:

$$\epsilon_{local} = \ln\left[\frac{(s_o+2r)\exp(\epsilon_{farfield})-2r}{s_o}\right] \qquad (5.4)$$

where:

s_o= inter-fibre spacing along horizontal or vertical between fibres
r= fibre radius
$\epsilon_{far\text{-}field}$= far-field applied strain

Using this formula and converting to von Mises equivalent strain, the strain in these regions for the 30 % volume fraction sample would be 0.31 or 0.59 for far-field applied strain of 0.1 and 0.2 respectively. This is in reasonable agreement with the values from the experimental and FEM calculations shown in shown in Table 4.3. Figure 5.8 also shows that the region at the centre of the fibres (marked F) will undergo a small amount of deformation in agreement with the results from the experiments and FEM calculations

In the case of triangular arrangement of fibres a more complicated pattern of deformation in the matrix is imposed by the presence of the fibres. The amplification of strain along the horizontal between particles (marked D in Figure 5.8) is a similar effect to that for the samples with a square arrangement of fibres. Once again a simple approach would expect the local strain to be related to the macroscopic strain by Eqn. 5.1. However, the region along the diagonal between the fibres (marked E) has a complicated mode of deformation. It consists of shear strains and rigid body rotations as shown schematically in Figure 5.8. This may also be seen in the finite element method calculations, if individual components of the strain tensor are plotted as in Figure 5.9. These observations are especially important because a consideration of a scalar parameter such as von Mises strain would not be sufficient to describe the material behaviour in these regions.

It is apparent that a relatively simple argument based on geometric considerations of macroscopic shape change required during deformation can produce a physically sound basis for the observations of the pattern of flow in the matrix. It is also clear that scalar representations of deformation (i.e. von Mises equivalent strain) do not provide a complete description of the matrix behaviour.

5.5 Texture Development

The observations of weaker deformation textures in the composite than in the unreinforced copper described in Section 4.5 are consistent with experimental results from other researchers described in Section 2.5. Qualitative agreement is observed

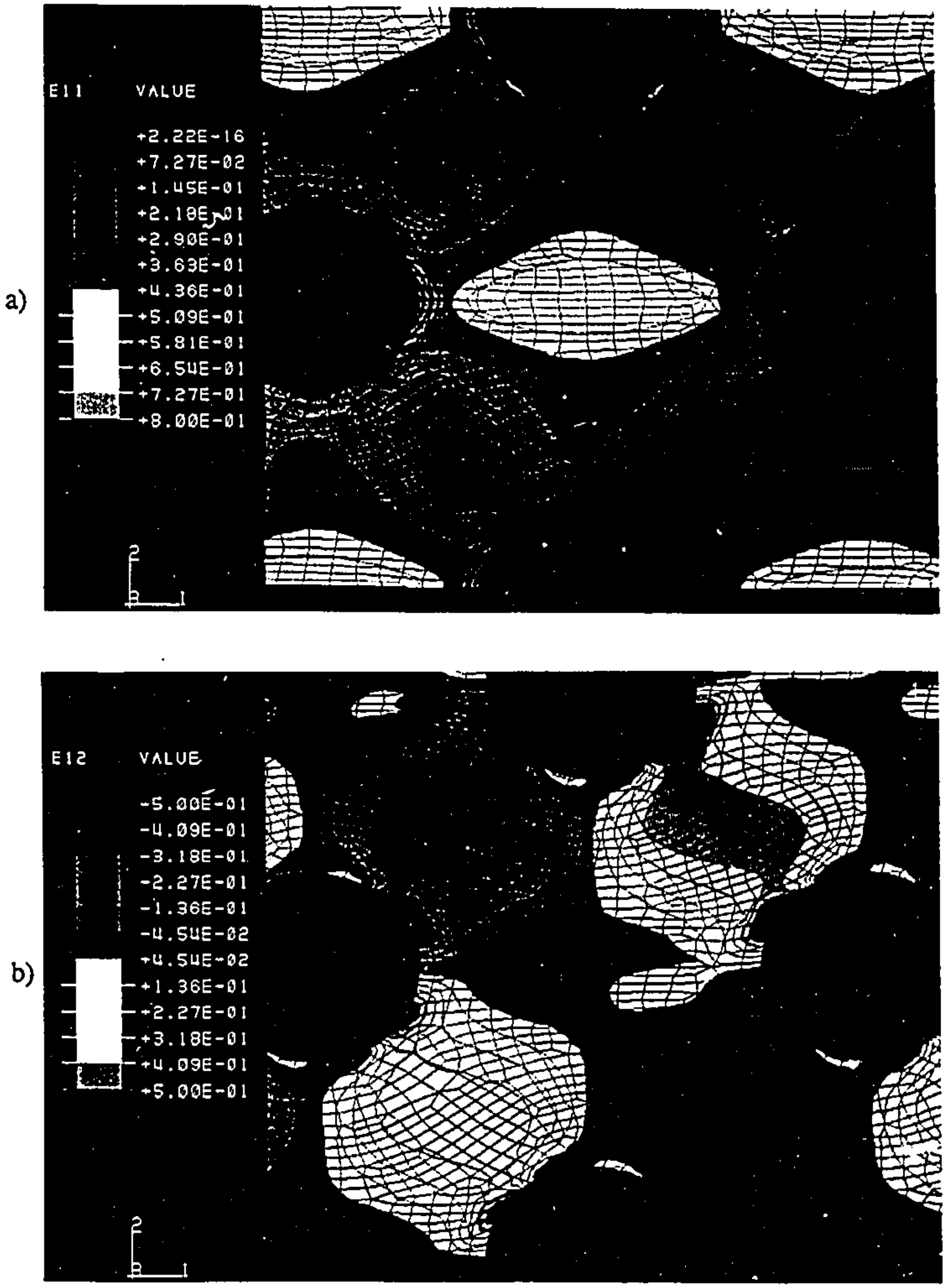

Figure 5.9 - Finite Element Method Calculations of a) ϵ_{11} and b) ϵ_{12} for 20 % volume fraction sample with triangular arrangement of fibres for an imposed deformation of 0.3.

between the experimental measurements and the predictions of Bolmaro et al. As was pointed out in Section 4.5, the predicted textures appear stronger than the experimentally determined textures. Two possible reasons for this are: i) although the local texture development was examined at many points in the matrix, the final predicted texture was a summation from only two representative points. Due to the local variations in strain and strain path, averaging over many points would have had the effect of producing a weaker texture. ii) texture simulation programs such as LApp are known to overestimate the sharpness of deformation textures .

The presence of a cube texture component in the experimental pole figure taken from the diagonal section (i.e. Figure 4.40) is interesting. This texture component has not been observed in deformed copper. It is, therefore, likely that this is a remnant from the recrystallization process. This would suggest that the texture produced upon recrystallization is a function of the local strain path. This was not pursued in this work but would certainly be of interest for future work.

While texture development in the samples with higher volume fractions and different geometric arrangements of fibres was not examined in detail by Bolmaro et al., it would be expected that the same general explanation for the retardation of texture development could be given. That is, a global texture measurement (i.e. by x-rays or neutrons) is an average of the local textures in the sample. As a result of averaging local textures (which may be weaker or stronger than the texture expected in a monolithic material) a weaker texture will be observed. For example, in the case where the fibres are arranged in a square arrangement, the global texture would be the sum of textures produced in regions of higher than average deformation and regions of very little deformation (i.e. regions D and E and region F in Figure 4.26, respectively).

Having obtained a good understanding of texture development in these composites, an important question arises as to whether or not the scale of the structure in these samples (viz. grain size to particle diameter) has a strong effect on the process of texture development. This is important since most commercial composite have grains sizes of the order of the particle diameter whereas the composite investigated here has a particle diameter to grain size ratio between 5:1 and 10:1. It is likely that as long as the matrix material is not highly plastically anisotropic (i.e. as might be expected in hexagonal materials), the flow pattern in the matrix will be similar to what was observed in this work. This can be validated to some extent (at least for very large grain sizes and particles) by the preliminary observations of the deformation pattern found during the initial deformations which were conducted to refine the grain size of the matrix. In the case of the square arrangements of fibres, it was clear that since there was no change in the surface roughness of the matrix at the centre of the four fibres little or no deformation had occurred in this region. The observation that the pattern of deformation was similar for these samples will be further discussed in the following section on recrystallization behaviour.

In summarizing this section, it is useful to reiterate the following points: i) the experimental observations of texture development in these composites under these loading conditions are in qualitative agreement with the predictions of Bolmaro et al. composites ii) the general ideas proposed by Bolmaro et al. can be extrapolated to other geometries particularly if the flow patterns for these cases are known and iii) it is believed that the essential idea that texture development is controlled by the local flow pattern in the matrix can be extended in certain cases to situations where the grain size is similar to the particle size (provided neither is of the order where dislocation-particle interactions dominate).

5.6 Recrystallization Behaviour

The observations of matrix microstructure after annealing described in Section 4.6 clearly indicated that the distribution of recrystallization events was related to the pattern of deformation. This pattern is reflects the local variations in the nature of the deformed state. In considering the transition from the deformed state to the recrystallized state, two structural elements are necessary: i.e. a) a sufficient level of global stored energy and b) the presence of high angle boundaries capable of subsequent migration (Embury, 1992). The role of stored energy has been examined by many investigators (for a comprehensive review, see Bever et al., 1973). However, the formation of nuclei for recrystallization is a more complicated problem. Doherty (1980) has pointed out that the mobility of high angle boundaries is greater than low-angle boundaries. The mobility of these boundaries is also strongly dependent on impurity content. The outstanding problem is to understand how large lattice misorientations develop during the deformation process. Recent advances in the ability to characterize the deformed structure by electron back-scattered channelling patterns are allowing new insights to be gained in this problem (Hjelen and Nes, 1986). The ability to characterize the local substructure as it relates to the formation of recrystallization nuclei (i.e. mobile boundaries) is a difficult problem even in the case of monolithic materials due to low density of subgrains which participate as recrystallization nuclei.

In order to examine the role of stored energy, the distribution of stored energy was plotted from the finite element calculations for the distribution of von Mises equivalent stress. This plot was constructed using the assumption that the local stored energy would be proportional to the square of the local flow stress. This is justified on the basis that the flow stress is related to dislocation density (Basinski and Basinski, (1979) by:

$$\sigma = \alpha\mu b\sqrt{\rho} \tag{5.5}$$

and that the stored energy will given by (Bever et al., 1973):

$$stored\ energy = \frac{\rho\mu b^2}{2}\ln\frac{R}{r_o} \tag{5.6}$$

where:

R - outer cutoff radius
r_o - inner cutoff radius

Substitution of equation 5.3 into 5.4 yields a relationship where the stored energy is proportional to the square of the flow stress. Using these assumptions, the distribution of stored energy for the 20 % volume fraction samples with triangular arrangement of fibres after an imposed deformation of 0.3 is shown in Figure 5.10. When this is compared with the micrograph of the partially recrystallized sample shown in Figure 4.45, it is clear that the majority of the recrystallization events have occurred in

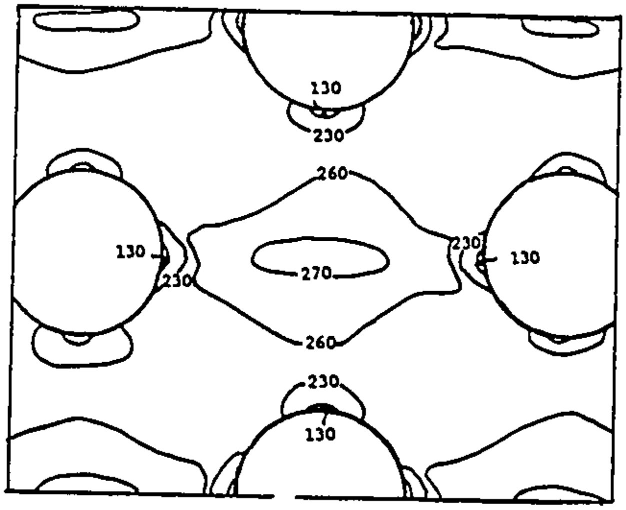

Figure 5.10 - Contour plot illustrating the local distribution of stored energy for 20 % volume fraction sample with triangular arrangement of fibres for imposed deformation of 0.3.

the region of the matrix which has the highest levels of stored energy.

In principle, the nature of the deformed state should be a function of the level of strain, strain path, strain rate and temperature. Bever et al. (1973) have reviewed the effects of these parameters on the stored energy of cold work. These authors concluded that the role of strain path has not been examined in sufficient detail. It would be expected that changes in strain path could affect both the local storage of energy and the formation of high angle boundaries. This effect could be examined in further detail with the present composite system since, as was noted in Section 5.4, regions of high shear strains and rigid body rotation exist adjacent to regions of normal strain.

A particularly effective site for nucleation of recrystallization events is at shear bands in the deformed structure (Doherty, 1980). A good example of this effect was observed in the present work. Figure 5.11a is a back-scattered electron image of the deformed grid for the 30 % volume fraction samples with triangular arrangements of fibres after a deformation of 0.3 illustrating the presence of shear bands in the diagonal regions of the matrix between fibres. In Figure 5.11b, it can be observed that these shear bands have acted as potent sites for nucleation of recrystallization events.

It is worth emphasizing that the recrystallization behaviour of the current copper-tungsten composites materials is very different from the results of Humphreys and co-workers described in Section 2.6. In their work, the initiation of recrystallization events was observed adjacent to the second-phase particle due to development of large lattice rotations near the particle. In the present work, it is clear that the majority of recrystallization events occur in the regions between the tungsten fibres (for example, see

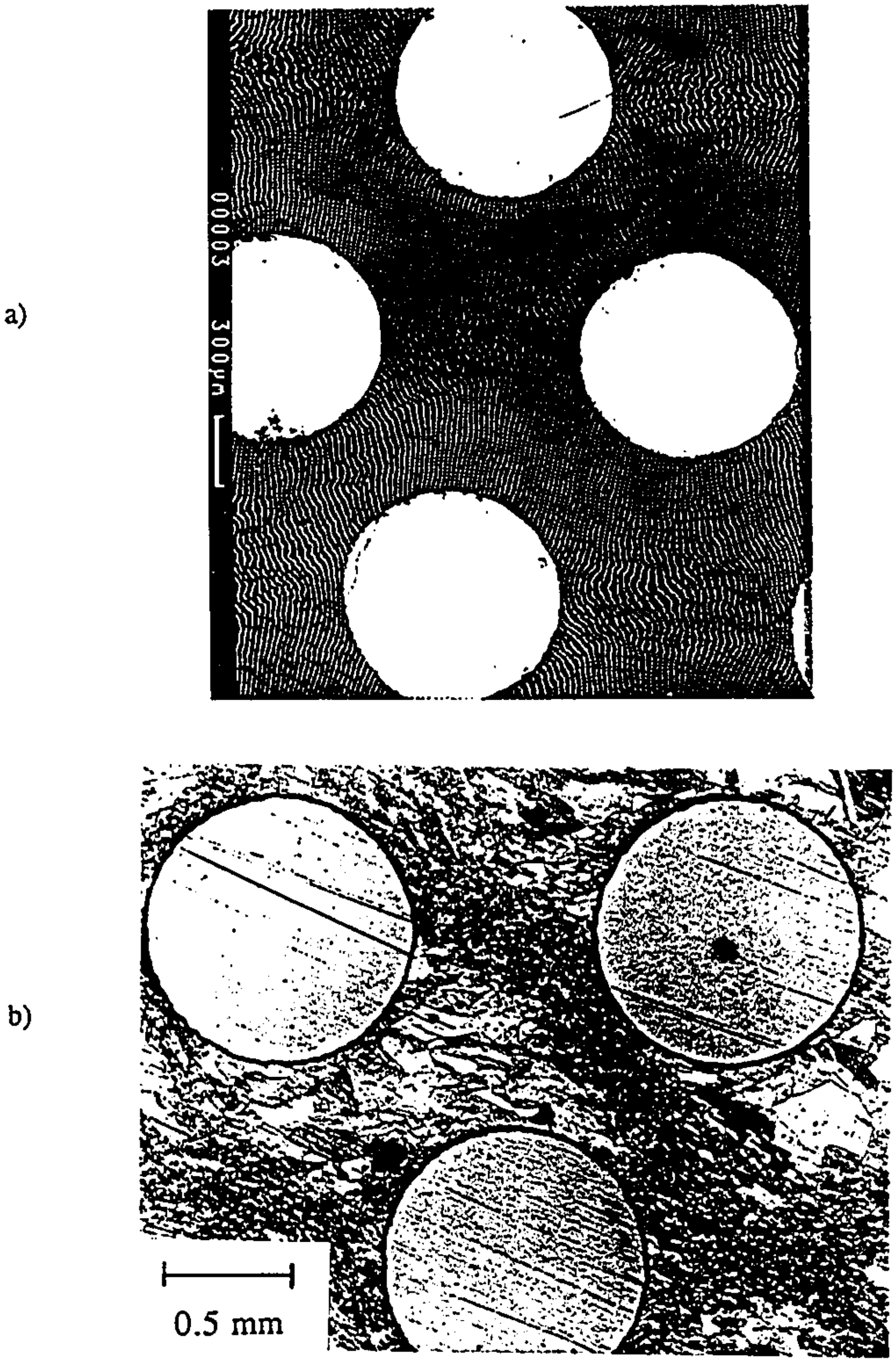

Figure 5.11 - a) Backscattered electron image of deformed gold grid showing presence of shear bands (30 % vol.frac. sample) for strain of 0.3, b) optical micrograph of recrystallized grains where shear bands were present (300 °C for 30 min.).

Figure 4.45). This arises due to the difference in scale of the two materials. In the work of Humphreys, the grain size is much larger than the particle diameter and the nucleation process is related to local storage of dislocations around the second-phase particle (i.e. the development of large misorientations in the matrix near the particle, e.g. Herbst and Huber, 1978). As a result of relationship between the size of the particles and the grain size, the effect of an individual particle effects only a small volume within a grain. In the present work, the grain size of the matrix is much smaller than the fibre diameter, thus the deformation of many grains are affected by each fibre. In this case, the pattern of recrystallization events is dominated by the deformation pattern in the matrix. It is also clear that the probability of creating a suitable nucleus for recrystallization would be related to the volume of material sampled. In this way, the copper tungsten samples are able to produce many more nuclei than in dispersion hardened system, for example.

The question of grain growth in composite materials is also one of scale. There are limits of grain growth in monolithic materials due to the reduction in driving force for the process as the level of curvature decreases (i.e. as the grains become larger). In this work this is dominant effect. However, in the case of the systems studied by Humphreys the inter-particle spacings are small so that the dragging effects of the particles on the migrating boundaries becomes important.

This leads to the question of how relevant the present results are to the recrystallization behaviour in metal matrix composites of commercial interest. This is a difficult question since materials such as Al-SiC$_p$ composites represent a class of materials that are on the borderline between continuum and dislocation models. It would be therefore, worthwhile to conduct a detailed analysis (including metallographic and transmission electron microscopy) of the recrystallization behaviour of these materials.

5.7 Summary

In this section, both global behaviour such as mechanical behaviour and texture development and local behaviour such as damage observations and recrystallization behaviour have been discussed. It is clear that a detailed understanding of the local behaviour can be used to understand macroscopic observations.

The next section will summarize some of the important conclusion of the present work and make suggestions for future work.

CHAPTER 6

CONCLUSIONS AND FUTURE WORK

6.1 - Conclusions

The purpose of this study was to examine the influence of fibre spacing and fibre arrangement on the deformation behaviour of a model composite. The model composite, fabricated from copper and tungsten fibres, was deformed to large strains in plane strain compression with the fibres perpendicular to the loading axis (i.e. in the direction of zero strain).

One of the main conclusions which may be drawn from the present work is that the flow pattern in the matrix is controlled by spacing and distribution of the reinforcing fibres. A kinematically admissible deformation pattern in the matrix must be maintained during the deformation process and this pattern is enforced by the geometric arrangement of the tungsten fibres. As a result of these compatibility considerations, simple geometric arguments can be made to give qualitative descriptions of the flow pattern. The essence of this problem would not have been elucidated by a consideration of a single fibre problem.

The comparisons between the experimental and finite element method calculations were good. The FEM calculations were validated by i) comparison of local strain measurements, ii) the macroscopic shape change of the sample during deformation, iii) the stress-strain behaviour of the composite and iv) the comparison of stress-distribution in the fibres and observations of fibre failure.

The stress-strain behaviour of the composite was found to be dependent on the volume fraction and spatial arrangement of fibres. At a volume fraction of 20 %, it was observed that the stress-strain curves when corrected for the volume fraction of non-deforming tungsten fibres were essentially the same as in the unreinforced copper. This implies that the level of load transfer to the fibres and the geometric arrangement of the fibres are not a significant factors in the strengthening of these composites. For the samples with a volume fraction of 30 %, the geometric arrangement of the fibres had an effect on the stress-strain behaviour and the correction for the non-deforming tungsten fibres was insufficient to explain the difference between the composite and the unreinforced copper. At these volume fractions, the level of load transfer to the fibres and plastic constraint in the matrix are beginning to have a significant dependence on the geometric arrangement of the fibres and the interactions between fibres. However, the load transfer process is still much less effective than for the case of loading parallel to the fibres.

As the stresses in the fibre and at the interface between the fibre and the matrix rose during deformation, alternative processes such as fibre cracking and interfacial decohesion intervened to relieve the local stresses. These processes were found to be controlled by a maximum tensile stress criterion. There was also some evidence that the distribution of hydrostatic pressure in the fibre had an effect on the fibre cracking process. The process which occurred was the one with the lowest critical stress. The intervention of alternative processes had important consequences for the stress-strain behaviour of the composite. The interaction between damage events and the local reduction in the work-hardening rate relative to the flow stress led to macroscopic instabilities in the sample and a resulting drop in the load carrying capacity of the composite.

Having obtained a qualitative and quantitative characterization of the flow pattern in the matrix it is possible to make some conclusions about texture development in the matrix. The experimental observation of weaker deformation textures in the composites arises from an averaging of the local deformation textures. While local textures are sometimes weaker or sometimes stronger than would be expected in the unreinforced material, the process of summing local textures leads to reduction in the global texture measurement as predicted by Bolmaro et al. (1993). While the details of the local flow pattern would be different for other particle shapes and straining paths such uniaxial compression of composites reinforced with particulates, a similar weakening of measurement of global texture development would be expected due to the summation of various local texture components.

From the observations of the recrystallized structures in the composites, it was clear that the flow pattern in the matrix had an important effect on subsequent recrystallization events. In the case of the samples with square arrangements of tungsten fibres, the low level of deformation (and resulting low level of stored energy) for the matrix region in the centre of the unit cell is not sufficient for the recrystallization process to proceed even at higher temperatures. For the samples with triangular arrangements of fibres, recrystallization events were observed to initiate in the regions with the highest local deformation which also corresponded to the region with the highest level of stored energy. At a volume fraction of 30 %, the presence of macroscopic shear bands in the matrix also provided suitable sites for the nucleation of recrystallization events.

This work demonstrates the value of trying to examine a complicated problem, such as the mechanical behaviour of composite materials, with a series of simple model experiments. By eliminating the effects of complicated particle shapes and complex spatial distributions of the particles, the present work has allowed for the unambiguous interpretation of important results such as the nature of the flow pattern in the matrix of composite materials. The ability to perform a detailed comparison between the experimental results and FEM calculated results has resulted in validation of the ability to model this type of behaviour with the finite element method. Equally important for this work was the fact that the modelling work was performed in parallel with experimental work. This allowed for the results from the modelling work to influence the direction of experimental work. A good example of this was the modification of the processing path for the samples with square arrangements of fibres to produce a uniform matrix microstructure (see Section 3.2).

Finally, it is important to point out that there exists an opportunity to extend the experimental and modelling work to a series of other interesting problems involved in the behaviour of composite materials. Some ideas for future work will be presented in the next section.

6.2 - Future Work

The development of these techniques for examining the behaviour of composite materials at both local and macroscopic levels offers many opportunities for future work. In the present work, only regular arrangements of fibres have been examined. It would be of interest to study the effects of perturbations in the arrangements of the fibres on the distributions of stress and strain in the sample. This could also include examinations of clustering effects on macroscopic mechanical response and local damage observations. It would also be valuable to develop new techniques for characterizing the spatial distribution of the reinforcing phase.

The extension of the modelling work to include the effects of damage on the subsequent behaviour of composite would also be valuable. A criterion for damage could be incorporated in to the finite element model. A particularly interesting phenomenon relating to damage is the extrusion of matrix material in to the region between cracked particles. This process of damage healing is important to understanding the behaviour of inclusions during large strain forming processes of alloys. The work could also be extended to examine effects of particle shape by incorporating fibres with square or elliptical cross-sections in to the matrix. The reinforcing material could also be changed to study the effects of reinforcing materials that plastically yield during the deformation process (e.g. substitution of Nb or Ta for W). It would also be valuable to extend the model experiments to 3-dimensional situations. However, the experimental difficulties (both for fabrication of the composites and analysis of the deformation pattern) would be more difficult than in the present case.

REFERENCES

Ashby, M.F., 1971, Strengthening Mechanisms in Crystals, ed. A. Kelly and R.B. Nicholson, Applied Science Publishers, London, 137.

Attwood, D.G. and Hazzledine, P.M., 1976, Metallography, 9, 483.

Bao, G., 1992, Acta metall. mater., 40, 2547.

Bao, G., Hutchinson, J.W. and McMeeking, R.W., 1991, Acta metall. mater., 38.

Basinski, S.J. and Basinski, Z.S., 1979, Dislocations in Solids, Volume 4, ed. F.R.N. Nabarro, North-Holland Publishing, New York, 261.

Bergmann, H.W., Frommeyer, G. and Wassermann, G., 1978, In: Proceeding of the Fifth Int. Conf. on Textures of Materials, ed. G. Gottstein and K. Lucke, Springer-Verlag, Vol. II, 371.

Bever, M.B., Holt, D.L. and Titchener, A.L., 1973, Prog. Mats. Sci., 17, 1.

Bohm, H.J. and Rammerstorfer, F.G., 1991, Materials Sci. and Eng., A135, 185.

Bolmaro, R.E., Kocks, U.F., Guerra, F.M., Browning, R.V., Dawson, P.R., Embury, J.D. and Poole, W.J. Acta metall. mater., in press.

Brechet, Y., Embury, J.D., Tao, S. and Luo, L., 1991, Acta metall. mater., 39, 1781.

Brechet, Y., Newell, J., Tao, S. and Embury, J.D., 1993, Scripta metall. mater., 28, 47.

Brockenbrough, J.R., Suresh, S. and Wienecke, H.A., 1991, Acta metall. mater., 39, 735.

Brown, L.M. and Clarke, D.R., 1977, Acta metall., 25, 563.

Brown, L.M. and Stobbs, W.M., 1971a, Phil. Mag., 23, 1185.

Brown, L.M. and Stobbs, W.M., 1971b, Phil. Mag., 23, 1201.

Brown, L.M. and Stobbs, W.M., 1976, Phil. Mag., 34, 351.

Bunge, H.J., 1985, Z. Metallkde., 76, 92.

Chawla, K.K., 1987, Composite Materials, Springer-Verlag, New York, p. 180.

Chawla, K.K. and Metzger, M., 1972, J. Mat. Sci., 7, 34.

Chawla, K.K. and Metzger, M., 1977, Met. Trans. A, 8A, 1681.

Cheskis, H.P. and Heckel, R.W., 1968, Metal Matrix Composites, ASTM STP-438, p.76.

Cheskis, H.P. and Heckel, R.W., 1970, Met. Trans., 1, 1931.

Christman, T., Needleman, A. and Suresh, S., 1989, Acta metall. mater., 37, 3029.

Corbin, S.F., 1992, Low strain Behaviour of a Particulate Reinforced Aluminum Alloy, Ph.D. Dissertation, McMaster University.

Cotterill, P. and Mould, P.R., 1976, Recrystallization and Grain Growth in Metals, J. Wiley & Sons, New York.

Couper, M.J. and Xia, K., 1991, In: Metal Matrix Composites - Processing, Microstructure and Properties, ed. N. Hansen et al., Riso National Lab., Roskilde, Denmark, 291.

Dawson, P.R. private communication.

Doherty, R.D., 1980, In: Recrystallization and Grain Growth of Multi-Phase and Particle Containing Materials, ed. N. Hansen, A.R. Jones and T. Leffers, Riso National Lab., Roskilde, Denmark, 57.

Drucker, D.C., 1965, High Strength Materials, ed. V.F. Zackay, J. Wiley & Sons, New York, p. 795.

Drucker, D.C., 1966, J. Materials, 1, 873.

Embury, J.D., Newell, J.M. and Tao, S., 1991, In: Metal Matrix Composites - Processing, Microstructure and Properties, ed. N. Hansen et al., Riso National Lab., Roskilde, Denmark, 317.

Embury, J.D., Poole, W.J. and Koken, E., 1992, Scripta metall. mater., 27, 1465.

Eshelby, J.D., 1957, Proc. Royal Soc., A241, 376.

Ferry, M., Munroe, P., Crosky, A. and Chandra, T., 1991, In: Metal Matrix Composites - Processing, Microstructure and Properties, ed. N. Hansen et al., Riso National Lab., Roskilde, Denmark, 337.

Gil Sevillano, J., van Houtte, P. and Aernoudt, E., 1981, Prog. Mats. Sci., 25, 69.

Goods, S.H. and Brown, L.M., 1979, Acta metall., 27, 1.

Harris, B. and Ramani, S.V., 1975, J. Mat. Sci., 10, 83.

He, M.Y. and Hutchinson, J.W., 1981, 48, 830.

Herbst, P. and Huber, J., 1978, In: Proceeding of the Fifth Int. Conf. on Textures of Materials, ed. G. Gottstein and K. Lucke, Springer-Verlag, Vol. I, 453.

Hill, R., 1965, J. Mech. Phys. Solids, 13.

Hirsch, P.B. and Humphreys, F.J., 1970, Proc. R. Soc. A318, 45.

Hjelen, J. and Nes, E., 1986, In: Annealing Processes - Recovery, Recrystallization and Grain Growth, ed. N. Hansen et al., Riso National Lab., Roskilde, Denmark, 367.

Hodierne, F.A., 1962-63, J. Inst. Metals, 91, 267.

Hu, M.S., 1991, Scripta metall. mater., 25, 695.

Humphreys, F.J., 1979, Met. Sci.,13, 136.

Humphreys, F.J., 1980, In: Recrystallization and Grain Growth of Multi-Phase and Particle Containing Materials, ed. N. Hansen, A.R. Jones and T. Leffers, Riso National Lab., Roskilde, Denmark, 35.

Humphreys, F.J. and Juul Jensen, D., 1986, In: Annealing Processes - Recovery, Recrystallization and Grain Growth, ed. N. Hansen et al., Riso National Lab., Roskilde, Denmark, 93.

Humphreys, F.J. and Kalu, P.N., 1990, Acta metall. mater., 38, 917.

Humphreys, F.J., Miller, W.S. and Djazeb, M.R., 1990, Mats. Sci. Tech, 6, 1157.

Jaeger, J.C., and Cook, N.G.W., 1976, Fundamentals of Rock Mechanics, Chapman and Hall, London, p. 169.

Jin, I., Burger, G.B. and Lloyd, D.J., 1992, In: The 3rd Int. Conf. on Aluminium Alloys, ed. L. Arnberg, O. Lohne, E. Nes and N. Ryum, Trondheim, Norway, 21.

Juul Jensen, D., Liu, Y.L. and Hansen, N., 1991, In: Metal Matrix Composites - Processing, Microstructure and Properties, ed. N. Hansen et al., Riso National Lab., Roskilde, Denmark, 417.

Kallend, J.S., Kocks, U.F., Rollet, A.D. and Wenk, H.R., 1991, Materials Sci. and Eng., A132, 1.

Kelly, A. and Tyson, W.R., 1965, J. Mech. Phys. Solids, 13, 329.

Kelly, A. and Lilholt, H., 1969, Phil. Mag., 20, 311.

Kocks, U.F., 1988, Los Alamos Polycrystal Plasticity Code, Los Alamos Nat. Lab. report # LA-CC-88-6.

Kocks, U.F., 1989, popLA: preferred orientation package - Los Alamos, Los Alamos Nat. Lab. report # LA-CC-89-18.

Lee, R.E and Harris, S.J., 1974, J. Mat. Sci., 9, 359.

Levy, A. and Papazian, J.M., 1991, Acta metall. mater., 39, 2255.

Lewandowski, J.J. and Liu, C., 1989, Materials Sci. and Eng., A107, 241.

Lilholt, H., 1977a, Acta metall., 25, 571.

Lilholt, H., 1977b, Acta metall., 25, 587.

Lloyd, D.J., 1991, Acta metall. mater., 39, 59.

McDanels, D.L., Jech, R.W., and Weeton, J.W., 1963, NASA Technical Note, NASA TN D-1881, NASA, Washington, D.C.

McDanels, D.L., Jech, R.W., and Weeton, J.W., 1965, Trans. Metallurgical Society of AIME, 233, 636.

McHugh, P.E., Asaro, R.J. and Shih, C.F., 1991, Modelling the Deformation of Crystalline Solids, ed. T. Lowe, A.D. Rollet, P.S. Follansbee and G.S. Daehn, TMS, Warrendale, Pa, p. 369.

Meyers, M.A. and Chawla, K.K., 1984, Mechanical Metallurgy: Principles and Applications. Prentice-Hall, Eglewood Cliffs, NJ, USA, p. 496.

Mummery, P.M., Derby, B. and Scruby, C.B., 1993, Acta metall. mater., in press.

Mummery, P.M. and Derby, B., 1991, In: Metal Matrix Composites - Processing, Microstructure and Properties, ed. N. Hansen et al., Riso National Lab., Roskilde, Denmark, 535.

Mummery, P. and Derby, B., 1989, Fundamental Relations Between Microstructures and Mechanical Properties in MMCs, ed. Gungor and Lian, TMS, Warrendale, p. 161.

Muskhelishvili, N.I., 1953, Some Basic Problems of the Mathematical Theory of Elasticty, 4th edn., translated by J.R.M Radok, Groningen, Noordhoff.

Neumann, P. and Haasen, P., 1971, Phil. Mag., 23, 285.

Newell, J.M., 1990, The Effect of Stress State on Damage Accumulation and Fracture in an Al-SiC Metal Matrix Composite. Master's Thesis, McMaster University.

Pederson, O.B., 1983, Acta metall., 31, 1795.

Pedersen, O.B., 1990, Acta metall. mater., 38, 1201.

Porter, J.R. and Humphreys, F.J., 1979, Metal Science, 13, 82.

Poudens, A., Bretheau, T. and Bacroix, B., 1991, In: Metal Matrix Composites - Processing, Microstructure and Properties, ed. N. Hansen et al., Riso National Lab., Roskilde, Denmark, 595.

Povirk, G.L., Needleman, A. and Nutt, S.R., 1991, Mat. Sci. and Eng., A132, 31.

Ribes, H., Da Silva, R., Surey, M. and Bretheau, T., 1990, Materials Sci. Tech, 6, 621.

Semiatin, S.L., Lahoti, G.D. and Jonas, J.J., 1985, Metals Handbook: Mechanical Testing, vol. 8, 9th Edition, ASM, Metals Park, OH., p. 164.

Sowerby, R., Chu, E. and Duncan, J.L., 1982, J. Strain Analysis, 17, 95.

Tao, S., 1991, Damage Accumulation and Fracture in Metal Matrix Composites. Master's Thesis, McMaster University.

Taya, M. and Arsenault, R.J., 1989, Metal Matrix Composites: Thermomechanical Behaviour, Pergamon Press, Oxford, p. 52.

Wassermann, G., Bergmann, H.W. and Frommeyer, G., 1978, In: Proceeding of the Fifth Int. Conf. on Textures of Materials, ed. G. Gottstein and K. Lucke, Springer-Verlag, Vol. II, 37.

Weatherly, G.C., 1968, Met. Sci. Jnl., 2, 237.

Wenk, H.R., 1985, Preferred Orientation in Deformed Metals and Rocks: An Introduction to Modern Texture Analysis, ed. H.R. Wenk, Academic Press Inc., Toronto, p. 11.

Withers, P.J., Stobbs, W.M. and Pederson, O.B., 1989, Acta metall., 37, 3061.

Yang, J., Cady, C., Hu, M.S., Zok, F., Mehrabian, R. and Evans, A.G., 1990, Acta metall. mater, 38, 2613.

Yoda, S., Kurihara, N., Wakashima, K. and Umekawa, S., 1978, Met. Trans. A, 9A, 1229.

Zok, F., 1988, The Influence of Hydrostatic Pressure on Fracture. PhD Thesis, McMaster University.

Zok, F., Embury, J.D., Ashby, M.F. and Richmond, O., 1988, In: Metallic and Ceramic Composites, ed. S.I. Anderson, H. Lilholt and O.B. Pederson, Riso National Lab., Roskilde, Denmark, 517.